



**NTNU – Trondheim**  
Norwegian University of  
Science and Technology

# Structural Evolution of the Porsa Imbricate Stack (Finnmark, northern Norway)

Based on field mapping and microstructural  
analysis

**Hans Jørgen Kjøll**

Geology

Submission date: May 2015

Supervisor: Giulio Viola, IGB

Norwegian University of Science and Technology  
Department of Geology and Mineral Resources Engineering





## Abstract

This thesis presents the results from detailed lithological and structural mapping of the northwestern part of the RTW, which consists of the large-scale compressional Porsa Imbricate Stack (PIS) that formed during the Caledonian Orogeny. Detailed mesoscopic and microstructural analysis of fault rocks reveal that several different processes facilitated strain localization within the stack. Early Caledonian NW–SE shortening caused tightening of inherited NE–SW-trending Paleoproterozoic folds. Flexural slip led to ingress of fluids that promoted alteration of the host rocks and the production of phyllosilicates through extensive phyllonitization processes leading to strain localization and the formation of reverse faults parallel to the fold limbs. Further deformation was accommodated by localized slip along these faults. A weak layer consisting of metavolcanic tuffs may have acted as a relatively strong décollement promoting the formation of primarily foreland verging faults. At late stages of the PIS formation, a shift in deformation mechanisms caused folding of the PIS faults. Extensive normal reactivation of the inherited faults occurred during two phases of extension in the Paleozoic and the Mesozoic.

Microstructural investigations by optical microscopy and Electron Backscatter Diffraction (EBSD) of a pre- to syntectonic quartz vein deformed within the Nussirjávri Fault Zone are presented. Viscous deformation in the vein was initially accommodated by quartz basal  $\langle a \rangle$  slip. Under the prevailing deformation conditions, however, dislocation glide- and possibly creep-accommodated deformation of quartz was inefficient, and resulted in localized strain hardening. In response to the 1) hardening, 2) progressive and cyclic increase of the fluid pressure, and 3) increasing competence contrast between the vein and the weakly foliated host phyllonite, vein quartz crystals began to deform by brittle processes along specific, suitably oriented lattice planes, creating microgouges along microfractures. Nucleated new grains rapidly sealed these fractures as fluids penetrated the actively deforming system. The grains grew initially by solution-precipitation and later by grain boundary migration. It is suggested that the different initial orientation of the vein crystals led to strain accommodation by different mechanisms in the individual crystals, generating remarkably different microstructures. Crystals suitably oriented for basal slip, for example, accommodated strain mainly viscously and experienced minor fracturing. Instead, crystals misoriented for basal slip hardened and deformed predominantly by domainal fracturing.



## Sammendrag

Denne avhandlingen rapporterer resultatene fra detaljert litologisk og strukturell kartlegging av den nordvestlige delen av Repparfjord Tektoniske Vindu (RTW), som består av en stor kompresjons imbrikat struktur, kalt Porsa Imbrikat Stabel (PIS) som ble dannet under den kaledonske orogenesisen. Detaljerte mikrostrukturelle og mesoskopiske analyser av forkastningsbergarter viser at flere ulike prosesser var aktive under lokalisering av deformasjon og dannelsen av PIS. Tidlig kaledonsk NV-SØ kompresjon forårsaket fortetning av Paleoproterozoiske, NØ-SV rettede folder. Fleksurell slipp førte til inntrengning av fluider som fremmet kjemisk omvandling av vertsbergartene og produksjon av sjiktsilikater gjennom omfattende «phyllonitiserings» prosesser, som igjen førte til videre deformasjon og dannelse av forkastninger parallelt med folde sjenklene. Et svakt lag bestående av metavulkanske tuffer kan ha fungert som en relativt sterk såleforkastning og fremmet dannelsen av forkastninger med sørøstlig vergens. Sent i utviklingen av PIS var det et skifte i deformasjonsmekanismer som førte til folding av forkastningene. I Paleozoikum og Mesozoikum ble PIS forkastningene reaktivert som normalforkastninger.

Videre Presenteres undersøkelser med bruk av optisk mikroskopi og «Electron Backscatter Diffraksjon» (EBSD) av en pre- til syntektonisk kvartsåre som ble deformert i en av PIS forkastningene. Deformasjon i åren ble først tatt opp duktilt ved dislokasjons glidning langs basal planet i <a> retning. Under de rådende deformasjonsforhold var imidlertid ikke dislokasjons glidning eller kryp effektiv og resulterte i herding av krystallene. På grunn av 1) herdingen, 2) progressiv og syklisk økning av fluidtrykket, og 3) økende kompetanse kontrast mellom kvartsåren og den svake vertsbergarten begynte kvartsårekrystallene å deformeres ved sprø prosesser langs spesifikke og godt orienterte gitter plan og dannet deretter forkastningsmel langs de intrakrystallinske bruddene. Nye korn begynte raskt å vokse inne i bruddene og tettet sprekkene samtidig som væsker penetrerte det aktivt deformerende systemet. Kornene vokste først ved utfelling av kvarts fra fluiden, før korngrensemigrasjon tok over. Det blir foreslått at de forskjellige orienteringene til kvartsårekrystallene førte til at formforandring ble tatt opp med ulike mekanismer i de enkelte krystallene og det ble dannet bemerkelsesverdige ulike mikrostrukturer. Krystaller med en god orientering for basal slipp, tok opp deformasjonen hovedsakelig duktilt og gjennomgikk kun minimal oppsprekking. Krystaller som var orientert ugunstig for basal slip herdet og deformerte hovedsakelig ved oppsprekking.



## Acknowledgements

This thesis is part of my Master of Science degree in Bedrock and Resource Geology at the Department of Geology and Mineral Resources Engineering, Norwegian University of Science and Technology (NTNU). It has been funded in part by NTNU and NGU.

I am truly grateful for my supervisor Prof. Dr. Giulio Viola who has gone, in my opinion, far beyond what is expected for a M.Sc. supervisor and encouraged me to pursue a publication already during my masters. I want to thank you for all the constructive comments and feedback you have given me during the course of these two years. You have inspired me to work hard every day and I have learned so much from you during fieldwork and long days at the office. Thank you!

Espen, you know how grateful I am for all the discussions we have had through the last two years. I have bombarded you with questions and you have always taken the time to answer. I also want to thank you for all the loooong days at the office at NGU, all the burgers and all the good times we have had through the last three years! I am very glad that we have become such good friends and I look forward to coming years of friendship and collaborations.

I would also like to express my gratitude towards Bjørn Eske Sørensen for helping me out with the EBSD and answering all my questions. In addition, I would like to thank the staff at NGU's Berggrunnslag for being a great source of information and knowledge.

I had a short but unforgettable stay at Plymouth University together with Luca Menegon during preparation of the manuscript, thank you so much Luca, for contributing with your knowledge on quartz microstructures. Thank you Gustavo Viegas, for providing accommodation, food, Leblon and good jazz music.

None of this, however, would have been possible without the most supportive person in the world by my side, Julie. Thank you for sticking out with me all these years.

These five years at NTNU would not have been the same without the greatest bunch of students in the history of geology, the SHGC and G4 (Super Hardcore Geology Colloquium and Geologistuderendes Gutte Grotte Gruppe). Martin, Eero and Ivar, the five years spent at NTNU would not have been the same without you three.



# Table of content

<b>ABSTRACT .....</b>	<b>I</b>
<b>SAMMENDRAG .....</b>	<b>III</b>
<b>ACKNOWLEDGEMENTS .....</b>	<b>V</b>
<b>ABBREVIATIONS:.....</b>	<b>XI</b>
<b>1. INTRODUCTION AND AIMS OF THE STUDY .....</b>	<b>1</b>
<b>2. BRITTLE-VISCOUS DEFORMATION OF VEIN QUARTZ.....</b>	<b>5</b>
2.1 ABSTRACT .....	5
2.2 INTRODUCTION .....	6
2.3 GEOLOGICAL SETTING .....	7
2.3.1 <i>Regional geological setting</i> .....	7
2.3.2 <i>Nussirjávri Fault Zone</i> .....	9
2.4 ANALYTICAL METHOD .....	10
2.5 RESULTS .....	11
2.5.1 <i>Sample description</i> .....	11
2.5.2 <i>Microstructural and EBSD analysis</i> .....	14
2.5.2.1 Domain 1 .....	15
2.5.2.2 Domain 2 .....	17
2.5.2.3 Domain 3 .....	18
2.5.2.4 Domain 4 .....	20
2.6 DISCUSSION.....	22
2.6.1 <i>Strain localization history within the different domains</i> .....	22
2.6.2 <i>Sealing of the microfractures</i> .....	26
2.6.3 <i>Mechanical implications for the PIS development</i> .....	29
2.7 CONCLUSION .....	31
<b>3. METHODS.....</b>	<b>33</b>
3.1 FIELD TECHNIQUES.....	33
3.2 THIN SECTION PREPARATION AND MICROSCOPY .....	35
3.3 SEM.....	36
3.3.1 <i>BSE</i> .....	36
3.3.2 <i>SEM-EDS</i> .....	36
3.3.3 <i>EBSD</i> .....	36
2.3.3.1 <i>Pattern acquisition</i> .....	37
2.3.3.2 <i>Processing</i> .....	38
<b>4. GEOLOGICAL AND TECTONIC SETTING .....</b>	<b>41</b>
4.1 THE FENNOSCANDIAN SHIELD.....	41

4.1.2 RTW stratigraphy and correlations.....	42
4.1.2 Svecofennian orogeny and Neoproterozoic deformation episodes .....	46
4.2 CALEDONIAN INFLUENCE .....	46
4.3 PORSA IMBRICATE STACK .....	47
<b>5. MAPPED LITHOLOGIES / RESULT .....</b>	<b>51</b>
5.1 SALT VATN GROUP.....	52
5.1.1 Ulverygg Formation .....	53
5.1.2 Dypelv Formation.....	53
5.1.3 Stangvatn Formation .....	54
5.1.4 Gorahatjohka Formation .....	54
5.2 HOLMVATN GROUP (SE LIMB OF ULVERYGG ANTICLINE) .....	59
5.3 NUSSIR GROUP (NE LIMB OF ULVERYGG ANTICLINE).....	59
5.3.1 Krokvatn Formation .....	59
5.3.2 Svartfjell Formation .....	60
5.3.3 Mafic intrusive .....	60
5.4 PORSA GROUP .....	64
5.4.1 Vargsund Formation .....	64
5.4.1.1 Nussirjávri member.....	64
5.4.1.2 Fiskelv member .....	65
5.4.2 Kvalsund Formation .....	65
5.4.3 Bierajávri Formation .....	66
5.4.3.1 Rundvatn Member .....	66
<b>6. STRUCTURAL ANALYSIS OF THE MAPPED AREA.....</b>	<b>71</b>
6.1 FOLDING .....	73
6.2 FAULTING.....	75
6.2.1 Nussirjávri Fault Zone (NFZ).....	76
6.2.2 Skinnfjellet Fault Zone (SFZ).....	80
6.2.3 Western Skinnfjellet Fault Zone (WSFZ).....	86
6.2.4 Langvasstinden Fault Zone (LFZ).....	87
6.2.5 Beretsjord Fault Zone (BFZ).....	90
6.2.6 The Ausa Fault Zone (AFZ) .....	95
6.2.7 Solhaugen Fault Zone (SoFZ).....	97
6.2.8 Gjevebukta Fault Zone (GFZ).....	100
<b>7. DISCUSSION .....</b>	<b>105</b>
7.1 STRUCTURAL EVOLUTION OF THE PIS .....	105
7.1.1 The folding history of RTW.....	105
7.1.2 Dextral transpression .....	109
7.1.3 Thrust development and their evolution.....	110



7.1.3.1 Décollement vs. solitary thrusts .....	110
7.1.3.2 Dynamic evolution of the thrusts .....	111
7.1.3.3 Dolostone deformation .....	113
7.1.3.4 Major deformation structures within the PIS.....	113
7.1.4 <i>Timing of deformation along the SFZ</i> .....	117
7.1.5 <i>Reactivation history</i> .....	118
7.1.6 <i>Conceptual model for the structural evolution of PIS</i> .....	119
7.2 FAULT WEAKENING AND DEFORMATION MECHANISMS .....	122
7.2.1 <i>The role of fluid infiltration and overpressure</i> .....	122
7.2.2 <i>Phyllonitization</i> .....	124
7.2.2.1 Dolomite decarbonation.....	125
7.2.2.2 Metabasalt carbonation .....	126
7.2.2.3 Feldspar breakdown .....	126
7.2.3 <i>Mechanical evolution of imbricate systems</i> .....	127
7.2.4 <i>Stick-slip vs. creep</i> .....	128
<b>8. CONCLUSIONS</b> .....	<b>131</b>
<b>9. PERSPECTIVES</b> .....	<b>133</b>
<b>REFERENCES</b> .....	<b>135</b>
<b>APPENDIX A</b> .....	<b>1</b>
<b>APPENDIX B</b> .....	<b>5</b>
<b>APPENDIX C</b> .....	<b>15</b>
<b>APPENDIX D</b> .....	<b>17</b>



## Abbreviations:

- Ab** – Albite  
**AFS** – AUSA Fault Zone  
**BGS** – British Geological Survey  
**BLG** – Bulging Recrystallization  
**Cc** – Calcite  
**Chl** – Chlorite  
**CIP** – Computer Integrated Polarization microscopy  
**CPO** – Crystallographic Preferred Orientation  
**Dm** – Dolomite  
**EBSD** – Electron Backscatter Diffraction  
**ECC** – Extensional Crenulation Cleavage  
**FEb** – Fine Extinction Bands  
**GFS** – Gjevebukta Fault Zone  
**GPS** – Global Positioning System  
**HP-SEM** – High Pressure Scanning Electron Microscope  
**Ill** – Illite  
**KF** – Kvenklubben Fault  
**KNC** – Kalak Nappe Complex  
**(b/s/g)LEB** – (blocky/straight/granular) Localized Extinction Band  
**NFZ** – Nussirjavri Fault Zone  
**NGU** – Geological Survey of Norway  
**OIM** – Orientation Imaging Microscopy  
**PIS** – Porsa Imbricate Stack  
**Qz** – Quartz  
**RTW** – Repparfjord Tectonic window  
**SEM** – Scanning Electron Microscope  
**SFZ** – Skinnfjellet Fault Zone  
**SGRR** – SubGrain Rotation Recrystallization  
**SIP** – Seiland Igneous Province  
**Tlc** – Talc  
**TDR** – Tilt derivative  
**VP-SEM** – Variable Pressure Scanning Electron Microscope  
**WDS** – Wavelength-dispersive spectroscopy  
**WEB** – Wide Extinction Bands  
**WSFZ** – Western Skinnfjellet Fault Zone



## 1. Introduction and aims of the study

The geology of Finnmark county, northern Norway, has been studied in great detail over the last century (e.g. Holtedahl, 1918, 1932; Reusch, 1891; Reusch et al., 1891; Siedlecka, 1975; Sturt et al., 1975) partly due to its great economic potential. Recently, as a part of the initiative MINN (Mineral Resources in Northern Norway) launched by the Norwegian government with the goal to assess the mineral potential of this region, high-resolution airborne geophysics has been acquired over most of the county (Ofstad et al., 2013), including the 1200 km<sup>2</sup> geological domain known as the Repparfjord Tectonic Window (RTW; Reitan, 1963), a Paleoproterozoic basement culmination exposed within the Neoproterozoic to Phanerozoic Caledonian Nappe complex. This survey has provided excellent background data for follow-up geological field and mapping campaigns within many target areas. Among them the northwesternmost part of the RTW, which represents the starting point of this M.Sc. thesis. Particular attention has been paid to the RTW due to the great economic potential of the Nussir Cu deposit, a chalcopyrite-bornite stratabound deposit hosted within a doloarenitic sequence, currently estimated to contain 66 Mt of ore at an average 1,2% Cu grade (Nussir, 2014a, b).

In order to gain better understanding of the structural evolution and age of the deposit and to create new models for other smaller metal occurrences in the area and thus to refine the understanding of the metallogenic processes, an important mapping campaign was launched in the area. A part of this, one PhD thesis was conducted by Espen Torgersen on the dating of faults and mineralizations and revision of the RTW stratigraphy. Furthermore, a previous M.Sc. student, Håvard Smeplass finished his master thesis on structural and geological investigations in 2013 and several other researchers of the Geological Survey of Norway (NGU) have conducted studies in the area working mainly on regional correlation and metallogenesis (Sandstad, 2008, 2010; Viola et al., 2008).

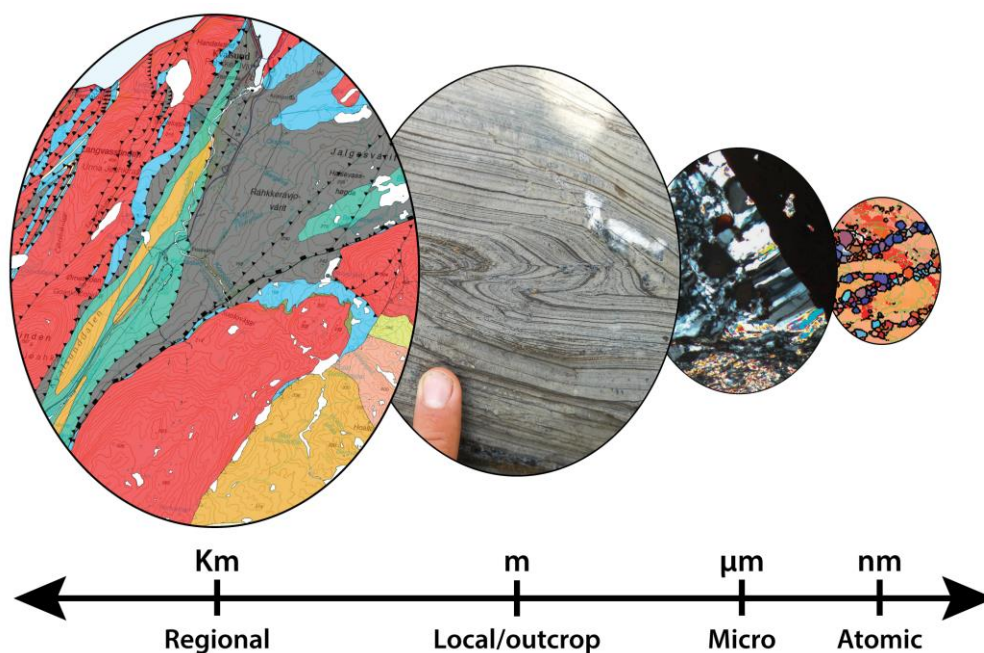
The RTW was investigated and described in good detail first by Reitan (1963) and was later remapped by Oftedahl (1980), Pharaoh et al. (1983) and Nilsen and Nilsson (1996). The window exposes the northernmost part of the Fennoscandian Shield, a multiply deformed terrane consisting of Paleoproterozoic metasedimentary and metavolcanic rocks (e.g. Pharaoh et al., 1982; Pharaoh et al., 1983; Reitan, 1963).

The northwestern part of the RTW consists of a compressional imbricate structure, the Porsa Imbricate Stack (PIS; Torgersen and Viola, 2014). The PIS was earlier referred to as the Porsa Duplex (Gayer et al., 1987), but (Torgersen and Viola, 2014) proposed the new definition because there is

little evidence for a discrete fault to flatten out and produce a roof thrust, therefore better describing the present days geometry of the stack.

Fold-and-thrust belts, their internal geometry, mechanics and governing factors steering their formation have been described in great detail by, for example, the pioneering work of Dahlen et al. (1984), Dahlen and Suppe (1988), Dahlen (1984), Davis et al. (1983) and Elliott (1980). However, there are still a number of conceptual questions regarding these structures, such as the understanding of faulting vs. folding (Simpson, 2009), their seismic behavior (e.g. Wang and Hu, 2006) and the role of fluid pressure (e.g. Strayer et al., 2001) that are not yet fully understood. Furthermore, as the use of numerical and analogue models has become increasingly more popular, researchers have been able to better constrain several factors that govern the geometry and architecture of fold-and-thrust belts, such as the nature of the basal décollement, the properties and the influence of fluids as well as the importance of surface processes (e.g. Bonini, 2007; Erickson, 1996; Fyfe and Kerrich, 1985; Gabellone et al., 2013; Hilley and Strecker, 2004; Simpson, 2006, 2009). Buiter (2012) provides a comprehensive review of the current status of knowledge on this broad subject.

If we zoom into the individual folds and faults and exploit the principle of scale invariance (Fig. 1-1), there are still a number of unanswered questions as to what mechanisms enable the imbricate structure to deform and how these mechanisms work at a variety of environmental conditions. These questions are universal and not bound by the conditions within a specific fold-and-thrust belt, and are thus valid for all systems deforming under upper- to mid-crustal conditions.



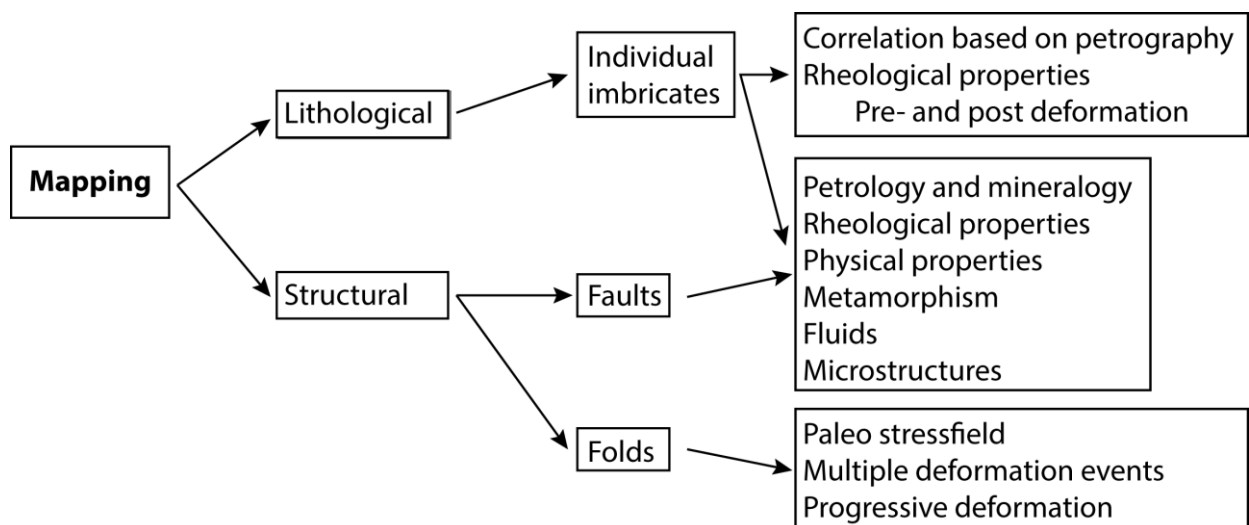
**Figure 1-1:** Scale invariance. Features in map view can also be recognized in the field, in thin section and all the way down to the crystal lattice, as constrained by Electron Backscatter diffraction.

## 1. Introduction and aims of the study

To investigate the active mechanisms during deformation it is necessary to look within the rocks' richest archive, that is, the microstructural evidence. In recent years a vast amount of work has been poured into understanding how minerals deform, and constraints have been derived on the role of pressure, temperature, strain rate and the contribution of fluids (e.g. Fitz Gerald and Stünitz, 1993; Hirth and Tullis, 1992; Kronenberg and Tullis, 1984; Stipp et al., 2002a; Stipp et al., 2002b). This research has enabled us to investigate how rocks deform under various environmental conditions at the scale of the crystal lattice.

Much of the understanding started with Sander (1911)'s paper on the qualitative quantification of microstructures through the use of a universal stage. This has enabled us to understand how the orientation of the c-axis of uniaxial minerals changes in response to the finite amount of deformation accommodated and to the prevailing environmental conditions during strain accommodation. Heilbronner and Pauli (1993) significantly improved the method by integrating computers to produce large datasets of quantitative measurements. However, as Scanning Electron Microscopes (SEM) became standard equipment in many geology laboratories, Electron Backscatter Diffraction (EBSD) detectors became readily available, enabling the complete quantification of all crystallographic axes in most minerals and thus a much better understanding of the fundamental processes active at the lattice scale during viscous deformation.

The aim of this MSc project is to understand the complex evolution and the first-order geometry of the PIS (Fig. 1-2). This is done through a multidimensional approach where the principle of scale invariance is utilized. First, the structures and lithologies of the northern part of the PIS were mapped. Fieldwork also permitted sampling of fault rocks for comprehensive petrographic investigations of the deformed lithologies and fault rocks in the mapped area.



**Figure 1-2:** Aims of the study. Mapping is an essential foundation on which more detailed analyses can be built on.

Secondly, by progressively zooming into the faults of the PIS, the processes that enabled the formation of the compressional stack have been investigated through detailed mineralogical and petrological investigations. By zooming even further, the fundamental mechanism that enabled strain to localize were investigated by the careful analysis of representative microstructures within individual minerals.

As a part of this study, the manuscript "Brittle-viscous deformation of vein quartz under fluid-rich lower greenschist facies conditions" by the author of this thesis, Giulio Viola, Luca Menegon and Bjørn Eske Sørensen has been accepted for publication in the special issue "Deformation mechanisms and ductile strain localization in the lithosphere" in the open access, peer-reviewed journal Solid-Earth. The manuscript is currently in press. It can be found in section 2 and can be downloaded from [www.solid-earth.net](http://www.solid-earth.net).

The thesis is organized in such a way that the paper is presented first as this is a self-standing, general work on deformation mechanisms in quartz at the brittle-ductile transition, before the results of the field work and thin section analysis are presented and discussed.



## 2. Brittle-viscous deformation of vein quartz

The content of this chapter has been accepted to be published in *Solid Earth*. *Kjøll H. J., Viola G., Menegon L., & Sørensen B. E., 2015. Brittle-viscous deformation of vein quartz under fluid-rich lower greenschist facies conditions.*

### 2.1 Abstract

We studied by EBSD and optical microscopy a coarse-grained (c. 0,5 - 6 mm) quartz vein embedded in a phyllonitic matrix to gain insights into the recrystallization mechanisms and the processes of strain localization in quartz deformed under lower greenschist facies conditions, broadly coincident with the brittle-viscous transition. The vein deformed during faulting along a phyllonitic thrust of Caledonian age within the Porsa Imbricate Stack in the Paleoproterozoic Repparfjord Tectonic Window in northern Norway. The phyllonite hosting the vein formed at the expense of a metabasaltic protolith through feldspar breakdown to form interconnected layers of fine, synkinematic phyllosilicates. In the mechanically weak framework of the phyllonite, the quartz vein acted as a relatively rigid body. Viscous deformation in the vein was initially accommodated by quartz basal slip. Under the prevailing deformation conditions, however, dislocation glide- and possibly creep-accommodated deformation of quartz was inefficient, and this resulted in localized strain hardening. In response to the 1) hardening, 2) progressive and cyclic increase of the fluid pressure, and 3) increasing competence contrast between the vein and the weakly foliated host phyllonite, vein quartz crystals began to deform by brittle processes along specific, suitably oriented lattice planes, creating microgouges along microfractures. Nucleated new grains rapidly sealed these fractures as fluids penetrated the actively deforming system. The grains grew initially by solution-precipitation and later by grain boundary migration. We suggest that the different initial orientation of the vein crystals led to strain accommodation by different mechanisms in the individual crystals, generating remarkably different microstructures. Crystals suitably oriented for basal slip, for example, accommodated strain mainly viscously and experienced only minor fracturing. Instead, crystals misoriented for basal slip hardened and deformed predominantly by domainal fracturing. This study indicates the importance of considering shear zones as dynamic systems wherein the activated deformation mechanisms may vary through time in response to the complex temporal and spatial evolution of the shear zone, often in a cyclic fashion.

## 2.2 Introduction

Deformation of quartz at low-grade metamorphic conditions has been the subject of a vast number of microstructural studies aiming to unravel the mechanisms that control strain accommodation therein and to derive parameters of general validity for the rheology of quartz-rich systems at shallow to mid crustal levels (e.g. Dell'Angelo and Tullis, 1996; Hirth and Beeler, 2015; Hirth and Tullis, 1992; Holyoke and Tullis, 2006; Menegon et al., 2008; Stipp and Kunze, 2008; Stipp et al., 2002a; Trepmann and Stöckhert, 2009). In spite of significant recent advances, however, much remains unexplored and unaccounted for, such as 1) The role of fluid-rock interaction on the microstructural development of quartz, 2) The effect of contrasting rheology and of the resulting strain partitioning between matrix and quartz porphyroclasts, and 3) The feedback mechanisms between brittle and viscous processes. Recent technological developments have made powerful methodologies such as electron backscattered diffraction (EBSD; e.g. Adams et al., 1993; Prior et al., 1999; Prior et al., 2009) readily available. This permits extremely detailed investigations and quantification of microstructures and, thereby, the derivation of refined conceptual models of the deformation mechanisms in quartz at the broadly defined brittle-viscous transition.

Intragrain quartz microstructures characterized by bands of fine new grains in large porphyroclasts have been noted and described as standard for low-grade deformed quartz in a number of studies, both experimental and natural (e.g. Menegon et al., 2008; van Daalen et al., 1999; Vernooij et al., 2006b). These microstructures tend to develop during the very early stages of viscous deformation in quartz and are thus studied to better understand strain localization under very low-grade metamorphic conditions. Four mechanisms have been proposed to explain their occurrence: 1) Progressive subgrain rotation recrystallization with subsequent grain boundary sliding (Bestmann and Prior, 2003), 2) Intra-pore growth by dissolution-precipitation (e.g. den Brok and Spiers, 1991; Hippertt and Egidio-Silva, 1996), 3) Fracturing along specific crystallographic planes with subsequent fragment rotation (e.g. den Brok, 1992; van Daalen et al., 1999; Vernooij et al., 2006b), and 4) Localized recrystallization along Dauphiné twins (Menegon et al., 2011b; Stipp and Kunze, 2008). van Daalen et al. (1999) observed that bands of new grains tend to develop preferentially along the rhomb direction within the deforming crystal. Trepmann et al. (2007) studied further the importance of these microstructures by means of carefully designed experiments, wherein they investigated deformation at the tip of a seismic fault. They could reproduce similar microstructures by deforming moderately wet quartz under high stresses before annealing it quasi-statically under dry conditions.

We aim herein to investigate further how these characteristic microstructures develop in quartz at the brittle-viscous transition in a tectonically active environment wherein fluids and competence contrasts between the actively deforming mineral phases induce cyclic oscillations between brittle

## 2. Brittle-viscous deformation of vein quartz

and viscous conditions. To do so, we studied in detail the microstructure of a quartz vein embedded in a phyllonitic matrix. The vein, which crystallized statically prior to deformation, permitted an assessment of the influence exerted by the different initial orientations of the deformed quartz crystals on the accommodation of subsequent strain increments by either brittle or viscous processes. The different initial orientations of vein quartz grains caused the development of drastically different end microstructures within a very small volume of rock, thus allowing the critical and comparative analysis of the different deformation mechanisms that acted simultaneously during deformation.

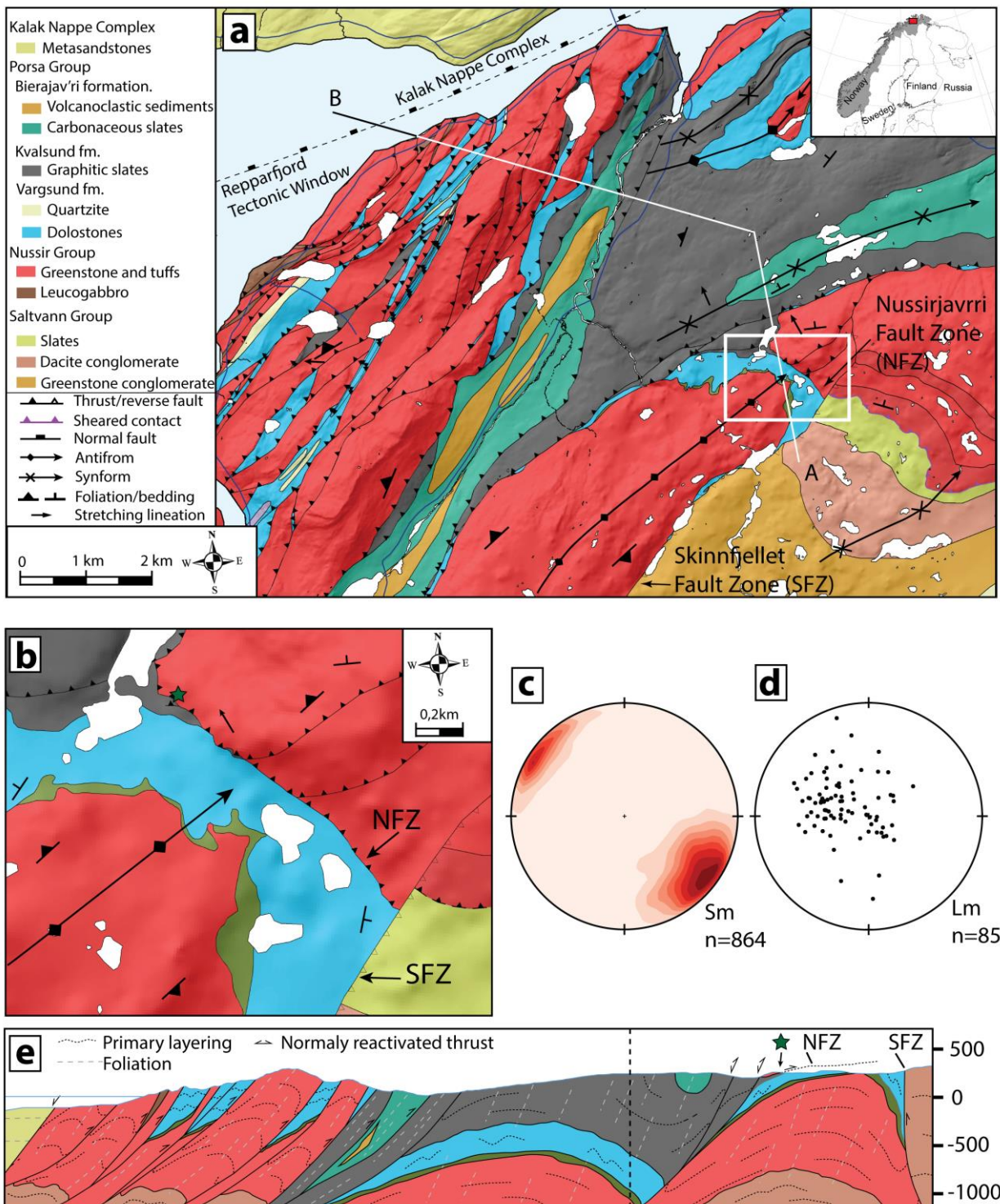
## 2.3 Geological setting

### 2.3.1 Regional geological setting

The study area is located within the Repparfjord Tectonic Window (RTW), the northernmost exposed termination of the Fennoscandian Shield in northern Norway (Fig. 1). The RTW is a window through the Scandinavian Caledonides, which in the study area consist of greenschist to amphibolite-facies metapelites, metapsammites and marbles, with intercalated gneissic slivers (e.g. Gee et al., 2008; Roberts, 2003; Torgersen et al., 2014). The RTW exposes a metasupracrustal sequence formed by greenschist to lower amphibolite facies metasedimentary and metavolcanic rocks, ranging from clastic and volcanoclastic rocks to ultramafic and rhyolitic calc-alkaline to tholeiitic volcanic rocks (Pharaoh, 1985a; Pharaoh et al., 1983). K-Ar dating suggests that they deformed under greenschist-facies conditions until c. 1840 Ma ago, with formation of km-scale upright folds (e.g. Pharaoh et al., 1982).

The northwesternmost part of the RTW shows a set of strongly deformed tectonic imbricates, stacked up to form the Porsa Imbricate Stack (PIS; Torgersen and Viola, 2014; Fig. 1a). Shortening and imbrication within the PIS occurred during the Silurian Caledonian orogeny, which accommodated overall NW-SE shortening and c. E-ward nappe transport (Rice, 1998). As deformation localized during development of the PIS, discrete thrust faults nucleated on the limbs of inherited Paleoproterozoic folds. These tightened and acquired a SE-vergence during the late stages of shortening of the PIS. The Caledonian overprint within the RTW becomes progressively less penetrative to the SE where the imbricate stack terminates against the sub-vertical Skinnfjellet Fault Zone, a dip-slip reverse fault (SFZ; Fig. 1a). Rocks in the immediate footwall of the floor Caledonian décollement underwent greenschist facies metamorphism and were openly refolded around NE-moderately to gently plunging fold axes. Regional metamorphism was constrained to 430-410 Ma by Dallmeyer et al. (1988) by Ar-Ar dating on rejuvenated micas.

In the north, the SFZ cuts a gently dipping thrust that accommodated SE-ward transport at the front of the PIS, the Nussirjávri Fault Zone (NFZ; Fig. 1a), which is where the studied quartz vein was sampled.

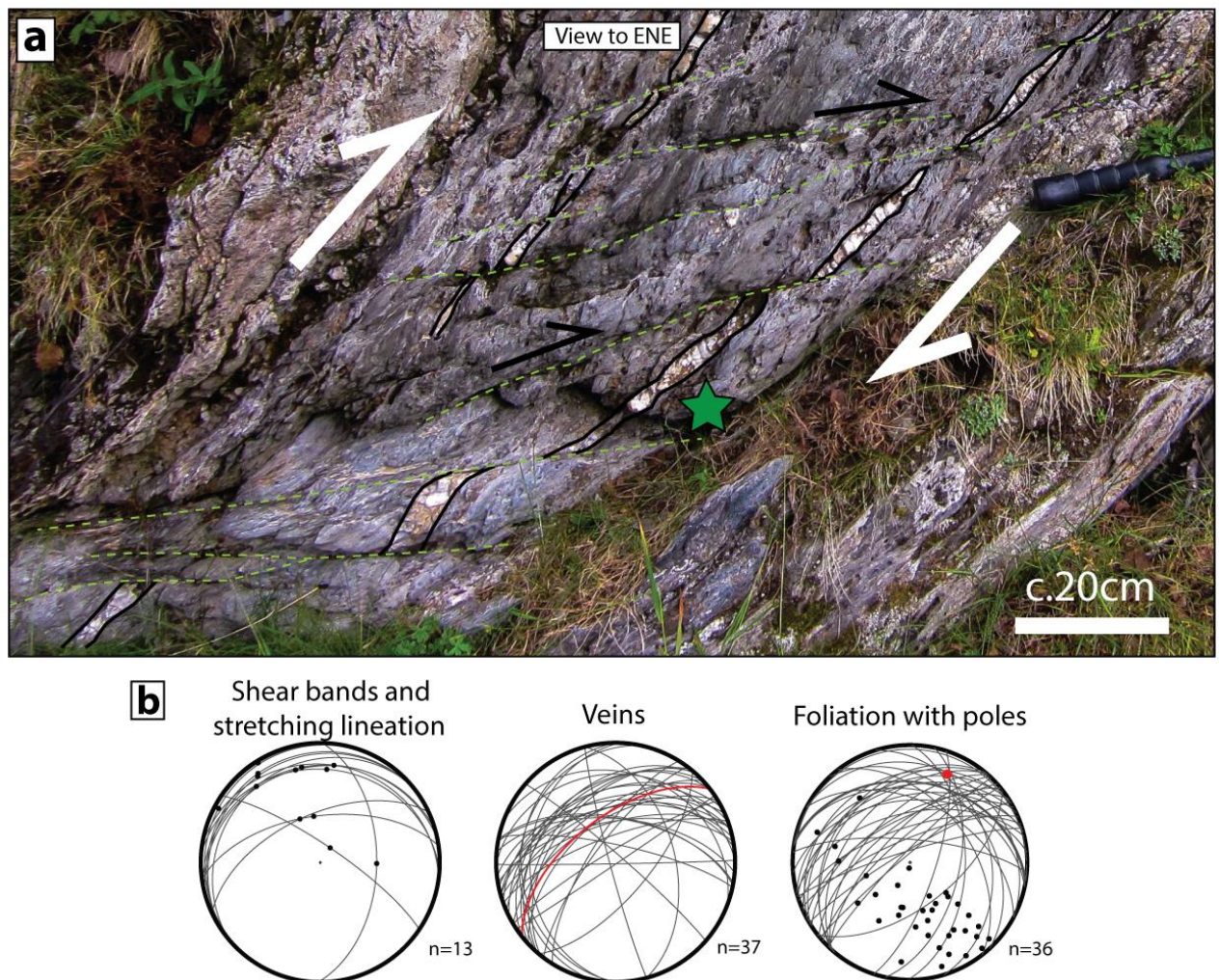


**Figure 2-1:** (a) 1:50000 geological map of the northwestern part of the Repparfjord Tectonic Window. Doglegged line: trace of cross section in (e). White rectangle: location of detailed map in (b). Inset shows the location of the study area in northern Norway. (b) Close-up of the Nussirjávri Fault Zone (NFZ) and sample location shown by green star. (c) and (d) Contoured foliation and stretching lineation measurements, respectively, from the mapped area (lower hemisphere projection). (e) Cross section along the doglegged line in (a). Black dashed line: folded primary layering, gray dashed line: axial planar foliation. Green star: sample location.



### 2.3.2 Nussirjávri Fault Zone

The NFZ is interpreted as an out-of-sequence thrust fault that juxtaposes sub-aqueous extrusive basalts interlayered with clastic to conglomeratic agglomerates and mafic tuffs in the hanging wall against younger slates and dolostones in the footwall. The fault plane is well exposed along strike for c. 1 km (Fig. 1b). It varies in thickness between 10 cm and several meters, it dips moderately towards the NNE and bears NW-plunging stretching lineations. Kinematic indicators, both at the meso- and micro-scale (Fig. 2a), indicate top-to-the-SE reverse kinematics, thus consistent with the regional transport direction of the PIS as a whole. The NFZ is folded openly around a fold axis plunging gently to moderately towards the NNE, consistent with the geometry of a sub-regional folding phase of inferred Caledonian age (e.g. Pharaoh et al., 1983; Rice, 1998; Torgersen and Viola, 2014; Fig. 2b)



**Figure 2-2:** (a) Veins (outlined by black lines) cut by gently NNW-dipping shear bands (green dashed lines) that create a pervasive ECC fabric at the outcrop scale. The NFZ fault core is located 2 m farther up. Sample location is indicated by the green star. Hammer handle for scale. (b) Orientation of key structural elements of the NFZ in lower hemisphere projections. Left stereonet: Shear bands related to the NFZ and related stretching lineations. Middle stereonet: Veins along the NFZ. The sampled vein is indicated by the red great circle. Right stereonet: Great circles and poles of NFZ mylonitic and phyllonitic foliation planes indicating that the NFZ is folded around a calculated axis oriented 024/19 as indicated with a red point.

The NFZ fault core varies in composition as a function of the lithologies affected by deformation. Where the fault deforms graphitic slates, the NFZ has a well-developed mylonitic core. Several large clasts of both graphitic slate and partially decarbonized dolostone are found within the mylonitic foliation. Elsewhere, where the hanging wall porphyritic basalt forms the fault core, a pervasive phyllonitic fabric consisting of chlorite, white mica and fine-grained quartz ( $< 50 \mu\text{m}$ ) together with scattered boudinaged clasts of Na-rich plagioclase usually  $< 500 \mu\text{m}$  in size defines the NFZ (Fig. 4a).

Numerous quartz-carbonate veins and veinlets are transposed along the phyllonitic foliation. They are locally imbricated, confirming the top-to-the SE kinematics. Locally the mylonitic fabric is deformed by a pervasive extensional crenulation cleavage (ECC; Platt and Vissers, 1980) with individual shear bands dipping gently towards the NNW invariably indicating top-to-the SE transport, which, in the present geometry, corresponds to SE-ward thrusting along the NFZ (Fig. 2a and b). Field relations indicate that vein emplacement was pre- to syntectonic as most veins are either boudinaged or cut by the ECC shear bands. One of these veins forms the subject of our study (green star in Fig. 2a).

## 2.4 Analytical Method

Standard oriented thin sections cut orthogonal to the foliation and parallel to the stretching lineation were used for classic petrographic investigations and to investigate the crystallographic preferred orientation (CPO) of the vein quartz by EBSD analysis at the SEM. To remove surface damage and thereby enhance the diffraction signal, the thin sections were polished using colloidal silica for 5 minutes (Moen et al., 2003) and placed in a Hitachi VP-SEM with a Nordif UF-1000 EBSD detector (Chen et al., 2012) at a  $70^\circ$  tilt to the horizontal (Prior et al., 1999). To acquire satisfactory pattern quality the accelerating voltage used was 20.0 kV at 35 nA absorbed current. The working distance was set to 25.3 mm and the step size to  $2 \mu\text{m}$ . The data was processed using the open source Matlab toolbox MTEX 3.5.0 (e.g. Bachmann et al., 2010; Mainprice et al., 2011). The confidence index for the produced maps was set at 0,0145. Partitions based on aspect ratio and grain size were used to generate data subsets of the new- and old grain fractions. Aspect ratio and grain size for the old grain fraction ranged from 1,3 to 4,0 and 56 to  $200 \mu\text{m}$  respectively, while for the new grains they ranged from 1,6 to 3,0 and 40 to  $56 \mu\text{m}$ . Further analysis of the EBSD data was conducted using NIH image (Schneider et al., 2012).

## 2.5 Results

### 2.5.1 Sample description

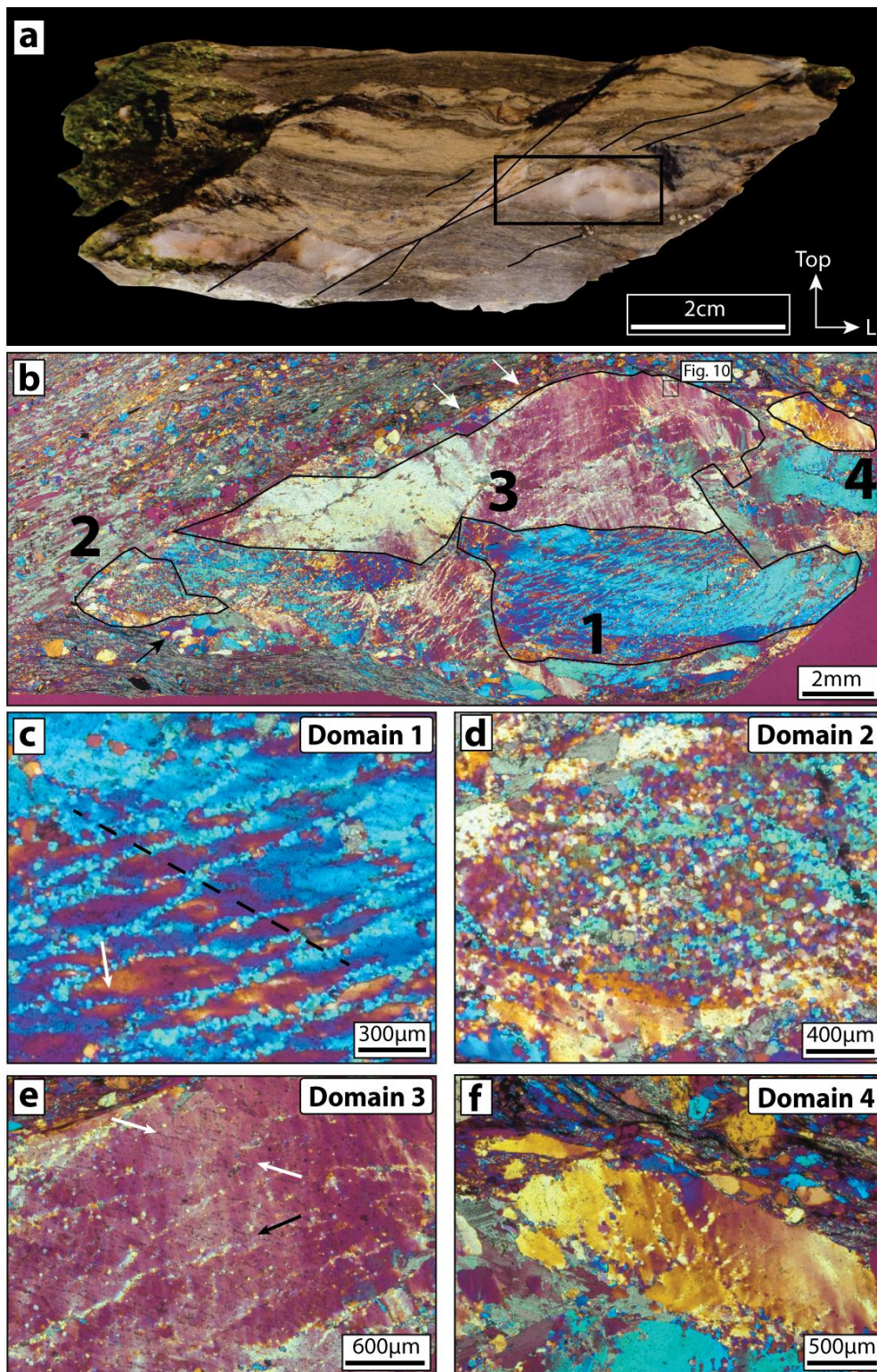
The studied sample is from a quartz vein and its host rock at an outcrop (green star in Figs. 1 and 2) where the main NFZ foliation developed at the expense of metabasalt. The vein is cut and offset by top-to-the SE  $C'$  shear bands that impart the outcrop a pervasive ECC. The hand specimen is a well-foliated phyllonitic rock containing a centimetric clast of the quartz vein bound by- and offset along one centimetric shear band, with numerous smaller shear bands also deforming the vein (Fig. 3a). The phyllonitic foliation is passively dragged into the shear bands confirming the kinematics determined by field observations (Fig. 2a, 3a and 4a).

The phyllonitic foliation is defined by layers consisting of varying amounts of feldspathic clasts with albitic composition within a phyllosilicate-rich matrix of chlorite and sericitic white mica. The grain size of the phyllonite is very fine, usually  $< 50 \mu\text{m}$ , except for some residual dolomitic porphyroclasts, which are up to  $> 1 \text{ mm}$  in size. Feldspar clasts range in size from  $< 200 \mu\text{m}$  to  $> 1000 \mu\text{m}$  and are locally asymmetrically boudinaged and deformed by small shear bands. The neck zones of the boudins are commonly filled with new grains of feldspars (Fig. 4a). Small-scale shear bands locally indicate both dextral and sinistral sense of shear, suggesting a component of flattening.

Several euhedral sulfide porphyroblasts, partially broken down to oxides, are dispersed in the phyllonite and within the vein; some are also symmetrically boudinaged and fibrous quartz is present in the neck domains and pressure shadows (Fig. 4b). Sigmoidal dolomite porphyroclasts are commonly observed. Syntaxially-filled calcite veinlets occur sub-parallel to the mylonitic foliation. These veinlets generally accommodated more than one opening event (Fig. 4e)

The studied vein clast consists primarily of quartz with only minor primary calcite. Secondary calcite and accessory sulfides are found both within the quartz crystals and along the grain boundaries. Quartz crystals within the vein range in size from  $< 0.5 \text{ mm}$  to  $> 6 \text{ mm}$  (Fig. 3b) and show neither a clear crystal preferred orientation (CPO; Fig. 6-9b) nor a shape preferred orientation (SPO). However, the number of primary quartz grains included in the studied thin section is low, so that we cannot rule out that the quartz vein displayed an initial SPO and CPO. In general, the boundaries between the individual grains are slightly irregular but straight, which gives the individual quartz crystals a blocky appearance (Fig. 3b), although the vein-matrix contact is generally more rounded.

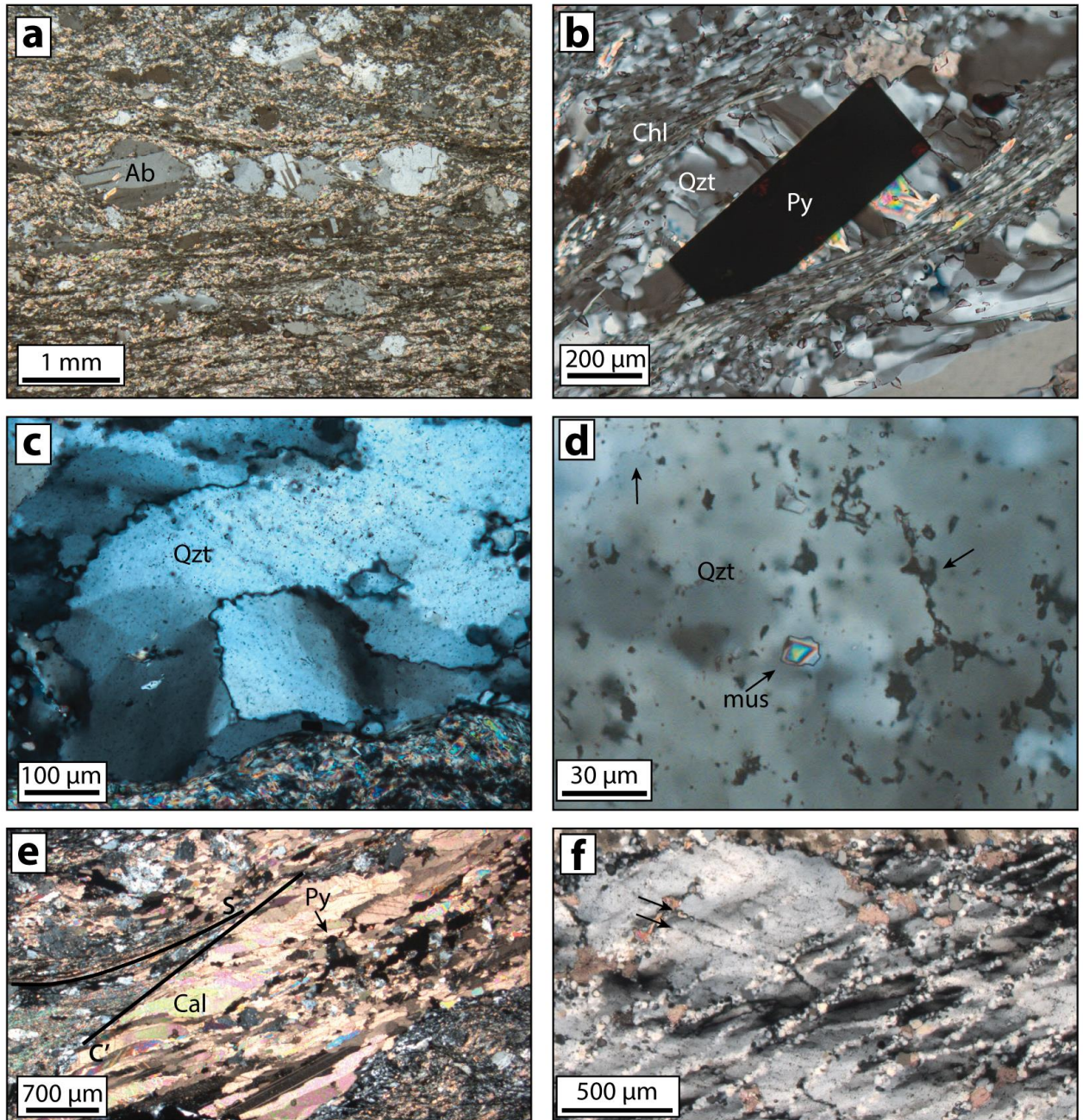




**Figure 2-3:** (a) Studied hand specimen. A discrete shear band cuts through the entire sample and offsets the studied quartz vein. Several second order shear bands are also visible and some deform the vein with a smaller displacement. Black square: Area of (b). Photomicrographs (b) to (f) are all taken with crossed polarizers and lambda plate inserted. (b) Stitched overview photomicrograph of the studied vein fragment. Black outline distinct textural domains, labeled 1 to 4. Black square in domain 3 indicates location of Figure 10. White arrows: sites of possible dissolution at vein-matrix contact. (c) Close up of a representative area of *Domain 1*. Black dashed line: Direction of wide extinction bands (WEB; Derez et al., 2014) seen as red-orange areas. White arrow: Bridging band of new grains. (d) Close up of representative microstructure of *Domain 2*. (e) *Domain 3*. White arrows: Trace of fluid inclusion plane. Black arrow: Direction of band with new grains. (f) Close up of *Domain 4* showing bands of new grains at a relatively high angle to each other.

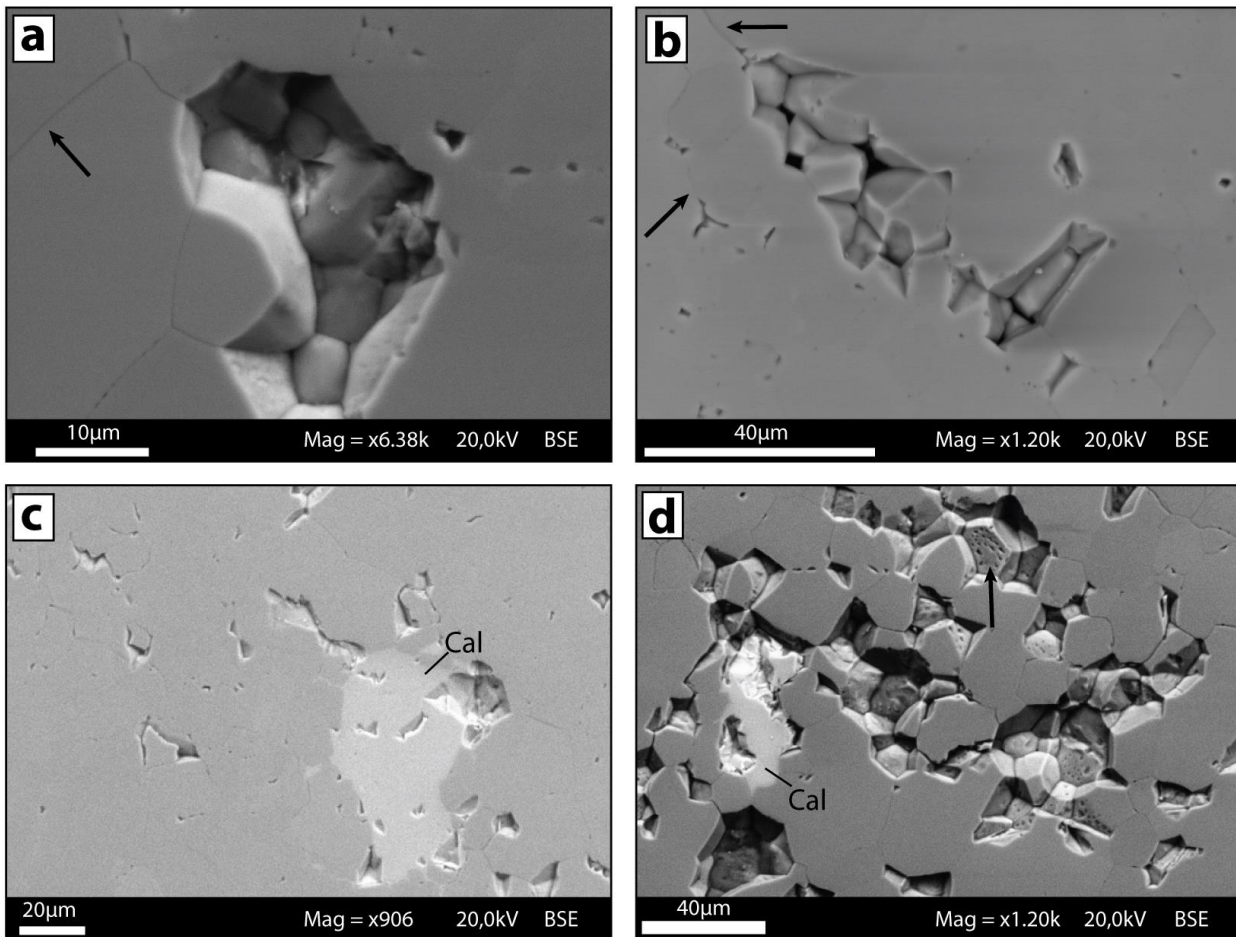


## 2. Brittle-viscous deformation of vein quartz



**Figure 2-4:** All the photomicrographs are taken with crossed polarizers. (a) Albitic feldspar crystals asymmetrically cut and offset by dextral shear bands within the sheared, phyllosilicate-rich foliation of the NFZ. Minor recrystallization of the plagioclase can be seen in some of the shear bands. (b) Euhedral pyrite crystal partially altered to oxides with fibrous quartz and mica growing in the fringes, surrounded by chlorite. (c) Bulging grain boundaries and subgrains indicate low-grade deformation of the vein quartz. (d) Small mica grain within a band of new grains in *Domain 3*. Fluid inclusions outline the new grains (black arrows) and partially define the band. New grains are seen as different shades of grey. (e) Calcite veinlet displaying several opening events, with fine-grained quartz at the matrix boundary with large, elongated calcite crystals and smaller equidimensional grains with some interspersed sulfides in the center. Foliation S dragged into the C' shear band. (f) Microcracks sub-parallel to the rhomb plane and WEB in *domain 1*, cut by bands of new grains. Microcracks contain secondary phases (calcite) and show incipient recrystallization of quartz. Bands of new grains also show secondary phases (calcite, muscovite).






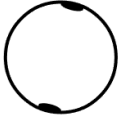
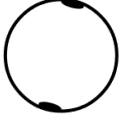

**Figure 2-5:** (a) Detailed BSE photograph showing the pitted grain boundaries of new quartz grains in *Domain 1*, indicative of fluid-present conditions during neo-crystallization of the new grains. Black arrow indicate grain boundary of new grain. (b) BSE image from *Domain 1*. Black arrows indicate grain boundaries between new grains. New grains have a slight different shade of gray, due to a channeling effect. (c) BSE image from *Domain 1*. Secondary calcite is present within a band. (d) BSE image from *Domain 2* showing pitted grain boundaries (black arrow) and secondary calcite.

## 2.5.2 Microstructural and EBSD analysis

Because of the marked microstructural differences that we have observed within the quartz vein, we have identified and studied in detail several domains, each characterized by internally consistent microstructures. Our study reports four representative domains that are described individually below. Table 1 and Figure 6-9 sum up the main CPO elements constrained by petrographic and EBSD analysis.

Several quartz crystals contain narrow bands of much finer grains. In the text these grains are referred to as nucleated “new grains” and are distinguished from the parent grains or “old grains” based on aspect ratio, grain size and misorientation angle to neighbor grains. In detail, all grain boundaries were defined as misorientations larger than  $10^\circ$  (e.g. Trepmann et al., 2007).

**Table 1:** Summary of microstructures.

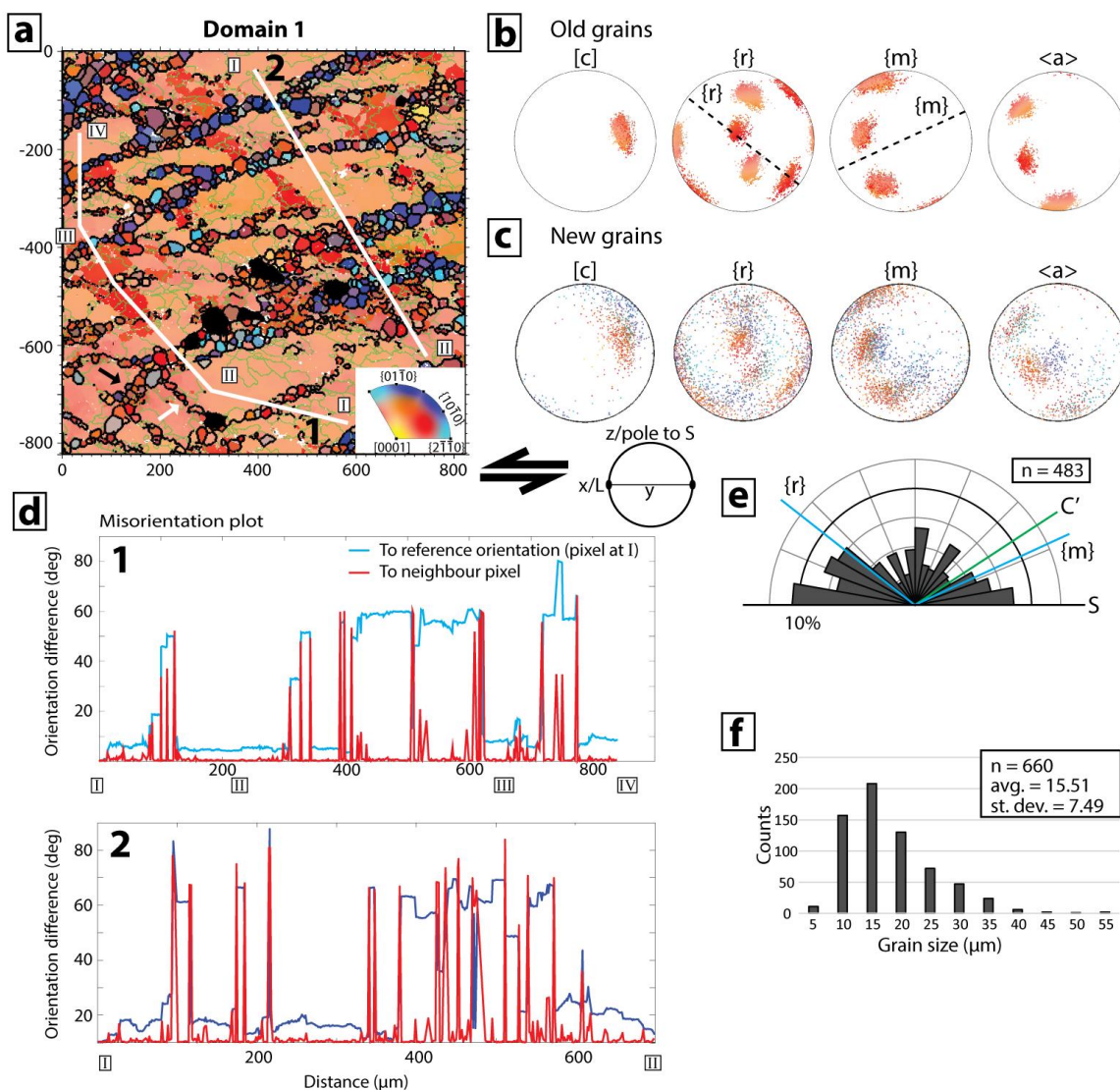
Domain	Old grain orientation	Microstructure type	Orientation of bands of new nucleated grains	Orientation of bands of new nucleated grains	Average grain size ( $\mu\text{m}$ )	Average aspect ratio
1	[c] 	Pervasive nucleation; "striped tiger" pattern	$\parallel$ to {m and $\parallel$ to {r	c. $25^\circ$ and c. $140^\circ$	Avg.: 15.51 Max.: 52.46 Min.: 4.47	1.63
2	[c] 	Dominated by new nucleated grains	$\parallel$ to basal plane	c. $170^\circ$	Avg.: 18.03 Max.: 55.32 Min.: 4.26	1.66
3	[c] 	Limited nucleation along a few bands	$\parallel$ to basal plane and $\parallel$ to {r	c. $15^\circ$ and c. $150^\circ$	Avg.: 13.96 Max.: 32.76 Min.: 5.09	1.59
4	[c] 	localized nucleation; minor "striped tiger" pattern and pockets of new grains	$\parallel$ to {m and $\parallel$ to {r	c. $120^\circ$ and c. $50^\circ$	Avg.: 15.48 Max.: 41.16 Min.: 4.26	1.60

### 2.5.2.1 Domain 1

*Domain 1* (Fig. 3b and c) is found within a single crystal measuring 6 x 3 mm. It contains a tightly spaced set of sub-parallel and semi-straight bands of nucleated grains. The bands are sub-parallel to the  $C'$  shear planes that offset the quartz vein. They are continuous for several millimeters and are on average 30  $\mu\text{m}$  thick (1-3 grains thick). We name this microstructure "striped tiger". Bridges between the most pronounced bands are observed (white arrow in Figure 3c). The nucleated grains vary in size between c. 10 and 60  $\mu\text{m}$ , have a slightly elongated shape and constitute c. 40% of the area of the domain. Fluid inclusions occur within the bands where they commonly encircle the nucleated grains. Much smaller fluid inclusions ( $<$  c. 2  $\mu\text{m}$ ) are instead abundant and apparently randomly distributed within the host old crystal (Fig. 4d). Some bands also contain small (c. 50  $\mu\text{m}$ ) calcite grains interspersed among the new quartz grains (Fig. 4f).

The host grain displays undulose extinction, which is defined by wide extinction bands (WEB; Derez et al., 2014; Black dashed line in Fig. 3c). These are sub-parallel to local fluid inclusion traces that

also appear to be cut by the bands of new grains (Fig. 4f). WEB's have an antithetic geometry to the large shear band that cuts through and offsets the quartz vein in the hand specimen (Fig. 3a, b and c) and are themselves cut by the bands of new grains (Fig. 3b, c and f).



**Figure 2-6:** Compilation of EBSD data from *Domain 1* (see Fig. 3b and c for location of the domain). (a) EBSD map color-coded according to the Inverse Pole Figures (IPF) for quartz shown in lower right corner of map. The IPF is with respect to the X-direction of the finite strain ellipsoid (stretching lineation of the phyllonite). Black lines: grain boundaries defined by misorientations  $> 10^\circ$ . Green lines: subgrain boundaries defined by misorientations  $< 10^\circ$ . Black grains are calcite. White line 1 (I-IV) and 2 (I-II) are the traces of misorientation profiles in (d). (b) and (c) Pole figures of quartz showing the orientation of [c], {r}, {m} and <a> for old and new grains, respectively. The stereograms are upper hemisphere projections of 10000 random points. Dashed lines represent the trace of the bands of new grains and the crystallographic plane they are parallel to. (d) Misorientation profiles displaying difference in orientation to neighbor pixel (red line) and to reference orientation (i.e. orientation of pixel at I; blue line). (e) Rose diagram displaying the orientation of the long axis of the new grains with respect to the trace of C', S (horizontal) and the crystallographic planes that the bands are parallel to. (f) Histogram displaying grain size distribution of the new grains.

EBSD analysis of the sub-parallel bands of new grains shows that they range in size between c. 5-50  $\mu\text{m}$  (Fig. 6f and Tab. 1), and have a different crystallographic orientation from the host (Fig. 6b-d).

## 2. Brittle-viscous deformation of vein quartz

The c-axis of the host grain in *Domain 1* is in the foliation plane at c. 15° from the stretching lineation and is visualized by the orange color in Figure 6a and b. The host grain contains a large amount of subgrains that are locally larger than the nucleated grains within the bands. The red color within the old grain (Fig. 6a) represents Dauphiné twins, which accommodate a 60° rotation around the c-axis and are thus not visible under the optical microscope (Fron del et al., 1962). As noted above, there are two sets of bands in the domain, one pervasively developed and one subordinate. The more developed set contains bands that are sub-parallel to the prism plane of the host old grain (dashed line in the of the pole figure of the prism, m; Fig. 6b) and thus are oriented sub-parallel to the sample-scale C' shear band and with an average 25° angle to the foliation, when measured counterclockwise. The less developed bands are seen in the lower left corner of the EBSD map (white arrow in Fig. 6a) and are sub-parallel to the rhomb (dashed line in the pole figure of the rhomb, {r}; Fig 6b) forming an angle of c. 142° to the foliation, S, measured counterclockwise. The new grains within the bands are slightly elliptical with an average aspect ratio of 1.63 and average grain size of 15.51 µm (Fig. 6 e and f). The new grains have a more scattered c-axis distribution with a counterclockwise rotation around the Y-axis (Fig 6c). They display large misorientations (locally > 40°) to each other and to the host. The new grains show no to very little internal deformation and there is no progressive rotation of the lattice when approaching the bands from the host, i.e. the change in misorientation is abrupt (Fig 6 d 1 and 2).

### 2.5.2.2 Domain 2

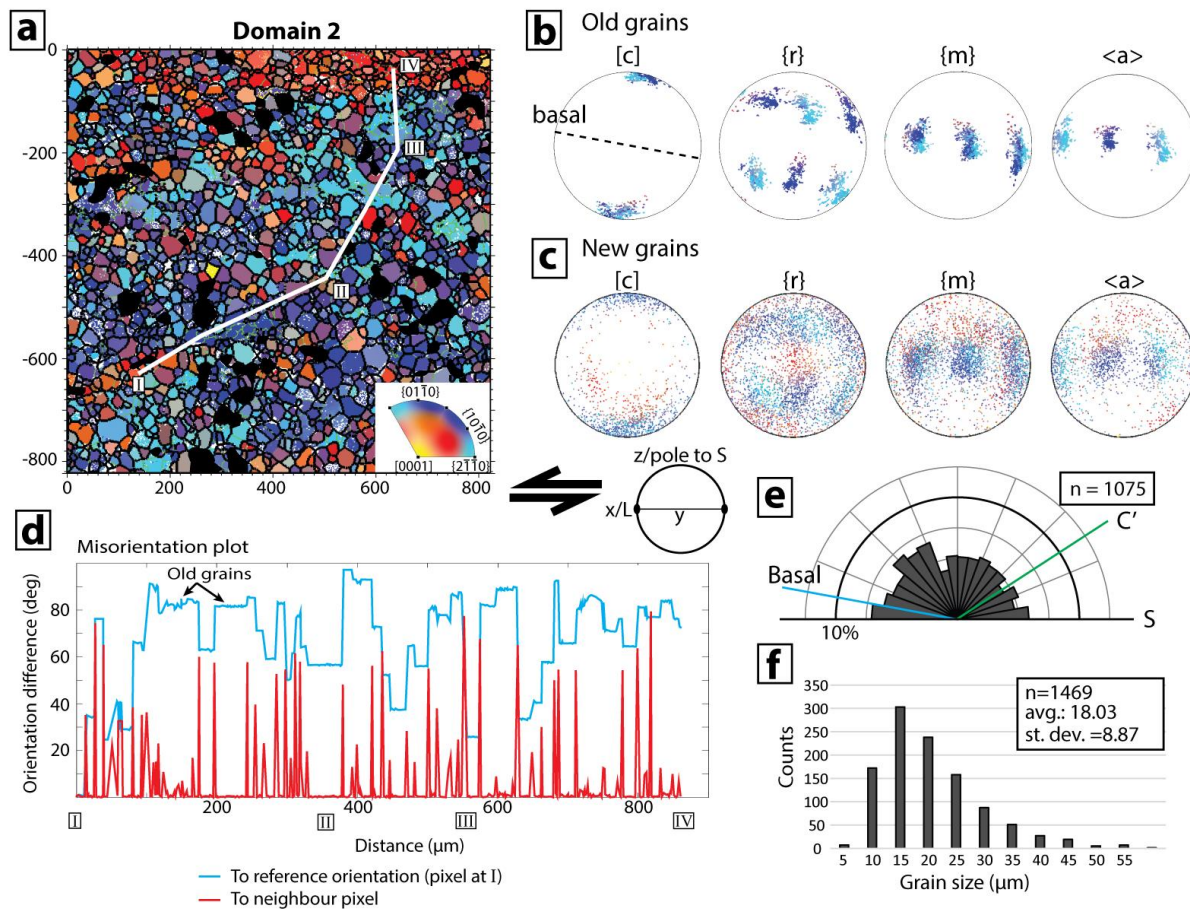
*Domain 2* is located at the tip of the quartz vein, where the latter is sandwiched by the foliation S and the micaceous shear plane C' of the host phyllonite (Fig. 3b). It contains abundant secondary calcite and cavities from sample preparation show pitted grain boundaries (Fig. 5d). Grain size distribution is unimodal, with relatively equigranular and equidimensional grains. The domain is almost completely made up of new grains (Fig. 3d and 7a), although local relics of a few host old grains (up to 80 µm in size) can still be recognized (Fig. 7a).

*Domain 2* is pervasively recrystallized (Fig. 3d) with only small amounts of preserved old grains, as shown by the presence of local subgrain boundaries within the larger and more irregular crystals (Fig. 7a and d). The old grains form a c-axis maximum around the Z-direction of finite strain in the pole figure, with only a weak clockwise rotation (Fig. 7b). As far as the new grains are concerned, *Domain 2* has the largest average grain size of all domains and the highest average aspect ratio, with 18.03 µm and 1.66, respectively (Fig. 7e, f and Tab. 1). There is no obvious preferred elongation direction of the new grains (Fig 7e). The new grain crystallographic orientations are broadly scattered around those of the old grains. The new grains have a high and sharp misorientation to each other and to the



old grains and they are relatively strain free. No progressive lattice rotation is visible towards the new grains (Fig. 7d).

Figure 7 Kjøl et al



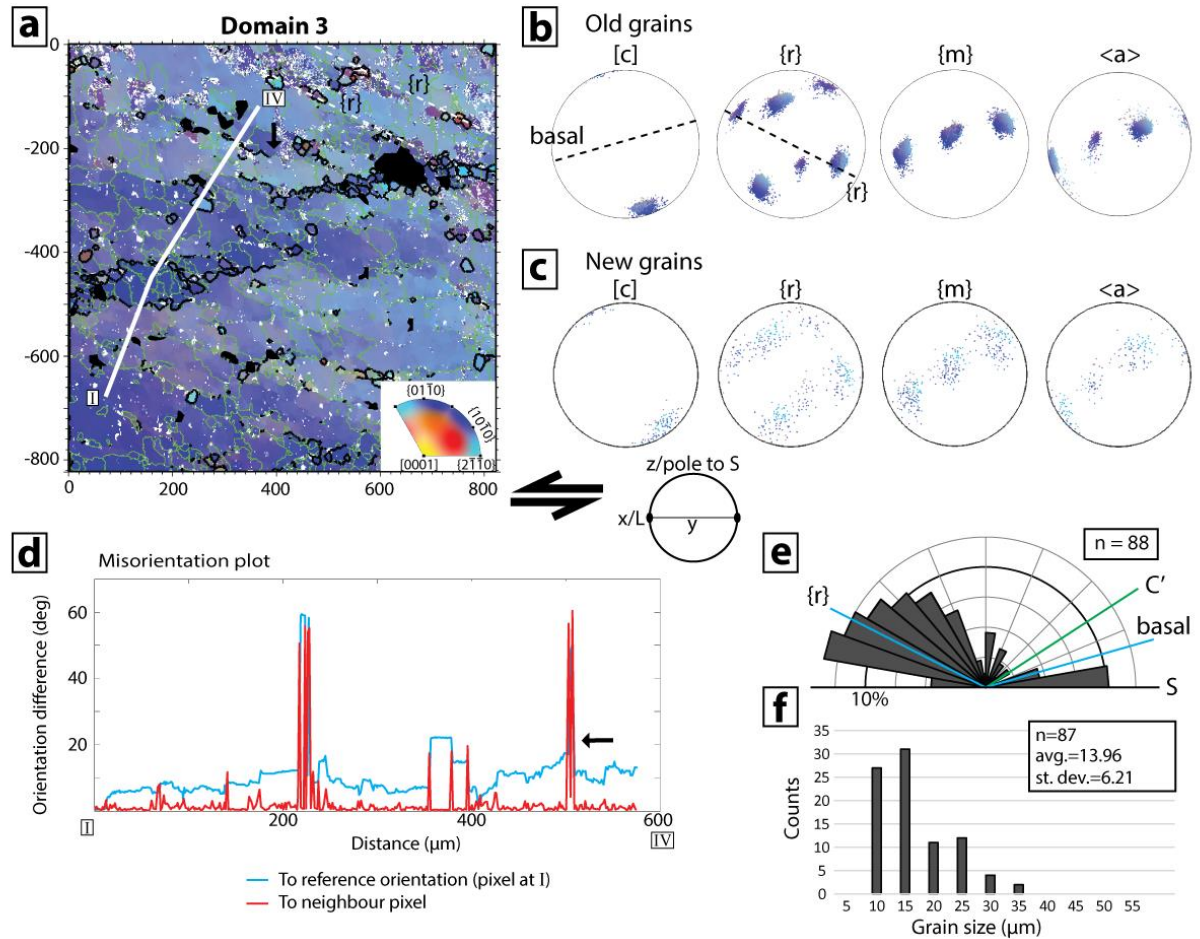
**Figure 2-7:** Compilation of textural data from *Domain 2* (see Fig. 3b and d for its location). (a) EBSD map of crystallographic orientation of quartz. Color-coding and boundary types like in Fig. 6. Black grains are calcite. White line I-IV: trace of misorientation profile in (d). (b) and (c) Pole figures of quartz showing the orientation of [c], {r}, {m} and <a> for old and new grains, respectively. The stereograms are upper hemisphere projections of 10000 random points. Dashed lines represent the trace of the bands of new grains and the crystallographic plane they are parallel to. (d) Misorientation profiles displaying difference in orientation to neighbor pixel (red line) and to reference orientation (i.e. orientation of pixel at I); blue line). (e) Rose diagram displaying the orientation of the long axis of the new grains with respect to the trace of C', S (horizontal) and the crystallographic planes which the bands are parallel to. (f) Histogram displaying grain size distribution of the new grains.

### 2.5.2.3 Domain 3

The upper part of the vein hosts a large grain measuring 5 x 3 mm, which hosts *Domain 3* of our study (Fig 3b and e). The grain displays sweeping and patchy undulose extinction with upright WEBS and two sets of bands of new grains. The new grains in these bands are less developed than in other domains. The most pronounced set is recognized due to its slightly different extinction direction compared to the host. Generally, there are few new grains within these bands, although some local, isolated pockets of new grains occur (Fig. 3e). The new grains are encircled by fluid inclusions and

## 2. Brittle-viscous deformation of vein quartz

some tiny muscovite grains (c. 20  $\mu\text{m}$ ; Fig. 4d), and their grain boundary microstructure shows evidence for porosity and dissolution-precipitation features (e.g. Mancktelow and Pennacchioni, 2004; Fig. 5). The bands and fluid inclusion trails define patchy undulose extinction patterns (bLEB; Derez et al., 2014). The second set of bands is seen as semi-straight trails of small fluid inclusions (< c. 2  $\mu\text{m}$ ), with no visible recrystallization. The left half of the domain is characterized by sub-parallel fluid inclusion trails. No nucleation of new grains is seen along these traces (white arrows in Fig 3e).



**Figure 2-8:** Compilation of textural data from *Domain 3* (see Fig. 3b and e for its location). (a) EBSD map of crystallographic orientation of quartz. Color-coding and boundary types like in Fig. 6. Black grains are calcite. White line I-IV: trace of misorientation profile in (d). (b) and (c) Pole figures of quartz showing the orientation of [c], {r}, {m} and <a> for old and new grains, respectively. The stereograms are upper hemisphere projections of 10000 random points. Dashed lines represent the trace of the bands of new grains and the crystallographic plane they are parallel to. (d) Misorientation profiles displaying difference in orientation to neighbor pixel (red line) and to reference orientation (i.e. orientation of pixel at I; blue line). (e) Rose diagram displaying the orientation of the long axis of the new grains with respect to the trace of C', S (horizontal) and the crystallographic planes which the bands are parallel to. (f) Histogram displaying grain size distribution of the new grains.

Only local bands and clusters of new grains are observed in *Domain 3*, which is the domain with the lowest density of new grains (Fig. 8a). The c-axis of the host old grain is sub-parallel to the Z-direction of finite strain, and slightly inclined with the bulk sinistral sense of shear (Fig. 8b). The host old grains display a clear single-crystal maximum with very little dispersion of the c-axis and <a> axes, although

some undulose extinction can be inferred. The bands and clusters of new grains are oriented at c.  $16^\circ$  to the foliation S, measured counterclockwise, which makes them sub-parallel to the basal plane of the old grain (dashed line in Fig. 8b). In the central and left parts of *Domain 3* fluid inclusion trails are observed. These trails are sub-parallel to the rhomb direction (white arrows in Fig. 3e, and dashed line in Fig. 8b) and are oriented at  $153^\circ$  measured counterclockwise from the foliation S.

The average grain size of the new grains is  $13.96\ \mu\text{m}$  (Fig. 8e and Tab. 1) and they have an average aspect ratio of 1.59 (Fig. 8f) with the preferred elongation at c.  $115^\circ$  measured counterclockwise from the foliation S. The crystallographic planes and directions of the new grains are scattered around those of old grains (Fig. 8c and b, respectively). The data seems to have been rotated counterclockwise around the Y-axis. This domain has the smallest grain size, both average and maximum and the lowest aspect ratio (Tab. 1 and Fig. 8e and f). The measured misorientation profile shows that the orientation difference between neighbor old grains is quite large. Locally, subgrain boundaries grade to high-angle boundaries with misorientations in excess of the threshold value of  $10^\circ$  (black arrows in Fig. 8a and d), whereas new grains display misorientations of up to  $20^\circ$  with respect to neighbor grains (Fig. 8d). In addition, misorientation profiles locally show what appears to be a progressive lattice rotation towards the grain boundaries.

#### **2.5.2.4 Domain 4**

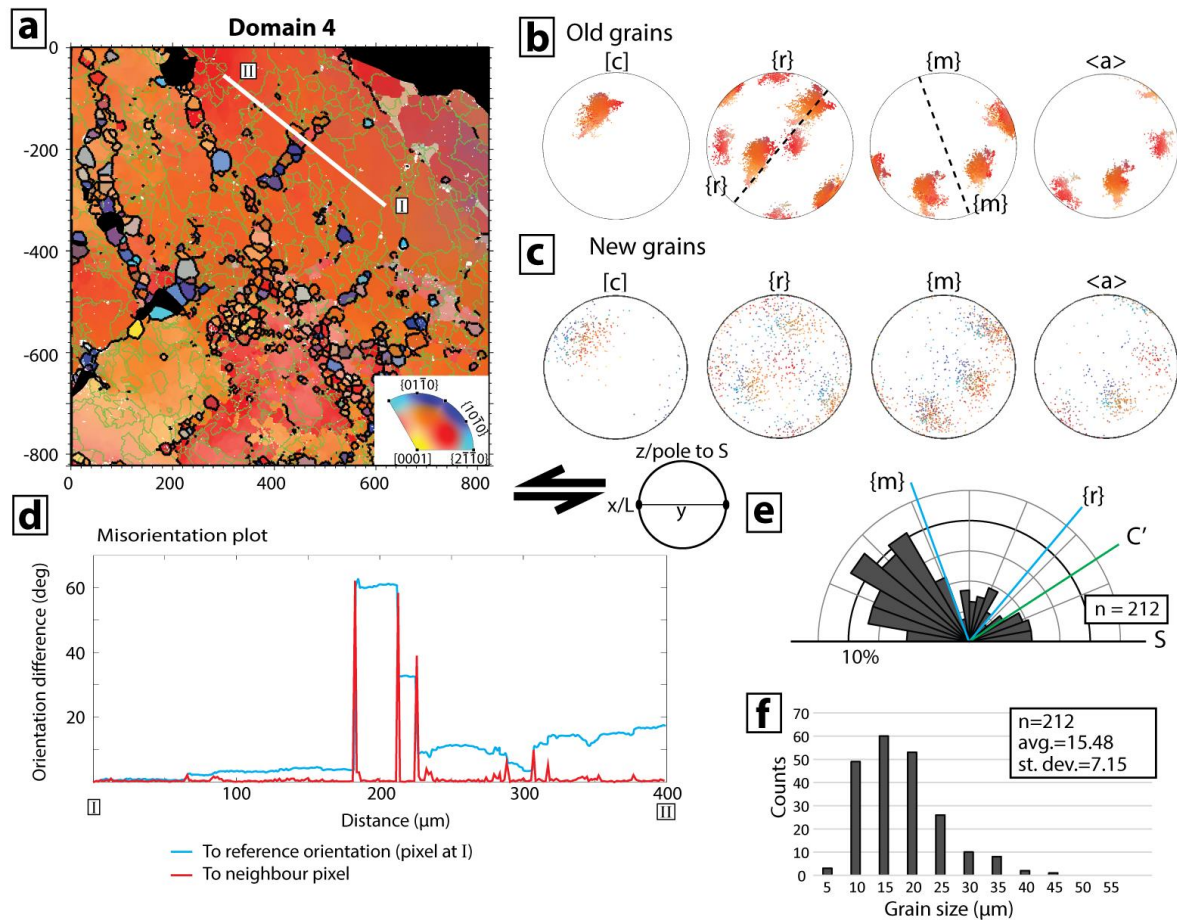
*Domain 4* is a relatively small, single crystal measuring  $2 \times 0.5\ \text{mm}$  (Fig. 3b and f). Above the crystal there is a high density of feldspar clasts wrapped in an anastomosed phyllonitic matrix with shear indicators suggesting opposite kinematics than the top-to-the SE regional sense of shear accommodated by the NFZ. Microstructurally the crystal resembles *Domain 1*, with a “striped tiger” microstructure. In *Domain 4*, however, two well-developed sets of bands with new grains occur, in contrast to *Domain 1* where there is only one well-developed direction. One direction, inclined towards the right, is the most pronounced, whereas the one inclined to the left is slightly less pervasive. The traces of the two bands are separated by c.  $70^\circ$ . Insertion of the lambda plate reveals that the main band of new grains also separates two sub domains within the single crystal with a slight misorientation to each other. The crystal contains some randomly arranged fluid inclusions.

*Domain 4* has an old grain with a c-axis located in an intermediate position between the Z and Y axis of strain and slightly inclined with the bulk sinistral sense of shear (Fig. 9a and b). Undulose extinction is seen as different shades of orange in the EBSD maps, and red represents Dauphiné twins (Fig. 9a). The old grain contains some subgrains that are generally larger than the new grains. The two identified sets of bands are parallel to the prism and the rhomb and form a  $50^\circ$  and  $110^\circ$  angle,



## 2. Brittle-viscous deformation of vein quartz

respectively, measured counterclockwise from the foliation S (dashed lines in the rhomb {r} and prism {m} pole figures in Fig 9b and Tab. 1). The average aspect ratio of the new grains is 1.60 and the average grain size is 15.48  $\mu\text{m}$  and (Fig. 9e and f) with an elongation direction of c.  $104^\circ$  measured counterclockwise from the horizontal S. In addition, the new grains define a more scattered c-axis distribution (Fig. 9c). A misorientation profile across one of the rhomb-parallel bands shows that the recrystallized grains are rather strain free, with very little internal misorientation. The boundary between the old grain and the recrystallized bands is sharp and not progressive (Fig. 9d), although a small shift in orientation is seen across the band. Furthermore, the boundary is  $60^\circ$ , which indicate that the band might exploit a Dauphiné twin boundary.



**Figure 2-9:** Compilation of textural data from *Domain 4* (see Fig. 3b and f for its location). (a) EBSD map of crystallographic orientation of quartz. Color-coding and boundary types like in Fig. 6. Black grains are calcite. White line I-IV: trace of misorientation profile in (d). (b) and (c) Pole figures of quartz showing the orientation of [c], {r}, {m} and <a> for old and new grains, respectively. The stereograms are upper hemisphere projections of 10000 random points. Dashed lines represent the trace of the bands of new grains and the crystallographic plane they are parallel to. (d) Misorientation plot displaying difference in orientation to neighbor pixel (red line) and to reference orientation (i.e. orientation of pixel at I; blue line). (e) Rose diagram displaying the orientation of the long axis of the new grains with respect to the trace of C', S (horizontal) and the crystallographic planes which the bands are parallel to. (f) Histogram displaying grain size distribution of the new grains.

## 2.6 Discussion

### 2.6.1 Strain localization history within the different domains

Our dataset documents examples of quartz microstructures developed in a fluid rich system deformed under low-grade metamorphic conditions. In our conceptual understanding, initial embrittlement of the host greenstones was accommodated by fracturing, fluid circulation and quartz (and carbonate) precipitation as vein material. The initial crystallization of the vein occurred statically, resulting in a seemingly random crystallographic orientation of the constituting large quartz crystals during the Paleoproterozoic. Later, pervasive viscous deformation led to strain accommodation within the vein and development of the ECC in the host greenstones. Viscous deformation, however, was interrupted by transient episodes of embrittlement, which we relate to both the crystallographic framework inherited from the statically crystallized vein and the oscillations of the pressure of the fluid phase that was present during continued deformation related to the thrusting history along the NFZ.

This structural evolution is summarized conceptually in Fig. 10, supported by the summary of Table 1 and discussed in detail below.

Following initial fracturing and vein crystallization (possibly related to early Caledonian deformation or even to the Paleoproterozoic evolution of the region; Fig. 10a), the vein became progressively involved in the Caledonian deformational history of the NFZ, wherein top-to-the SE thrusting led to the progressive development of the fault zone. Environmental conditions were such that quartz began to deform by low-grade crystal plastic deformation by dislocation glide and possibly creep (Fig. 10b). Two main mechanisms are believed to have controlled this stage of the microstructural evolution: 1) Strain partitioning resulting from the high competence contrast between the vein and the surrounding greenstone, which was evolving into a progressively foliated and finer-grained phyllonite as strain was accommodated in the core of the NFZ (Trepmann and Stöckhert, 2009); and 2) Presence of fluids as documented by the numerous veinlets, secondary phases trapped along grain boundaries, pitted grain boundaries and fluid inclusions (e.g. Drury and Urai, 1990; Mancktelow et al., 1998; Fig 10b; Mancktelow and Pennacchioni, 2004). Low-grade viscous deformation produced structures such as bulging grain boundaries (Fig. 4c) caused by slow grain boundary migration (Stipp et al., 2002a), sweeping undulatory extinction, subgrains, bLEBs and WEBs (Derez et al., 2014; Fig. 3b-f and Fig. 4f). EBSD analysis has shown remarkably different microstructures and CPO patterns in the analyzed domains that can be assigned to this microstructural stage. We ascribe this to the fact that each domain had a different crystallographic orientation, due to the static initial crystallization in the vein and the

location of individual domains with respect to the mesoscopic structural features, such as the C' shear band.

*Domain 1*, for example, would have been well oriented for viscous slip accommodated by either prism  $\langle a \rangle$  or c-slip (Fig. 6b). In order to be activated, however, these slip planes require higher-grade conditions than those at which the vein was deforming (Schmid and Casey, 1986; Stipp et al., 2002a). Synkinematic chlorite thermometry from similar faults in the area has established a peak temperature of  $< 300^\circ \text{C}$  (Torgersen and Viola, 2014), ideal for activation of basal  $\langle a \rangle$  slip (e.g. Stipp et al., 2002a). The crystal of *Domain 1* was, however, misoriented for basal  $\langle a \rangle$  slip. Some strain was nonetheless taken up in a ductile fashion in *Domain 1* by the development of WEBs (Derez et al., 2014) and possibly by dislocation creep, as shown by the subgrain boundaries. Since easy-glide planes were oriented at a high angle to the C' shear band, dislocation glide and creep soon resulted ineffective, leading to strain hardening, possibly by dislocation tangling, and localized embrittlement of the deforming quartz accommodated by fracturing. Transiently high fluid pressure is also believed to have contributed to localized and short-lived embrittlement as the fluid factor  $\lambda$  approached unit value (e.g. Cox, 2010; Hubbert and Rubey, 1959; Fig. 10c). Evidence for fluid-accompanied fracturing, such as fluid inclusion trails (Fig. 5b and c and Fig. 4d and f), is invariably found in the studied samples and within the NFZ in general.

The fractures developed during this stage of the structural evolution of *Domain 1* are invariably intra-granular, which points towards sub critical crack growth, by, for example, stress corrosion, microplasticity or general plasticity (e.g. Atkinson, 1982, 1984; Stünitz and Fitz Gerald, 1993). Development of volumetrically small gouges along the fracture planes is also envisaged (Stünitz et al., 2003; Fig. 10c, insert). The sub-parallel orientation of the fractures suggests in addition that they formed controlled by specific lattice planes, that is, planes with a low density of covalent bonds and thus low surface energy (e.g. Fairbairn, 1939; Flörke et al., 1981; van Daalen et al., 1999; Fig 6, 8 and 9; Vollbrecht et al., 1999).

The weakest crystallographic plane in quartz is the positive rhomb, both in terms of surface energy and elastic properties (Menegon et al., 2011b). van Daalen et al. (1999) report what they refer to as “micro shear zones”, that is, bands of new grains along the positive and negative rhomb planes. The two sets of bands with nucleated new grains within *Domain 1* are sub-parallel to the prism and the rhomb face of the crystal. The prism plane direction, parallel to which we find the most pervasive set of bands of new grains, was the optimally oriented direction for brittle failure, as it is sub-parallel to the actual slip plane of the mesoscopic system, that is, the C' shear band (Fig. 6e). The rhomb, although oriented at high angle to the shear band, is the weakest crystallographic plane in quartz, and,

therefore, it did also fail. The geometric orientation of the rhomb was such that it was suitably oriented to accommodate strain along the antithetic direction of a conjugate set of fractures.

Furthermore, the anisotropy of the elastic properties of quartz may also have contributed to promoting preferential failure along specific crystallographic planes (McSkimin et al., 1965; Menegon et al., 2011b). This is suggested by *Domain 3* (small square in Fig. 3b), wherein Dauphiné twins are deformed unevenly, with the r-twin accommodating more plastic strain than the z-twin (Fig. 11a; r-twin and z-twin terminology after Menegon et al. (2011b). The pole figures in Fig. 11b show that the pole to one of the positive rhombs is oriented close to the Z-direction of finite strain (bulk shortening direction). This orientation corresponds to the r-twin orientation and, accordingly, the r-twin is more deformed than the z-twin (as evident from the more pronounced dispersion of the poles to {r} compared to the poles to {z}, which indicates a higher degree of internal distortion of the r-twin). The twin with the negative rhomb facing the same direction (the z-twin) is stiffer and did not accommodate the same amount of viscous strain.

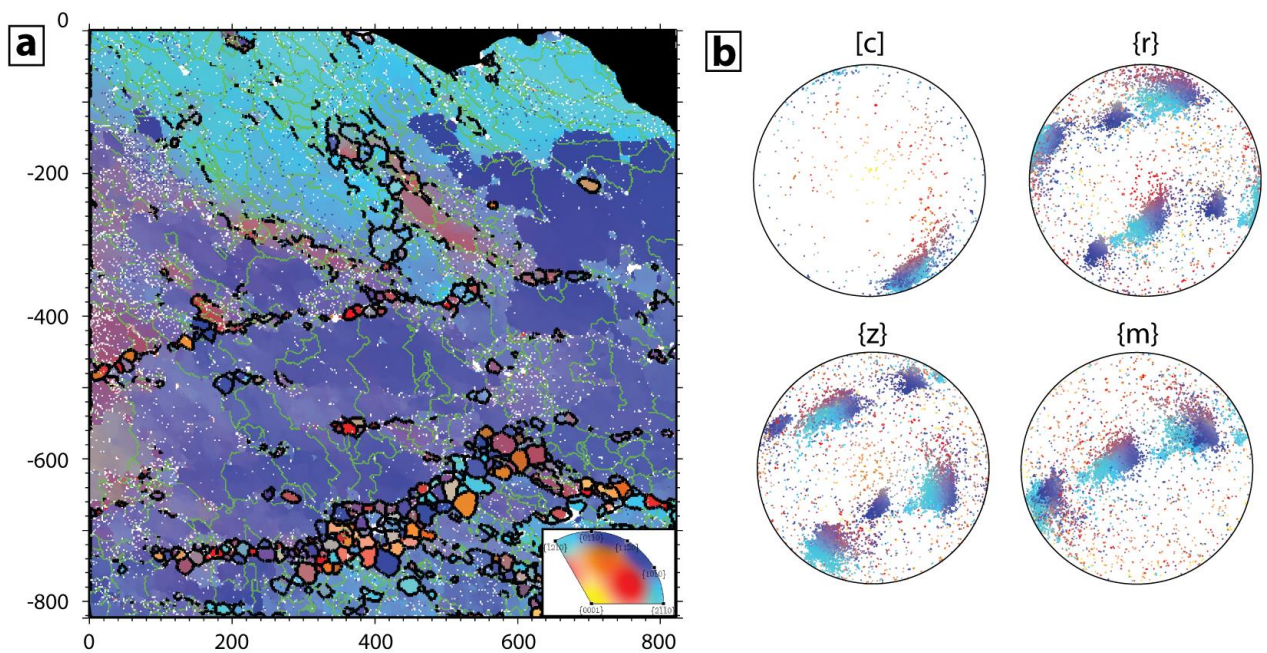
In summary, the “striped tiger” microstructure observed within *Domain 1* is best interpreted in terms of “sealing” of these earlier fractures by rotation of fracture fragments caused by micro-displacements and subsequent nucleation of the new grains (Fig. 10c, insert and d, insert). This mechanism is discussed in more detail in section 5.2.

In contrast to *Domain 1*, *Domain 3* was more suitably oriented for effective accommodation of viscous deformation, with the basal plane oriented close to the C' shear band, that is, well oriented for slip along the basal  $\langle a \rangle$  (Schmid and Casey, 1986). *Domain 3*, however, also contains two sets of bands with new grains, although more poorly developed than in *Domain 1* (Fig. 3e and 8). The bands parallel to the basal planes show a larger amount of recrystallization than those parallel to the rhomb planes. Furthermore, misorientation profiles locally show a progressive misorientation from the old grain to the new grains along the basal-parallel bands. This suggests that subgrain rotation recrystallization was probably operative in *Domain 3*. A crystal with the orientation of *Domain 3* would have been more prone to accommodate strain by dislocation glide and creep, and would thus not strain harden as much as *Domain 1*. In addition, one set of fractures would have had to form along the basal plane of the crystal, which is not a crystal plane with particularly low surface energy or Young's modulus. We interpret the second set, sub-parallel to the rhomb, as sealed fractures. It is worth noting that the positive rhomb is the most compliant crystallographic plane in quartz and, therefore, tends to localize fracturing (Lloyd, 2000; McSkimin et al., 1965; van Daalen et al., 1999). EBSD analysis reveals that some new grains developed also along these fractures, but mostly in the junctions where the two fracture sets intersect. However, new grain nucleation along fracture planes parallel to the rhomb is not nearly as pervasive as along the other fracture in the same domain or any

## 2. Brittle-viscous deformation of vein quartz

of the other fractures in *Domain 1* (Fig 8a and 6a). We suggest that these fractures opened during an earlier embrittlement event, possibly under different physical boundary conditions, wherein the fractures healed by epitaxial growth on the fracture wall, thus not creating an orientation difference, but rather parallel trails of fluid inclusions. In summary, we argue that less pervasive domainal fracturing affected *Domain 3*, and that crystal plastic deformation and recovery were locally operative due to the suitable orientation of the domain for slip along the basal  $\langle a \rangle$  system.

The quartz crystal of *Domain 4* was oriented similarly to the one in *Domain 1* and it thus underwent only limited crystal-plastic deformation, with the latter strongly inhibited by early strain hardening, possibly promoted by dislocation tangling, resulting in undulose extinction and domainal fracturing. Similarly to *Domain 1*, *Domain 4* is also characterized by fracturing along the prism and the rhomb planes (Fig. 9b). Both directions are fairly well developed, but the prism-parallel bands are more continuous. In this domain the rhomb-parallel set has a similar orientation as the  $C'$  shear band, while the prism-parallel set developed along the antithetic direction of the conjugate set. This fits well with the mesoscopic geometry of the vein, which is boudinaged (Fig 3a).



**Figure 2-10:** (a) EBSD map crystallographic orientation of quartz of area located within *Domain 3* (see Fig. 3b for location). Color-coding and boundary types like in Fig. 6. The map shows Dauphiné twins where one twin, the r-twin, has accommodated more viscous strain than the z-twin, as seen from the pole figures in (b). See text for further explanation.

*Domain 2* is remarkably different from all other sites. In it, the orientation of the now almost totally obliterated old grains is similar to that of *Domain 3*, that is, optimal for glide-accommodated creep with slip along the basal  $\langle a \rangle$ . Despite the similarity in orientation, however, the microstructures observed are remarkably different, with *Domain 2* displaying a significant volume of new grains and

with only very few remnants of the old grains (Fig 3d and 7a and d). We ascribe the pervasive nucleation of *Domain 2* to its location. The domain is located in a relatively high strain zone between the *C'* shear plane and the foliation, where the tip of the vein is dragged into the *C'* shear bands. We argue that *Domain 2* represents a high-strain equivalent to *Domain 3*, where crystal plastic deformation along the basal plane possibly coupled with nucleation and growth of new grains along rhomb-parallel fractures (like in *Domain 2*) resulted in extensive recrystallization. The high density of subgrain boundaries in the remnant old grain (Fig. 7a and d) suggests that crystal plasticity has been active to the same extent as in *Domain 3* and has contributed in developing the microstructures observed in the sample.

### 2.6.2 Sealing of the microfractures

As discussed above, domainal fractures were sealed by equigranular and slightly elongated, strain free quartz crystals that show a slight rotation about the bulk vorticity axis (Y-direction of finite strain). We propose that two main mechanisms were responsible for the formation of the observed microstructure: 1) Precipitation of new grains into the fracture promoted by circulating fluids (Hippertt and Egydio-Silva, 1996; Menegon et al., 2008; Vernooij et al., 2006a). New grains started to grow by a solution-precipitation mechanism promoted by the fluids that were forced into the fracture because of the high fluid pressure; and 2) As fractures propagated through the crystal, possibly by localized stress corrosion (e.g. van Daalen et al., 1999; Vernooij et al., 2006b), fragments of the host grain were ripped loose generating micro gouges, especially in volumes with jogs and geometric irregularities along the fracture planes (Fig. 10c). This mechanism explains the rotation of the crystallographic axes as shown by the EBSD data (Fig. 6c, 7c and 10c, insert). Subsequent growth of the new grains occurred either by precipitation from the actively infiltrating over pressured fluid (solution-precipitation; Vernooij et al., 2006a) or by solution transfer from one pore wall to another (dissolution-precipitation; Hippertt and Egydio-Silva, 1996). This model explains *Domain 1* and *4*, where fractures formed pervasively.

In *Domain 3*, where fracturing was minimal due to the favorable orientation of the crystal for basal  $\langle a \rangle$  dislocation glide, less energy was required to maintain steady state crystal-plastic deformation and significant embrittlement was not achieved; hence, no bands of new grains sealing older fractures were produced, and instead only local pockets of newly formed, strain free grains crystallized. These pockets and a few only poorly developed bands are all oriented along discrete subgrain- to grain boundaries with relatively high misorientations ( $10^\circ \pm 3^\circ$ ; Fig 8a and d), which may have acted as conduits for fluids during deformation and initiated dissolution-precipitation in pores and micro fractures oriented along the subgrain- and grain boundaries. Fluid infiltration may also have led to

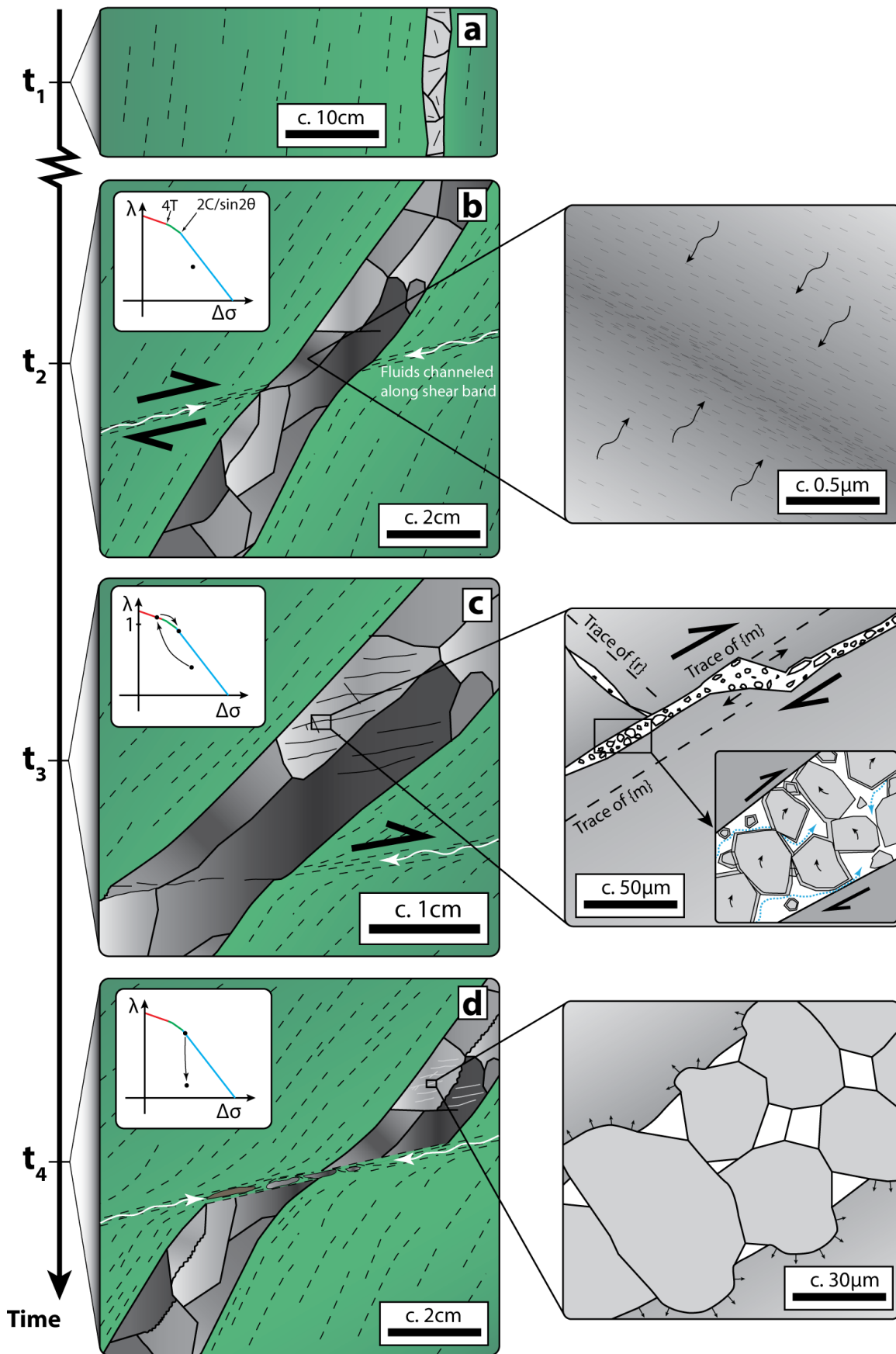


## 2. Brittle-viscous deformation of vein quartz

hydrolytic weakening, which is known to promote local climb-accommodated dislocation creep (e.g. Kronenberg et al., 1990; Mancktelow and Pennacchioni, 2004). This could account for the few observed bands of subgrains. The growth of new grains within pores is well described by Hippertt and Egydio-Silva (1996) and results in intrapore grains, which first grow by dissolution-precipitation followed by grain boundary migration when they touch the opposite fracture wall (Fig. 10c, insert and d, insert). Because the new grains are largely strain free, they grew at the expense of the old grains, which are more deformed and have a higher dislocation density (e.g. Drury and Urai, 1990). Furthermore, Schmid and Casey (1986) proposed that grains growing by grain boundary migration tend to grow optimally oriented for basal slip, i.e. with the basal plane at  $45^\circ$  to  $\sigma_1$  (Vernooij et al., 2006a). This mechanism could have also contributed to the rotation of the new grain crystals seen in the EBSD data (Fig. 6).

As also proposed by several authors (e.g. Derez et al., 2014; Trepmann et al., 2007; Vernooij et al., 2006a), we conclude that dynamic recrystallization by subgrain rotation recrystallization can be excluded for the formation of the bands containing new grains in domain 1 and 4. We base our interpretation on the following: 1) No progressive lattice rotation towards the bands of new grains is observed (Fig 6d and 9d); 2) The new grains show large misorientations to the host (Fig 6d and 9d) at low strains, making grain boundary sliding unlikely; 3) New grains are subhedral to euhedral with  $120^\circ$  angles between the crystal faces, indicating growth within a fluid (Hippertt and Egydio-Silva, 1996); 4) Fluid inclusions encircle the new grains and their pitted grain boundaries (Fig. 4d and 5); and 5) Secondary mineral phases occur between the new grains indicating that fluids penetrated the crystal (Fig. 4d and 5c and d).

New grains, however, have also accommodated some crystal plastic deformation, because the embrittlement of the system is believed to have occurred only transiently as fluid pressure reduced the effective stresses and caused failure by brittle processes. As stress was released by the opening of intracrystalline fractures and venting of the overpressured fluid phase, viscous deformation became dominant, possibly also promoted by residual fluids (Segall and Simpson, 1986). This renewed viscous environment during ongoing deformation enhanced dislocation glide and possibly even local climb, which caused bulging grain boundaries, subgrain formation (Fig. 10d and 4c) and, as noted above, growth of new grains at the expense of old grains by grain boundary migration (Fig. 10d, insert). Vernooij et al. (2006a) and Trepmann et al. (2007) also report partially deformed new grains that show flattening and hence elongation perpendicular to  $\sigma_1$ . Recrystallization in *Domain 2* and *3* was largely the result of crystal plasticity and subgrain rotation due to the suitable orientation of the crystal for the activation of the basal  $\langle a \rangle$  slip system. Only a minor component of fracturing and neo-crystallization along the rhomb plane is envisaged.



**Figure 2-10:** Conceptual sketch of the temporal evolution of the studied quartz vein with associated microstructures. See text for further details.  $\lambda$ - $\Delta\sigma$  diagrams (Cox, 2010) illustrate the transient evolution of fluid overpressure.



## 2. Brittle-viscous deformation of vein quartz

In summary, we propose a model of alternating brittle and viscous deformation localized in intracrystalline bands hosted in vein quartz crystals (e.g. Hirth and Beeler, 2015; Fig. 4f). The relative role of subgrain rotation recrystallization as opposed to neocrystallization along microcracks is determined by the crystallographic orientation of the host grain, which results in remarkably different microstructures and internal partitioning of strain. TEM analysis of dislocation microstructures in the interior of the old grains and next to the bands of new grains would be necessary to verify and confirm some of our conclusions.

### 2.6.3 Mechanical implications for the PIS development

The described microstructures and the proposed conceptual model have implications on both the local geological history and on the rheological properties of quartz and phyllonitic rocks.

The exact timing of vein emplacement remains largely unconstrained. The fact that the vein crystallized statically prior to being cut by a shear band of Caledonian age within the fault core of the NFZ and that it belongs structurally to a Caledonian imbricate structure (Torgersen and Viola, 2014; Torgersen et al., 2014) demonstrates that the vein is pre- to syntectonic. Whether the vein crystallized during the Paleoproterozoic and was later reworked during Caledonian deformation or it formed during the Paleozoic Caledonian orogeny is not known.

Irrespective of the time of initial vein formation, as the Caledonian nappes were translated towards the foreland within the highly deformed PIS, deformation localized under lower greenschist facies conditions. The host metabasalt acquired a penetrative foliation through the growth of fine-grained white mica and chlorite at the expense of feldspar, transforming the host rock into a weak phyllonite and leading to strain partitioning (Tullis and Wenk, 1994). Syndeformational carbonation reactions have been proposed as a viable mechanism for the transformation of the originally massive metabasalts into foliated, weak phyllonites (Torgersen and Viola, 2014). Progressive metabasalt phyllonitization localized strain efficiently within the NFZ due to the reduction of internal friction and grain size reduction as the rock could deform more readily by grain boundary sliding and dissolution-precipitation creep (e.g. Bos and Spiers, 2002; Stünitz and Fitz Gerald, 1993; Torgersen and Viola, 2014). Within such a structural framework, plagioclase and quartz represented relatively competent porphyroclasts, deforming predominantly by fracturing (Fig. 4a). The studied quartz vein remained mostly unaffected by phyllonitization, thus becoming a rigid object that escaped most deformation (Bell, 1985; Menegon et al., 2008; Tullis and Wenk, 1994), although some dissolution at the vein-matrix contact may have occurred (white arrows in Fig. 3b). The progressively increasing competence contrast between the phyllonitic matrix and the quartz vein generated significant strain

partitioning, wherein coaxial deformation was accommodated by the quartz vein (e.g. the described conjugate shear bands) and non-coaxial deformation by the matrix, as shown by, for example, rotated porphyroclasts and asymmetric shear bands (e.g. Goodwin and Tikoff, 2002; Menegon et al., 2008). This rheological contrast is also believed to be crucial for the transient embrittlement of the quartz vein as already argued for in the discussion above. Both the phyllonite S and C' planes, due to their interconnected anastomosing geometry and low coefficient of friction, deformed at a significantly higher strain rate than the quartz vein. This contrast enhanced quartz strain hardening, possibly by dislocation tangling within the vein, because deformation mechanisms within the matrix (such as dissolution-precipitation creep and grain boundary sliding) were much more effective than glide-accommodated dislocation creep.

The NFZ deformed in a fluid rich system as shown by a plethora of microstructures within both the matrix and the vein quartz (e.g. Fig. 4). Several authors have stressed the importance of fluids in promoting viscous deformation in quartz (e.g: Kronenberg and Tullis, 1984; Mancktelow and Pennacchioni, 2004) and the role played by fracturing in distributing fluids within a rigid body located in a weak matrix (Menegon et al., 2008). Calcite veinlets within the C' shear bands indicate multiple opening events and thus point towards a fluid pressure cyclicity ( $\lambda/\Delta\sigma$  plot in Fig. 10b-d). Similar conditions are also described from other parts of the PIS, such as the Kvenklubben Fault some kilometers west of the NFZ (Torgersen and Viola, 2014).

Although the weak phyllonitic core of the NFZ could be interpreted as suggesting that the fault deformed mainly by aseismic creep, the current fault architecture has to be projected against its temporal dynamic evolution. Initial strain accommodation occurred in fact under different rheological conditions, with transient embrittlement of a > 20 m thick dolostone layer possibly inducing seismic stick-slip behavior as also suggested by other localities within the PIS. Comparison of the microstructures described here with the results of Trepmann et al. (2007) and the work by Hirth and Beeler (2015) corroborates the interpretation of the NFZ as a fault that possibly accommodated coseismic deformation.

The cyclic fluid overpressuring in the NFZ might have played an important role in steering deformation towards a more discrete accommodation style, resulting in cyclic oscillations between brittle and viscous deformation in a fault-valve behavior that facilitated the translation of the KNC to the foreland (Viola et al., 2006), but also possibly promoted seismic activity by stick-slip behavior.

## 2.7 Conclusion

The microstructures presented in this study contribute to the refined understanding of the mechanisms that accommodate strain in quartz during deformation at the brittle-viscous transition. Our observations confirm results from earlier studies and in addition allow refining existing conceptual models by showing that:

1. Under fluid-rich conditions typical of lower greenschist facies metamorphism, quartz may fracture pervasively along several intracrystalline planes such as the prism, the rhomb, and, to a minor extent, the basal plane. The exploited direction of preferential fracturing depends on the orientation of the crystallographic planes with respect to the imposed stress field.
2. Viscous weakening mechanisms, such as effective crystal plastic deformation, may reduce the need for embrittlement. However, if crystals are misoriented for optimal dislocation glide, strain hardening occurs, which promotes the onset of fracturing. Microfracturing and viscous deformation may occur, however, broadly coevally and cyclically.
3. Nucleation processes can heal and seal the microfractures. Solution-precipitation is the mechanism believed to control the process. Only minor recovery by subgrain rotation recrystallization is observed, selectively on those grains suitably oriented for slip on the basal  $\langle a \rangle$  system.
4. Cyclic fluid pressure oscillations promoted continuous switches in deformation mechanisms that resulted in transient and possibly seismogenic brittle deformation processes. Aseismic creep rapidly followed these as fluids were vented and the host phyllonite developed a penetrative, thoroughgoing anastomosing network of weak slip planes.

Fluid-assisted breakdown of the host metabasalt formed the weak phyllonite, which promoted strain partitioning into the matrix rather than in the quartz vein, which escaped most strain. Rheological contrasts between the weak, foliated host and the more rigid quartz vein also contributed to the transient embrittlement of quartz in the vein, providing positive feedback to the embrittlement caused by the presence of overpressured fluids.

## Acknowledgements

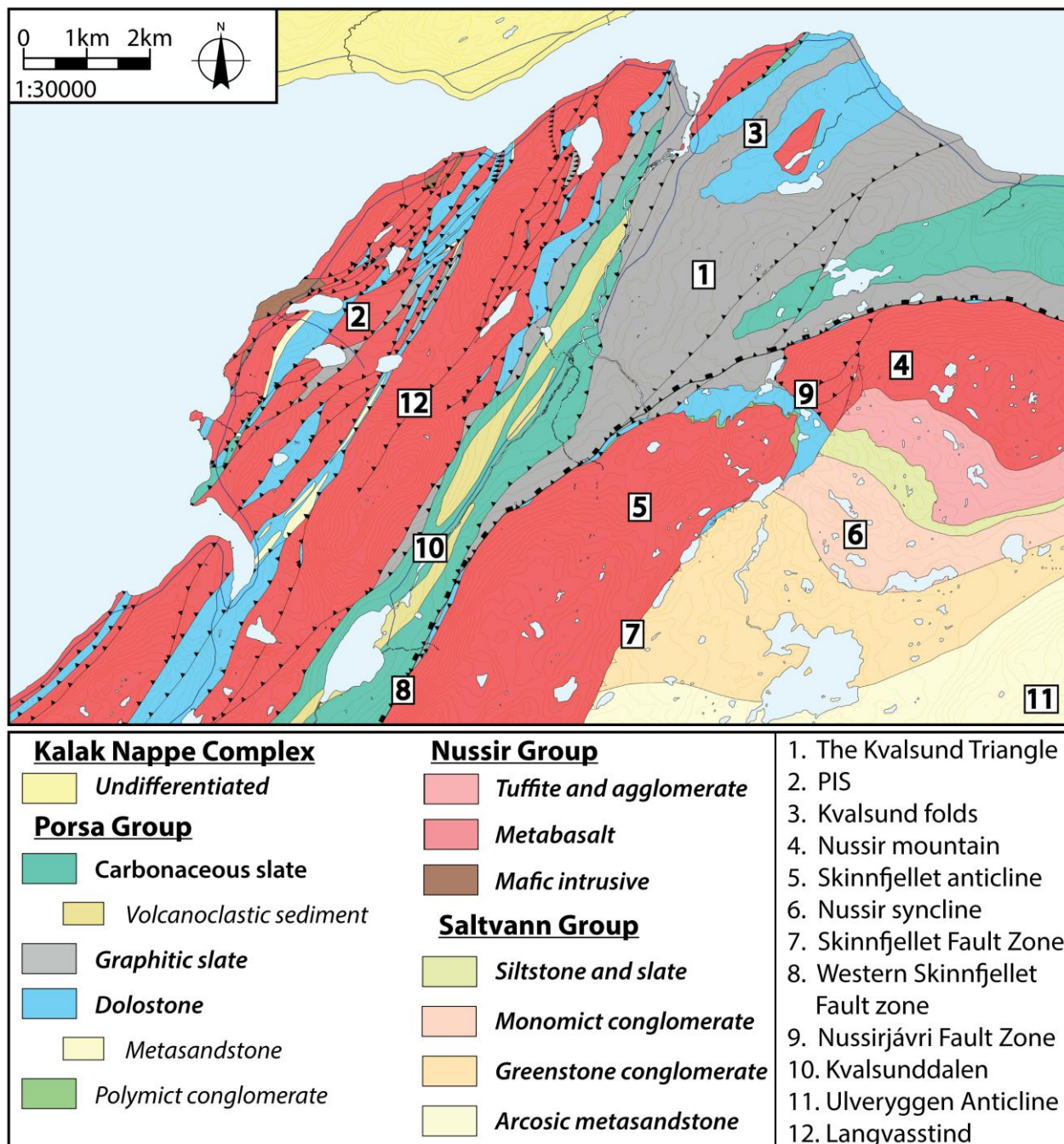
The Geological Survey of Norway and the Norwegian University of Science and Technology have supported financially the preparation of this manuscript. The reviewers, Luis Morales and Michel Bestmann, are thanked for their constructive comments and input. The guest editor Giorgio Pennacchioni is thanked for important suggestions and a very efficient editorial handling. Tine Derez

is thanked for constructive feedback. Espen Torgersen is warmly thanked for very many, long and fruitful discussions!

### 3. Methods

#### 3.1 Field techniques

Approximately six weeks of fieldwork were spent over two mapping campaigns to produce the map presented in this thesis and to gather observations and sample material.

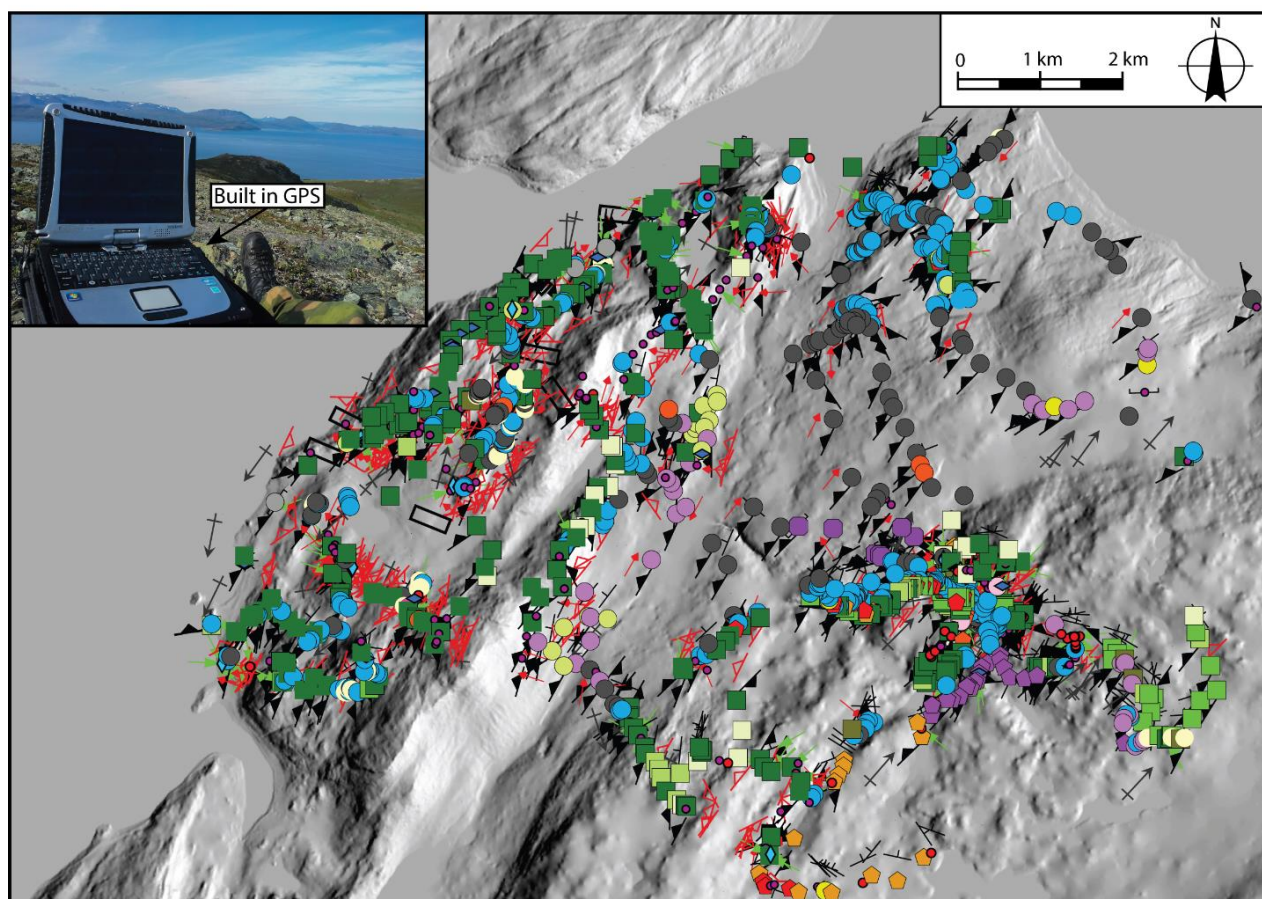


**Figure 3-1:** Geological map with locations of interest that will be referred to throughout the text.



The main focus area of the first year mapping campaign was the southeastern part of the map (Fig. 3-1; 4, 5, 6, 7 and 9). Transportation methods used were quad bikes and cars, but mostly walking. Several nights were spent camping in the field area to reduce transportation time.

The focus of the second year mapping campaign was the PIS, Kvalsunddalen and the Kvalsund triangle in the western and northern region of the field area (Fig. 3-1; 1, 2, 3, 8, 10 and 12). A car was used for the transportation to the field, but the fieldwork was conducted by foot every day for a three week period.



**Figure 3-2:** Map showing almost all registered observation points (> 1600) during the six weeks of fieldwork. The color and shape of the observation points represent different lithologies. Structural symbols are also shown. Insert show the Toughbook with its built in GPS.

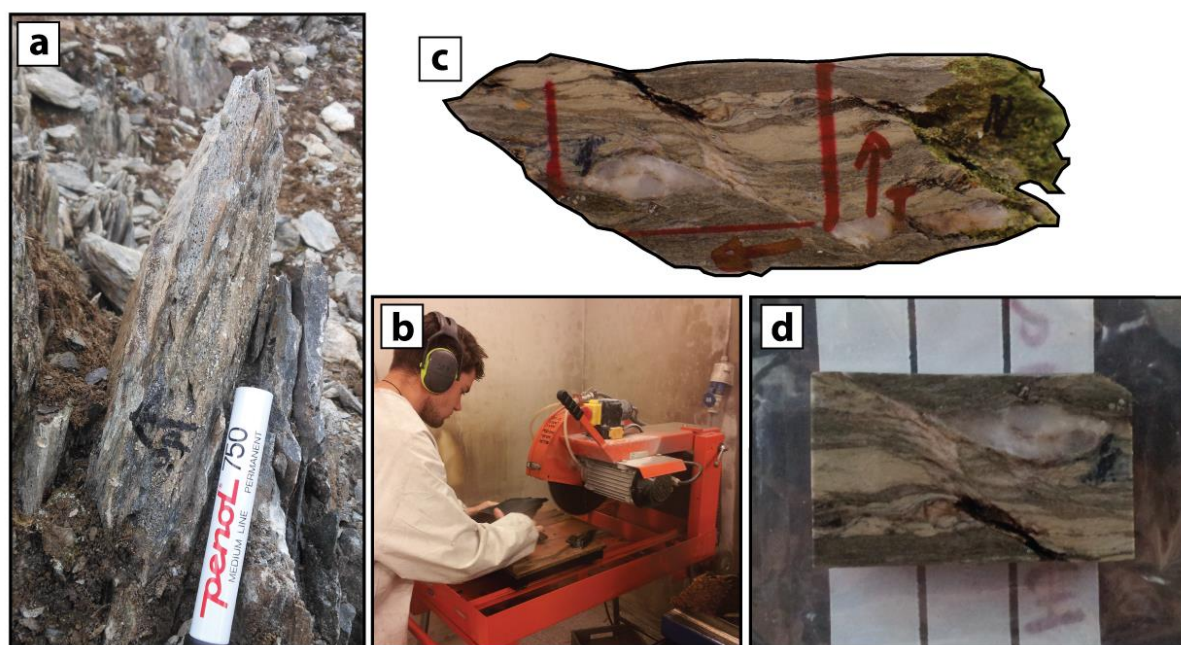
Both years, mapping was conducted digitally on a Toughbook, provided by the Geological Survey of Norway (NGU). The Toughbook is a ruggedized laptop that tolerates extreme conditions and withstands water, dust and shocks. It contains a built-in GPS (Fig. 3-2; insert), which is directly utilized by the software ArcMap from ESRI. For registration of field observation points the software Sigma was used (Fig. 3-2). This software is developed by BGS, the British Geological Survey, and is an add-on for ArcMAP (Henderson and Viola, 2011). Within Sigma the user can register

observation points and describe lithology, record structural measurements, samples and add comments, place georeferenced photos, and sketches.

Digital mapping allows the mapper to bring digitized and geo-referenced maps, such as geophysical maps, previous geological maps etc. into the field. Furthermore, all types of software, e.g. stereonet, strain calculation-, 3D mapping software and literature may be brought out into the field and are readily accessible. In addition, data exchange among mappers and colleagues working in the same area is greatly facilitated. This is all extremely valuable when in the field and helps to ensure better and more accurate mapping and, in my opinion, no mapping geologist should embark new mapping projects without the aid of digital mapping techniques.

### 3.2 Thin section preparation and microscopy

Samples collected in the field were cut with a diamond saw parallel to the stretching lineation and normal to the foliation at the NGU laboratory. The samples were photographed before and after they were cut. The desired location of the thin section was then marked on the cut surface and the arrows representing the stretching lineation and the stratigraphic way up were transferred from the top of the sample to the backside of the area that would be prepared as a thin section (Fig. 3-3).



**Figure 3-3:** (a) Sample in the field, before it is dislodged. Arrows indicate geometric up and the plunge of the lineation (not visible in the photo). Stratigraphic up or geographic coordinates are used for samples with sub-vertical foliation. (b) Assistant cutting the sample parallel to the lineation and orthogonal to the foliation. (c) Cut rock section with arrows transferred from the field specimen indicating geographic up (open arrow) and plunge direction of lineation (closed arrow). Red lines indicate thin section location. (d) Slice cut along red lines in (c) and ready for thin section preparation. Arrows on the backside of rectangle.

The rock slices were then cut into the rectangle and handed over to the thin section laboratory where the rocks were prepared into 30 µm thick thin sections. The thin sections used in the SEM were polished to ensure good results in the SEM. Thin sections prepared for EBSD underwent a special polishing technique, as described in detail below.

Microscopy was conducted at both NGU and NTNU at standard petrographic polarization microscopes. Overview photographs were taken at NGU and stitched together using Adobe Photoshop.

### **3.3 SEM**

#### **3.3.1 BSE**

Backscatter electrons (BSE) images were produced for some fault rock samples to image the porosity within the quartz crystals (Fig. 2-5). BSE images are in shades of grey that vary as a function of the average atomic number of the imaged mineral. Minerals with high average atomic number, such as sulfides, appear almost white in a BSE image, while minerals like quartz appear darker (e.g. Fig. 6-22).

#### **3.3.2 SEM-EDS**

SEM-EDS (Scanning Electron Microscope – Electron Dispersive Spectrometer) work has been carried out at NGU for qualitative chemical composition to determine the mineralogy of some of the samples. The method relies on an electron beam to excite atoms in the crystal lattice, which produces X-rays that are registered by a crystal within the EDS detector. The energy from the X-rays is transformed into electric power and since each element has a specific X-ray intensity, a specific amount of eV will be registered depending on which elements are present in the sample. This yields a semi-quantitative mineral chemistry, which is sufficient to identify a mineral phase and its main chemical signature.

#### **3.3.3 EBSD**

Electron Back Scatter Diffraction (EBSD) is a SEM technique that enables the quantification of complete crystallographic orientations within a polished sample. The EBSD detector acquires diffraction patterns from the crystal lattice of a sample mounted obliquely to the incident electron beam (Fig. 3-4). The diffraction pattern can further be used to calculate Miller indices for each specific point analyzed. By measuring several points, large areas may be mapped, yielding the



complete crystallographic orientation of the mapped area. In quartz, the step size between contiguous analyses can be as low as 250 nm (that is, the size of the beam damage halo in quartz) and the accuracy of the method is usually  $< 1^\circ$  (Prior et al., 2009).

### 2.3.3.1 Pattern acquisition

The EBSD detector itself is a phosphorous screen mounted in front of a high-sensitivity camera (Nordif UF-1000) registering electrons that have been diffracted in the upper 20 nm of a mineral (Prior et al., 2009). The investigated sample surface needs to be perfectly flat. In standard EDS or wavelength-dispersive spectroscopy detection (WDS), a mechanical polish is sufficient. For EBSD analysis, however, sample must undergo a chemical polishing where 400 Å colloidal silica in suspension, called OP-U, is used.

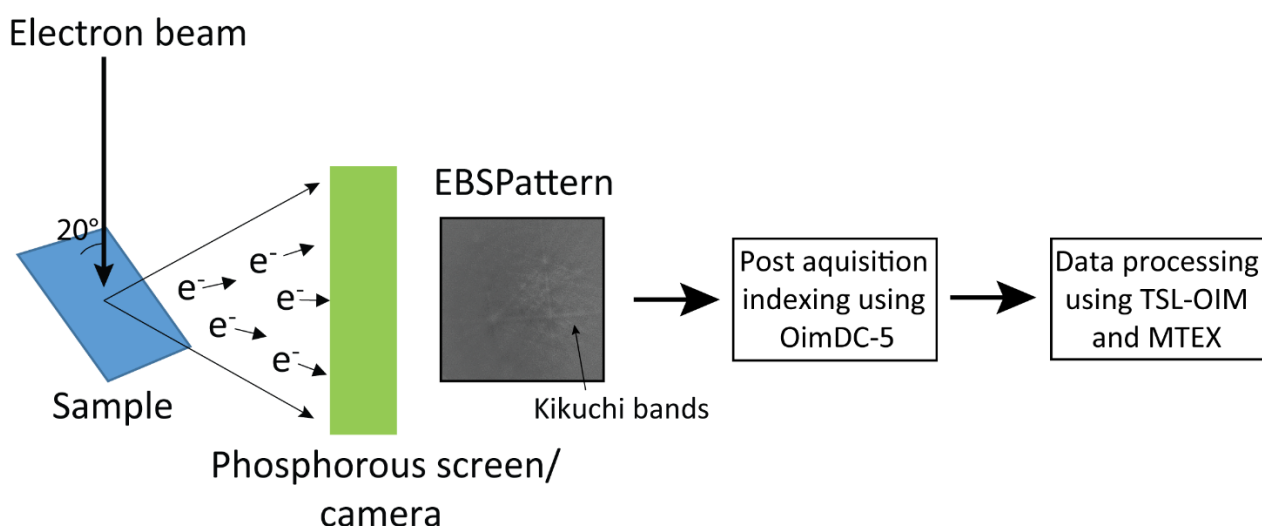
Before polishing with OP-U, the thin section must be polished mechanically as in the case for reflected light microscopy thin sections. The subsequent chemical polishing is carried out by soaking the polishing mat with OP-U. The thin section is then mounted on a sample holder and placed on the mat for 5-12 minutes before it is rinsed in 96% alcohol. The quality of the polish can be assessed by looking at the thin section in reflected light microscopy. The method followed was developed at NTNU by Moen et al. (2003).

After sufficient polishing, the thin section is mounted into a Hitachi SU6600 Variable pressure VP-SEM. To avoid any contamination, latex gloves were used at all times when handling the sample and sample holder. Note that the sample was not coated by neither carbon, nor gold, as is common practice when investigating geological materials, due to the low electric conductance of quartz. This is because of the very shallow acquisition depth of the EBSD signal. To avoid problems with electron charging on the surface of the sample a high-pressure HP-SEM (or a VP-SEM) is commonly used. When running low vacuum (high pressure), the diffracted electrons may collide with air particles on their way to the detector, which contributes to impairing the signal from the sample and weakens the pattern quality. However, running on low vacuum is necessary to avoid charging and a compromise must be made.

When the diffracted electrons hit the EBSD detector, a pattern called Electron Back-Scatter Pattern (EBSP) appears (Fig. 3-4). The pattern consists of bands of different thickness and orientation, called Kikuchi bands. These bands represents the gnomonic projection of the crystallographic axes of the investigated mineral (Schwartz et al., 2009). By calculating the angle between these bands and comparing them to already known patterns, the Miller indices at the exact measured point can be computed.

To acquire the best possible EBSP's there is an entire range of settings on the SEM that require fine-tuning. These vary with material parameters, e.g. accelerating voltage and working distance, which were set to 20 kV and approximately 25 mm respectively. In order to maximize the area investigated by EBSD and to avoid poor data quality, which generally occurs at too low magnifications, a compromise had to be made concerning the desired magnification. Therefore, the magnification was set to 150 x for all maps. For a complete list of settings, see Appendix A.

Before recording can start an acquisition area was defined from optical microscope photographs. The areas chosen in this study measured 824x824  $\mu\text{m}$  and the step size was set to 2 $\mu\text{m}$  with an exposure time of 9950 $\mu\text{s}$ /EBSP, yielding a total of 169744 EBSPs per map. Ten acquisition patterns (two in each corner and two in the middle) were collected to aid the indexing process after acquisition. One calibration pattern was acquired in the middle of the acquisition area for height and dip corrections of the patterns.



**Figure 3-4:** Schematic sketch of the EBSD workflow. Electron beam hit highly tilted sample and diffract within the upper lattice planes of the sample. The diffraction pattern (EBSP) is registered on a phosphorous screen with a high resolution camera. After acquisition of the EBSP's they are indexed (given a Miller index) before further processing can be conducted.

### 2.3.3.2 Processing

After the complete recording of the EBSP's, the data were loaded to a computer for offline indexing. Some SEM and EBSD detectors, such as those by Oxford Instruments, offer online indexing, i.e. indexing is performed live during acquisition. This does not give the possibility to vary parameters after the acquisition is done, while offline indexing saves the raw data and enables data processing and reduction to be run multiple times. The indexing process was carried out in OimDC-5 NordifUF indexing software. In it, the calibration patterns are loaded and viable solutions are chosen based on selected Hough-transformation (mathematical transformation of lines into points) settings. These

calibration patterns help to ensure a better solution during the indexing process, since the thin section is placed at an angle to both the electron beam and the EBSD detector, yielding different position of the Kikuchi bands at the top and at the bottom of the sample. A previously produced indexation standard is loaded into the program before indexing can begin.

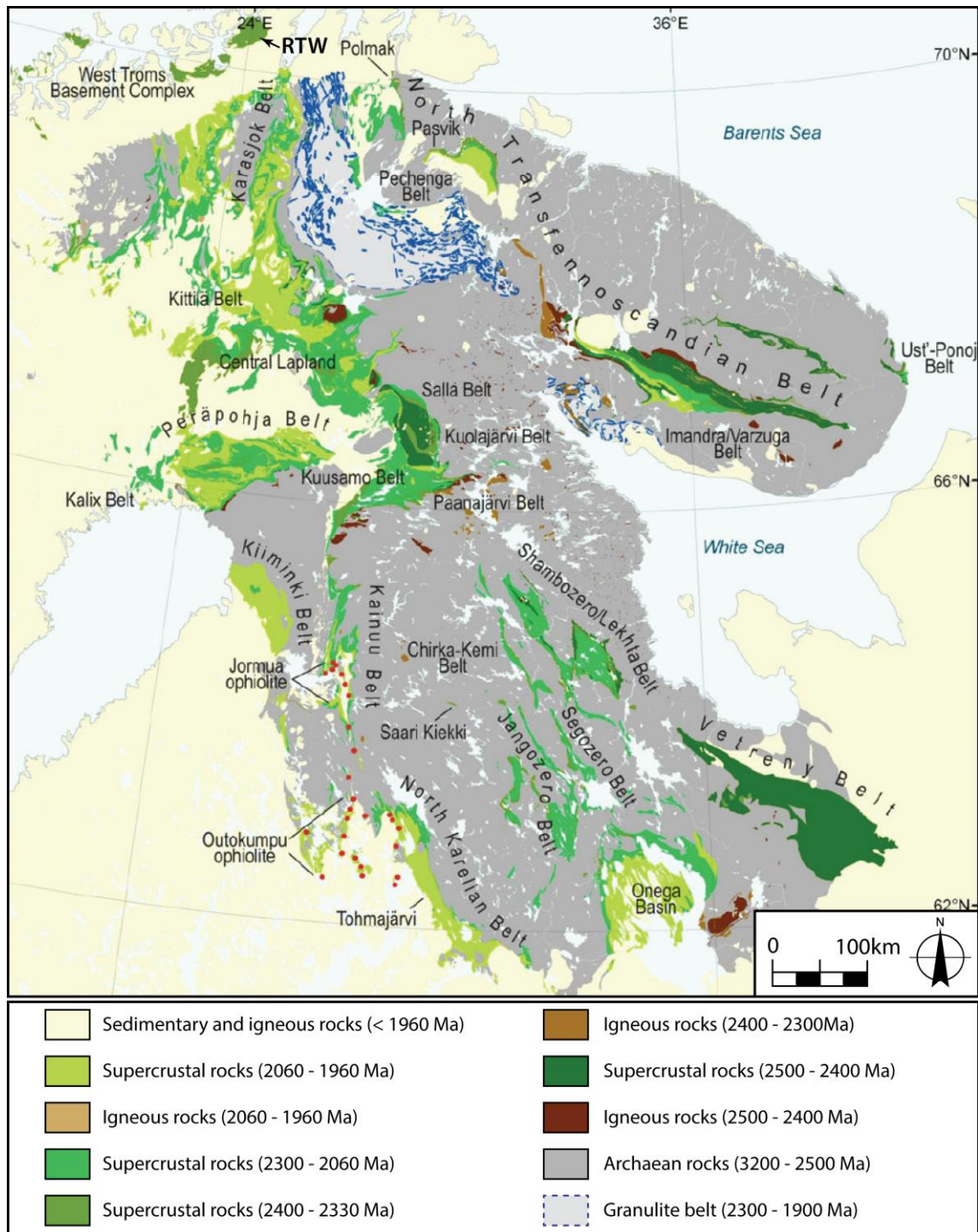
Further work was carried out using MTEX 3.5.0, an open source toolbox for MATLAB. In it, the data were processed, grain boundaries and subgrain boundaries were calculated based on misorientation data, before EBSD maps and pole figures were generated. A total of 13 EBSD maps were acquired from the sample HJK\_001 (see Appendix B and section 2).



## 4. Geological and tectonic setting

### 4.1 The Fennoscandian shield

The RTW is a basement culmination through the Kalak Nappe Complex (KNC) of the Scandinavian Caledonides that records at least two major orogenic episodes: The Paleoproterozoic Svecofennian-, and the Silurian Caledonian orogeny.



**Figure 4-1:** Map of the Fennoscandian Shield from Melezhik and Hanski (2013).

The RTW is the northernmost exposed part of the Archean to Paleoproterozoic Fennoscandian Shield (Fig. 4-1). The Fennoscandian Shield is a large basement complex that stretches from northern Norway into northern Finland and Sweden and into northwestern Russia, the Kola Peninsula and the Karelia. Melezhik and Hanski (2013) proposed that five major geological complexes form the Fennoscandian Shield. The oldest core is represented by late Archean granitic gneisses (> 2500 Ma) constituting the basement rocks of the shield. On top of the gneisses are early Paleoproterozoic (c. 2500 - 2000 Ma) metavolcanic- and metasedimentary rocks and c. 2100-1930 Ma amphibolite to local granulite facies metasedimentary and metavolcanic terranes (Fig. 4-1). These are post-dated by ophiolite complexes and, in turn, by middle Paleoproterozoic (c. 1920-1880 Ma) accreted metavolcanics and metasedimentary rocks representing microcontinent collision during the Svecofennian orogeny. Although no Archean basement is observed within RTW, the metasedimentary and metavolcanic rocks outcropping in RTW are correlated with the belts of similar lithologies on the Fennoscandian Shield (Fig. 4-2 and Fig. 4-3).

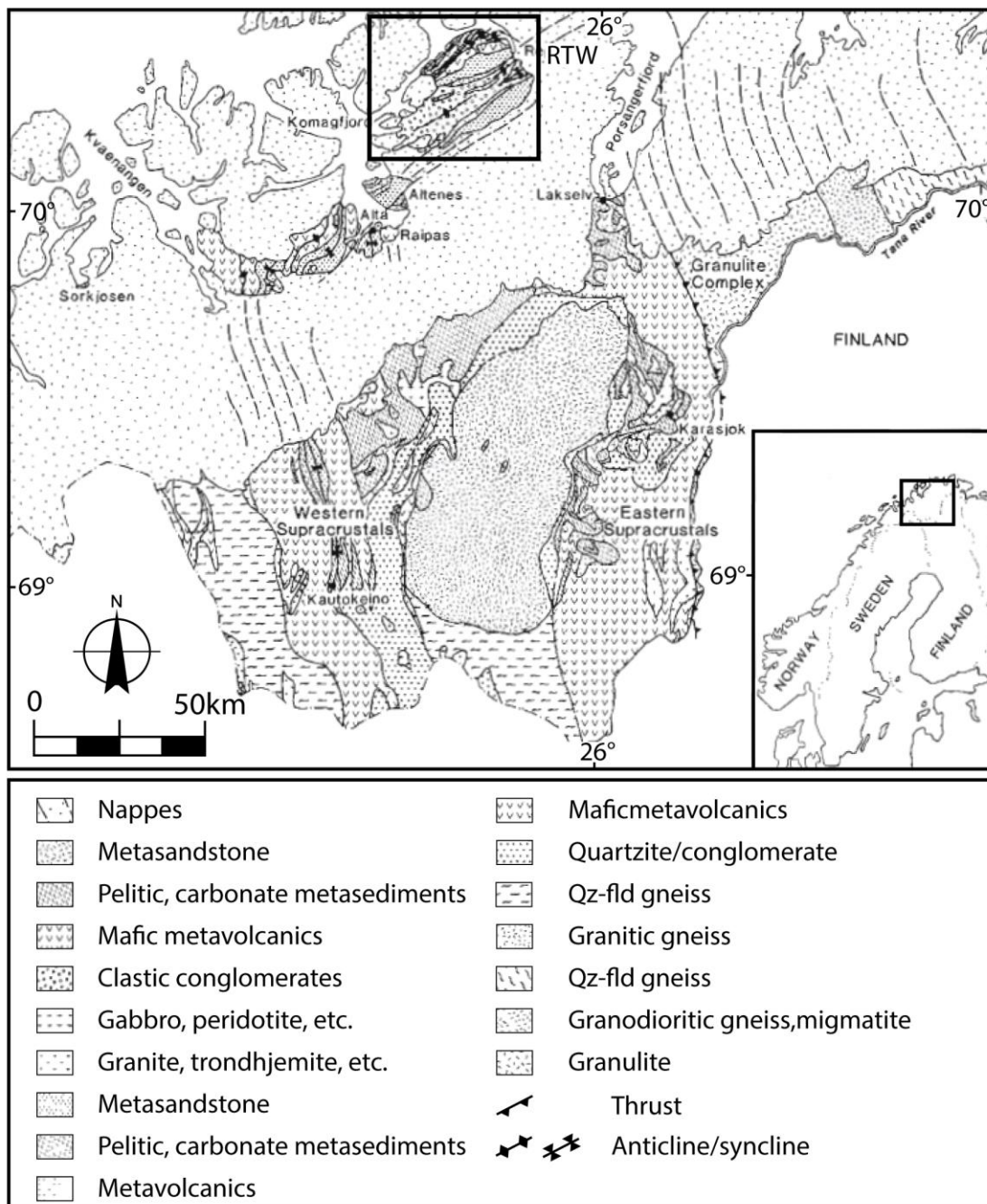
#### **4.1.2 RTW stratigraphy and correlations**

All the basement rocks of the RTW belongs to the Raipas Supergroup (Reitan, 1963). These rocks are mainly metasedimentary sequences, mafic metavolcanic- and extrusive metavolcanic rocks that were intruded by ultramafic, mafic and felsic rocks (e.g. Pharaoh et al., 1983; Viola et al., 2008; Fig. 4-3). The metasediments were deposited as both alluvial, fluvial and marine sediments on a rifted volcanic margin (e.g. Pharaoh, 1985b; Pharaoh et al., 1983; Reitan, 1963; Torgersen, 2015).

The stratigraphic order of the lowermost groups of RTW is currently under discussion. It has long been an accepted theory that the lowermost group of the RTW is the Holmvatn Group (Nilsen and Nilsson, 1996; Pharaoh et al., 1983; Reitan, 1963), which core a large anticline with the Saltvatn- and Nussir Group stratigraphically above. The detailed stratigraphic and structural investigations of Smeplass (2013) and Torgersen (2015), however, suggest that the Saltvatn Group rests stratigraphically below the Holmvatn Group and that the latter possibly can be correlated, from its position on the southeastern limb of the Ulverygg Anticline, with the Nussir Group on the northwestern limb (Fig. 4-4).

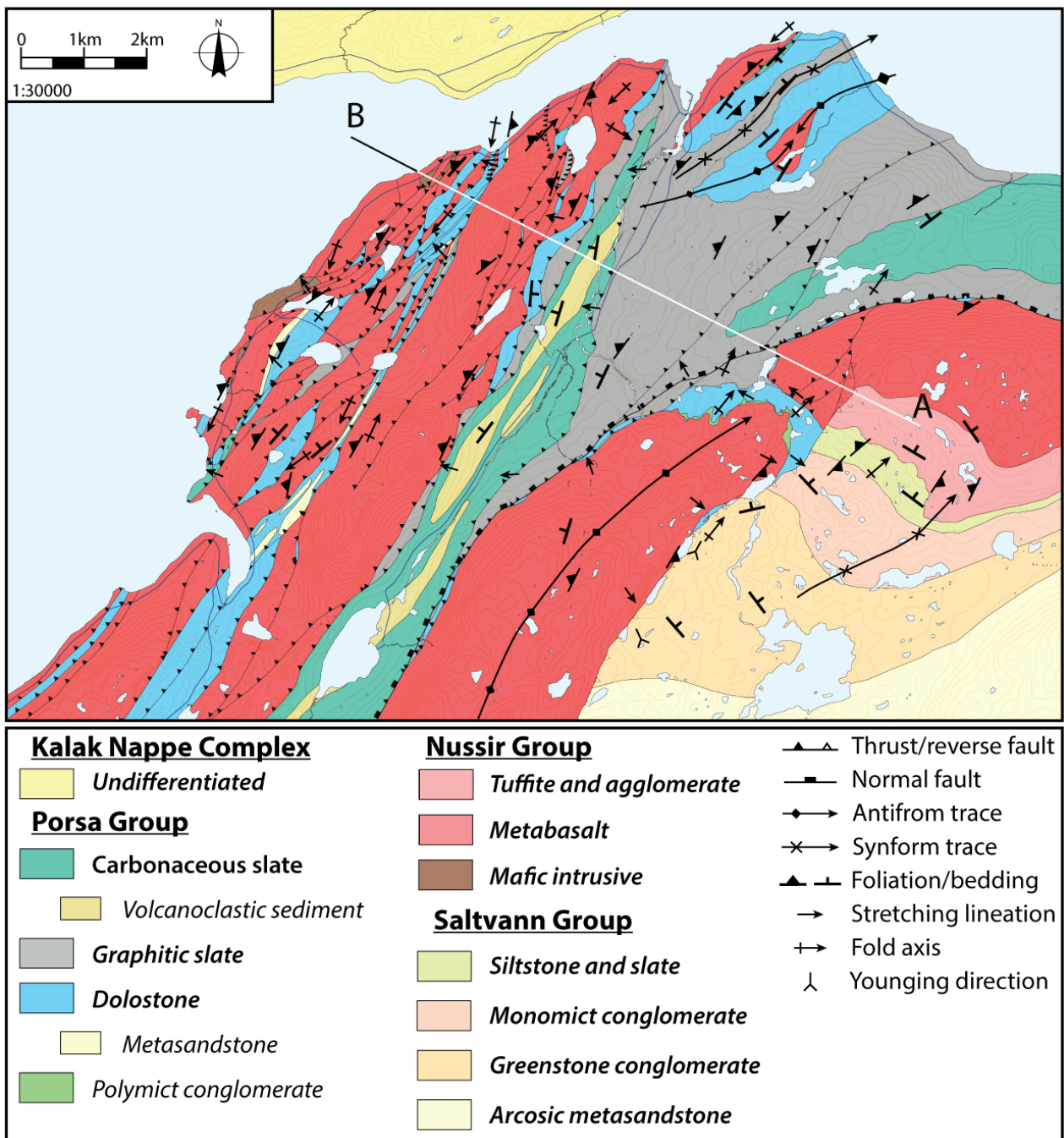
The Saltvatn Group is composed of a large package of fluvial sediments (Fig. 5-1) that is generally rich in magnetite and locally shows enrichments in fuchsite. This enables the correlation to other fuchsite-rich metasedimentary units, such as the Masi-quartzite on the Finnmarksvidda and possibly even farther to the Kuusamo area in northern Finland and the Ust'-Ponoy Belt on the eastern coast of the Kola Peninsula (Hanski and Melezhik, 2013). Stratigraphically above these metasandstones are





**Figure 4-2:** The geology of Finnmark, after Pharaoh et al. (1983)

more locally derived volcanoclastic conglomerates with significant lateral thickness variations (Fig. 5-1 and Fig 4-4). The lateral variations in thickness are explained in terms of sedimentation during fault activity in a fault bounded half-graben (Torgersen, 2015). Pharaoh et al. (1983), on the other hand, suggested that the observed lateral thickness variations are not a primary feature, but are rather due to thickening in the hinge zone of a large syncline. The syndeformational thickening would have happened in a transgressive system within which marine clastic- and carbonaceous sediments were deposited over aerial fluvial and alluvial sediments (Pharaoh et al., 1983; Torgersen, 2015). Part of the marine carbonaceous succession hosts the large Nussir Cu-deposit.



**Figure 4-3:** Geological map of the northwestern part of the RTW. See Appendix D for larger version and Figure 4-5 for cross section.

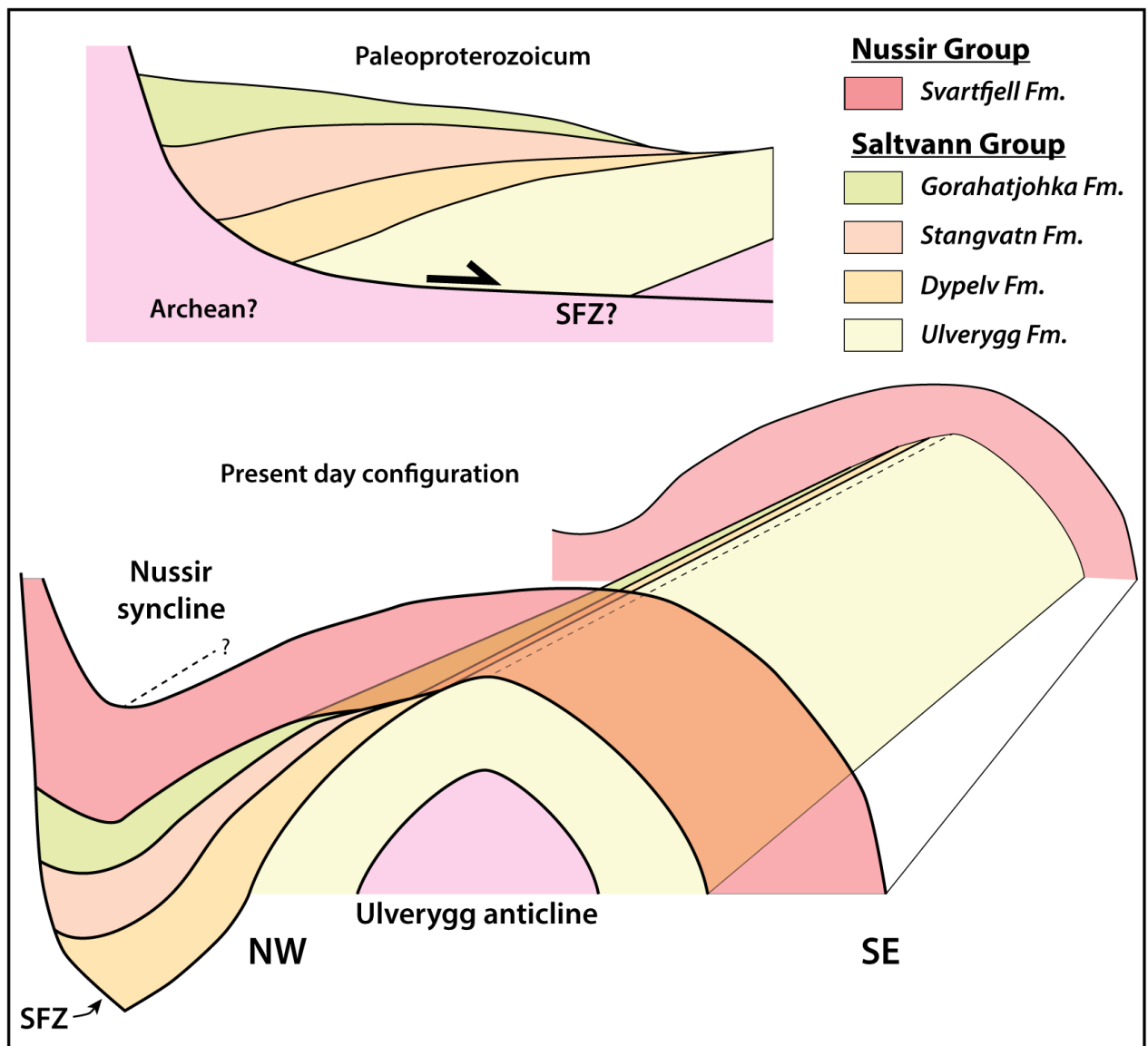
Conformably above the Saltvatn Group is the Nussir Group (Fig. 5-1), which comprises mafic, often magnetite-rich volcanoclastic tuffs and metabasalts. Unconformably over the Nussir Group is the Porsa Group, which documents a progressive sea-level change from shallow marine dolostones with oncolitic and stromatolitic horizons, to relative deep marine or anoxic environment with no clastic input where graphitic slates were deposited, and back to shallow marine and tidal-influenced, intercalated micritic and fine-grained (volcano)clastic sediments. The graphitic slates can be possibly correlated to similar systems found elsewhere in the Fennoscandian Shield, like the supergiant



#### 4. Geological and tectonic setting

Pechenga petroleum field that were deposited between 2060 Ma and 1960 Ma, most possibly due to a global change in atmospheric oxygen, the Lomagundi-Jatuli event (Hanski and Melezhik, 2013).

A thin sequence of autochthonous to parautochthonous, strongly deformed shales, siltstones and quartzites belonging to the Lomvatn Formation are found as a discontinuous layer around the RTW, directly below the Caledonian nappes. The Lomvatn Formation is proposed to be deposited during the Neoproterozoic Vendian phase as constrained by a discontinuous layer of tillite diamictites exposed in the southern part of the window (Jansen, 1976; Pharaoh, 1985a; Pharaoh et al., 1983; Reitan, 1963; Rhodes, 1976).



**Figure 4-4:** 3D conceptual cross section of the Ulverygg anticline and Nussir syncline. Insert at the top show possible pre-Svecofennian architecture of the Skinnfjellet Fault Zone (SFZ).

### 4.1.2 Svecofennian orogeny and Neoproterozoic deformation episodes

The sediments of the Raipas Supergroup were deformed during a c. 150 Myr, NW-SE compressional phase of the Svecofennian orogeny from 1900-1750 Ma (Pharaoh and Pearce, 1984). The generally agreed upon model for the Svecofennian orogeny propose a subduction type orogeny with arc formation and microcontinent accretion (e.g. Lahtinen et al., 2008; Lahtinen et al., 2009). Within RTW, the Svecofennian peak metamorphic grade reached upper greenschist – lower amphibolite facies conditions. The peak metamorphic event was dated by Pharaoh et al. (1982) to c.1840 Ma. In the study area, this compressional episode resulted in kilometer scale wavelength, upright, open folds with sub-horizontal, NE-SW-trending fold axis, with most primary sedimentary structures preserved.

Evidence for several tectonometamorphic events that took place between the Svecofennian and the Caledonian orogenies are found in the surrounding areas. These are the Porsanger orogeny at c. 850-800 Ma (Corfu et al., 2007; Daly et al., 1991; Kirkland et al., 2006) and the younger Timanian orogeny with a peak metamorphic event at c. 600-575 Ma, constrained by recalculated K-Ar whole rock analysis (Roberts and Siedlecka, 2002). These events may have also affected the RTW and may be partially recorded in the geological features preserved within the PIS (e.g. Torgersen et al., 2014), although no clear cut evidence could be documented by this project.

## 4.2 Caledonian influence

A significant portion of Finnmark is covered by flat-lying Caledonian nappes, first described and recognized by Holtedahl (1918, 1932). These nappes override the Archean to Neoproterozoic basement in Finnmark along thin tectonic contacts (Fig. 4-2). One of the largest nappe complexes is the Kalak Nappe Complex (KNC), which stretches through most of coastal Finnmark (Roberts, 2003; Siedlecka and Roberts, 1996). It consists primarily of two lithologies: 1) amphibolite facies psammitic and pelitic metasediments (Rice, 1984; Rice, 1998), and 2) intercalated gneiss slivers (e.g. Gee et al., 2008; Menegon et al., 2011a; Roberts, 2003; Slagstad et al., 2006), which are thought to represent allochthonous basement slivers (Ramsay and Sturt, 1977). A large igneous province to the west of the RTW, the Seiland Igneous Province (SIP), intruded these lithologies at 560-570 Ma. It is interpreted as the product of a short lived alkaline magmatic event that generated primarily gabbro and is genetically related to a pre-Caledonian extensional phase (Menegon et al., 2011a; Roberts et al., 2006).

Sturt et al. (1978) proposed an earlier, late Cambrian - early Ordovician emplacement of the KNC (the Finnmarkian phase). The KNC, however, is over-thrusting the late Vendian – early Cambrian Lomvatn Formation in the RTW and contains the SIP, which has the same age as the Lomvatn

Formation, therefore, the term “Finnmarkian” was dismissed by Corfu et al. (2007). Isotopic data, on the other hand, suggest that both metamorphism and a cleavage did develop around 520-470 Ma (Dallmeyer et al., 1989; Kirkland et al., 2008; Rice and Frank, 2003; Sundvoll and Roberts, 2003); however, a more comprehensive review of the “Finnmarkian” is beyond the scope of this study.

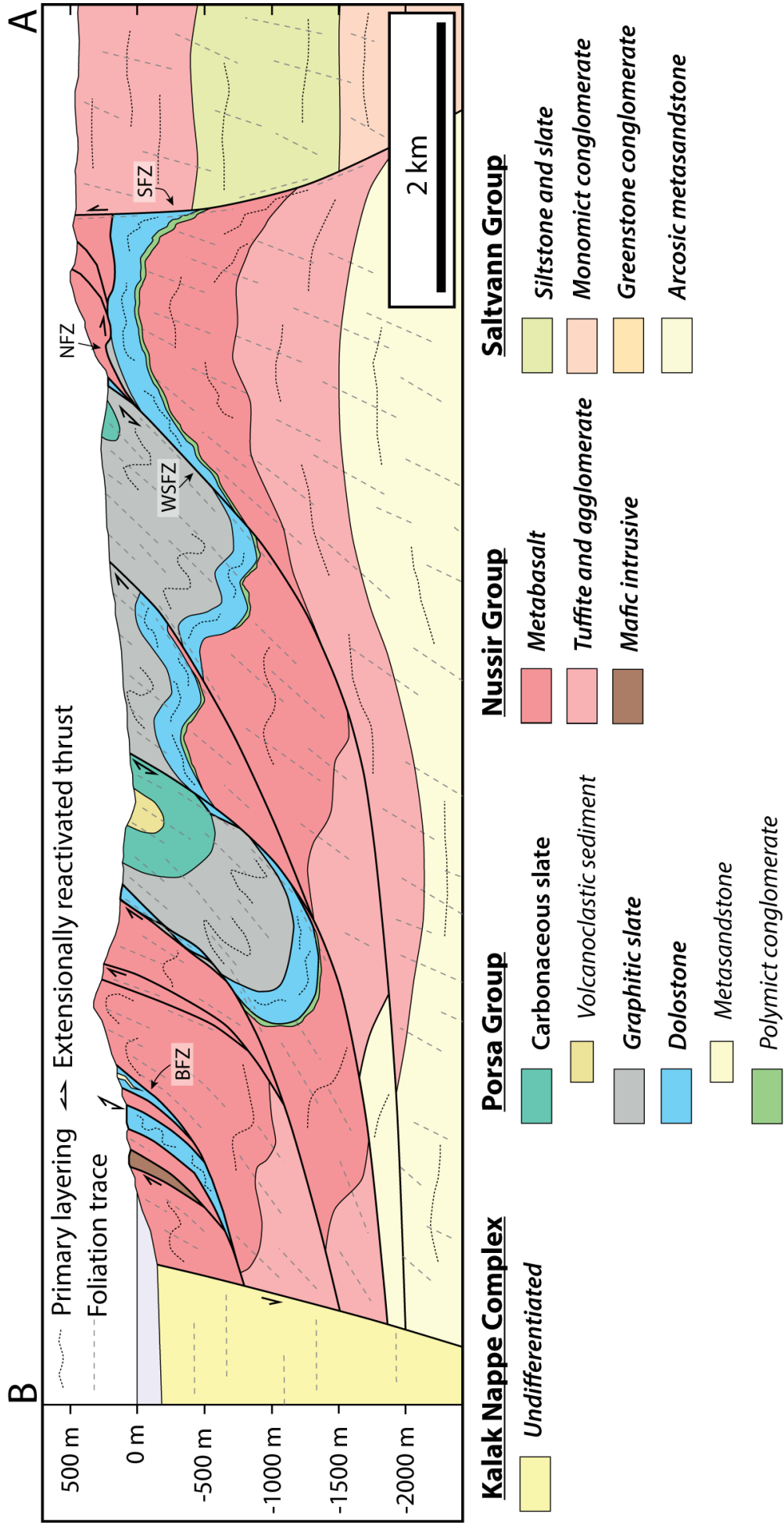
The Caledonian orogenic collapse is dated by Kirkland et al. (2007) to 410 – 400 Ma by Ar-Ar cooling ages of muscovite and biotite.

### **4.3 Porsa Imbricate Stack**

The northwesternmost part of the exposed RTW, which also represents the main study area for this master’s project, is formed by several tectonic slivers, imbricated and stacked up to form the Porsa Imbricate Stack (PIS; Torgersen and Viola, 2014; Fig.3-1; 2 and Fig. 4-5). This compressional imbricate structure was originally named the Porsa Duplex by Gayer et al. (1987). Shortening and imbrication within the PIS occurred during the early stages of Caledonian nappe emplacement (e.g. Rice, 2013; Torgersen et al., 2014), in response to overall NW-SE shortening and c. ESE nappe transport direction (Rice, 1998). As deformation progressed during the development of the PIS, the inherited Paleoproterozoic folds tightened and discrete thrust faults nucleated on the limbs as deformation started to localize (Kjøll et al., 2015; In Press; Torgersen and Viola, 2014; see section 7 for further discussion). Fault rocks developed along the discrete tectonic contacts separating the individual slivers and were themselves subsequently folded in an open to close fashion, locally asymmetrically, during progressive shortening and translation of the KNC.

The PIS-related Caledonian overprint within the RTW becomes progressively less penetrative to the SE where the imbricate stack is abruptly terminated by the > 6 km long, sub-vertical Skinnfjellet fault zone (SFZ; Figure 3-1 7 and Figure 4-5). The SFZ is interpreted as a possibly reactivated fault (see section 6.2.2 and section 7.1.4), acting as a back thrust bounding the PIS in the most advanced foreland position. The SFZ juxtaposes greenstones of the Nussir Group against the stratigraphically lower Saltvatn Group. Farther towards the center of the RTW, the Caledonian nappe emplacement had less to no impact on the Raipas sequence and its structural framework (Torgersen and Viola, 2014). Rocks in the immediate footwall of the floor Caledonian décollement, however, underwent greenschist facies metamorphism (Viola et al., 2008) and were refolded around a NE- moderately to gently plunging fold axes.

**Figure 4-5:** Cross section through the PIS. Trace of cross section given in Figure 4-3.



#### 4. Geological and tectonic setting

The regional metamorphism in the RTW was dated by Dallmeyer et al. (1988) by  $^{40}\text{Ar}/^{39}\text{Ar}$  on rejuvenated micas to 430-410 Ma, which corresponds well with the peak Scandian phase at c. 425 Ma of the Caledonian orogeny.

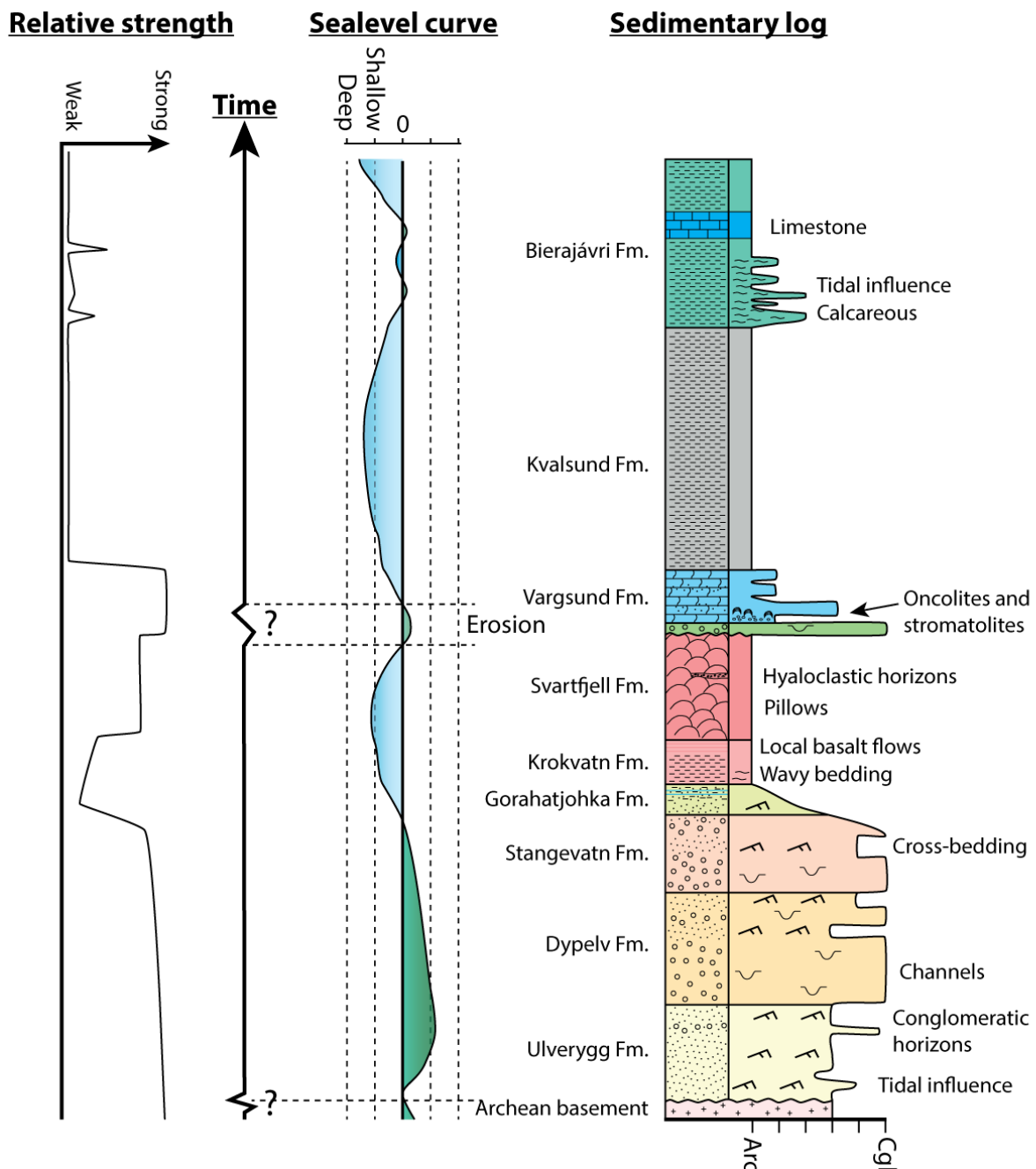
During the Paleozoic and Mesozoic, rifting in the present SW Barents Sea created large NE-SW basins bounded by extensional structures (Faleide et al., 2010; Lippard and Prestvik, 1997). Some of these structures exploited preexisting Caledonian weakness planes as far out as onshore Finnmark (Davids et al., 2013; Roberts and Lippard, 2005) and the RTW (Torgersen et al., 2014). This caused significant normal reactivation of some of the steep reverse faults in the PIS as constrained by K-Ar on authigenic illite from fault gouges (Torgersen and Viola, 2014).





## 5. Mapped lithologies / Result

The text below provides a description of the lithologies mapped during this project and integrates the 1:30000 geological map attached to this MSc thesis (Appendix D and Fig. 4-3). The age of the lithologies ranges between > 2060 and c. 950 Ma. Most of the sedimentary contacts in the mapped area are now sheared contacts due to the post depositional deformation.



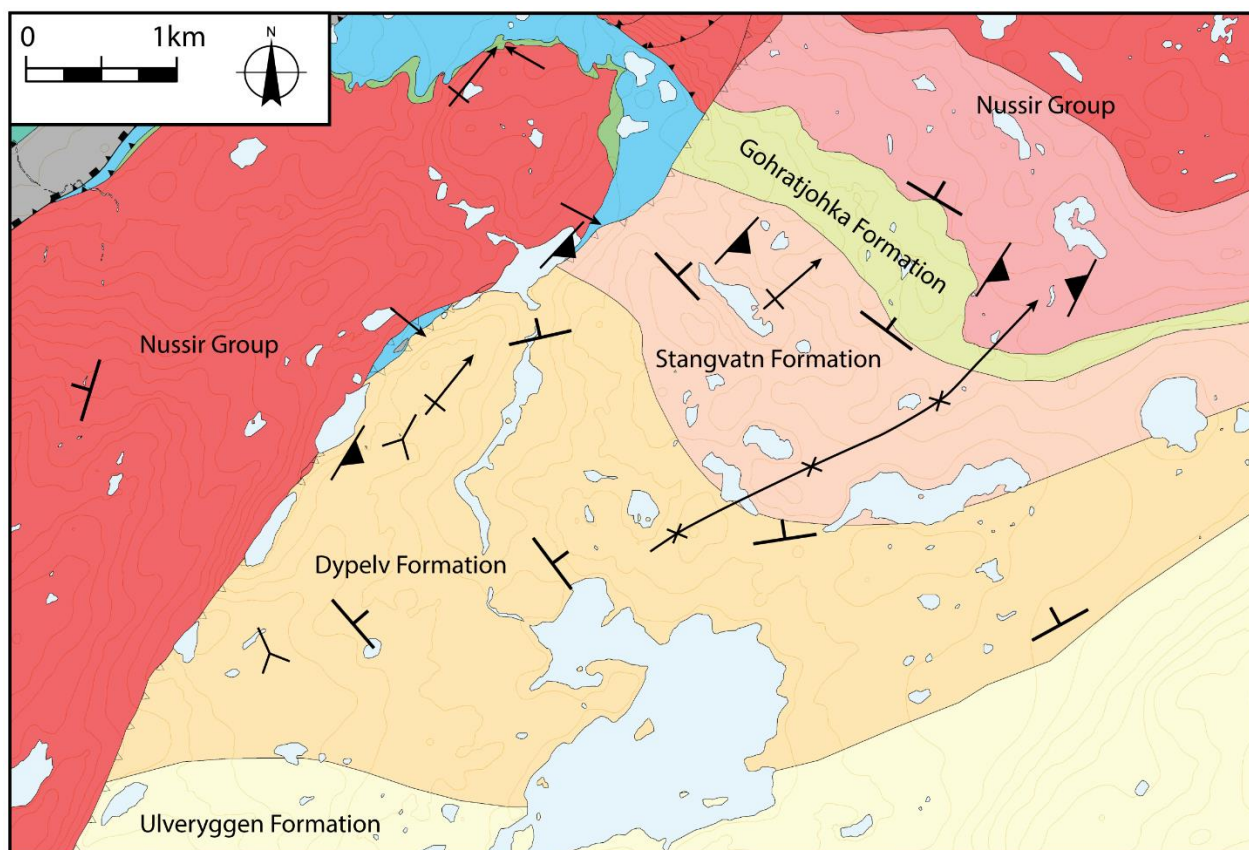
**Figure 5-1:** From right to left: Schematic sedimentary log from RTW. An unconformity with Lomvatn Formation above is found stratigraphically above the Bierajávri Formation. Note that Gorahatjohka, Stangvatn and Dypelv formations are included although they lack a significant lateral continuity. Only Formations are included in the stratigraphic column. Sea-level curve show relative sea level during deposition. Right graph show a qualitative strength profile through the sedimentary column.

The Holmvatn Group has not been mapped in significant detail, but it is an important element in the relatively new view of the stratigraphy of the RTW (see section 4.1.2 and section 5.2), and therefore a short description is provided based on previous work.

## 5.1 Saltvatn Group

The Saltvatn Group consists of four formations: Ulverygg-, Dypelv-, Stangvatn- and Gorahatjohka Formation. They are primarily comprised of clastic metasediments deposited prior to 2060 Ma (Torgersen, 2015). Due to lateral sedimentary facies variations, the thickness of the individual formations varies greatly from west to east. The contact towards the Holmvatn Group to the SE has not been observed by the author.

The Saltvatn Group terminates in the northwest abruptly against SFZ, where its individual formations, except the Ulverygg Formation, display a significant thickening from an average of c. 500 m to c. 4000 m (both measured in map view) at the contact with the SFZ (Fig. 5-2). This possibly results from syntectonic sedimentation within a Paleoproterozoic half graben. (Fig. 5-2 and Fig. 4-4).



**Figure 5-2:** Geological map displaying the thickening of the Saltvatn Group, particularly the Dypelv Formation, and the abrupt termination towards the Skinnfjellet Fault Zone.

These formations (Dypelv-, Stangvatn- and Gorahatjohka) are only exposed on the NE flank of the Ulverygg anticline, thus strengthening the interpretation of syn-tectonically deposited sediments. Pharaoh et al. (1983), on the other hand, argued that the thickening was primarily due to a large fold structure, the Nussir syncline (Fig. 3-1; 6), with thickening in the hinge zone. During fieldwork in the area, however, only locally deformation was observed within the Dypelv Formation and very little in the Stangvatn Formation (see also Torgersen, 2015). The magnetic signature of the Saltvatn Group indicates that the eastern continuation of the group is covered by the KNC on the northern side of the Repparfjord.

### 5.1.1 Ulverygg Formation

The Ulverygg Formation consists of well-bedded, gray, feldspathic-quartzitic cross-bedded metasandstones (Fig. 5-1), with locally interbedded argillaceous levels and conglomeratic horizons of quartz pebbles (c. 1 - 5 cm) set in a quartz-rich sandy matrix. Thin layers rich in magnetite (Fig. 5-3 a) define relatively large-scale cross-beds. Herringbone cross bedding is observed in some of the beds (Fig. 5-3 b). Pharaoh et al. (1983) reported large lensoidal bodies of polymict conglomerate from the center of the formation (Fig. 5-3 e). Locally the formation is mineralized with bornite and chalcopyrite. Current work involves the correlation of the Ulverygg Formation to the Masi quartzite some hundred kilometers to the south on the Finnmarksvidda, and further into the Fennoscandian Shield, where horizons mineralized with > 1 % Cu have been observed (Torgersen, 2015, Pers. comm.). The formation is folded and an axial planar cleavage has developed in some argillaceous horizons (Fig. 5-3 c and d).

### 5.1.2 Dypelv Formation

The Dypelv Formation consists of a chaotic polymict conglomerate (Fig. 5-1). Greenstone clasts are most common, but several types of volcanic clasts have been found (Fig. 5-4). Amygdaloidal quartz clasts are common (Fig. 5-4 d and e) and locally carbonate clasts are observed. The clasts are set in a fine-grained, green and sandy matrix and the conglomerates vary from being clast- to matrix supported. The clasts are usually < 15 cm in diameter. Sand channels are common and vary in thickness from < 1 m to several meters and display erosional bases (Fig. 5-4 c). To the west, where the formation terminates abruptly against the SFZ and where the thickening is most important (Fig. 5-2), clasts can be up to 30 cm in diameter and sand channels become more common in association with argillaceous horizons (Fig. 5-4 b).

### 5.1.3 Stangvatn Formation

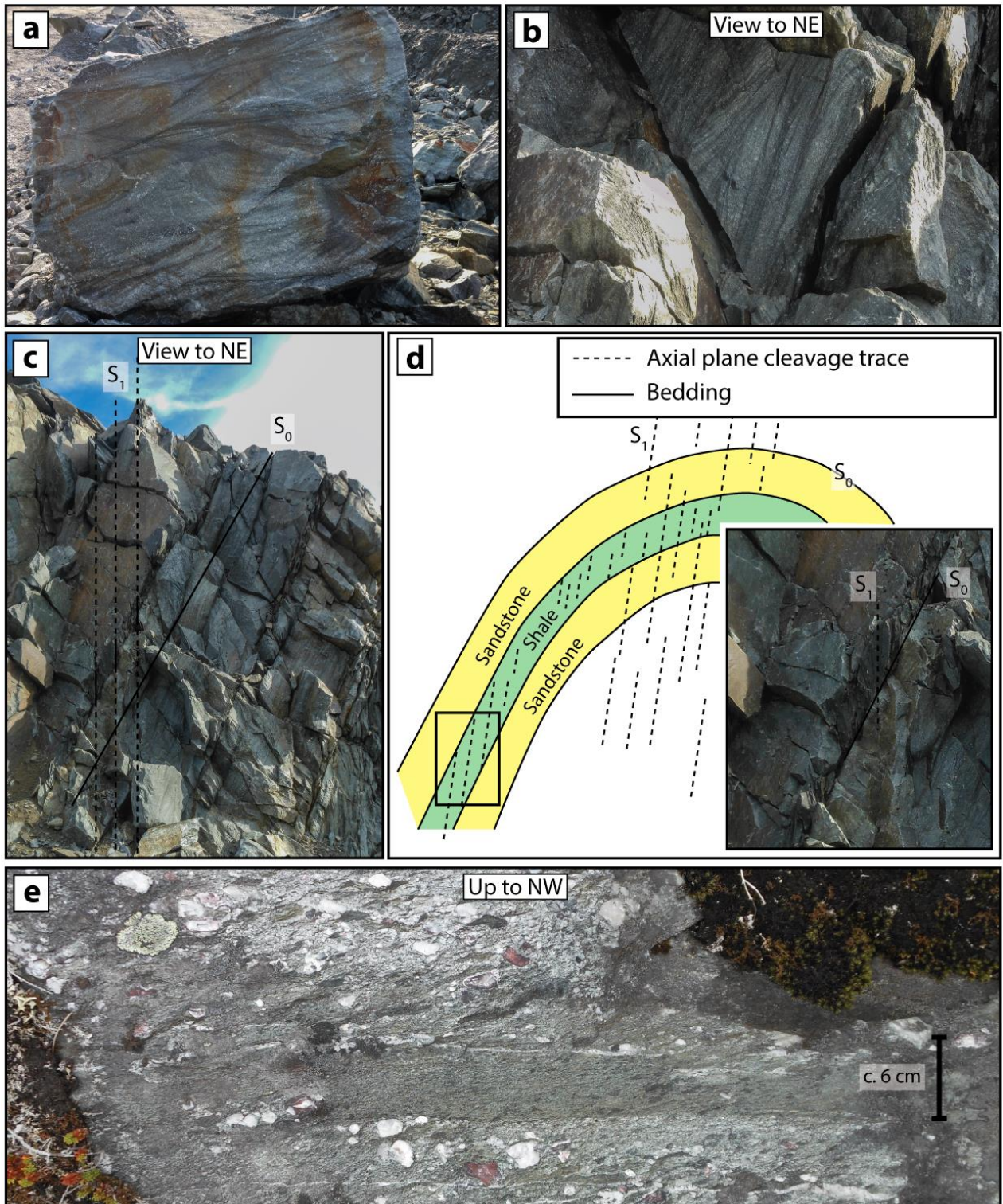
The transition from the Dypelv Formation to the overlaying monomict, matrix supported Stangvatn Formation is generally abrupt, although close to the SFZ, the transition is more gradual and defined by a change in clast type from primarily greenstones in the Dypelv Formation to purple, micro-porphry clasts of dacitic composition in the Stangvatn Formation. It contains multiple sand channels and three major normal graded sequences going from conglomerate to fine-grained sand and silt (Pharaoh et al., 1983; Fig. 5-1 and Fig. 5-5 a). The clasts are generally equidimensional (c. 3 to 10 cm in diameter, measured along the long axis) and show a tendency towards being oblate (Fig. 5-5 b). The matrix is generally sandy with some argillaceous material (Fig. 5-5 d). Locally, the conglomerate has a dolomitic matrix, seen as a distinctive brown weathering color (Fig. 5-5 c). C isotopes from these dolomitic horizons suggest that they were deposited around the termination of the Lomagundi-Jatuli event at c. 2060 Ma (Torgersen, 2015). The sequence vary from clast-supported conglomerate that progressively becomes more sandy as one moves up the stratigraphy.

### 5.1.4 Gorahatjohka Formation

The Gorahatjohka Formation is the top formation of the Saltvatn Group and conformably overlies the Stangvatn Formation (Fig. 5-1). It consists of silty slates, immature, fine-grained metasediments and three dolomitic horizons, two associated with the Nussir Cu deposit and one un-mineralized sedimentary breccia. The silty slates are generally pale and consists of very fine-grained feldspar and quartz grains (Fig. 5-6 a and b). The matrix is relatively rich in very fine-grained phyllosilicates (Fig. 5-6 d). Mechanically, the Gorahatjohka Formation is a relatively weak lithology and locally has a pervasive secondary fracture cleavage (Fig. 5-6 c). Close to the SFZ, the silty layers of the Gorahatjohka show a plethora of shear bands throughout (Fig. 5-6 b).

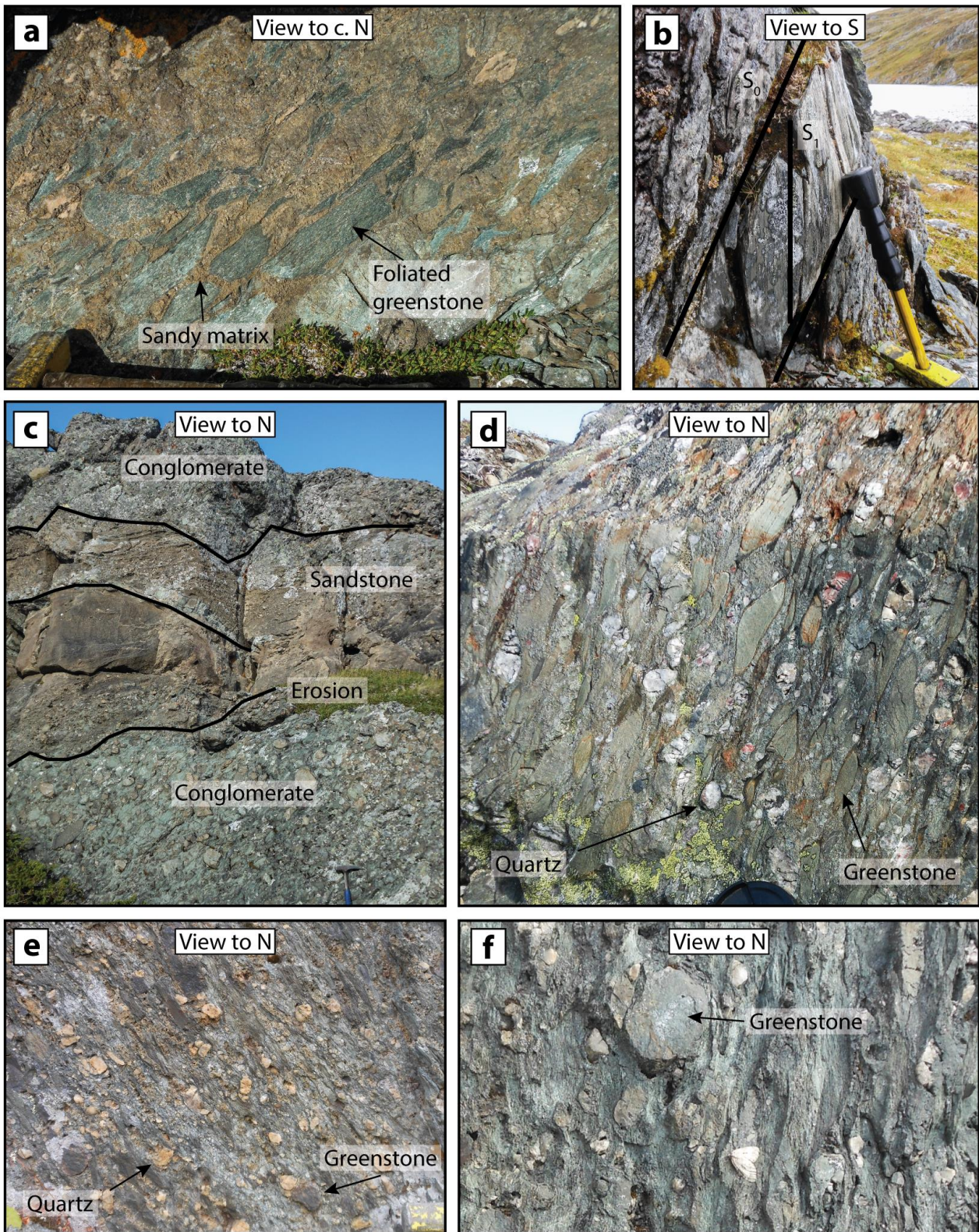
In thin section, the silty slates show a pervasive foliation defined by partially recrystallized quartz clasts completely embedded in very fine-grained phyllosilicates, possibly chlorite and sericite (Fig. 5-6 d). Symmetric quartz clasts (generally < 100  $\mu\text{m}$ ) are locally recrystallized to a very fine grain size. The phyllosilicates form interconnected bands and appears to have accommodated strain as shown by numerous asymmetric shear bands. Euhedral and subhedral biotite grains are interspersed within the foliation, indicating a period of static biotite growth. They all have fringed edges. Some static overgrowth of sphene is also observed. The pervasive secondary fracture cleavage is filled with fibrous calcite with a centerline defined by equidimensional grains (Fig. 5-6 c).





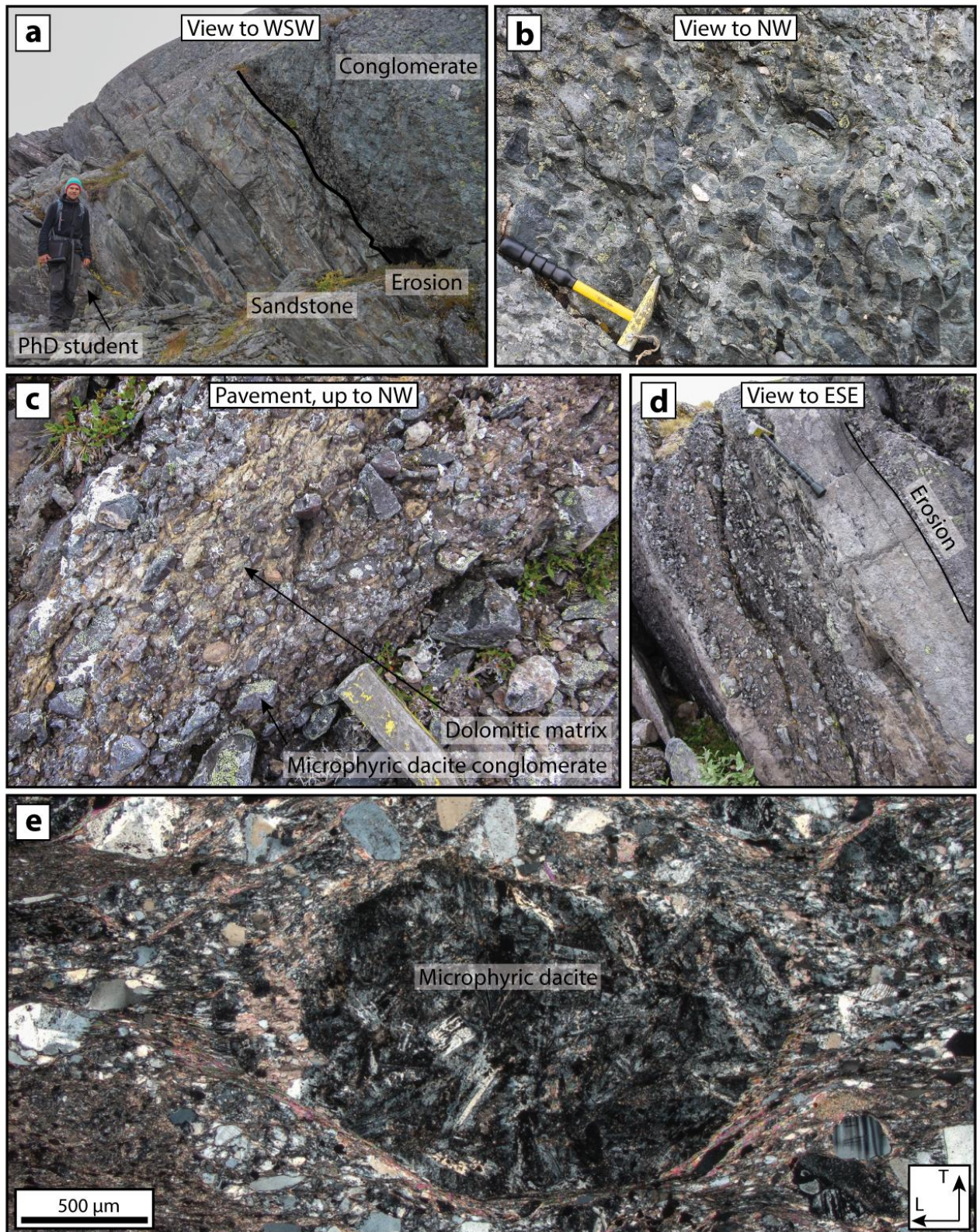
**Figure 5-3:** Typical field characteristics of the Ulverygg Formation. (a) large scale cross-bedding in an arkosic sandstone defined by magnetite-rich levels. (b) Herringbone cross-bedding from the same locality as (a). (c) and (d)  $S_0/S_1$  relationship indicate large scale folding and that the locality is on the NW limb of a large anticline. (e) Quartzitic conglomerate close to the Dypelv Formation contact.





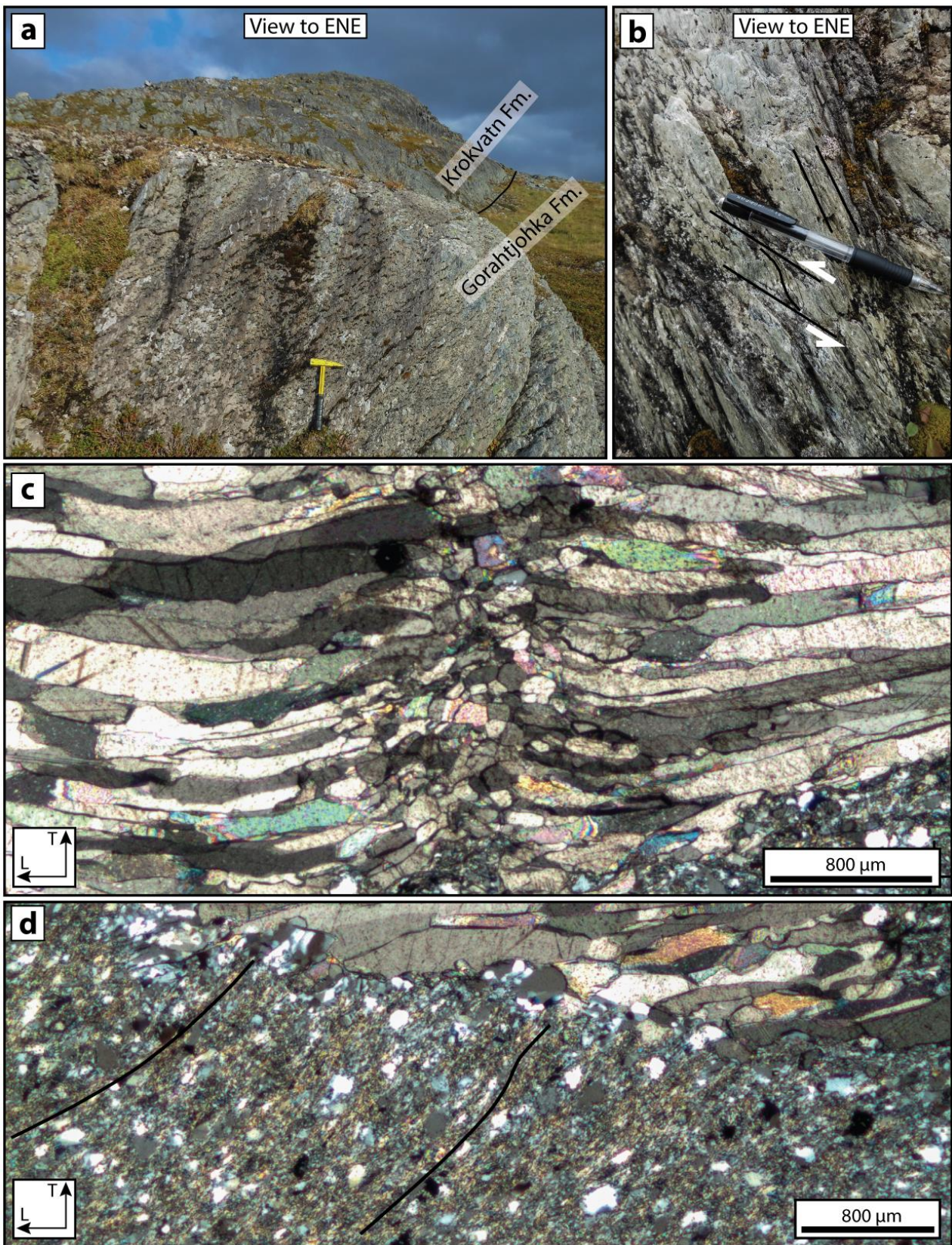
**Figure 5-4:** Typical field characteristics of the Dypelv Formation. (a) Typical sheared conglomerate found throughout the formation. Clasts are generally of volcanic origin and embedded in a sandy, greenish matrix. (b)  $S_0/S_1$  relationship close to SFZ. (c) River channels with erosional bases are found throughout. Large cross-bedding. (d) Greenstone, quartz conglomerate. (e) Sheared quartz conglomerate. Matrix possibly contain smeared out clasts. (f) deformed greenstone, quartz conglomerate (moth for scale).





**Figure 5-5:** Typical field- and microscopic characteristics of the Stangvatn Formation. (a) Large normal-graded sequence with erosional base. (b) Oblate conglomerate clasts set in a sandy matrix. (c) Some horizons have clasts cemented in a dolomitic matrix. (d) Sandy channels with erosive base. (e) Thin section photomicrograph of a sheared conglomerate. The dacite clast appears to be severely altered, but some remnant feldspar laths are present. Photomicrograph taken with crossed polarizers. X-pl.





**Figure 5-6:** Overview of characteristic features of the Gorahatjohka Formation. (a) Outcrop displaying a well defined fracture cleavage. The contact towards the stratigraphically higher Krokvatn Formation is seen in the background. (b) A symmetric C' shear bands close to the SFZ. (c) Fibrous calcite filling in a fracture cleavage. X-pl. (d) Fracture cleavage cut the phyllitic foliation of the sample. In addition, it appears to bend the foliation in a sinistral fashion. X-pl.



## 5.2 Holmvatn Group (SE limb of Ulverygg anticline)

The Holmvatn Group is a > 3 km thick package consisting of metasedimentary and metavolcanic rocks divided into three formations: The Markfjell, Båtdalselv and Magerfjell formations (Pharaoh et al., 1983). These formations consist primarily of matrix-supported, polymict conglomerates, quartzo-feldspathic schists and sub-aerial, extrusive metabasalts with tholeiitic composition and interbedded with mafic tuffs and tuffites (Pharaoh et al., 1983). Locally the Holmvatn Group is intruded by ultramafic, mafic rocks (Pharaoh et al., Op. cit.). As described above, Torgersen (2015) and Smeplass (2013) propose a correlation of the Holmvatn Group with the Nussir Group.

## 5.3 Nussir Group (NE limb of Ulverygg anticline)

The Nussir Group primarily consists of metavolcanic tuffs, tuffites and metabasalts and can be divided in two formations: the Krokvatn- and the Svartfjell Formation. (Fig. 5-1). The most complete section of the Nussir Group is found around the Nussir Mountain (Fig. 3-1; 4, 6), where both formations are well exposed. Indications for subaqueous deposition and extrusion are observed throughout (Fig. 5-7). The contact between the Saltvatn Group and the Nussir Group is somewhat ambiguous. At one locality the contact is sheared with local imbrication and drag folding (Fig. 5-8) However, along strike the contact and the surrounding lithologies appear pristine with no significant deformation. Furthermore, the contact is folded around a moderately, NE-plunging fold axis with a pervasive axial planar cleavage defining the Nussir syncline (Fig. 3-1; 6).

### 5.3.1 Krokvatn Formation

The lowermost formation in the Nussir Group, the Krokvatn Formation, consists primarily of tuffaceous greenstones and meta-agglomerates interbedded with beds of extrusive metabasalt (Pharaoh et al., 1983; Fig. 5-1). Some of the metatuffs are well bedded and possess a normal grading with sand or silt as the coarsest fraction deposited on an erosional surface (Fig. 5-7 a and f). Cross-bedding are observed in the coarser fractions (Fig. 5-7 a). This, together with the upward fining sections and the erosional bases, indicate that these formed as turbiditic flows. The tuffaceous layers are generally strongly foliated and commonly contain amygdaloidal quartz and locally jasper, which forms clasts within the locally strong foliation (Fig. 5-7 b). The tuffs are commonly rich in magnetite, which results in a clear geophysical signature, as shown by the magnetic anomaly maps (see map in Appendix D and Fig. 6-1 – black arrows on the right side of the map). Locally, large beds of extrusive basalt flows lay concordant over the tuffaceous layers.

### 5.3.2 Svartfjell Formation

The uppermost Formation in the Nussir Group is the Svartfjell Formation, which consists primarily of extrusive metabasalt with local tuffaceous horizons (Fig. 5-1). The lower part of the formation contains massive, well-bedded basaltic flows. Higher up in the stratigraphy primary, sub-aqueous pillow-basalt structures are observed (Fig. 5-7 d), commonly with well-preserved chilled margins and interstitial, amygdaloidal quartz (Fig. 5-7 d). Locally, hyaloclastite breccias are observed (Fig. 5-7 c and e). These breccias are indicative of a shallow sub-marine formation by nonexplosive shattering (Batiza and White, 2000). The breccias are common in the stratigraphically higher parts of the Skinnfjellet anticline, where they form a thick layer. These breccias have also been described by Pharaoh et al. (1983).

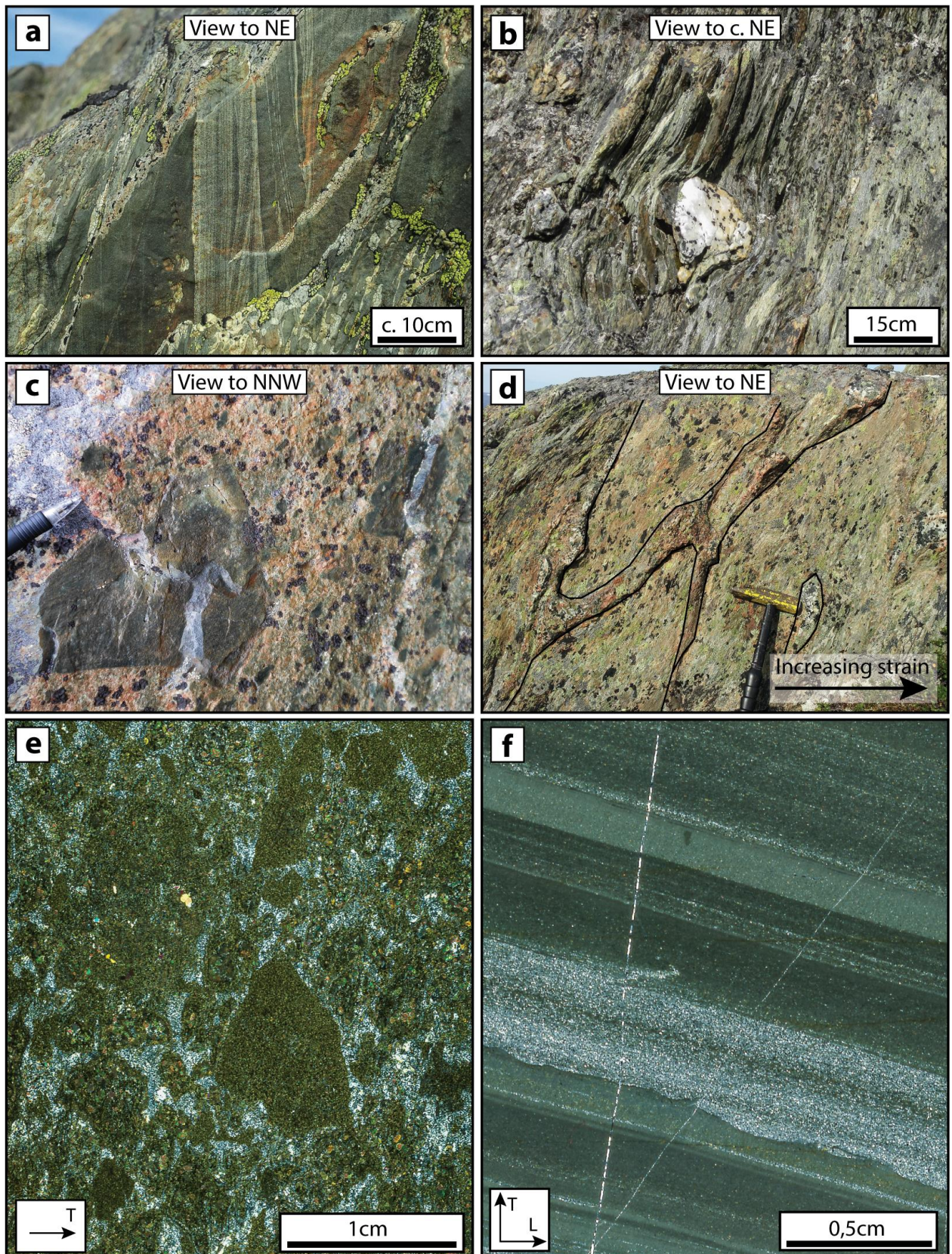
Due to the tectonic repetition of lithologies within the PIS, the Nussir Group can be found throughout the imbricate stack. Greenschist metamorphism has resulted in a severe alteration of the basalts and primary structures may be observed locally and generally in the low strain domains of the PIS.

### 5.3.3 Mafic intrusive

In the westernmost parts of the PIS, a metagabbroic suite intrudes the metabasalts (Fig. 4-3). This suite is formed by coarse- to medium-grained, mesocratic gabbro composed of large feldspar laths (c. 1 - 2 mm) and finer-grained, equidimensional interstitial pyroxene and amphiboles crystals, measuring c. 500  $\mu\text{m}$  (Fig. 5-9 e). The rock is locally very rich in sulfides and secondary epidote (Fig. 5-9 c and d). Fractures are commonly filled with coarse-grained, close to pegmatitic, feldspar and amphiboles (Fig. 5-9 b). A c. 1-5 m thick layer of gray phyllonite generally confines the eastern termination of the gabbro.

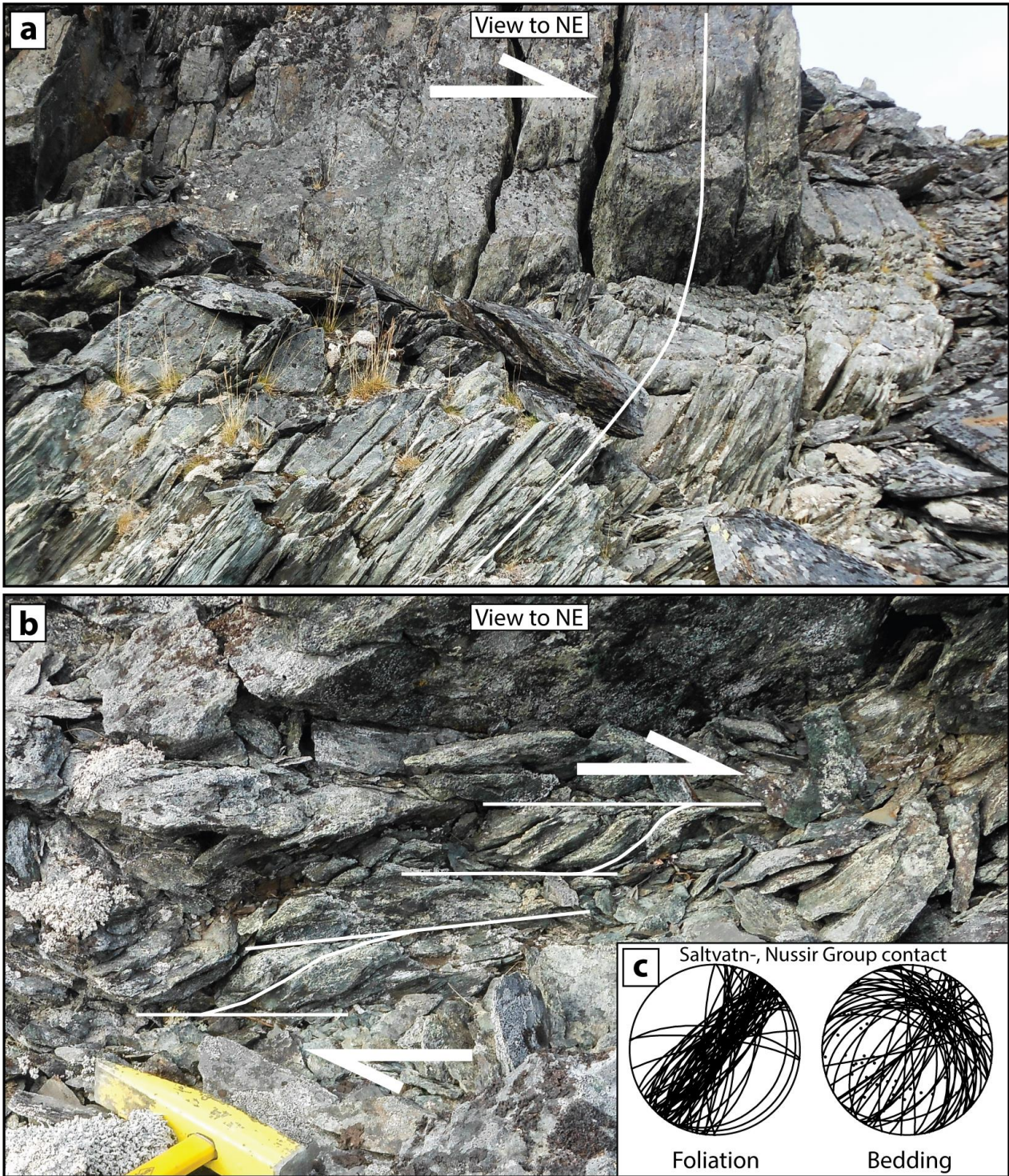
Scattered coarse- to medium-grained gabbroic dikes with large thickness variations (c. 30 cm to > 10 m) intrude greenstones and older, larger gabbroic bodies, indicating a complicated emplacement history (Fig. 5-9 f). The dikes dip towards the N and are generally E-W striking. Some of the dikes are associated with pervasive slickenlines rich in talc and sub-horizontal tension gashes filled with calcite. They are generally strongly retrogressed and contain coarse-grained epidote (Fig. 5-9 f). U-Pb zircon ages from a similar gabbroic dikes in the interior of the RTW yielded  $1908 \pm 13$  Ma and is interpreted as a syn-orogenic intrusion (Torgersen, 2015). It is unknown, however, if the dated intrusions from the interior and those from the PIS are contemporaneous.





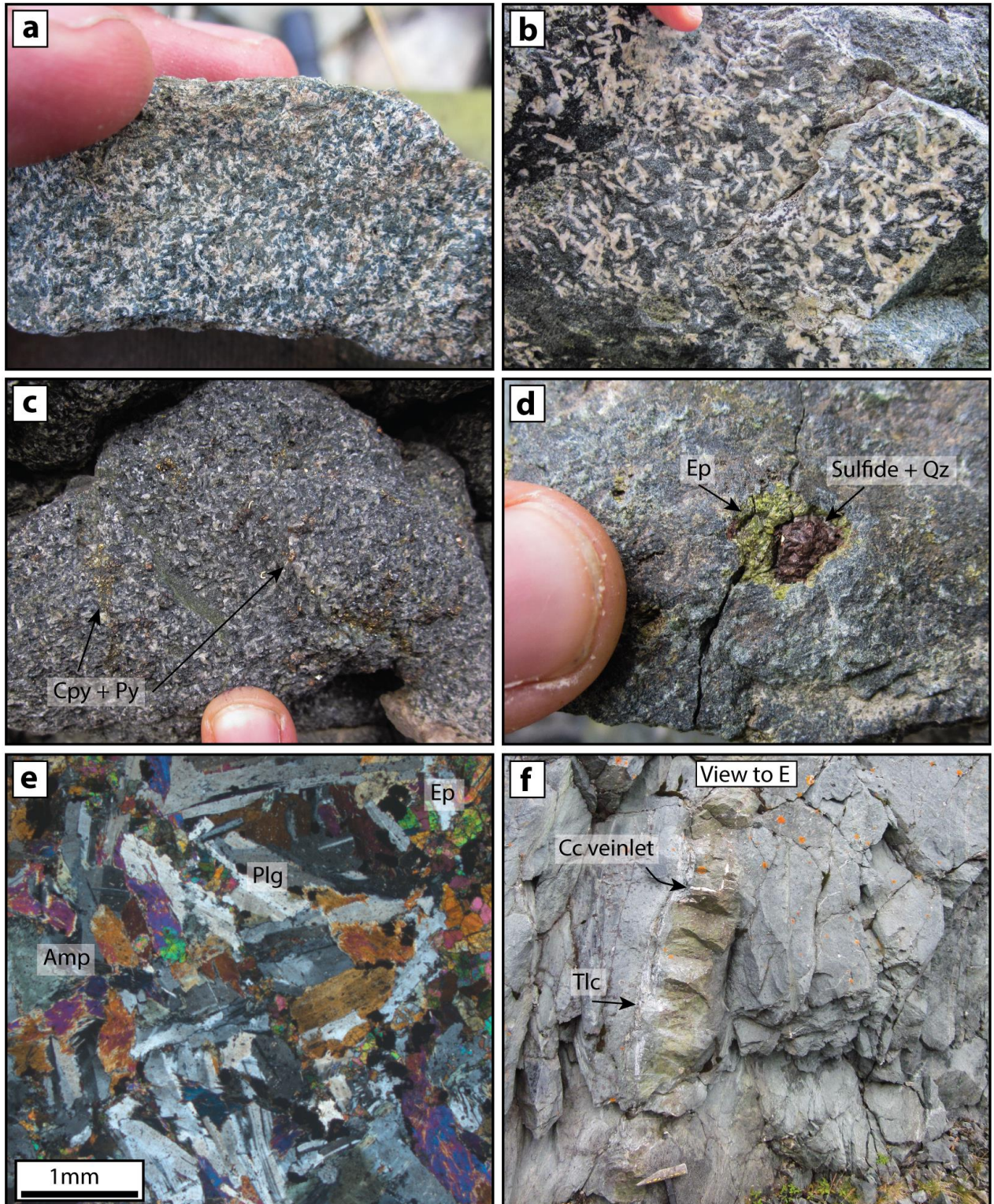
**Figure 5-7:** Typical field and microscopic characteristics of the Krokvatn- and Svartfjell formations. (a) Normally graded sequence with cross bedding defined in the coarsest fraction, which was deposited on an erosional surface. (b) Coarse-grained amygdaloidal quartz draped by a strongly foliated metatuff. (c) Outcrop photo of a relatively coarse hyaloclastic breccia clast. (d) Primary pillow structures. Locally, amygdaloidal quartz (chert) is found between the pillows. (e) Stitched photomicrograph of a hyaloclastic breccia. X-pl. (f) Stitched photomicrograph of a normally graded sequence deposited on an erosional surface, interpreted to be deposited sub-aqueously, possibly by a turbidite flow. X-pl.





**Figure 5-8:** Folding of the foliation in the Krokvatn Formation directly overlying the Gorahatjohka Formation interpreted as drag folds. (b) Imbricated clasts below the dragged foliation. (c) Stereonets displaying foliation and bedding measurements along the contact. They indicate a strong axial planar cleavage. Right stereonet show the folded nature of the contact. Fold axis plunging moderately towards the NE-NNE.





**Figure 5-9:** Overview of typical features of the mafic intrusives. (a) Mesocratic gabbro with well-defined plagioclase laths. (b) Coarse-grained gabbroic dike/vein. Note finger for scale. (c) Sulfide-rich gabbro. (d) Cavity coated by coarse epidote with sulfide grain in the center. (e) Photomicrograph of gabbro displaying coarse-grained plagioclase and amphibole. X-pl. (f) Epidote-rich gabbroic dike intruding the mafic intrusive. Dike has fibrous talc as slickenfibers on the side and is cut by sub-horizontal calcite veinlets that are confined to the dike.

## **5.4 Porsa Group**

The Porsa Group consists of three formations, the Vargsund-, Kvalsund- and Bierajávri Formation. Included in the Vargsund Formation is a polymict basal conglomerate called the Nussirjávri member. There is an unconformity between the conglomerate and the underlying Nussir Group, representing an erosional surface and change in sea level as the Porsa Group is interpreted to have been deposited in a marine environment (Fig. 5-1). In general, the sedimentary succession in the Porsa Group indicates a transitional deepening of the basin from the Vargsund Formation to the Kvalsund Formation and a subsequent shallowing as the Bierajávri Formation was deposited (Fig. 5-1; sea level curve). The age of the Porsa Group sediments is constrained by C-isotope dating in the Skinnfjellet anticline area (Fig. 3-1; 5 and 9) and by U-Pb on zircons from a crosscutting gabbro south of the study area. The dating constrains the time of deposition to be post 2060 Ma (Torgersen, 2015).

### **5.4.1 Vargsund Formation**

The Vargsund Formation is deposited unconformable on top of the Nussir Group (Fig. 5-1) with a clast-supported polymict conglomerate at the base, the Nussirjávri member (see below; Fig. 5-10 a). The main part of the Vargsund Formation consists primarily of dolostone or dolomitic marble with some metasandstone layers. Generally, the dolostone is well bedded with individual beds ranging in thickness from 5 cm to more than 40 cm. They often also contain gritty horizons with distinct color differences (Fig. 5-10 d and e). Locally, the lower levels of the formation contain oncolites, while stromatolitic domes are found regionally (Fig. 5-10 b and c). The dolostone is generally characterized by gray layers of chert with thicknesses varying between 1 and 10 cm. These layers are interpreted to be blue-green algae mats (Fig 5-10 d). The entire formation at the Tappen anticline was calculated to be 250 m thick by Pharaoh et al. (1983). Within the folded layers of dolostone there are abundant sub-vertical quartz veins orthogonal to the bedding (Fig. 5-10 d).

The Vargsund Formation is generally folded and locally developed into calc-mylonites. This is elaborated further in section 7.1.3.

#### **5.4.1.1 Nussirjávri member**

The conglomerate is found throughout the study area, although it is best exposed around the Skinnfjellet anticline and the Kvalsund folds (Fig. 3-1; 3 and 5). Clasts are composed of greenstone, coarse-grained quartz, possibly amygdaloids and locally jasper. Lithic sandstone clasts have also been observed. The clast diameter averages at around 5-10 cm, but varies significantly. The matrix comprises immature, fine-grained quartz sand with varying proportions of clay.



#### 5.4.1.2 Fiskelv member

In the central PIS area (Fig. 3-1; 2), along the Beretsjord Fault Zone (BFZ; section 6.2.5) a layer of the Vargsund Formation outcrops more or less continuously for several kilometers. Here, a several meters (locally tens of meters) thick sequence of quartzitic metasandstones is found at several localities, blocks of dolostone are found within these metasandstones layers (Fig. 5-10 f).

#### 5.4.2 Kvalsund Formation

The Kvalsund Formation consists of strongly foliated graphitic slate to phyllite, which is generally pervasively crenulated (Fig. 5-1). The protolith of this rock was probably a shale sequence rich in organic carbon (Hanski and Melezhik, 2013). Locally, the Kvalsund Formation is mineralized and contains abundant cubic pyrite crystals (Fig. 5-11 b). Pharaoh et al. (1983) proposed that the formation was deposited at medium depth in a marine environment. Furthermore, they pointed out that the basin must have had reduced circulation leading to anoxic conditions. The original thickness of the formation is difficult to infer due to the lithologies low mechanical strength causing folding and dissolution. Reitan (1963) proposed a minimum thickness of 500 m, while Pharaoh et al. (1983) suggested it to be c. 400 m. Melezhik et al. (2012) concluded that a large scale oxygenation of the earth atmosphere, called the Lomagundi-Jatuli event, contributed to the formation of these organic carbon-rich lithologies that are found throughout the Fennoscandian Shield.

Because of the high graphite content, which has low resistivity, the Kvalsund Formation is easily identified on electromagnetic maps. This has proven to be a valuable tool when mapping the lithology, as the lithological contacts can be traced very easily (Fig. 6-1 and Appendix D).

Solution-precipitation has been an active process within the Kvalsund Formation as seen by the strong crenulation cleavage and locally developed into a solution cleavage (Fig. 5-11 b and d), which most likely contributed to significant shortening during deformation. The crenulation cleavage has produced clear crenulation lineations, which generally has a sub-horizontal to shallow NE plunge direction.

In thin section, Kvalsund Formation samples show a clear compositional foliation or slaty cleavage. In addition, locally a solution cleavage has developed at a high angle to the compositional foliation (Fig. 5-11 d, f). Small porphyroblasts in the range from 50 to 200  $\mu\text{m}$  are also visible in this sample and they invariably show slightly rotated fringes composed of fibrous quartz (Fig. 5-11 d, f). Locally a static overgrowth of sulfides may be observed (Fig. 5-11 e).

### 5.4.3 Bierajávri Formation

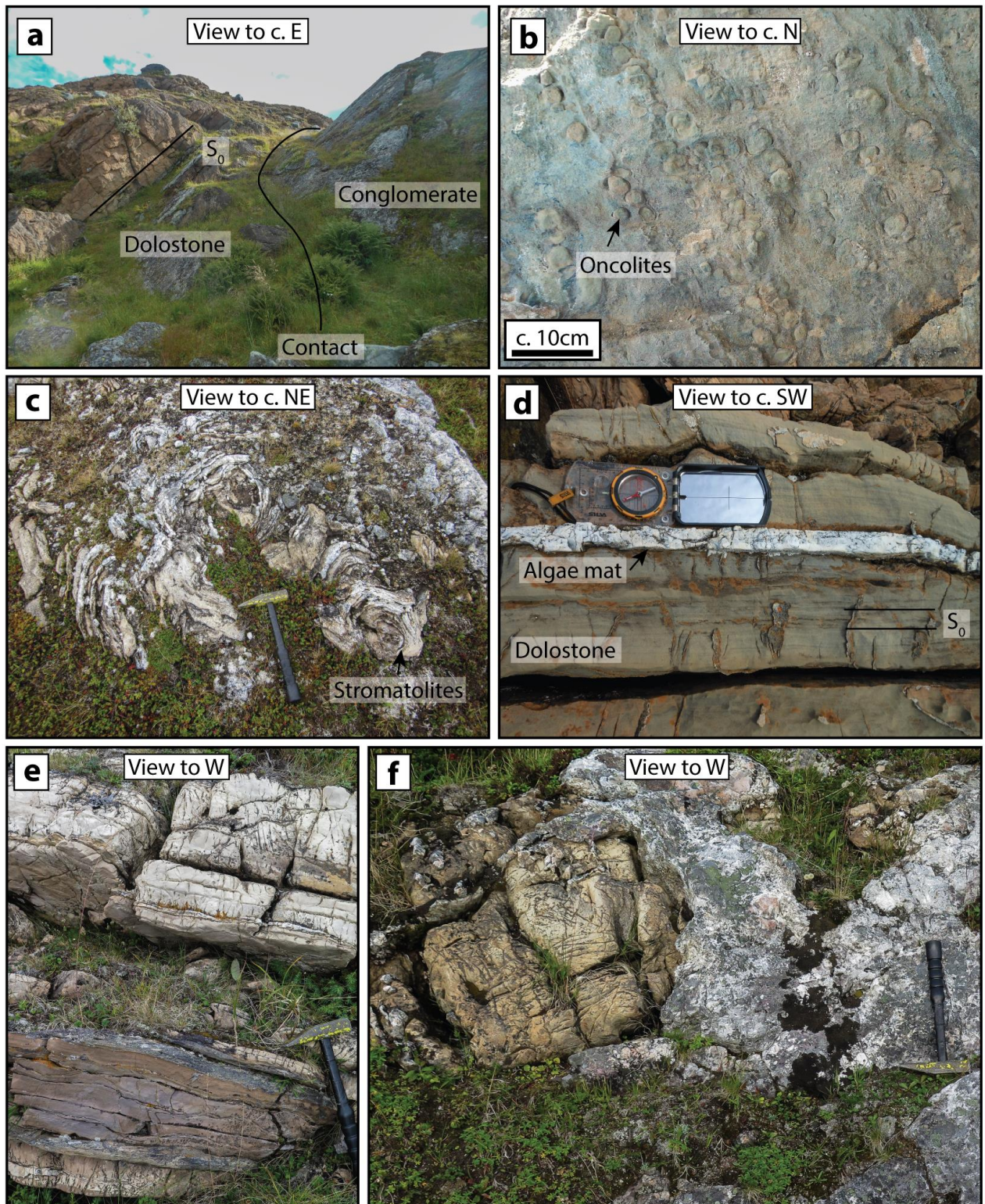
The transition between the Kvalsund and the Bierajávri formations is uncertain as it is not well exposed. Nonetheless, it is assumed that the latter conformably overlies the Kvalsund Formation, as also suggested by Pharaoh et al. (1983). The Bierajávri Formation is lithologically very heterogeneous, but contains mainly fine-grained, carbonaceous silt- and claystones, silty sandstones and volcanogenic tuffs (Fig. 5-1 and Fig. 5-12). The latter of which define the Rundvatn member in Kvalsunddalen (see below). Locally a rock interpreted to be volcanogenic bombs deposited in ash is observed (Fig. 5-12 e). The Bierajávri Formation was deposited in a more shallow environment than the Kvalsund Formation, as suggested by diagnostic sedimentary structures such as wavy and lenticular bedding. These constrain a component of tidal influence, as also proposed by Pharaoh et al. (1983; Fig. 5-1). Both the source of the sediments and the environmental conditions in the basin must have changed dramatically from the deposition of the Kvalsund graphitic shales to the deposition of the Bierajávri Formation as the latter contains calcareous sediments, fine sand to chert and volcanoclastic sediments. Pharaoh et al. (op. cit.) also observed a plethora of well-preserved sedimentary structures, such as slumps and ripple lamination. In addition, the Bierajávri Formation displays features suggesting that it was subjected to significant dissolution, possibly genetically linked to the development of a pervasive axial planar cleavage (Fig. 5-12 d).

Within the PIS, the Bierajávri Formation is rarely observed except for possibly in the footwall of the AUSA Fault Zone (AFZ; section 6.2.6), where significant strain localized in a lithology with a similar composition as the Bierajávri Formation. These rocks have recrystallized and are now a fine-grained, hard slate, with some remnant porphyroclasts (see section 6.2.6 and Fig. 6-17 c and Fig. 6-18 a).

#### 5.4.3.1 Rundvatn Member

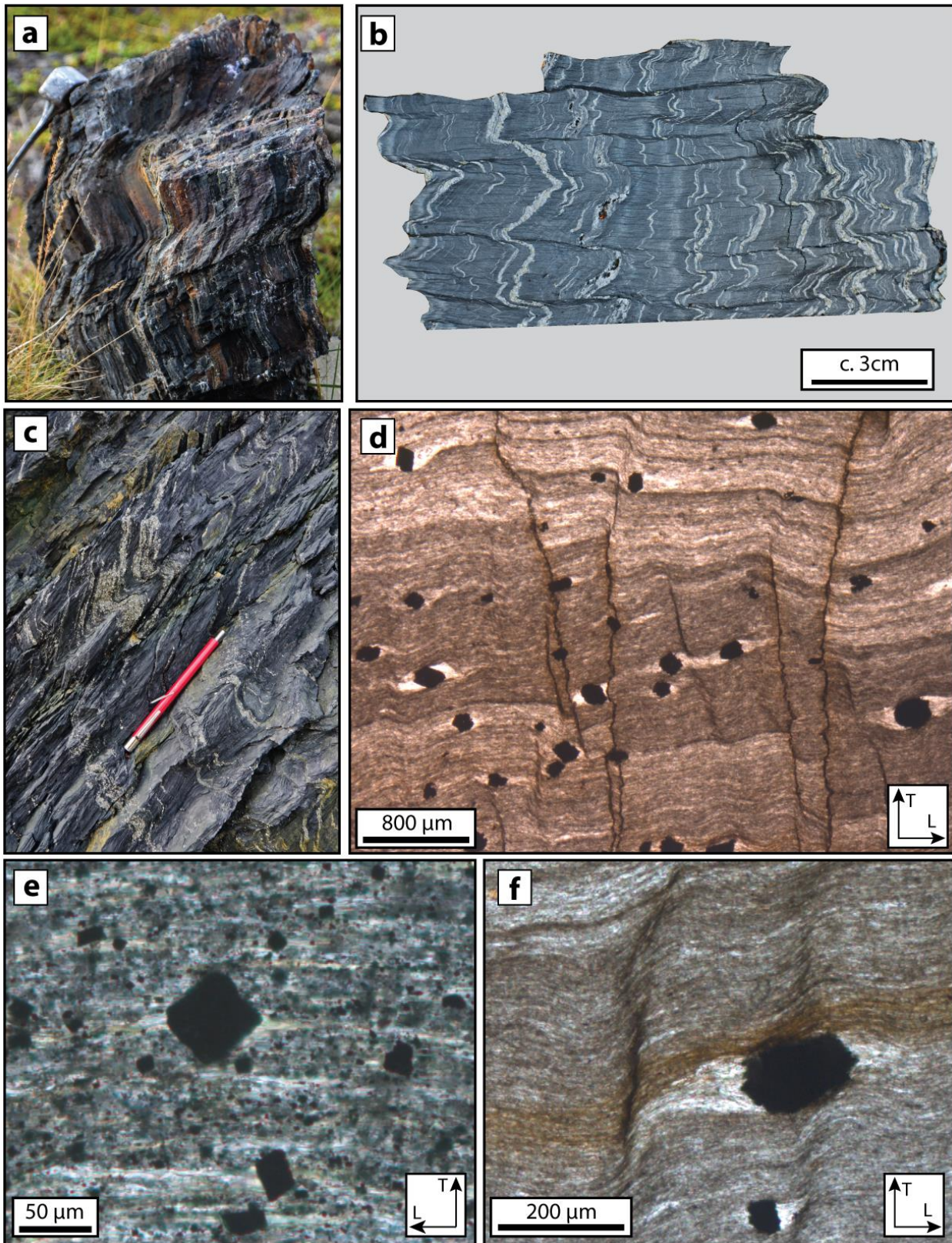
Conformably above the Bierajávri Formation there is a transitional zone, where several zones of volcanogenic green tuffites become more common. These tuffites are magnetic, very fine-grained and laminated, and are interpreted to be re-sedimented tuffs i.e. tuffites. They are observed and mapped at several localities within Kvalsunddalen (Fig. 3-1; 10). Due to their magnetic nature they are easily distinguished in tilt derivative magnetic map from the more silty-carbonaceous metasediments in the true Bierajávri Formation (Fig. 6-1 - black arrows in the center of the map). The member has previously been characterized as lenses within the Bierajávri Formation, but thanks to the availability of the new potential field airborne geophysical maps it is proposed in this thesis that the lithology is upgraded to “member” status, as it may indeed be mapped and is laterally continuous for > 5 km within the Kvalsunddalen.





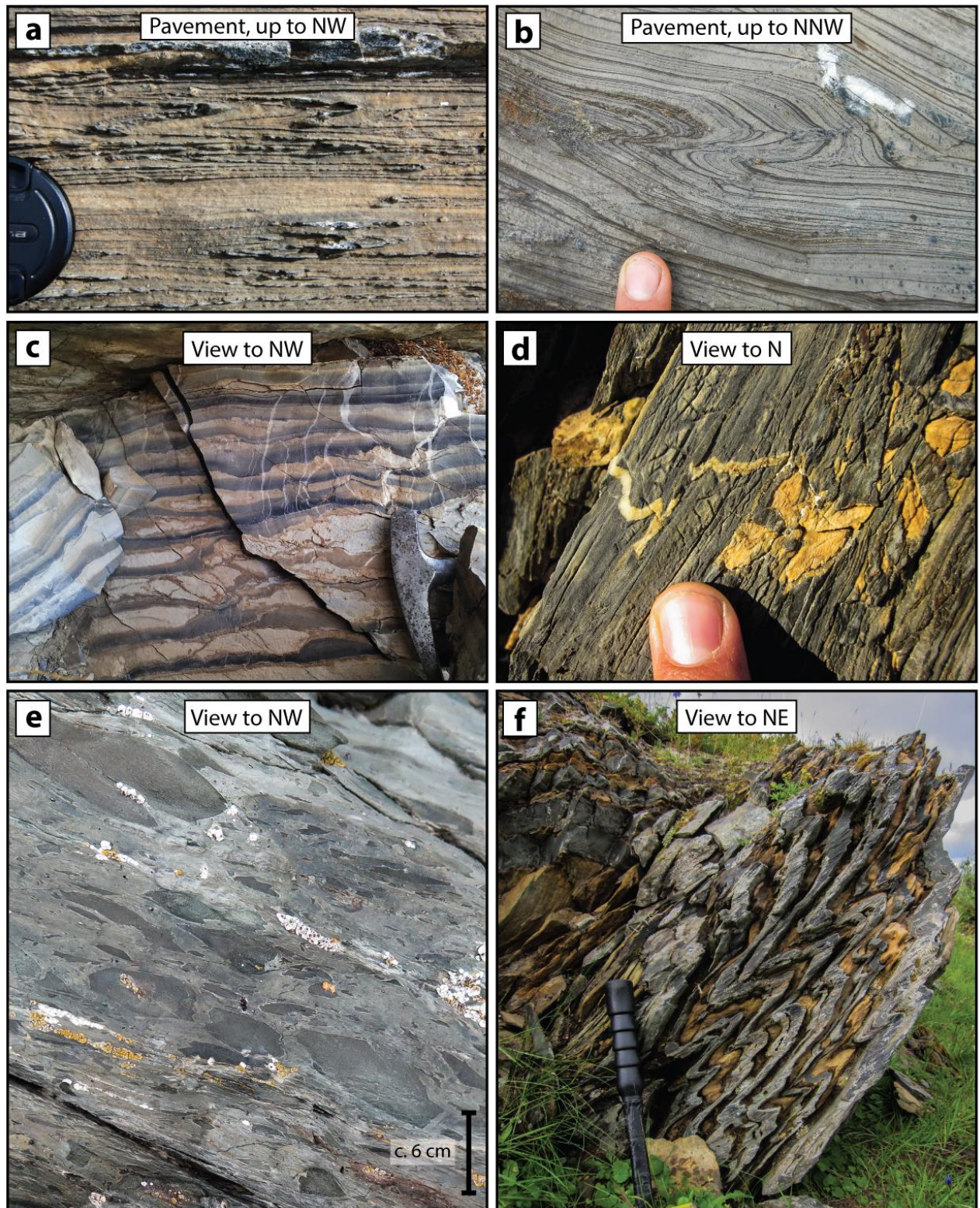
**Figure 5-10:** Typical field characteristics of the Vargsund Formation. (a) The contact between the lowermost part of the Vargsund dolostones and the quartz-greenstone-jasper basal conglomerate. (b) Rounded oncolites embedded in stratified dolostone. (c) Stromatolitic dolostone with cabbage head structure from the Kvalsund folds. (d) Stratified dolostone with cherty horizon representing an algae mat. Note vertical quartz veins. (e) Gritty dolostone beds show different colors. (f) Clasts of dolostone embedded in quartzite. Indicating karst?





**Figure 5-11:** Main field and microscopic characteristics of the Kvalsund Formation. (a) Strongly foliated graphitic slate with rusty horizons and activated crenulation surfaces. (b) Cut rock slab displaying an incredible solution cleavage at a high angle to the compositional foliation, which also contain sulfides. Sample comes from the locality in (c). Photo courtesy E. Torgersen. (c) Strongly crenulated, pyrite-rich graphitic slate. Photo courtesy E. Torgersen. (d) Strongly crenulated slate with a pervasive solution cleavage, locally resembling styloites. P-pl. (e) Static pyrite overgrowth. P-pl. (f) Strain fringes bend into solution cleavage, indicating that they predate the solution cleavage. P-pl.





**Figure 5-12:** Typical field characteristics of the Bierajávri Formation. (a) Isoclinally folded calcareous metasediments. (b) Asymmetrically folded calcareous metasediments. (c) Primary sedimentary structures show upwards fining sequences starting with very fine sand at an erosional base. (d) Solution cleavage in calcareous metasediments. (e) Volcanic bombs deposited in ash. Later tectonically reworked. (f) Asymmetrical folds in a heterogeneous sequence of dolomitic/calcitic marble and chert.



## 6. Structural analysis of the mapped area

The RTW has been affected by four major deformational events. According to the traditional structural notation system, these episodes are here referred to as D, with sub-indices 1 to 4 to show their temporal sequence from the oldest to the youngest, respectively. D<sub>1</sub> is thus the oldest event recognized and corresponds to the Svecofennian orogenic episode. Hornblende <sup>40</sup>K-<sup>40</sup>Ar cooling ages at about 1840 Ma in the south-central parts of the RTW (Pharaoh et al., 1982) are the only direct geochronological constraint available. In addition, evidence for a period of dextral transpression is also found throughout the PIS. Torgersen (2015) dated an early increment of this event by Re-Os sulfide geochronology at  $2069 \pm 14$  Ma.

D<sub>2</sub> represents the Caledonian orogeny at c. 550 – 430 Ma (Dallmeyer et al., 1988; Torgersen et al., 2014).

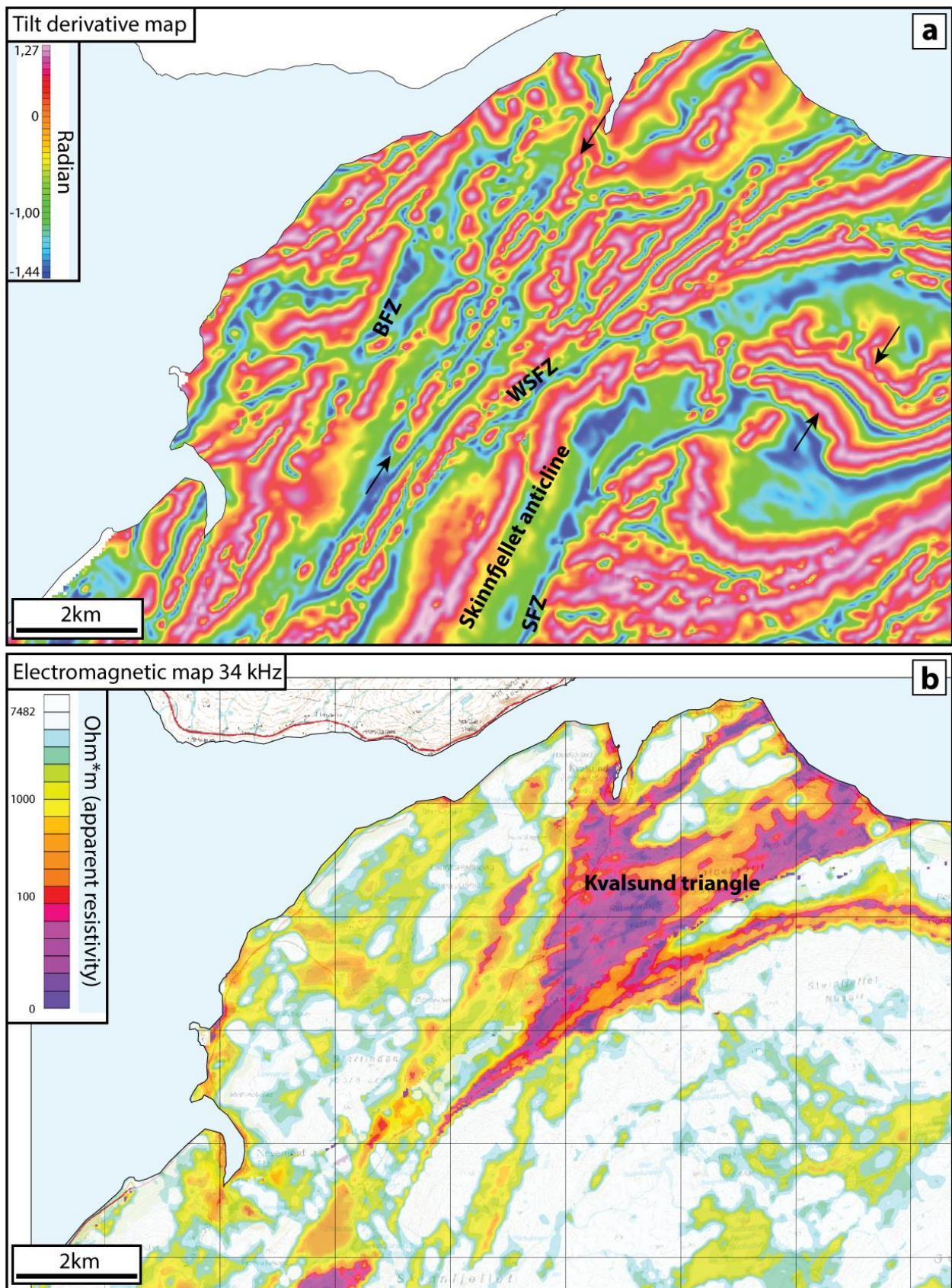
D<sub>3</sub> refer to extension and basin formation in the Barents Sea in the Devonian-Carboniferous (e.g. Faleide et al., 2010; Faleide et al., 1984; Hansen et al., 2012). Torgersen et al. (2014) dated a fault gouge by K-Ar on authigenic illite from the RTW that yielded a late Paleozoic age (c. 300 Ma from < 4 μm fraction).

D<sub>4</sub> represents a Mesozoic extension during the Triassic-Cretaceous (Faleide et al., 1984; Torgersen, 2015).

All of the deformation events created fabrics and deformational structures that can, to a certain extent, be separated through detailed structural analysis and geochronological investigations.

D<sub>1</sub> deformed the RTW in a continuous manner generating kilometric scale, open, upright folds. D<sub>2</sub> took place as a more discrete deformation event with large thrusts and reverse faults duplicating the stratigraphy and creating complex geometries. Discrete D<sub>2</sub> localization, however, occurred only after further tightening of the F<sub>1</sub> folds. D<sub>3</sub> and D<sub>4</sub> (generally merged as they are difficult to separate in the field) was discrete deformation events caused by extension of the crust and is found to be simultaneous to e.g. the opening of the Hammerfest basin in the southern Barents Sea (Faleide et al., 2010). One of the normal faults created during this extensional event is the stipulated Vargsund-Langfjorden fault (Roberts and Lippard, 2005), which strikes NE-SW and juxtaposes the KNC in the hanging wall to the Raipas Supergroup metasediments in its footwall. Torgersen et al. (2014) showed that several of the inherited reverse faults from D<sub>2</sub> were reactivated extensionally at  $121 \pm 5$  Ma, which contributed to the development of the complex geometries revealed by the mapping of this and previous projects.





**Figure 6-1:** (a) Map showing the tilt derivative of the total magnetic anomaly. Some key faults and structures are labeled (SFZ = Skinnfjellet Fault Zone, BFZ = Beretsjord Fault Zone, WSFZ = Western Skinnfjellet Fault Zone). (b) 34000Hz electromagnetic map show areas with low resistivity, such as the Kvalsund Triangle.

## 6.1 Folding

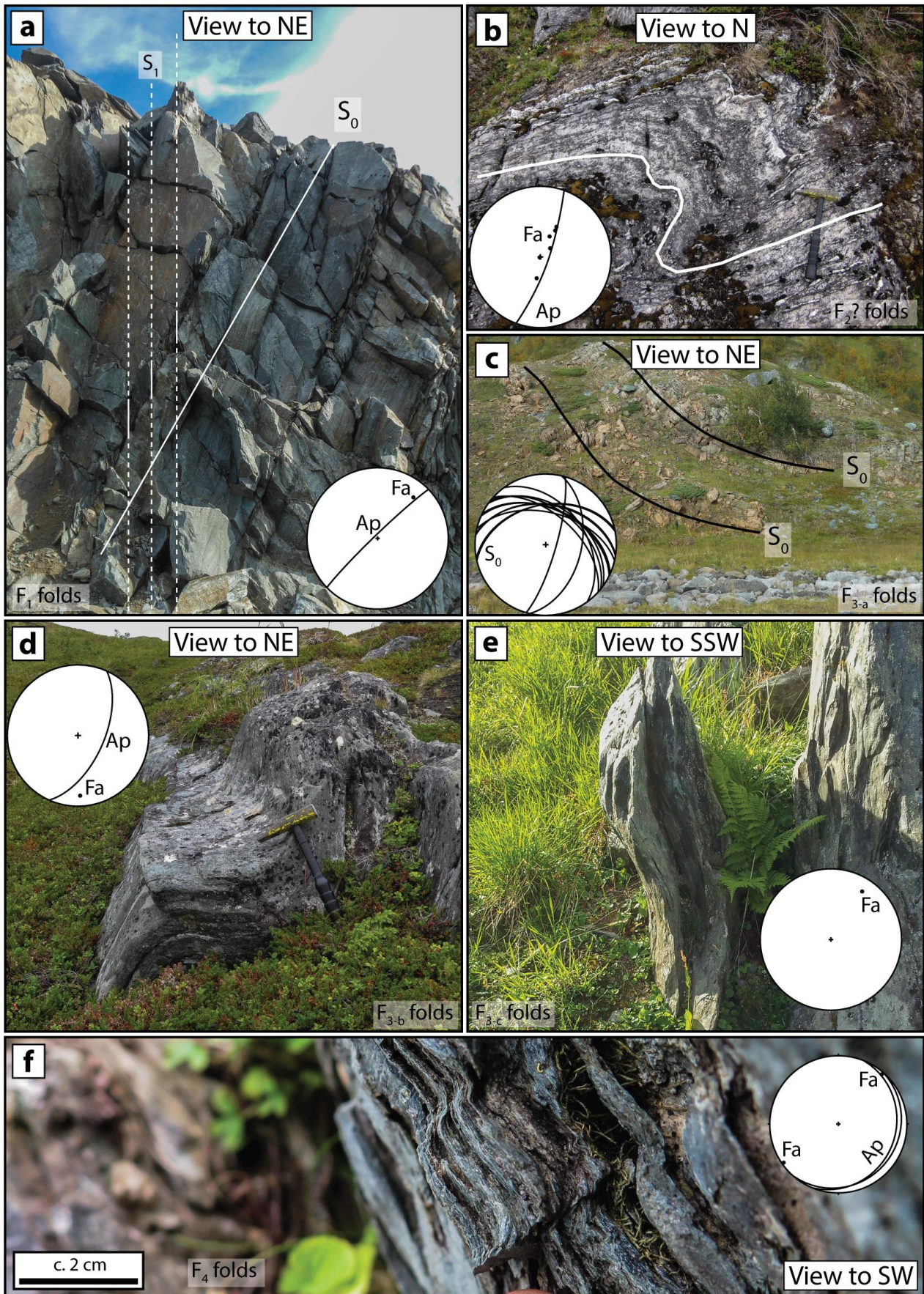
In order to simplify the description of the complex folding history of the study area, the multiple generations of folds are here categorized based on their relative age: starting with the first generation produced by the Svecofennian orogeny, the second generation during pre-Caledonian nappe emplacement, third generation by syn-Caledonian nappe emplacement and the fourth during Paleozoic and Mesozoic extension.

**Table 2:** Fold characteristics in the northwestern RTW, as constrained by field mapping. Figure 6-2 shows photographs of all the various types. See text for further details

<b>F<sub>n</sub></b>	<b>D<sub>n</sub></b>	<b>Geometry</b>	<b>Wavelength</b>	<b>Fold axis (Trend/Plunge)</b>	<b>Axial plane geometry</b>	<b>Locality</b>
1	1	Symmetric Open	Kilometric	NE-SW to ENE- WSW gentle	Upright	Saltvatn Group
2	?	Asymmetric Tight to isoclinal	Meter	NE to NNE moderate to steep	Vertical to reclined	Window and PIS
3-a	2	Symmetric- asymmetric Open to close	10's – 100's of meters	NNE to NE gentle - moderate	Upright to inclined	Porsa Gr. Skinnfjellet
3-b	2	Asymmetric Open to tight	Meter	NE-SW sub- horizontal	Moderate SE dip	Faults within PIS
3-c	2	Symmetric Gentle to open	Centimeter	NE-SW sub- horizontal	Sub- horizontal	Everywhere
4	3/4	Asymmetric Open to tight	Meter to millimeter	NE-SW sub- horizontal	Moderate to gentle SE dip	Faults within PIS

**F<sub>1</sub> folds** were produced during the Svecofennian orogeny and are characterized by kilometer scale wavelength and open, upright geometry. They are well preserved in the southeastern part of the RTW (Fig. 6-2 a). The folds that are found in the Kvalsund triangle are interpreted to be F<sub>1</sub> folds, although possibly structurally reworked during the subsequent F<sub>3</sub> folding phases (see section 7.1.1 for further discussion). F<sub>1</sub> folds are also interpreted to be responsible for the axial planar cleavage variably developed throughout the RTW (Viola et al., 2008).





**Figure 6-2:** Examples of all fold types documented in the RTW. See text and Table 2 for further details.



## 6. Structural analysis of the mapped area

**F<sub>2</sub> folds** are asymmetric, inclined and with axial planes with a moderate to steep dip towards the ESE and generally vergence suggesting dextral kinematics (Fig. 6-2 b). In Kvalsunddalen, F<sub>2</sub> folds are more developed due to the weak rheological properties of the Kvalsund and Bierajav'ri formations. Here, the folds are generally isoclinal with a steeply plunging fold axis and generally upright axial planes (Fig. 5-12 a and b).

**F<sub>3</sub> folds** are syn-Caledonian folds. Three sub-generations have been recognized based on their geometric configuration and these are denoted F<sub>3-a</sub>, -b and -c, in the following description:

**F<sub>3-a</sub> folds** have moderately NE- to NNE-plunging fold axes, with an axial plane dipping steeply to moderately to the NW. Good examples of F<sub>3, a</sub> folds are found in the Vargsund dolostones draping the Skinnfjellet anticline (Fig. 6-2 c).

**F<sub>3-b</sub> folds** differ from the above sub-set in that they are generally more asymmetric and tighter, with moderately SE-dipping axial planes. In addition, they have sub-horizontal NE-SW-trending fold axes. Several of the shear zones within the PIS, both phyllonites and calc-mylonites, are folded by these folds (Fig. 6-2 d).

**F<sub>3-c</sub> folds** are separated from the above in that they are symmetric with sub-horizontal axial plane and fold axis. These folds are generally developed in weak lithologies, such as Gorahatjohka, Kvalsund and Bierajávri formations (Fig. 6-2 e).

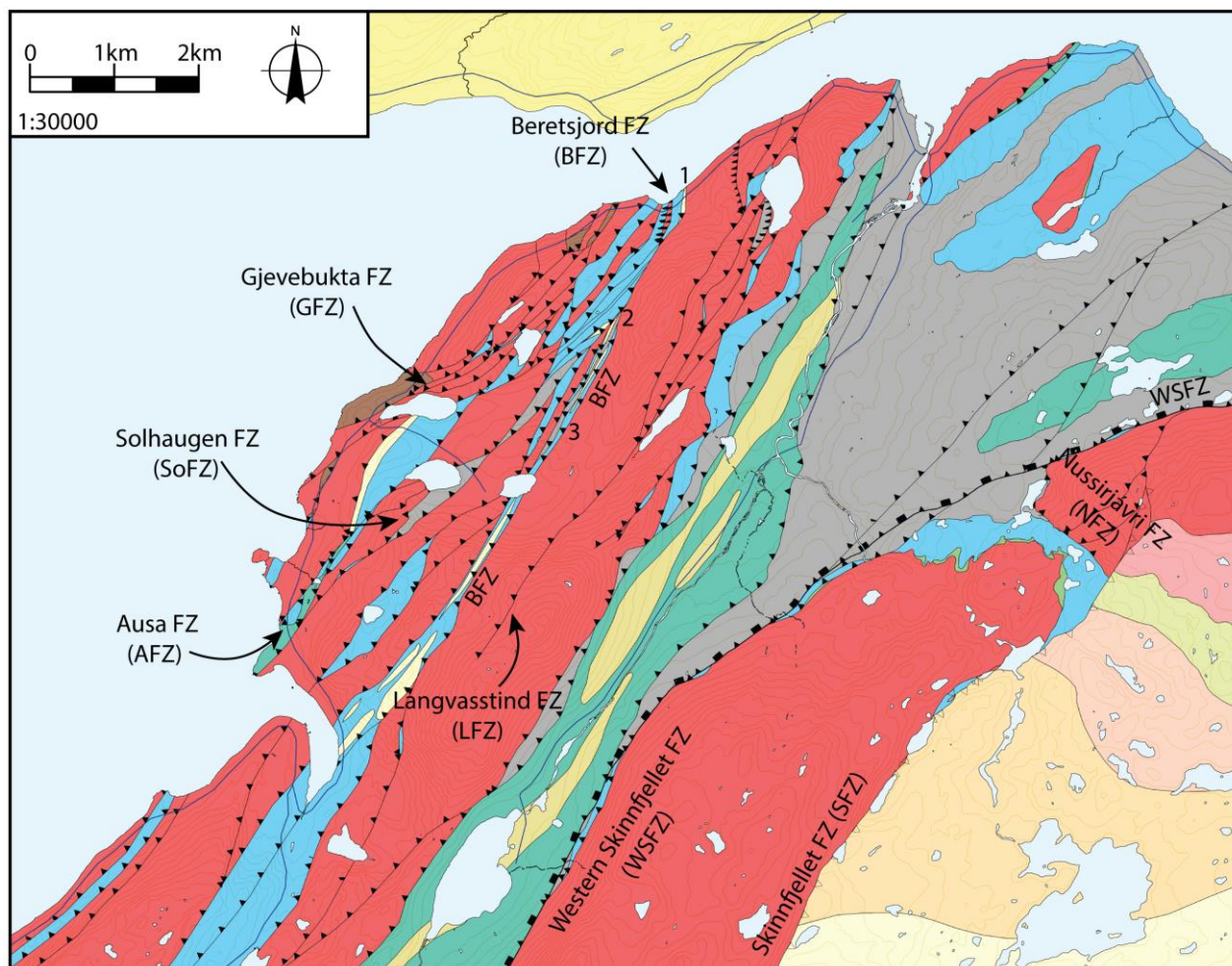
**F<sub>4</sub> folds** are asymmetric, open to tight folds with SE-dipping axial planes and NE-SW sub-horizontal plunging fold axes. They formed during Paleozoic and/or Mesozoic extension and are mostly developed within extensionally reactivated fault zones, where they are generally mesoscopic to microscopic (Fig. 6-2 f). F<sub>4</sub> folds are commonly found in conjunction with shear bands and crenulations.

## 6.2 Faulting

During Caledonian deformation a shift in deformation mechanism occurred from continuous to more discrete strain localization along the limbs of the F<sub>1</sub> inherited folds. Simultaneous with the progressive strain localization, further tightening of F<sub>1</sub> folds was accommodated by flexural slip (see section 7.1.3 for further discussion). During the early stages of the Caledonian deformation, the RTW underwent sub-greenschist facies metamorphism. However, as the nappes were translated over the RTW, the metamorphic grade increased in the immediate footwall of the sole thrust.

Thin section analysis of fault rocks from specific faults in the area shows that these represent complex deformational histories with a variety of different deformation mechanisms active at different times

during the evolution of the faults. Therefore, when reviewing the fault characteristics it is important to bear in mind the full temporal evolution of the faults (e.g. Torgersen and Viola, 2014).

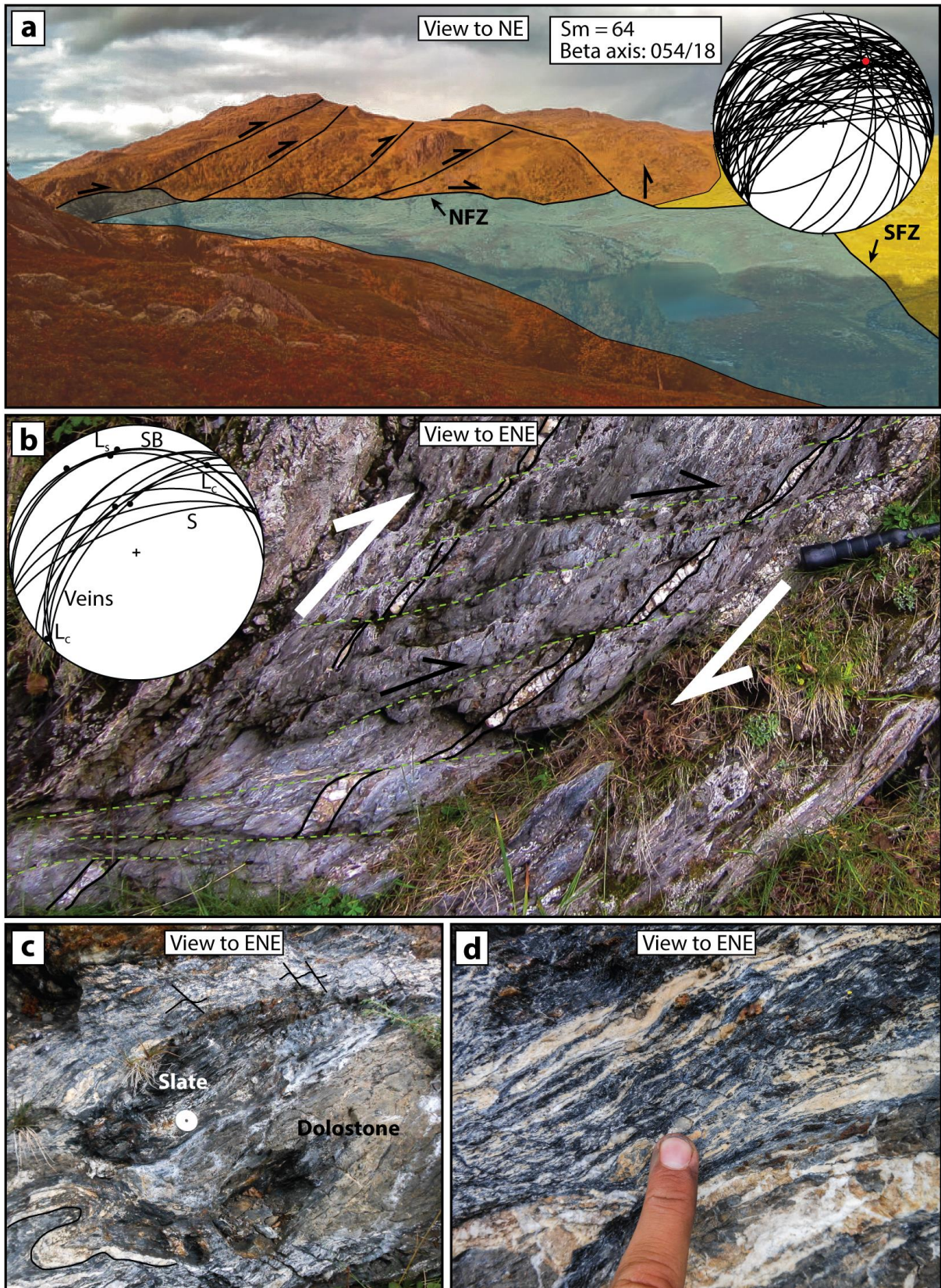


**Figure 6-3:** Map with fault names. Beretsjord Fault Zone is labeled 1, 2 and 3, which represents specific locations described below. Legend same as Figure 4-4.

### 6.2.1 Nussirjávri Fault Zone (NFZ)

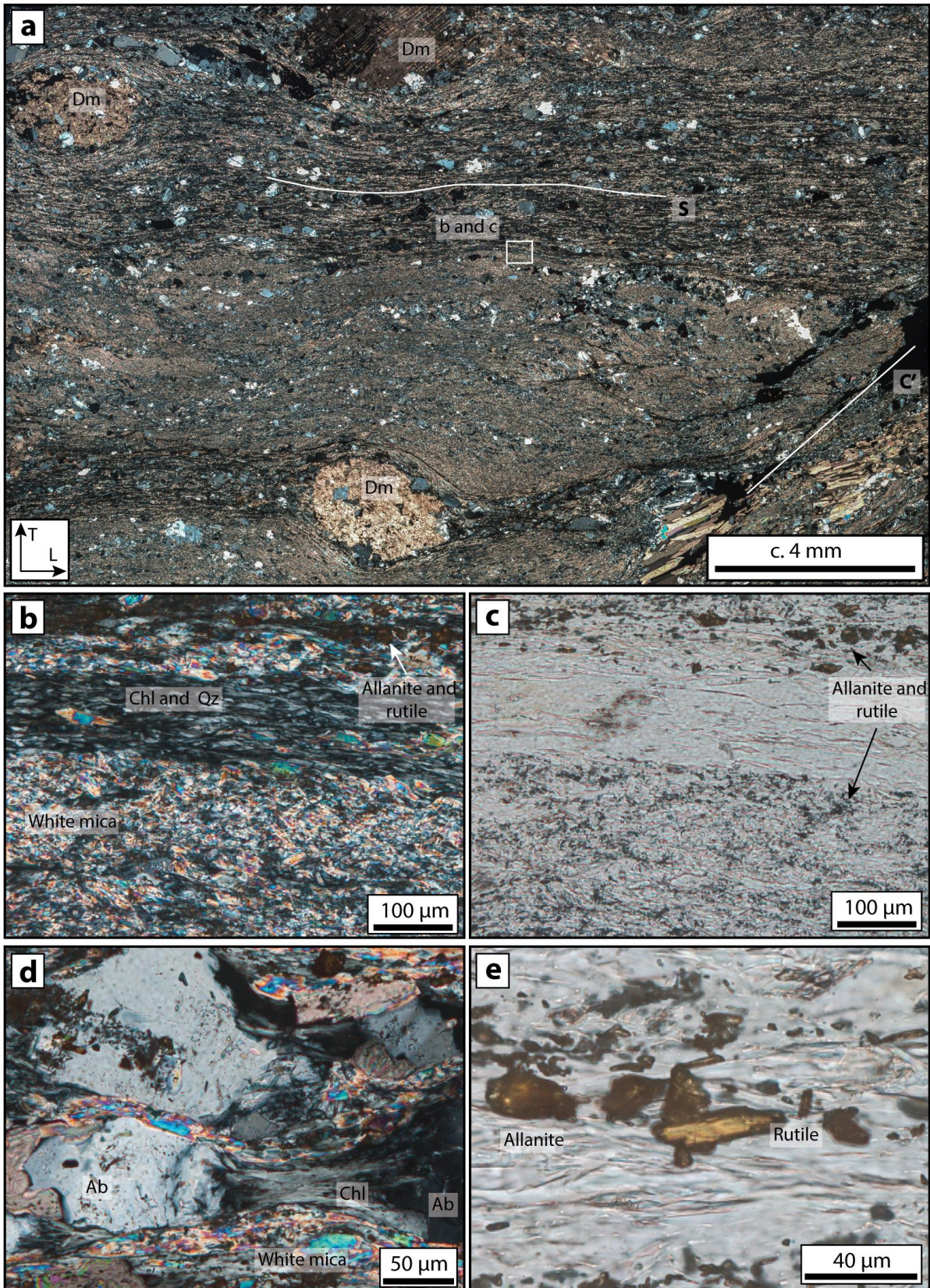
The NFZ cuts the Skinnfjellet anticline at its northernmost exposure (Fig. 3-1; 9 and Fig. 6-3). It is exposed for c. 1 kilometer and displays a ramp-flat geometry with a steep NW dip at the easternmost exposed part (Fig. 6-4 b) and shallow NW-dipping central and western segments (Fig. 6-4 c and d). Several ramps branch from the flatter segment of the fault (Fig. 6-4 a). The NFZ appear to be truncated by the SFZ to the west (Fig. 6-4 a). The fault juxtaposes Nussir metabasalts and volcanoclastic sediments in the hanging wall against Porsa Group graphitic slates and dolostones to the west and east, respectively (Fig. 6-4 a). Stretching lineations and striations measured on the fault plane and shear bands plunge NW to NNW (Fig. 6-4 b stereonet). Abundant kinematic indicators (porphyroclasts, dragged foliation, shear bands and asymmetric folds) in combination with the pervasive stretching lineation constrain a SSE-SE-ward transport direction (Fig. 6-4 b, c and d). The kinematics can be further





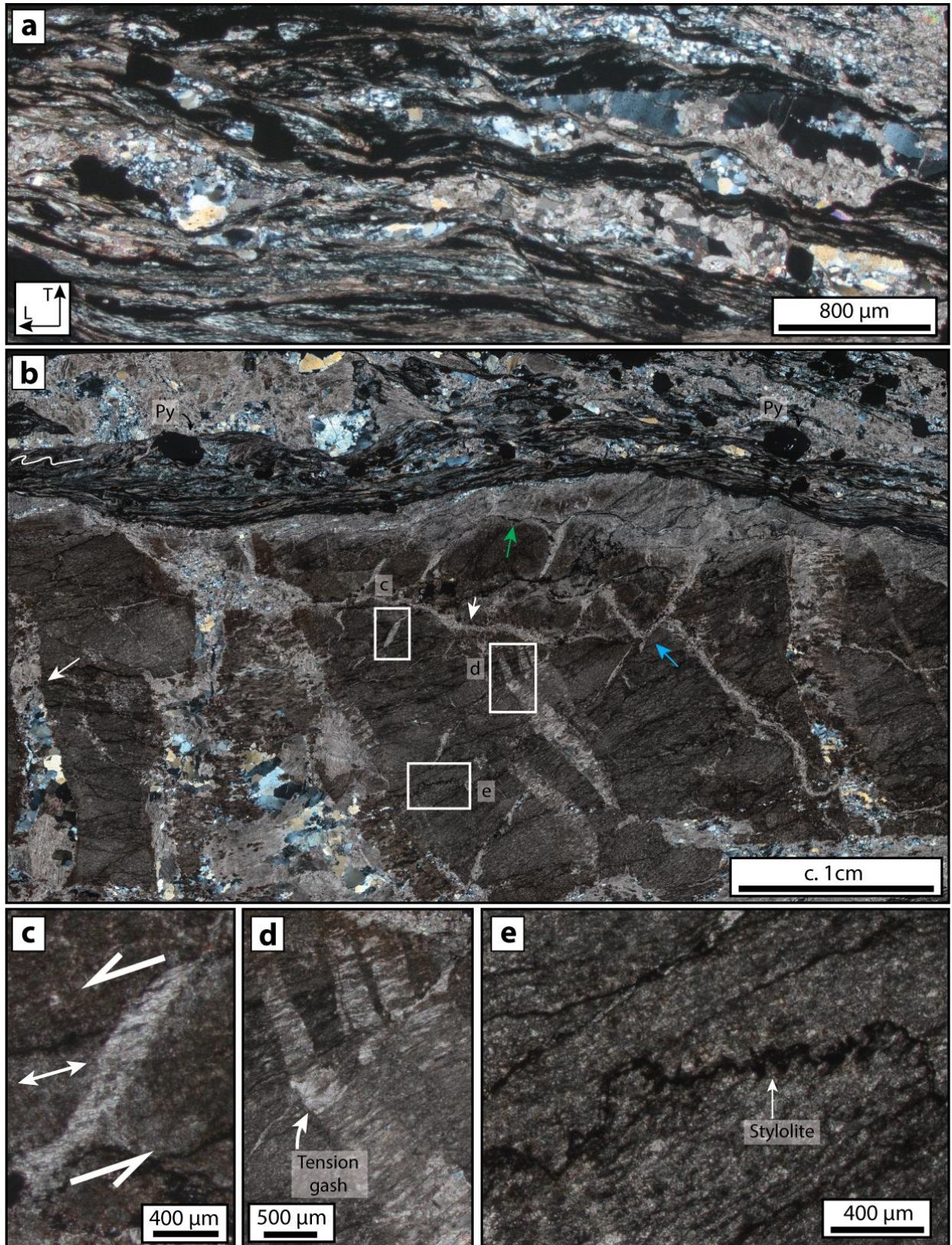
**Figure 6-4:** Typical field characteristics of the Nussirjávri Fault Zone (NFZ). (a) Overview photograph showing the NFZ and its relationship with the Skinnfjellet Fault Zone, in addition to the branching ramp faults. Red=greenstone, Blue=dolostone, Gray=graphitic slate, Yellow=slate. Stereonet show fault plane measurements with poles. (b) Phyllonite with a pervasive foliation and C' shear bands. Stereonet show that veins and shear bands have a slightly different orientation than the foliation. SB = shear band (c) Large clast of dolostone and graphitic slate preserved in a mylonitic foliation displaying a plethora of kinematic indicators. (d) Detailed photograph of mylonitic foliation with C' shear bands.





**Figure 6-5:** Plate of microphotographs from the Nussirjavri fault zone phyllonite. All photomicrographs are oriented as in (a). (a) Stacked photomicrograph of phyllonite shown in Figure 6-4 b. Areas containing large dolomite clasts generally contain more feldspar and chlorite. White square indicate location for (b) and (c) X-pl. (b) Textural difference between the bands. Upper band contain coarser chlorite and accessory phases. X-pl. (c) Same area as (b). Show grain size difference of the accessory phases between the two bands. P-pl. (d) Boudinaged feldspar clast with chlorite in the neck zone. X-pl. (e) Relatively coarse allanite and rutile as constrained by EDS analysis. Allanite is partially metamict. P-pl.





**Figure 6-6:** Microscopic details of the NFZ mylonite. All photomicrographs are oriented as (a) and acquired using crossed polarizers. (a) Mylonitic fabric with C' shear band. Quartz microstructures suggest dynamic recrystallization by slow grain boundary migration and possibly subgrain rotation recrystallization. (b) Stitched overview photomicrograph displaying mylonitic horizon and deformed dolomite clast with alteration rim. (c) Tensional step-over fracture in dolomite clast filled with calcite fibers that are stretched in the direction of the double arrow. (d) Tension gashes in dolomite clast filled with calcite. (e) Stylolite in dolomite clast.



constrained by sub-horizontal tension gashes found throughout the hanging wall. The hanging wall above the mylonites is commonly strongly fractured and oxidized. The NFZ fault plane is folded around a gently NE-plunging fold axis (Fig. 6-4 a).

Where the fault affected metabasalts, the fault rock is made up of a fine-grained, grey to green phyllonite (Fig. 6-4 b and Fig. 6-5 a), locally rich in sulfides. Thin section analysis show that the phyllonitic foliation is defined by alternating layers of fine-grained white mica with minor chlorite and some feldspar porphyroclasts and strongly foliated and relatively coarse-grained chlorite, white mica and feldspar porphyroclasts (Fig. 6-5 b and d). The latter coarse-grained layers contain relatively coarse accessory phases such as rutile and allanite (constrained by EDS data; Fig. 6-5 c and e) that are generally confined to horizons containing large dolomite porphyroclasts (Fig. 6-5 a). Feldspar porphyroclasts are often either symmetrically or asymmetrically boudinaged (Fig. 6-5 d).

Where the fault affects graphitic slates, a pervasive mylonitic fabric has developed (Fig. 6-4 c and d) with alternating dark and light colored layers consisting of graphite and phyllosilicates, and quartz and carbonates, respectively. The bands are locally isoclinally folded and show C' shear bands (Fig. 6-6 a). Quartz within the mylonitic foliation show microstructures indicative of dynamic recrystallization by bulging- and subgrain rotation recrystallization. The mylonitic zone holds several larger porphyroclasts of dolostone that mainly has deformed by frictional processes. The style of deformation of the porphyroclasts indicates that they have deformed under various environmental conditions, as well as under different stress regimes. This is also well demonstrated by several generations of tension gashes (Fig. 6-6 d and white arrows in b), micro faults (Fig. 6-6 blue arrow in b) and tensional step-over fractures (Fig. 6-6 c). In addition, purely stress induced physio-chemical and chemical processes have been active as displayed by frequent stylolites (Fig. 6-6 e) and an alteration halo around the dolostone towards the mylonite (Fig. 6-6 b green arrow).

### **6.2.2 Skinnfjellet Fault Zone (SFZ)**

The Skinnfjellet Fault Zone (SFZ) is a > 10 km long, sub-vertical fault that strikes roughly NE-SW (Fig 6-3) along the eastern segment of the Skinnfjellet anticline (Fig. 3-1; 5). It dips consistently, but very steeply to the SE and juxtaposes the Saltvatn Group in the hanging wall against the Nussir greenstones and Vargsund dolostones in the footwall (Fig. 4-3 and Fig. 6-7 a). The fault bears sub-vertical stretching lineations together with sub-horizontal crenulation lineations (Fig. 6-7 a). Kinematic indicators such as sigma clasts, shear bands and deformed conglomerate clasts suggest top-to-the NW reverse sense of shear (Fig. 6-7 b, c, d).

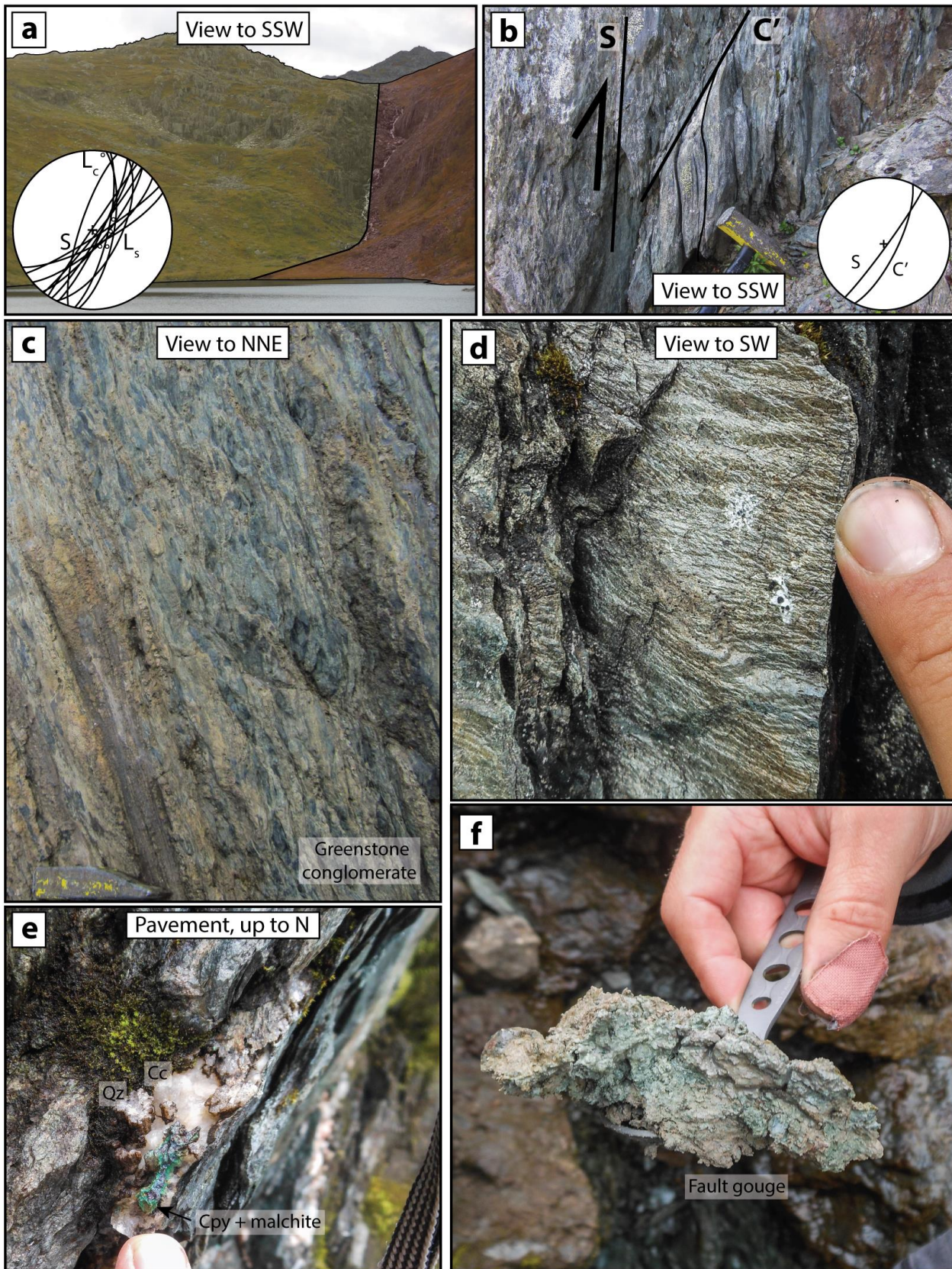
## 6. Structural analysis of the mapped area

In a gorge (Fig. 6-7 a) in the southernmost exposed part of the fault, the entire SFZ fault zone is exposed, including the c. 10 m thick fault core. At this locality, the fault juxtaposes a greenstone conglomerate of the Dypelv Formation in the hanging wall against the Nussir greenstone (metabasalt/metatuff) in the footwall. A section across the fault zone was mapped in detail (Fig. 6-8) to investigate strain partitioning and localization. It demonstrates an asymmetric deformation pattern, wherein the conglomerates in the hanging wall are deformed furthest from the fault core. Strongly foliated metatuffs in the footwall contain idioblastic magnetite crystals growing on the foliation planes. C' shear bands constrain top-to-the WNW/NW. The number of C' shear bands increases together with the phyllosilicate content and intensity of the shear foliation (Fig. 6-7 b and d and Fig. 6-8 a) towards the fault core. Even closer to the core is a strongly foliated phyllonitic lithology with a dense, sub-horizontal crenulation lineation that plunges gently to the N-NNE (Fig. 6-7 d and Fig. 6-8 b). Adjacent to the fault core there is a c. 40 cm wide green phyllonite that is loosely consolidated and contains some clay-rich horizons. This phyllonite is rich in ECC shear bands and invariably suggests top-to-the NW sense of shear.

The actual fault core is c. 20 cm thick and comprises a green to pale brownish, highly plastic fault gouge with no clasts (Fig. 6-7 f and Fig. 6-7 c). A sample of this gouge was collected to date authigenic and synkinematic illite. Although the analyses are not yet complete, preliminary results from a second-order fault segment of the SFZ indicated a Caledonian faulting age ( $584 \pm 12$  Ma;  $< 2$   $\mu\text{m}$  fraction; Torgersen, 2015).

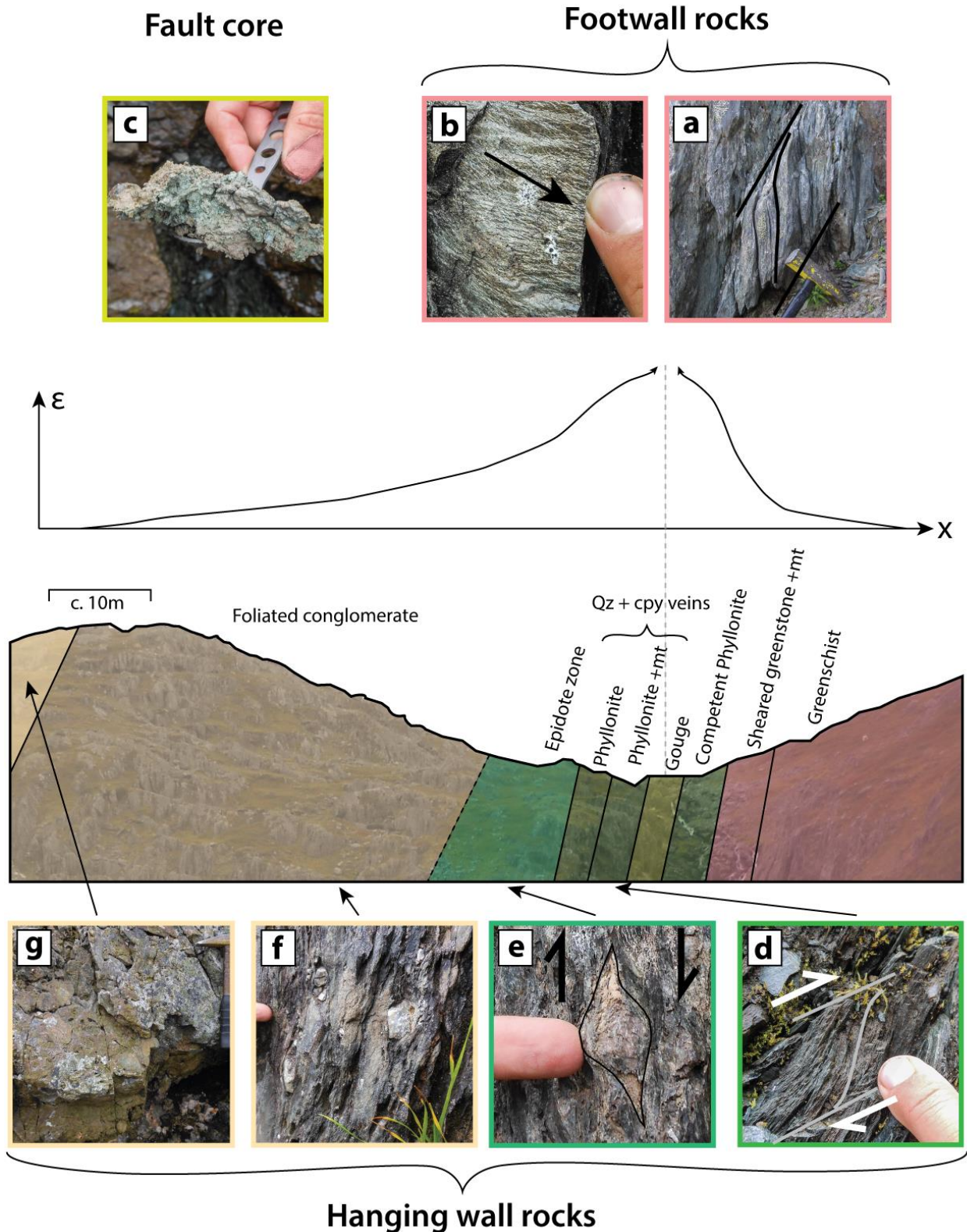
Closest to the fault core in the hanging wall is a c. 2,5 m thick sequence of a fine-grained, dark green, chloritic phyllonite (Fig. 6-8 d) with abundant non-mineralized quartz-calcite veins. There is a decrease in magnetite content as one moves away from the fault core. Locally, coarse-grained epidote occurs together with quartz in steep foliation-parallel veins. Further from the core, the amount of phyllosilicates decreases and some clasts, possibly inherited from the conglomerate, are visible (Fig. 6-7 c and Fig. 6-8 e). The zone is lineated by chlorite and possibly actinolite needles. A reddish hematite staining and idioblastic magnetite crystals are observed together with steep quartz-calcite veinlets mineralized with chalcopyrite and malachite (Fig. 6-7 e). In thin section, this zone contains interconnected planes of phyllosilicates (Fig. 6-9 a). Fine-grained ( $< 50$   $\mu\text{m}$ ) dynamically recrystallized quartz is found interstitially between the phyllosilicate-rich planes (Fig. 6-9 b). As one progressively moves away from the fault zone the foliation becomes less pervasive (Fig. 6-8 f). Epidote-rich sequences are observed several tens of meters from the fault core (Fig. 6-8 g). (Text continues below figures)





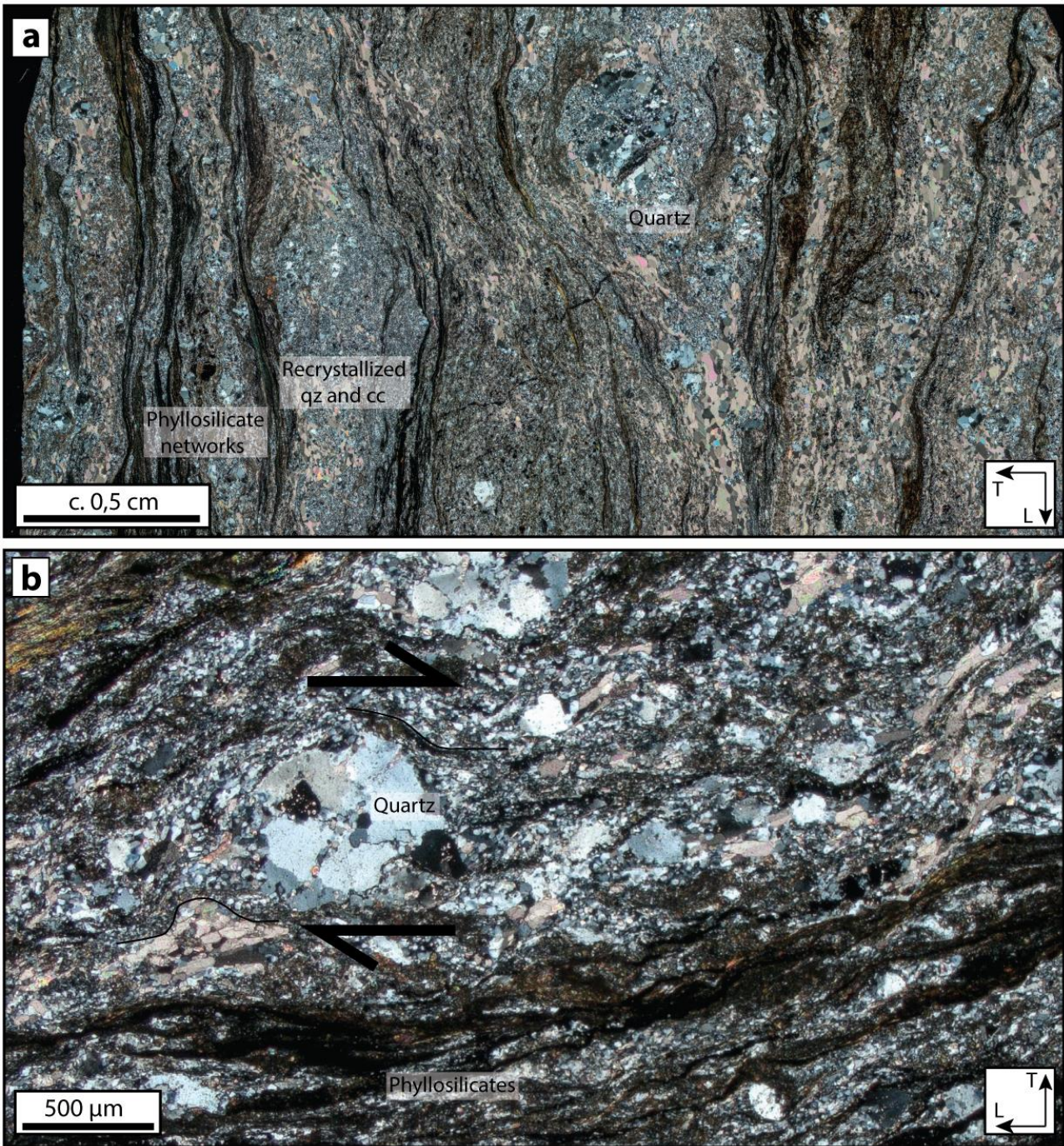
**Figure 6-7:** Key structural features of the Skinnfjellet Fault Zone (SFZ). (a) The best exposure of the SFZ is within this gorge. Stereonet show foliation measurements, dip-slip striation and sub-horizontal crenulation lineations. (b) C' shear bands constrain E-block up. (c) Deformed greenstone conglomerate. (d) Sub-horizontal crenulation lineations. (e) Quartz-carbonate veinlets that are locally mineralized with chalcopyrite and malchite. (f) Fault gouge from the c. 40 cm thick fault core.





**Figure 6-8:** Strain partitioning along a transect orthogonal to the SFZ. The smaller photographs are color coded. From right to left: (a) Shear bands from footwall greenschist. (b) Phyllosilicates are progressively introduced and crenulated. (c) Gouge from fault core. (d) Small shear bands in hanging wall phyllonite. (e) Strongly deformed conglomerate clast. This zone is often associated with coarse epidote. (f) Weakly deformed conglomerate. (g) Hanging wall conglomerate is locally enriched in epidote.

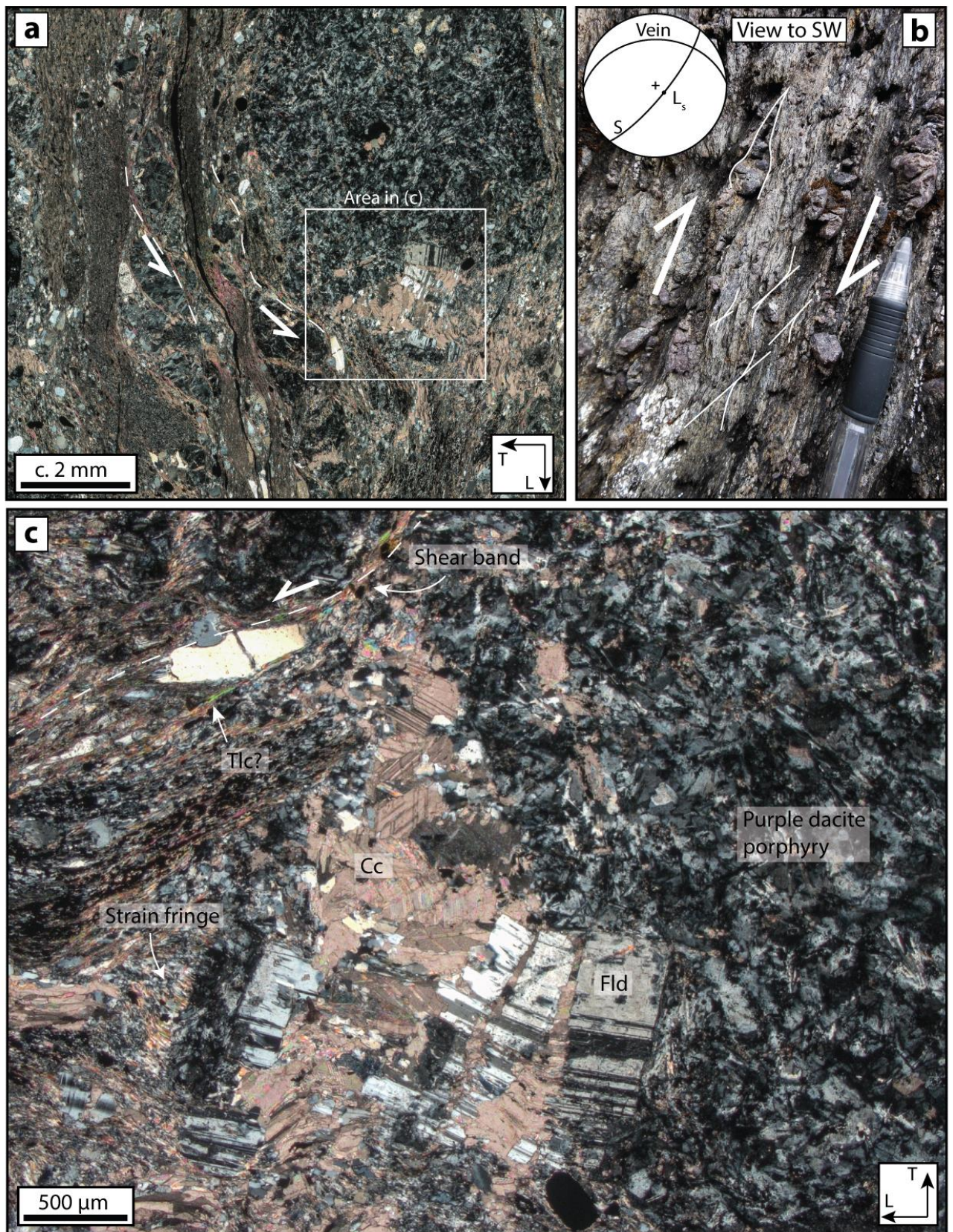




**Figure 6-9:** (a) stitched photomicrograph (crossed polarizers). Interconnected network of fine-grained phyllosilicates, with dynamically recrystallized quartz and calcite in the relatively less deformed areas in-between. (b) Quartz clast displaying microstructures which indicate that it has undergone low grade dynamic recrystallization. X-pl.



6. Structural analysis of the mapped area



**Figure 6-10:** Plate of photomicrographs from where the SFZ deform the Stangvatn formation. (a) Stretched photomicrograph showing micro shear bands that indicate both normal and reverse movement around competent clasts. X-pl. (b) Meso-scale shear bands displaying reverse movement. (c) Deformed feldspar clast shows that fluids were present during deformation. X-pl.



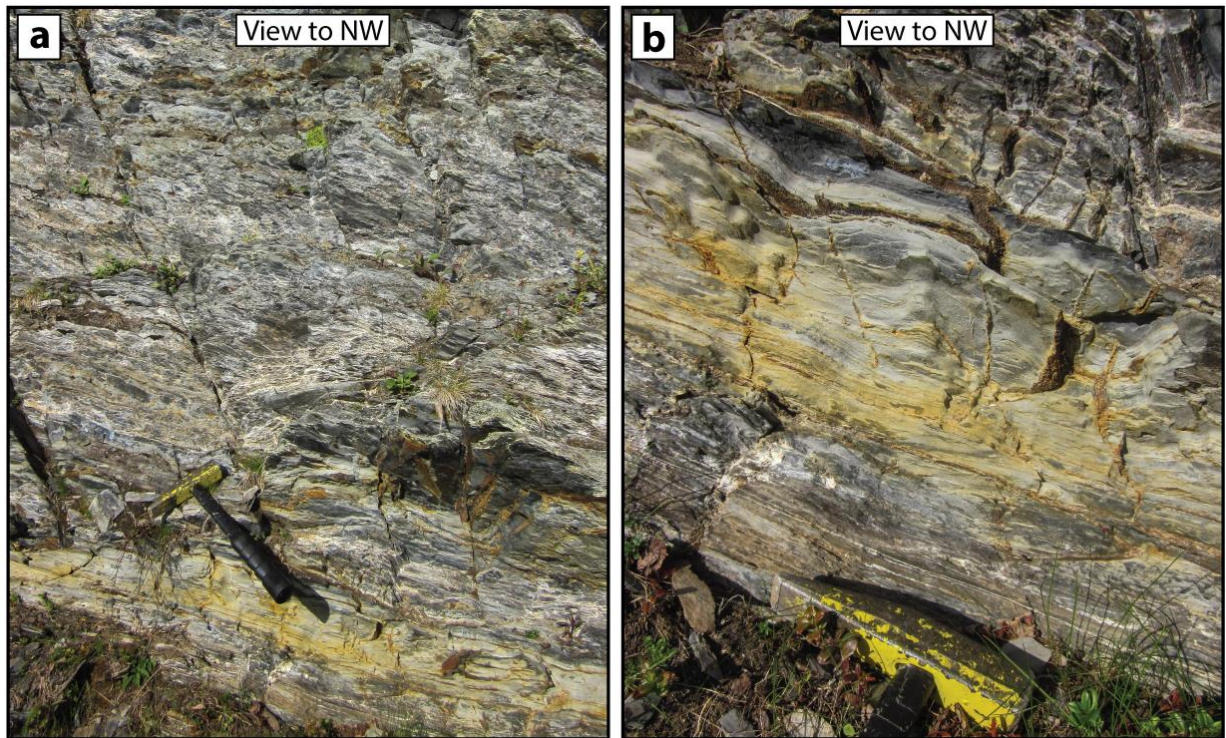
Where the SFZ cuts through the Stangvatn conglomerate, asymmetrically deformed conglomerate clasts associated with shear bands constrain east-block-up reverse movement. Quartz carbonate veins dipping shallower than the steeply dipping foliation, substantiate further that the SFZ is indeed a reverse fault (Fig. 6-10). Petrographic analysis of samples from this locality shows a stockwork of calcite veinlets, which indicates that deformation has been accompanied by ingress of fluids into the system, possibly as numerous dilation events. In addition, evidence for fluid-assisted hydraulic fracturing is observed in all studied samples (Fig. 6-10 c).

### **6.2.3 Western Skinnfjellet Fault Zone (WSFZ)**

The Western Skinnfjellet Fault Zone stretches for > 25 km along the western edge of the Skinnfjellet anticline and the Nussir Mountain (Fig. 3-1; 4, 5 and Fig 6-3). It is only partly exposed at one locality where a rusty zone of locally brecciated graphitic slate with layers of varying color is observed (Fig. 6-11). The rock is highly fractured and sealed by numerous calcite veinlets and veins, similar to the Kvenklubben Fault described in Torgersen and Viola (2014) and Torgersen et al. (2014). The inferred fault plane dips moderately towards the NW. The fault zone contains very fine-grained phyllosilicate-rich domains, some of which are phyllonitic and comprise a very fine-grained, green-yellow rock with a finely spaced foliation, possibly reflecting a consolidated gouge (see section 7.2.2). The deformation intensity increases towards the east. Immediately to the east of the locality there is a c. 30 m wide valley with relatively steep walls and no outcrops, which could possibly represent the effects of differential negative erosion at the expense of a weak fault core.

Although poorly exposed, the trace of the WSFZ can be deduced from the airborne magnetic maps where it is defined by an approximately 9 km long continuous magnetic low along the western edge of the Skinnfjellet, particularly clear on the tilt derivative (TDR) map. The TDR magnetic low corresponds with a topographic low that can be followed for c. 3 kilometers (Fig. 6-1).

Previous workers (Nilsen and Nilsson, 1996; Pharaoh et al., 1983; Reitan, 1963) have not described this boundary as tectonic, but rather proposed an “inferred boundary” without any specifications. In the maps of Pharaoh et al. (1983) and Nilsen and Nilsson (1996), a 3 kilometer continuous dolostone layer has been drawn parallel to the Skinnfjellet anticline. Detailed fieldwork for this thesis, however, suggests that the dolostone layer is disrupted by sheared horizons, possibly related to WSFZ.



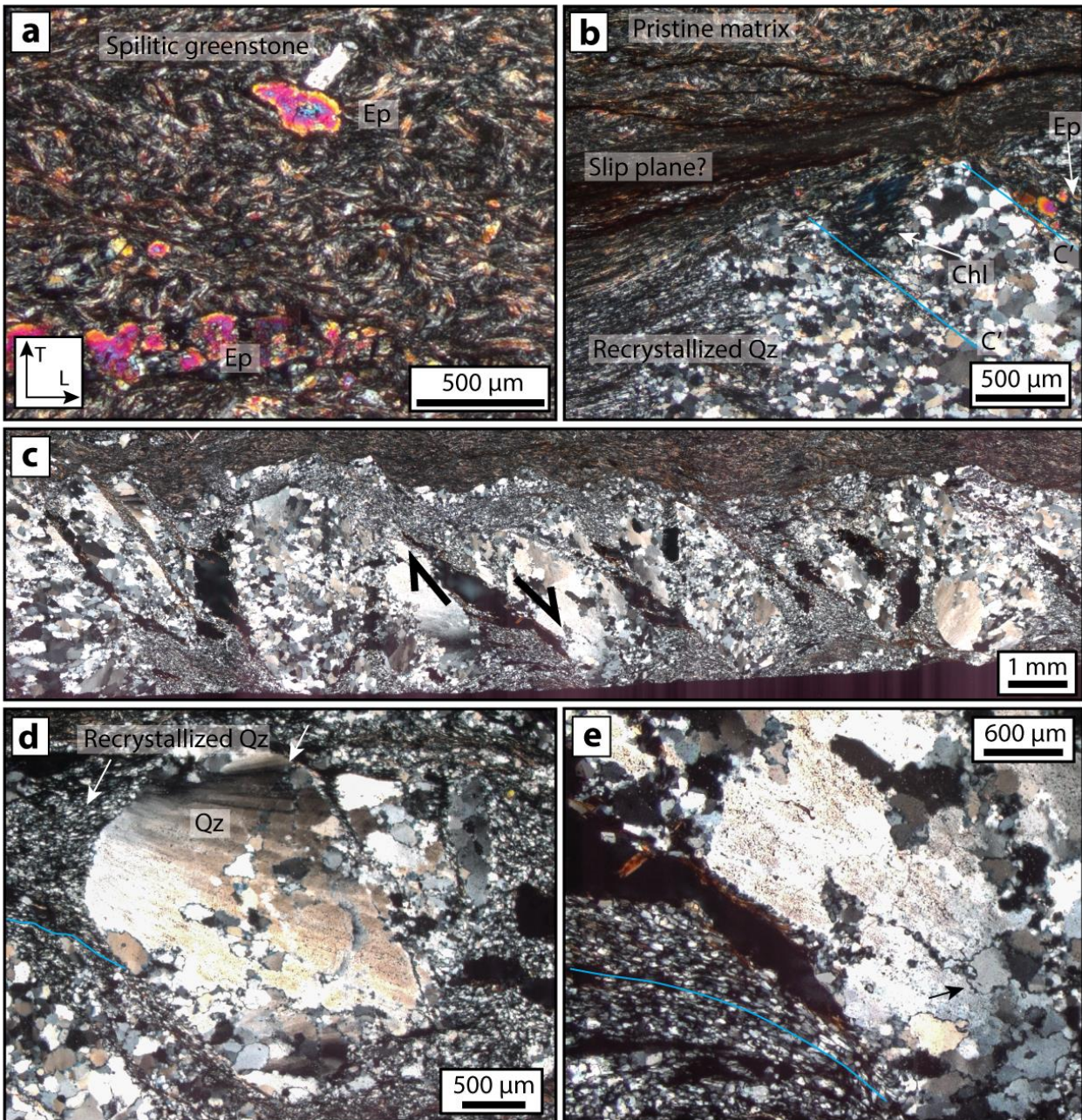
**Figure 6-11:** Field characteristics of the Western Skinnfjellet Fault Zone. (a) Hanging wall (above hammer) show a pervasive stockwork of calcite veinlets. (b) Phyllonitic zone with rusty horizons.

#### 6.2.4 Langvasstinden Fault Zone (LFZ)

This fault is poorly exposed and is probably a subsidiary strand of the main fault separating the Vargsund Formation and the Nussir metabasalts on the western flank of Kvalsunddalen (Fig. 3-1; 10 and Fig 6-3). In the field, the fault rock is hardly recognizable. Thin section analysis (Fig. 6-12 and Fig. 6-13) reveals that the host rock displays a spilitic texture consisting mainly of amphibole, plagioclase and phyllosilicates (Fig. 6-12 a). Epidote and chlorite fill secondary fractures (Fig. 6-13 b). The matrix also contains several, thin (c. 10-50  $\mu\text{m}$ ) interconnected layers of very fine-grained phyllosilicates, defining minor slip planes (Fig. 6-12 b).

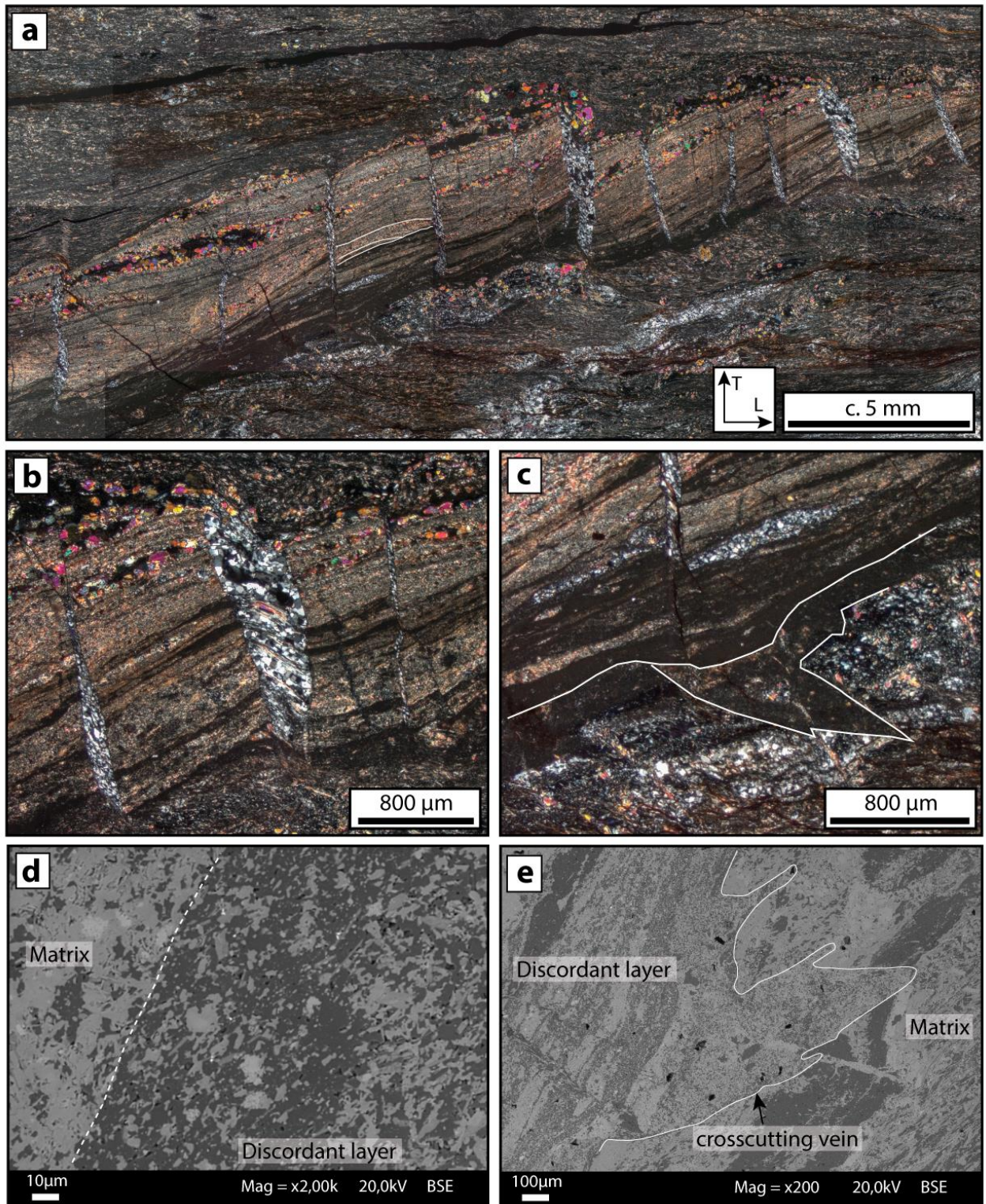
Thin section analysis shows also an asymmetrically boudinaged vein with crystals from c. 200  $\mu\text{m}$  to c. 1 mm in size (Fig. 6-12 c). Internally, these grains have bulging grain boundaries and undulose extinction with some large subgrains (50-100  $\mu\text{m}$ ; Fig. 6-12 d). In the boudin neck-zones, quartz is completely recrystallized into very fine-grained (10-70  $\mu\text{m}$ ) elongated individual crystals tracing the rotation of the blocks (Fig. 6-12 c, d and e). Several other, large (> 2 mm) quartz clasts are located within the matrix and generally show asymmetries indicating dextral sense of shear.  $C'$  shear bands are common throughout the sample and deform both quartz clasts and matrix (Fig. 6-12 b and c).





**Figure 6-12:** Photomicrographs showing the general microscopic characteristics of the Langvasstinden Fault Zone. All photomicrographs are taken using crossed polarizers and have the same orientation as in (a). (a) Greenstone displaying a spilitic texture with relatively coarse-grained epidote. (b) Phyllosilicatic slip plane draping a quartz porphyroclast with local pervasive recrystallization. Porphyroclast is cut by C' shear bands and gaps filled with epidote and chlorite with anomalous interference colors. (c) Dextral, asymmetrically boudinaged quartz vein with pervasive recrystallization in boudin neck zones. (d) Remnant clast of vein quartz with large subgrains. Subgrain boundary indicated by white arrow. Recrystallized grains show a well-developed SPO. (e) Recrystallized grains between boudinaged blocks show a well-developed SPO. Their long axis trace the rotation of the blocks (blue line). Black arrow indicates bulging grain boundaries.





**Figure 6-13:** Photomicrographs and SEM images from the Langvasstinden Fault Zone. All photomicrographs are taken using crossed polarizers and have same orientation as in (a). (a) Asymmetrically boudinaged, discordant layer. (b) The discordant layer is finely laminated and quartz fills in the boudin necks. The rotation of the blocks can be traced by the SPO of the quartz grains. (c) Lower part of discordant layer show dark laminae with some clasts of lighter colored material. White lines indicate crosscutting, tapered vein. (d) BSE image of the boundary between discordant layer and matrix show very fine grain size. Quartz is  $< 10 \mu\text{m}$ . (e) BSE image displaying the entire discordant and tapered vein with a sharp contact to the surrounding matrix.

A discordant laminated layer of very fine-grained minerals crosscut the foliation of the greenstone (Fig. 6-13 a). The thickness and color of the individual laminas vary greatly and locally the individual laminas show cross-cutting relationships (Fig. 6-13 a and c). At the top of this discordant layer, there is a c. 400  $\mu\text{m}$  thick zone that contains fine- and relatively coarse-grained epidote together with fine-grained phyllosilicates. A darker layer, which is too fine-grained to be resolved by the optical microscope, appears to cut the above layer (Fig. 6-13 a). The next 200  $\mu\text{m}$  contain interchanging layers of different color, where the lighter colored layers contain phyllosilicates and epidote and the darker horizons contain quartz with a grain size  $< 10 \mu\text{m}$  and some interstitial phyllosilicates (Fig. 6-12 d). The last c. 100  $\mu\text{m}$  contain mostly fine-grained quartz, although clasts of coarser-grained unidentified minerals appear throughout and crosscutting relationships are abundant (Fig. 6-13 c and e). The interface between the layer and the matrix is generally straight, but discordant. At one location, the fine-grained quartz layer form a discontinuous, tapered, veinlet (Fig. 6-13 c and e)

The discordant layer is asymmetrically boudinaged as shown by sub-vertical fractures filled with elongated quartz grains that trace the movement of the blocks (Fig. 6-13 a and b).

### **6.2.5 Beretsjord Fault Zone (BFZ)**

The BFZ stretches for  $> 5$  kilometers through the outermost exposed parts of the PIS. It has been mapped in great detail from the Bertesjord in the north to Neverfjord in the south (Fig. 3-1 and Fig. 6-3). Generally, the BFZ juxtaposes the Vargsund Formation in the hanging wall against Nussir greenstones in the footwall (Fig. 4-3). The fault zone is complex and display both forward and back thrusts. Slip has localized both intraformational and at the contacts between lithologies. Three main localities are described for the BFZ, which were mapped in detail to investigate strain partitioning and localization (Fig. 6-4; 1, 2 and 3).

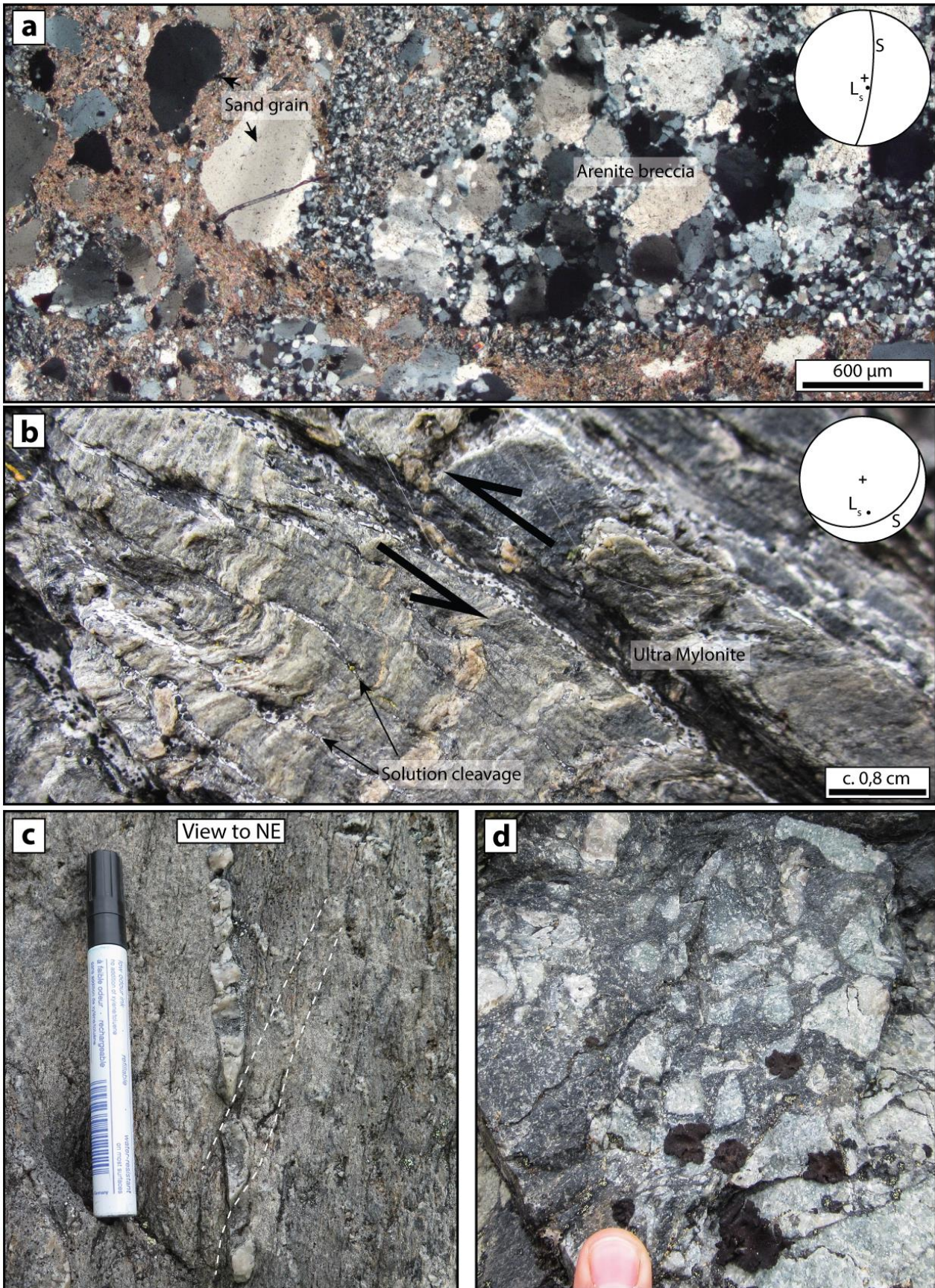
In Beretsjord (Fig. 6-4 ;1), the BFZ juxtaposes a quartzite against metabasalt and dips steeply towards the E. Striations measured on the fault plane indicate oblique slip with transport towards the NW to NNW (Fig. 6-14 a stereonet). The fault rock is a gray, highly crenulated and openly folded phyllonite. The hanging wall quartzite contains a c. 2 m wide cohesive breccia, with angular clasts varying in diameter from  $< 1 \text{ cm}$  to c. 5 cm and are set in a fine-grained greenish matrix (Fig. 6-14 a and d). The breccia is silicified and show microstructures indicating low to medium grade dynamic recrystallization (Hirth and Tullis, 1992). The brecciated clasts indicate that the protolith was a relatively pure quartzitic sandstone with sub-rounded grains ranging in size from c. 200 to 800  $\mu\text{m}$ . The matrix is generally rich in phyllosilicates such as sericite and chlorite together with very fine-grained ( $< 80 \mu\text{m}$ ) recrystallized quartz (Fig. 6-14 a).

## 6. Structural analysis of the mapped area

The next exposure of the BFZ is several kilometers to the south (Fig. 6-4; 2), where the fault dips steeply towards the ENE. Approaching the greenstone, the quartzite becomes red and foliated. Strain is distributed along a several meters wide zone defined by a pervasive, densely spaced shear foliation with some remnant quartz clasts. Asymmetrically deformed, foliation-parallel veins appear throughout (Fig. 6-14 c). They display a weak clockwise rotation, which suggests thrusting kinematics. Within the footwall, an anastomosing network of < 1 cm thick, ultramylonitic, SSE-dipping zones appear (Fig. 6-14 b). Asymmetric kinematic indicators, such as shear bands, porphyroclasts, and striations on the fault plane suggest oblique thrusting with a top-to-the north kinematics. Parallel to the ultramylonites are relatively undeformed “islands” of a phyllosilicate-rich rock with a pervasive solution cleavage and crenulations (Fig. 6-14 b).

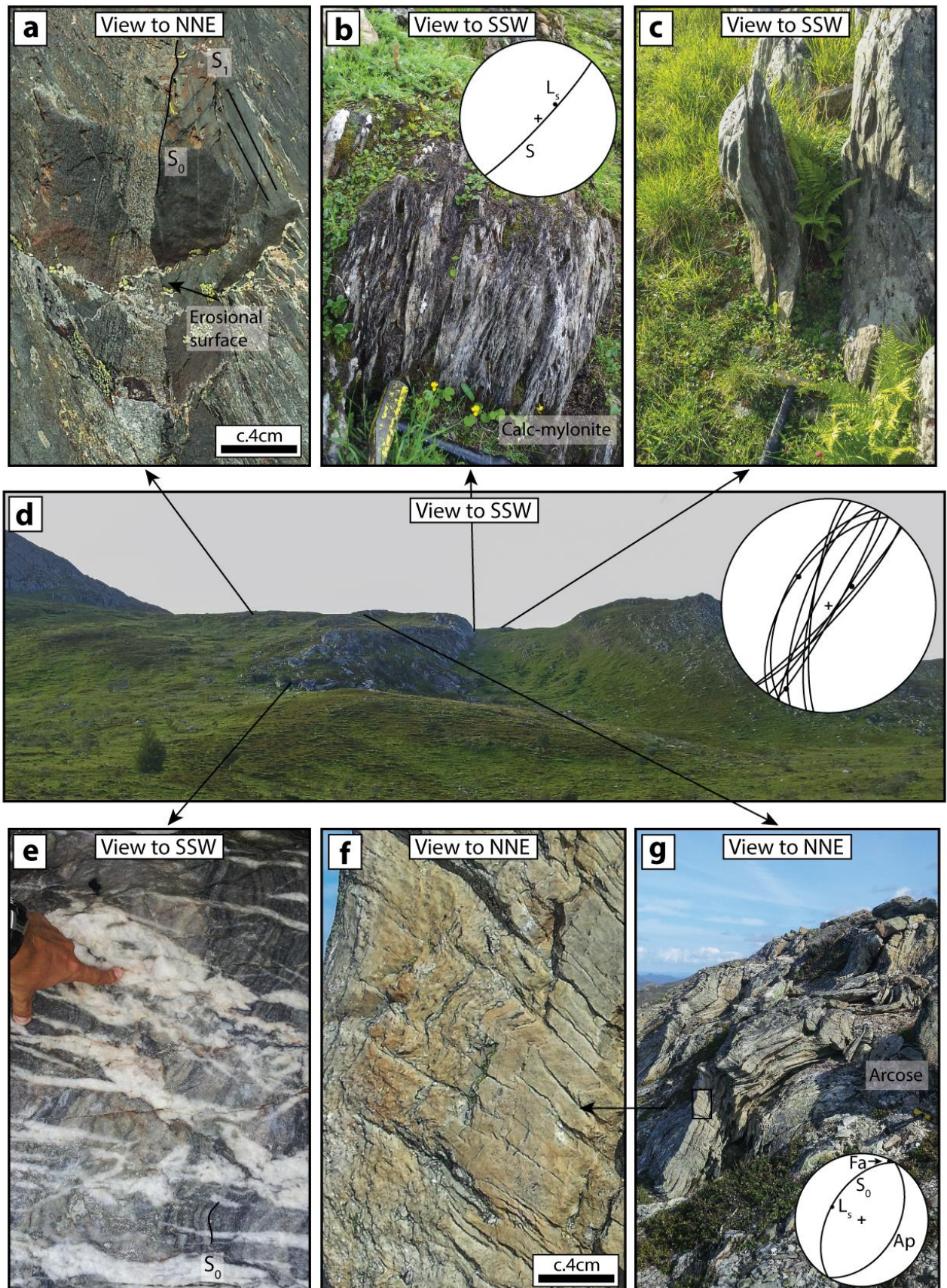
The next locality (Fig. 6-4; 3) display a well exposed section through the entire BFZ (Fig. 6-15 d). At this locality, the BFZ strikes NE-SW and juxtaposes an argillaceous metasedimentary sequence against metatuffs of the Krokvatn Formation (Fig. 6-15 c and a respectively). The hanging wall slates rest against a steeply dipping, c. 4 meters thick calc-mylonite with alternating layers of calcite and quartz (Fig. 6-15 b) and a steeply SE-dipping shear foliation. Striations on foliation planes within the calc-mylonite suggest oblique-slip and, coupled with kinematic indicators, a top-to-the SW transport direction. Some remnant dolomitic clasts are preserved within the mylonite (Fig. 6-16 a and c), but in general the calc-mylonite display interchanging layers of fine-grained phyllosilicates, calcite and quartz, with shear bands further substantiating the sense of shear (Fig. 6-16 b and d). Directly below the calc-mylonite is a heavily veined quartzite with a steeply dipping transposed bedding (Fig. 6-15 e). The veins are generally sub-horizontal tension gashes and thus indicate a sub-horizontal  $\sigma_1$ . Further away from the calc-mylonitic fault core, the quartzite gradually becomes a fine-grained arkosic metasandstone (Fig. 6-15 g). It is asymmetrically folded around a sub-horizontal fold axis that trends NE-SW. The foliation/bedding planes contain a dip-slip striation and a sub-horizontal crenulation lineation, indicating flexural slip during folding. The fold is SE vergent with a c. 45° dipping axial plane, which also imparts a pervasive axial planar cleavage in the folded metasandstone (Fig. 6-15 f). Thin section analysis reveals that the metasandstone is rich in phyllosilicates and contains microstructures that indicate low to medium grade dynamic recrystallization, such as bulging grain boundaries and very fine grain size, probably formed by subgrain rotation recrystallization, (Fig. 6-16 e and f).





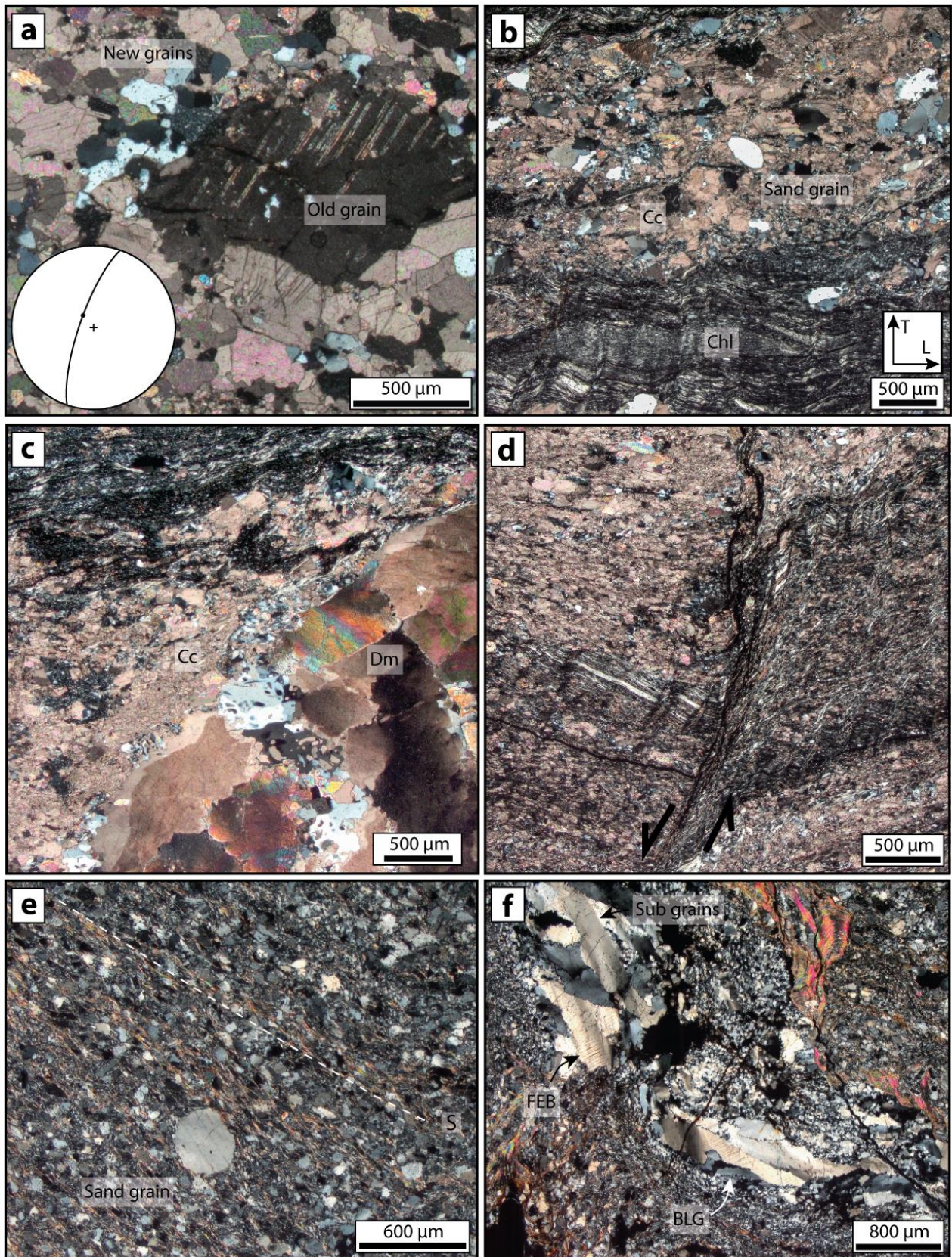
**Figure 6-14:** (a) Photomicrograph of the Beretsjord quartzitic breccia showing a relative pure quartzitic sandstone clast in a phyllosilicate-rich matrix. Quartz microstructures indicate low- to medium-grade dynamic recrystallization. X-pl. (b) Thin ultramylonites indicate back-thrusting. Host rock contains well-developed solution cleavage. (c) Shear bands offset a foliation parallel quartz vein embedded in a quartzite-hosted fault zone. (d) Quartzite breccia from Bertsjord, hand specimen for thin section in (a).





**Figure 6-15:** Field photographs from locality number three (Fig. 6-3). (a) Footwall metatuffs, possibly deposited by turbiditic flows. (b) Beretsjord Fault Zone calc-mylonite. Stereonet display the orientation of shear foliation and striations. (c) Openly folded hanging wall slate. Deformation increase towards the calc-mylonite. (d) Photograph showing the transect as explained in the text. (e) Stockwork veining in quartzite, indicating a fluid-rich deformation environment. (f) Axial planar cleavage for fold in (g). (g) Asymmetrically folded arkosic metasandstones.





**Figure 6-16:** Photomicrographs from the Beretsjorda Fault Zone (crossed polarizers and oriented as in b). (a) Remnant, “old” calcite grain surrounded by a mantle of fine-grained calcite derived from old grains. (b) Thin section from calc-mylonite in Figure 6-15 b (same for (c) and (d) as well). Fine-grained, crenulated phyllosilicate-rich horizons interlayered with relatively fine-grained quartz and calcite. (c) “Old” dolomite crystals breaking down to calcite and quartz. (d) Discrete shear bands deforming the mylonitic foliation. (e) Partially recrystallized arkosic metasandstones with some relict sand grains. (f) Quartz microstructures indicate low to medium grade dynamic recrystallization.



### 6.2.6 The Ausa Fault Zone (AFZ)

The Ausa Fault Zone (AFZ) is exposed at one locality (Fig. 6-3 and Fig. 6-17a) where it juxtaposes Vargsund dolostones in the hanging wall against an undifferentiated lithology tentatively interpreted as the Bierajavri Formation in the footwall (Fig. 6-17 a and c). The amount of strain in the deformed footwall prevents the confident identification of the protolith. The fault plane dips moderately to the WNW and display dip-slip stretching lineations (Fig. 6-17 a). Shear bands and small duplexes give invariably top-to-the ESE thrusting (Fig. 6-17 b, e and f).

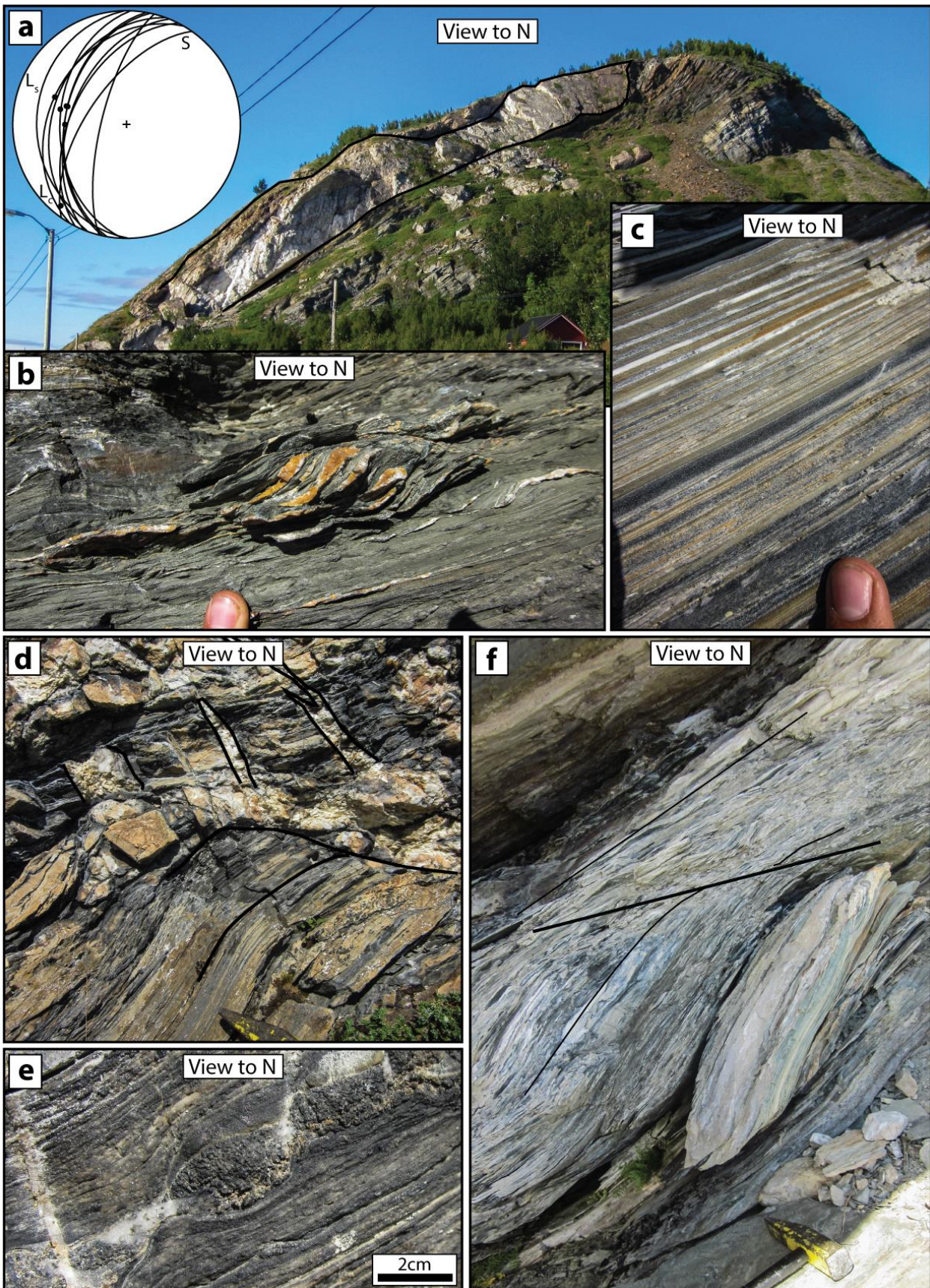
A section orthogonal to the AFZ is given below and can be followed in the conceptual Figure 6-18 c:

The lowermost exposed footwall contains a finely laminated carbonaceous slate with individual lamina ranging in thickness from < 1 mm to 10 mm and color ranging from gray to brown to white (Fig. 6-17 c). The sequence is more than 20 m thick. Generally, the rock is composed of fine-grained (20-50  $\mu\text{m}$ ) calcite derived from recrystallization of coarse-grained (> 600  $\mu\text{m}$ ) porphyroclasts (Fig. 6-18 a). The pervasive schistosity is derived from thin (c. 100-600  $\mu\text{m}$ ) horizons rich in phyllosilicates and locally amphiboles. Locally, centimetric veins are asymmetrically boudinaged with secondary calcite filling in the boudin neck zone (Fig. 6-17 e). The foliation planes are pervasively lineated and locally activated as faults that are coated with specular hematite with a high cobalt content (Fig. 6-18 b).

Above the carbonaceous slate is a rusty black slate that shows local, meter-scale imbrications along shallow dipping thrust faults generally accompanied by sub-horizontal quartz-carbonate veins (Fig. 6-17 d). Locally, though, the quartz-carbonate veins are themselves imbricated, suggesting multiple generations of veining and imbrication. Towards the main fault plane, the veining becomes less pervasive and the black slate becomes strongly foliated with rusty horizons. Dextral C' shear bands oriented with a shallow eastward dip becomes frequent towards the fault core. Locally, small dolomitic duplexes are observed (Fig. 6.17 b). There is a gradual transition from the rusty slate into a light gray-green, very fine-grained phyllonite with interchanging layers of more competent dolomite. The fault core is several meters thick and consists of a greenish phyllonite or consolidated gouge, possibly with a significant content of talc (Fig. 6-17 f). Some metric-scale C' shear bands are observed within the fault core and constrain top-to-the ESE movement. A large, pristine dolostone block is situated directly on top of the fault core (Fig. 6-17 a and Fig 6-18 c). The block is interpreted to be a large clasts within the fault zone as the foliation appears to drape around it.

Pervasive sub-vertical veining and fracturing occur throughout and point towards a late deformation episodes, possibly related to the Mesozoic extension (Fig. 6-17 d and Fig. 6-18 c).

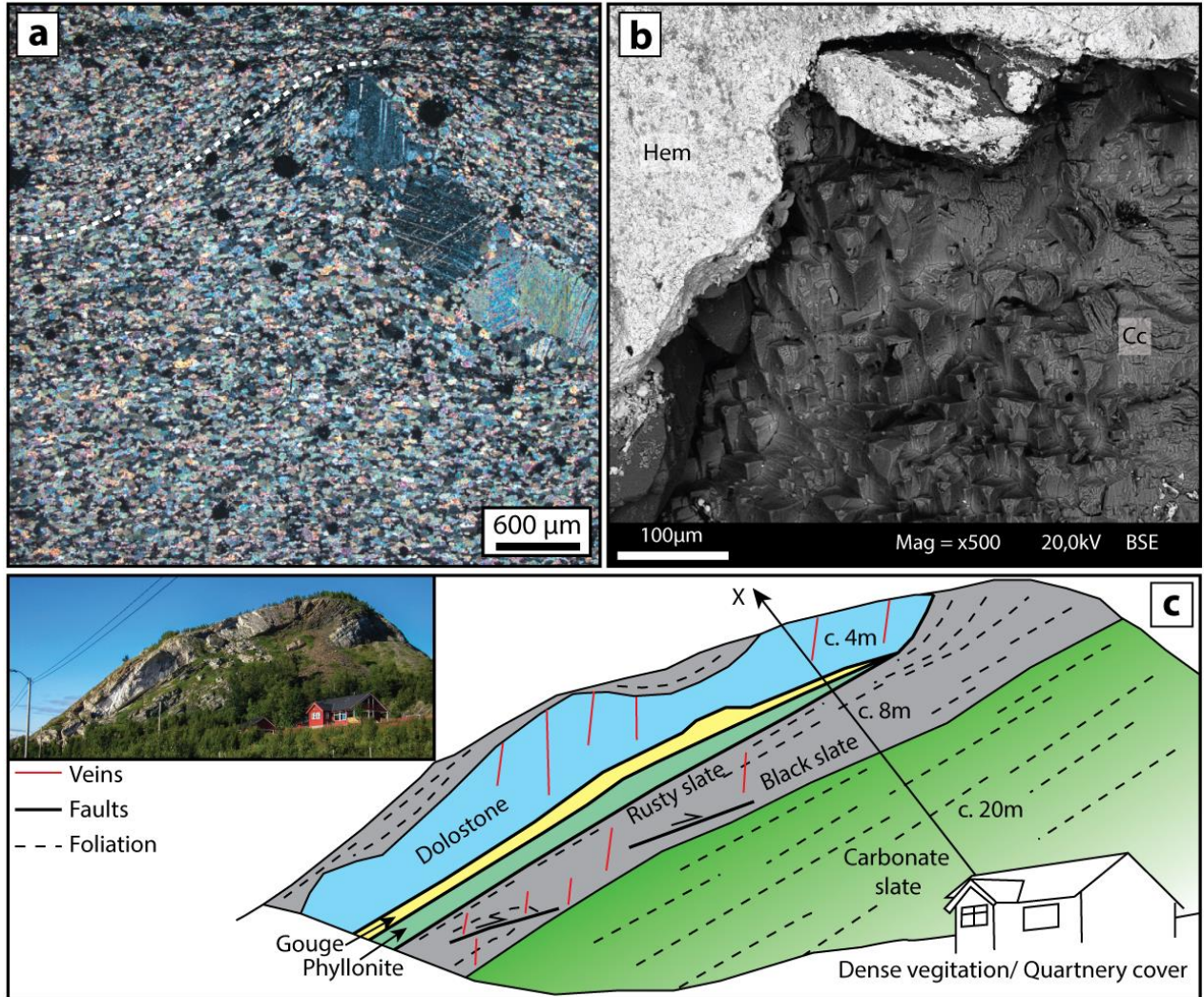




**Figure 6-17:** Key field characteristics of the AUSA Fault Zone. (a) Main outcrop of the AUSA Fault Zone. Lagre-scale dolostone clast outlined in black. Stereonet shows shear foliations and lineations. (b) Dolostone duplex in a rusty slate. (c) Fine-grained carbonaceous slate from the footwall. (d) Imbricated quartz-carbonate veins in small thrust cut by late sub-vertical veins. (e) Asymmetrically boudinaged vein. Sub-vertical vein crosscut everything. (f) Phyllonite/gouge with large scale C' shear band.



F

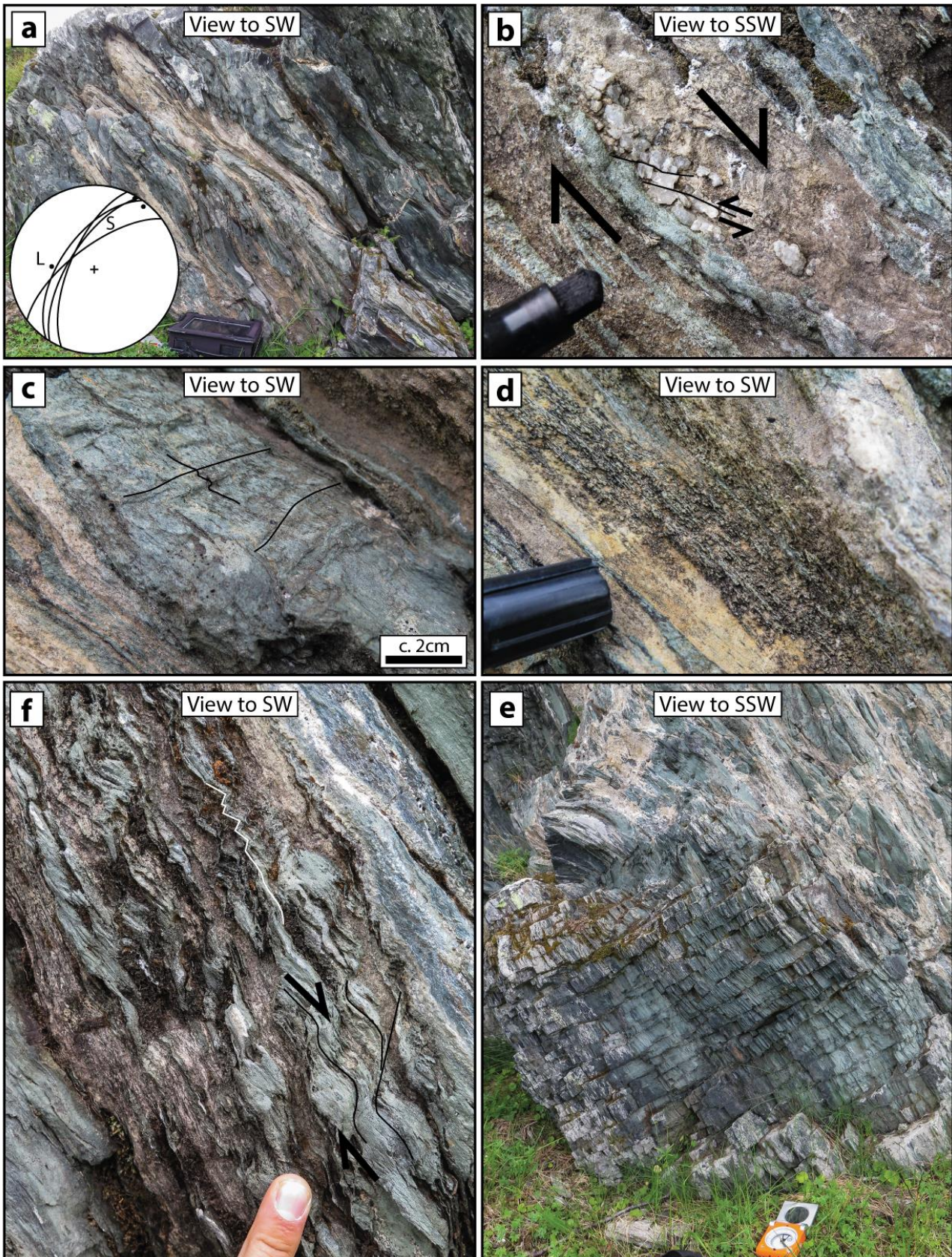


**Figure 6-18:** (a) Photomicrograph displaying the relict of coarse-grained calcite crystals that have partly recrystallized to fine-grained calcite. Foliation drapes the clast and grain size is generally larger in the strain shadows. X-pl. (b) BSE image of a fault plane coated with very fine-grained specular hematite (Hem; light gray). Euhedral calcite is found directly beneath the coating. (c) Schematic sketch of the AFZ showing the mapped lithologies and some structures. See text for further details.

### 6.2.7 Solhaugen Fault Zone (SoFZ)

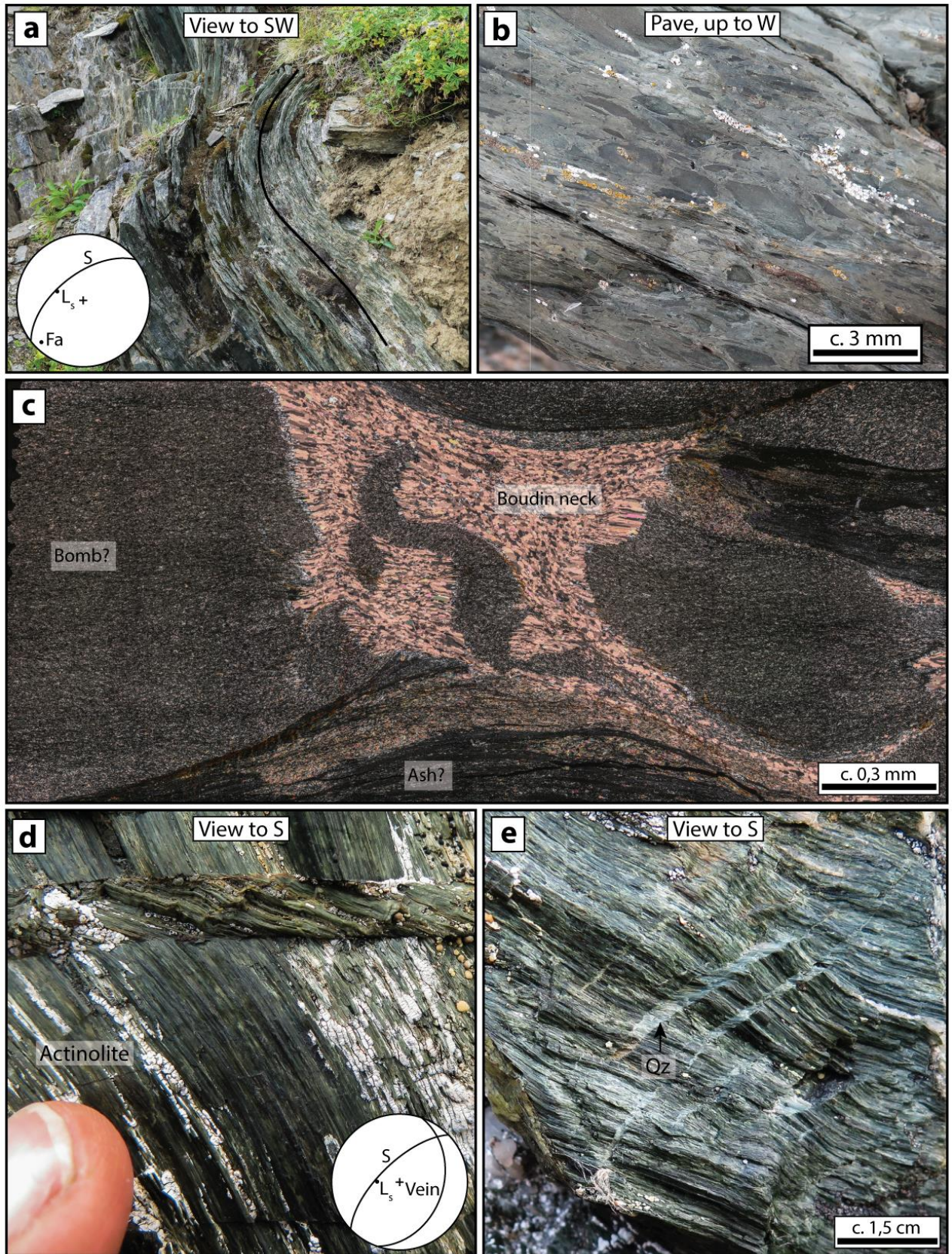
The Solhaugen Fault Zone is located between the BFZ and AFZ in the middle of the central PIS (Fig. 6-3) and juxtaposes graphitic slates in the footwall against metabasalts in the hanging wall. The fault strikes NE-SW and dips steeply towards the NW. Stretching lineations plunge moderately to the W, while the crenulation lineations are sub-horizontal (Fig. 6-19 a). Kinematic indicators, such as asymmetric folds and C' shear bands suggests that this is a normal fault with top-to-the W displacement. The fault constitutes a strongly deformed carbonaceous mélangé (Fig. 6-19 a) that pertain a strong foliation. Quartz veins are locally asymmetrically boudinaged (Fig. 6-19 b). Several greenstone clasts are observed and contain invariably a sub-horizontal crenulation lineation defined





**Figure 6-19:** Plate of field photographs showing key characteristics of the Solhaugen Fault Zone. (a) Fault zone mélange of smeared out calcitic and graphitic rocks. Stereonet show WNW-dipping shear foliation and W-plunging lineation. (b) Mosaic fragmented porphyroclast showing dextral movement. (c) Asymmetric crenulations displaying dextral movement. (d) Smeared out dolomitic and calcitic rock. Strung out quartz sticks out. (f) C' shear bands with related folds give normal movement. (e) Clast of graphitic slate within the fault rock.





**Figure 6-20:** (a) Asymmetric (drag) fold indicates dextral movement. Lination suggests a component of oblique slip. (b) Possibly bombs deposited in an ash flow. (c) Stitched photomicrograph of boudinaged bomb. X-pl. (d) Shear band in fibrous actinolite display sinistral movement. (e) Quartz fibers grown in a tension gash indicate relatively flat  $\sigma_1$ .



by asymmetric folds, also indicating normal movement along the fault (Fig. 6-19 c). Within some of the carbonaceous horizons an intricate network of elongated, foliation parallel quartz grains are observed. These are set in a dolomitic and calcitic matrix (Fig. 6-19 d). Domains characterized by fine-grained phyllosilicates are present throughout, and generally display well-developed C' shear bands and asymmetric folds that further constraining the normal movement along the SoFZ (Fig. 6-19 f). In addition to coarse-grained vein quartz, some large clasts of graphitic slate are present (Fig. 6-19 g).

No true fault core is observed within the SoFZ; however, close to the slate-greenstone contact the slate becomes strongly sheared with a pervasive foliation that is asymmetrically folded around a sub-horizontal, NE-SW-trending fold axis. Stretching lineations give dip-slip movement and the asymmetry suggests top-to-the NW normal transport direction (Fig. 6-20 a). Symmetrically boudinaged volcanic bombs embedded in a weak matrix, possibly reflecting ash as a protolith, are also found close to the contact (Fig. 6-20 b and c).

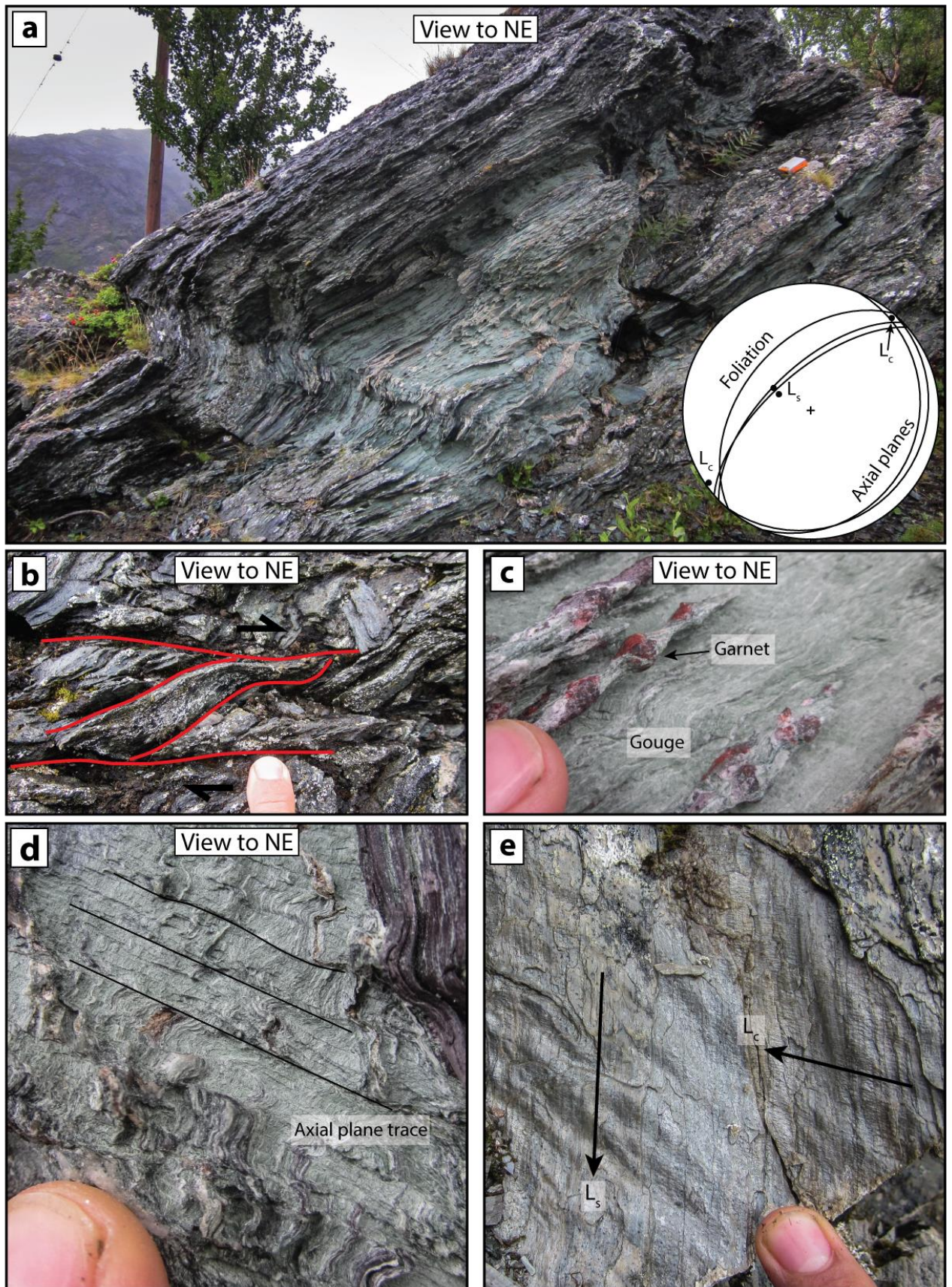
Within the immediate hanging wall of the SoFZ, a discrete fault zone with similar orientation is present. This fault is interpreted to be the same as the SoFZ due to the geometric relationship between the two, however, this fault gives exact opposite kinematics, top-to-the east. The fault is characterized by domains of coarse-grained actinolite needles that individually measure several centimeters in length. Some of these have been deformed and provide excellent strain markers (Fig. 6-20 d and e) indicating compression and top-to-the E sense of shear. The fact that this is a reverse fault is further substantiated by several shallowly dipping hybrid tension gashes filled with fibrous quartz indicating top-to-the E movement (Fig. 6-20 e).

### **6.2.8 Gjevebukta Fault Zone (GFZ)**

The Gjevebukta Fault Zone (GFZ; Fig. 6-3) is one of the outermost faults within the PIS. The fault duplicates Nussir greenstones and is exposed for c. 2 kilometers. The fault plane dips moderately to steeply towards the NW with dip-slip stretching lineations and sub-horizontal crenulation lineations (Fig. 6-21 a and e).

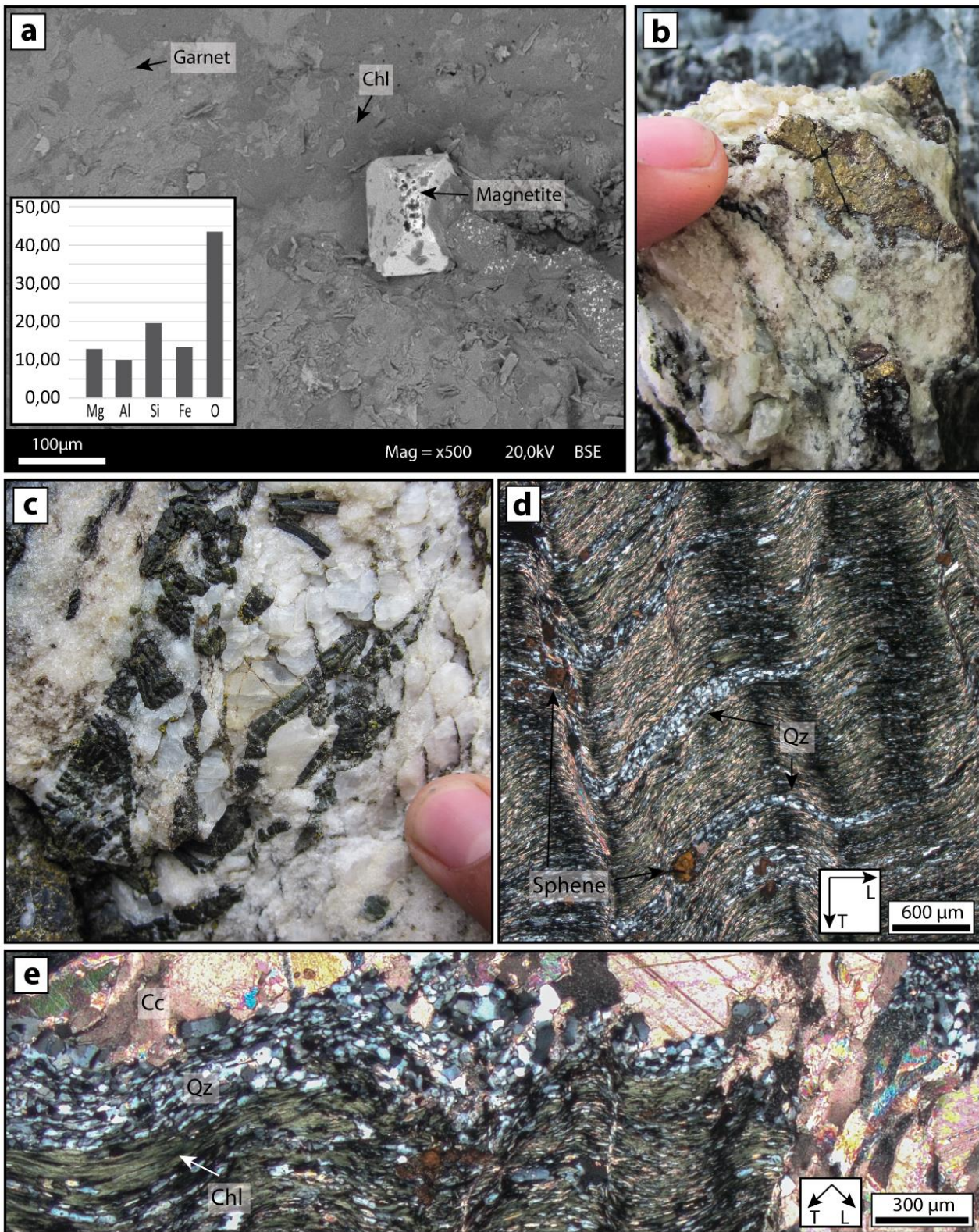
The fault is characterized by domains rich in very fine-grained phyllosilicate that form a relatively chaotic mélangé with some intercalated horizons of thin, more competent domains. The interpreted fault core is approximately 40 cm thick and consists primarily of very fine-grained, phyllosilicate-rich, consolidated and foliated “gouge” (Fig. 6-21 a and c). Within the core there are thin layers (< 1 cm) of quartz and calcite, together with red garnets that appear to be inherited from the greenstone protolith (Fig. 6-22 a).





**Figure 6-21:** Main field characteristics of the Gjevebukta Fault Zone. (a) Asymmetrically folded fault zone displaying dip-slip stretching lineations and sub-horizontal crenulation lineations. (b) S/C shear bands constrain top-to-the SE sense of shear. (c) Red Fe and Mg-rich garnets within a consolidated gouge. (d) Axial planes show solution cleavage. (e) The immediate footwall is comprised of phyllite.





**Figure 6-22:** (a) Garnet chemistry constrained from qualitative EDS analysis. Euhedral magnetite crystal grows on the garnet. (b) Quartz-carbonate pegmatite contains large amounts of sulfides. (c) Locally, coarse-grained actinolite has grown within veins in the immediate footwall of fault. (d) A crenulation/solution cleavage cuts the slaty cleavage at a high angle. Relatively coarse-grained sphene overgrows the slaty cleavage. X-pl. (e) Where quartz-carbonate veinlets cut the slate a halo of chloritization occur at the contact. X-pl.

## 6. Structural analysis of the mapped area

The immediate footwall and hanging wall consist of crenulated phyllites rich in *S/C* shear bands, indicating thrusting with top-to-the SE (Fig. 6-21 b). The fault is folded asymmetrically around a sub-horizontal fold axis with a pervasively developed axial planar cleavage that dips gently towards the SE (Fig. 6-21 a and d). Axial planes preserved in the phyllite are locally activated as small-scale thrusts with < 1 cm displacement, possibly to accommodate strain in relation to the fold structure. These axial planes also define a solution cleavage in the rock (Fig. 6-21 d and Fig. 6-22 d, e).

Some mineralizations are associated with the fault. These are found in the immediate footwall of the fault in quartz-carbonate-actinolite pegmatites (Fig. 6-22 b and c). Most of the sulfides observed are pyrite and chalcopyrite.

In thin section, the phyllite found in the immediate footwall (Fig. 6-21 e) consists of a very fine-grained white mica, chlorite, epidote, and possibly some biotite forming a pervasive slaty cleavage (Fig. 6-22 d). Layers of fine-grained (10-50  $\mu\text{m}$ ) quartz are present parallel to the slaty cleavage. A secondary asymmetric, zonal crenulation cleavage with local evidence for dissolution is oriented about orthogonal to the slaty cleavage (Fig. 6-22 d). Interspersed within the foliation are relatively large c. 50 – 400  $\mu\text{m}$ , brown, anhedral, sphene crystals that appear not to be affected by the crenulation and solution cleavage. Some of the crystals are pulled-apart with fibrous quartz growing orthogonal to the fractures. Veinlets of very fine-grained quartz at the veinlet walls and coarse-grained calcite in the center appear parallel to the slaty cleavage of the rock and are generally defined by a chloritized halo (Fig. 6-22 e).





## 7. Discussion

### 7.1 Structural evolution of the PIS

This section discusses the formation and complex structural evolution of the PIS, first by considering the described folding history in the RTW, before analyzing some of its key aspects such as timing and spatial-temporal development. Finally, a conceptual model of the PIS is proposed.

#### 7.1.1 The folding history of RTW

The unraveling of the complete folding history of the RTW is a difficult task given the coaxial nature of the Svecofennian and the Caledonian deformation events and the progressive evolution of the stress field during both of these tectonic episodes. In an effort to make the folding history manageable, the individual fold generations, as proposed by Pharaoh et al. (1983) and Viola et al. (2008) are charted in a Table 3 together with the fold analysis and interpretation proposed in this thesis. All in all, the folding phases proposed in this thesis are in agreement with what Pharaoh et al. (1983) and Viola et al. (2008) describe. Pharaoh et al. (1983) focused his description of the Caledonian folding phases to the Lomvatn Formation (Tab. 3), an autochthonous Neoproterozoic cover beneath the KNC that was strongly deformed during the Caledonian orogeny.

Pristine  $F_1$  folds are most common in the interior of the RTW where they trend NE-SW with a shallow dip and upright axial planes. All authors agree upon this folding phase.  $F_1$  folds can locally be observed within the PIS, although then they are generally structurally reworked and show different geometries (Fig. 7-1 and Fig. 7-2), as shown by the Langvasstind- and Skinnfjellet anticline (Fig. 3-1; 12 and 5 respectively). These are both interpreted as structurally reworked  $F_1$  folds that have been tightened asymmetrically during the Caledonian Orogeny. The Langvasstind anticline is located farther to the NW and is therefore more strongly reworked than the Skinnfjellet anticline, as seen from the generally more upright trend of the latter (Fig. 7-1 and Fig. 7-2 b). Indeed, structural analysis reveals that the axial planes become progressively more steep when moving from the NW towards the SE, as visualized in Figure 7-3. Viola et al. (2008) and Pharaoh et al. (1983) linked the Skinnfjellet anticline to a  $F_2$  folding phase, related to  $D_1$ . It is proposed, however, that this  $F_2$  is the progressive refolding of  $F_1$  structures, as described above, during  $D_2$  Caledonian compression. In the scheme proposed above this folding phase is called  $F_{3-a}$  (Tab. 2).



**Table 3:** Overview of previously reported folds from the RTW. Pharaoh et al. (1983) in orange, Viola et al. (2008) in green and this thesis in blue. See text for further details.

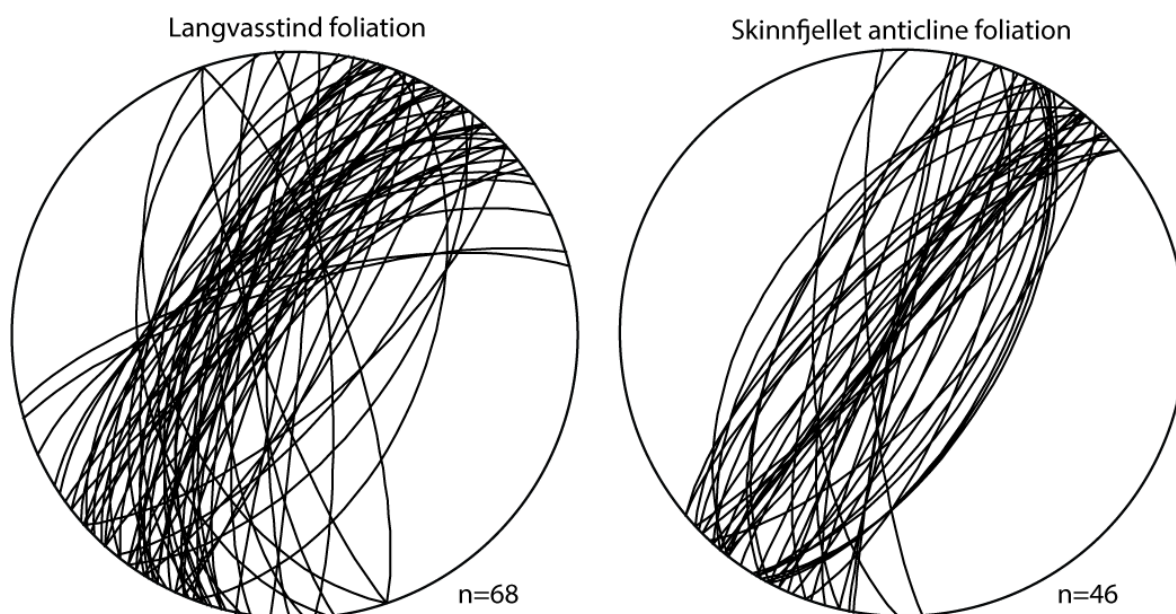
<b>F<sub>n</sub></b>	<b>D<sub>n</sub></b>	<b>Geometry</b>	<b>Wavelength</b>	<b>Fold axis</b>	<b>Axial plane</b>	<b>Locality</b>
1	1	Open - tight	-	Horizontal NE-SW	Upright	Porsa Gr
2	1	-	-	-	Steep dip towards SE	Holmvatn
3	2	Tight	-	Shallow NE (variable plunge)	Steep dip towards NW	Lomvatn
4	2	Kink-bands	-	NE-SW	-	Lomvatn?
5	2	Gentle	-	SW-NE	-	Lomvatn
1	1	Open - tight	-	-	Upright	Saltvatn Group
2	1	Tight - isoclinal	-	SE-NW moderately	Upright to inclined (NW)	Skinnfjellet anticline
3	2?	-	Kilometric	NE moderately	-	-
4	2	-	-	-	Sub-horizontal	-
1	1	Symmetric Open	Kilometric	NE-SW to ENE-WSW gentle	Upright	Saltvatn Group
2	?	Asymmetric Tight to isoclinal	Meter	NE to NNE moderate to steep	Vertical to reclined	Window and PIS
3-a	2	Symmetric-asymmetric Open to close	10's – 100's of meters	NNE to NE gentle - moderate	Upright to inclined	Porsa Gr. Skinnfjellet
3-b	2	Asymmetric Open to tight	Meter	NE-SW sub-horizontal	Moderate SE dip	Faults within PIS
3-c	2	Symmetric Gentle to open	Centimeter	NE-SW sub-horizontal	Sub-horizontal	Everywhere
4	3/4	Asymmetric Open to tight	Meter to millimeter	NE-SW sub-horizontal	Moderate to gentle SE dip	Faults within PIS

The  $F_2$  folds reported herein are thought to be related to a dextral transpression event (Torgersen, 2015; Viola et al., 2008) and are observed at several localities within the RTW, such as the Skifergangen mine in the southeastern part (Smeplass, 2013) and in the Porsa mine located within the southernmost exposed part of the PIS (Torgersen, 2015). These folds correspond to  $F_3$  folds in Viola et al. (2008). The timing of this folding history is not well constrained and is discussed further in section 7.1.2, below.

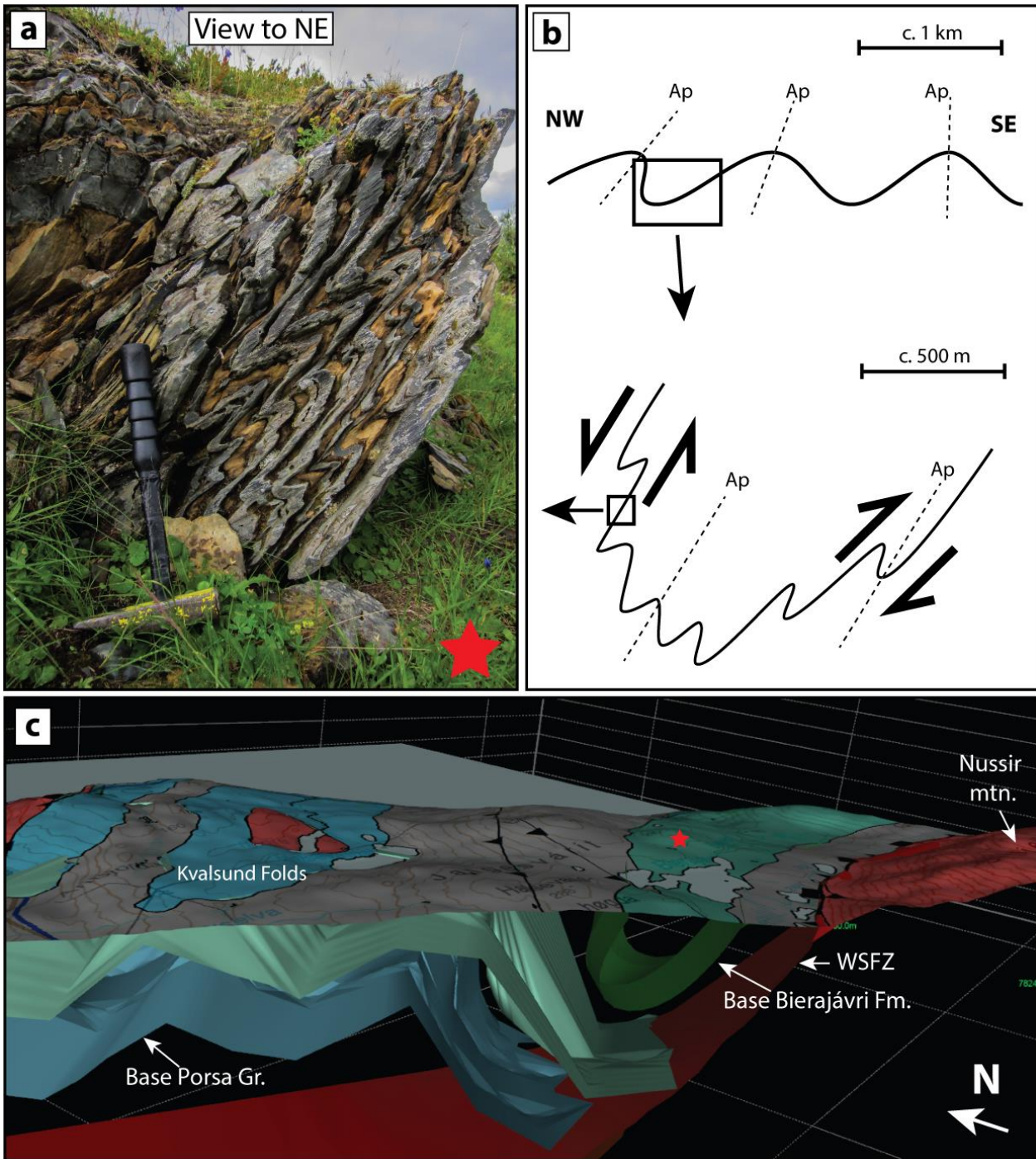
Pharaoh et al. (1983) observed a  $F_4$  folding phase composed of kink bands within the Lomvatn Formation. These have not been observed within the study area of this thesis.

Both authors propose a folding phase that created gentle folds with sub-horizontal axial planes (Viola et al., 2008) with SW-NE fold axis (Pharaoh et al., 1983). This folding phase corresponds to  $F_{3-c}$  in this thesis and is interpreted to be due to vertical loading as the nappes were emplaced.

The  $F_4$  structures proposed herein are localized deformation structures generally found within specific fault zones that have been reactivated normally. The reactivation may be associated with post-Caledonian orogenic collapse, or with Paleozoic and Cretaceous extension as have been constrained by radiometric dating of authigenic illite (Torgersen et al., 2014). The  $F_4$  folds are not described by either Pharaoh et al. (1983) or Viola et al. (2008), but they have been recognized by Torgersen and Viola (2014; see section 7.1.5).

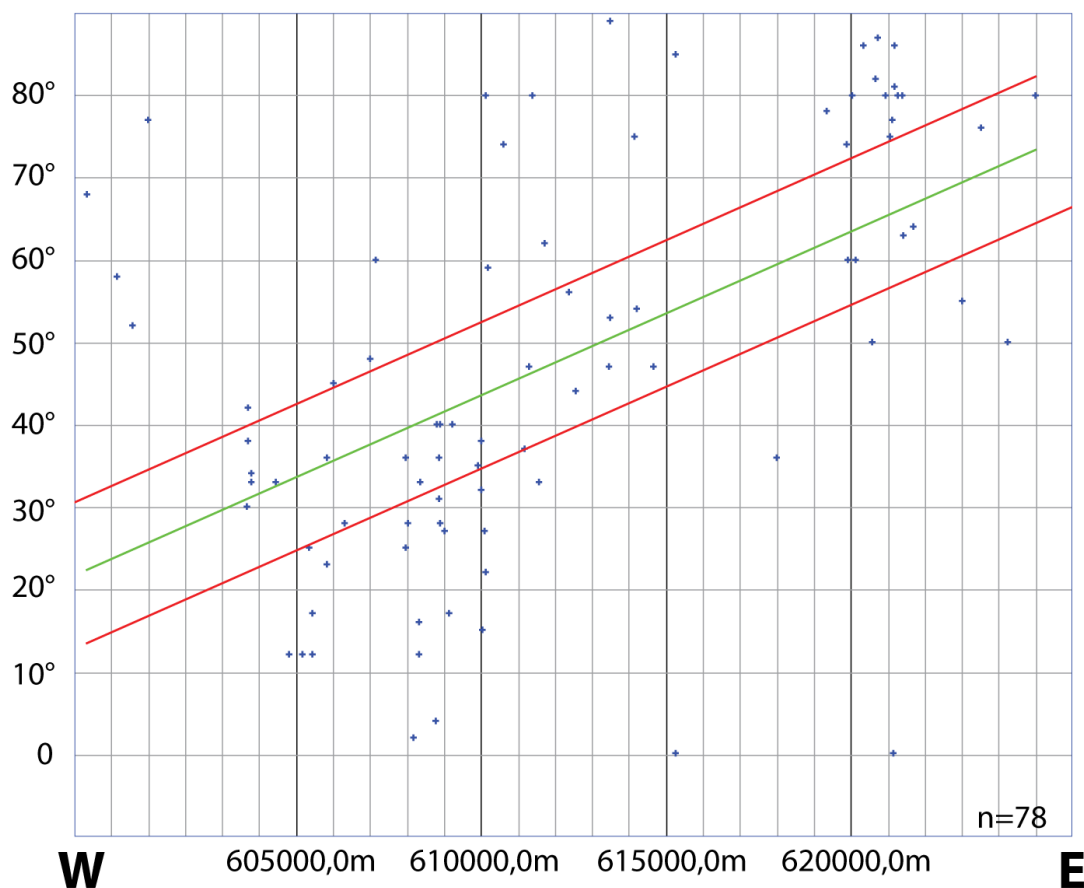


**Figure 7-1:** Stereonets displaying foliation measurements of the Langvasstind (left stereonet) and Skinnfjellet anticlines (right stereonet). The foliation at Langvasstind is generally more inclined due to the geographic position, which is closer to the NW and thus underwent a more pervasive Caledonian reworking.



**Figure 7-2:** (a) Parasitic  $F_1$  folds that have been structurally reworked by  $F_{3-a}$  folds and are now overturned. (b) Axial planes have a shallower dip in the NW part of the PIS (see also figure 7-3) because of the larger influence of Caledonian structural reworking. (c) 3D model made using Move (Midland Valley) show the overturning of the reworked  $F_1$  fold. Red star indicate locality for photograph in (a).





**Figure 7-3:** Dip of axial planes (y-axis) plotted against geographic coordinates (from west to east; x-axis). Green line is the regression line. Red lines show the 90% range. The axial planes are measured by Espen Torgersen and the author.

### 7.1.2 Dextral transpression

Viola et al. (2008) was the first to propose a model where an episode of dextral transpression is a key aspect of the geological evolution of the RTW. The model is based on observations of dextral strike-slip faults throughout the window and the overall shape of the frontal part of the PIS, which forms a dextral “shear clast”. Smeplass (2013) described in detail one of these dextral, strike-slip shear zones from the eastern part of the window and Torgersen (2015) described a set of strike-slip associated mineralized veins from within the PIS. Fieldwork conducted for this thesis shows several folds with moderately to steep fold axis throughout the PIS. One locality, close to the GFZ, shows dextrally folded dolomite with a NE-trending, steeply plunging fold axis and a steeply dipping axial plane (Fig. 6-2 b), that does not correspond to any of the classic PIS folds that generally show relatively shallow fold axes and moderately dipping axial planes. Similar observations have been done in Kvalsundalen (Fig. 3-1; 10) and in the Kvalsund triangle (Fig. 3-1; 1)

The timing of the transpression event is still largely unaccounted for and reflects the difficulty of directly dating fabrics and structures of rock volumes deformed coaxially by two major deformational

episodes. However, Viola et al. (2008) proposed that the transpression is essentially syn- to post-Caledonian and related to either 1) Post PIS shearing, or 2) early PIS development where strain partitioning caused a component of dip-slip top-to-the NE thrusting and a component of dextral strike-slip. Smeplass (2013) also proposed a Caledonian age for the transpression based on K-Ar dating of a thrust that is proposed to have formed under the same stress conditions as the strike-slip fault. Torgersen (2015), on the other hand, have constrained a transpression event to be likely Paleoproterozoic ( $2069 \pm 14$  Ma) based on previously unavailable geochronological results such as Re-Os isotopic dates from sulfides deposited in syn-transpression mineralized veins. This age indicate that the transpressive event predate the Svecofennian orogeny at c. 1840 Ma (Pharaoh et al., 1982). Field relations, however, such as the asymmetry of the WSFZ observed in the geologic map (Fig. 4-3) and also proposed by Viola et al. (2008) suggest that the early D<sub>1</sub> structures are reworked by a later dextral transpressive event, possibly indicating that there has been several events with components of dextral transpression. In order to constrain this theory, more focused fieldwork and geochronological work would be favorable. In addition, the folded dolostone layer, interpreted to be a F<sub>2</sub> fold (Fig. 6-2 b), indicate very different deformation conditions than what is constrained for F<sub>3</sub> folds, which tend to deform dolostone by frictional processes or assisted by severe chemical alteration (see section 7.2.1 and 7.2.2). The folded dolostone layer described above, however, deformed by viscous mechanisms suggesting higher-grade environmental condition than is generally constrained for the development of the PIS.

### **7.1.3 Thrust development and their evolution**

#### **7.1.3.1 Décollement vs. solitary thrusts**

Foreland fold-and-thrust or thrust belts commonly deform foreland to foredeep sediments, without basement rock involvement. Classical examples of such thin skinned thrust belts are the Jura mountains in Germany (e.g. Becker, 2000) and parts of the Zagros mountains in Iran (e.g. McQuarrie, 2004). These belts generally contain a thick and weak layer (evaporites or argillaceous rocks) at the base of the belt, where a basal décollement or detachment fault may localize (e.g. Allen and Allen, 2013; Davis and Engelder, 1985) and accommodate large amounts of strain, thus steering the first order geometric and kinematic evolution of the entire belt (Chapple, 1978). Storti et al. (2003) investigated what role the décollement properties may play on the structures of a large thrust imbricate in Gibraltar, where parts of the basal layer are a competent horizon of limestones while the central part is an incompetent, viscous décollement of evaporites. The frictional domain was completely dominated by foreland verging thrust faults and back-thrusts were scarce to non-present. Above

viscous décollements, on the other hand, back-thrusts and fore-thrusts are abundant and close to equally common (Davis and Engelder, 1985). Another feature of viscous décollements is the delocalization of deformation, i.e. more intense folding (Simpson, 2009; Storti et al., 2003), such as fault propagation folds, fault bend folds and detachment folds (e.g. Fossen, 2010; Simpson, 2009). Such large-scale folds are not observed within the PIS; rather, foreland verging thrust faults completely dominate the PIS, indicating that a thick, incompetent décollement horizon comprised of e.g. salt is unlikely to be the controlling factor of the structures observed at the surface. Instead, a relatively strong décollement horizon could help explain the nearly complete absence of hinterland verging thrusts, as well as the absence of fault related folding (Fig. 4-5).

The PIS contains several lithologies that are relatively weak, such as the Krokvatn Formation (fine-grained volcanogenic metatuffs), Kvalsund Formation (fine-grained graphitic slates) and Bierajávri Formation (fine-grained volcanogenic metatuffs and tuffites) that could act as a mechanically weak décollement horizon. Mapping of the PIS, however, (Fig. 4-3) show a pervasive duplication and repetition of greenstone levels, but rarely of the Kvalsund and Bierajávri formations. Therefore, the regional decollement (if present) must reside at a deeper level than the Kvalsund and Bierajávri formations. Furthermore, Saltvatn Group sediments are not observed within the PIS, indicating that the thrust faults do not cut down through the Saltvatn Group. A reason for this may be the strong competence contrast between the Saltvatn Group (e.g. the lowermost continuous Ulverygg metasandstone) and the Krokvatn Formation, which generally overly the Ulverygg Formation due to the inferred limited lateral continuity of the Dypelv, Stangvatn, and Gorahatjohka formations (Fig. 4-4). This implies that the Krokvatn Formation is the best candidate to have acted as a weak layer, possibly even as décollement, accommodating a significant amount of shortening (Fig. 7-4). In order to prove this theory, however, deep drill holes and/or deep seismic imaging would be necessary.

### 7.1.3.2 Dynamic evolution of the thrusts

Another interesting issue of the PIS development is the dynamic evolution of the thrusts, that is, how they evolved through time in response to varying deformational conditions (strain, temperature, fluid availability, strain rate etc.; Fig. 7-5). Viola et al. (2008) and Torgersen and Viola (2014) proposed that the PIS faults nucleated on the limbs of inherited Paleoproterozoic folds that were increasingly tightened and underwent flexural slip (Fig. 7-4 and Fig. 7-5) as a consequence of Caledonian shortening. The refolding could be due to the presence of an southeastern buttress, a rigid block of competent metasediments previously uplifted by the SFZ, (Fig. 7-4). This process would most likely have lead to the formation of solitary thrusts, as the faults formed individually at a high angle along fold limbs (Fig 7-5). Most of the thrusts within the PIS, however, show significant displacement and



hence, flexural slip alone might not be sufficient to explain the observations. In addition, it is generally believed that propagation of thrusts (as constrained by e.g. fault propagation folds) occur from the deep, towards the surface (e.g. Boyer and Elliott, 1982; Butler, 1982, 1992). This suggests that the thrust faults nucleated and localized in the deforming Krokvatn Formation and branched up from the décollement, exploiting the already weakened limbs of folds that had previously undergone flexural slip (Fig. 7-4 b and Fig. 7-5) and thereby connecting the fold limbs with the weak basal layer (Fig. 7-4 c). Another indication in support of this model is the lack of a hinterland verging fault or foliation along the southeastern flank of the Langvasstind anticline (Fig. 3-1; 12), which indicate that the fault responsible for the superposition of Nussir metabasalts on top of Kvalsund- and Bierajávri formations metasediments in the Kvalsunddalen is a foreland verging thrust (Fig. 4-3 and Fig. 4-5).

The switch in deformation mechanism from continuous-, (Fig. 7-5 a, b), to discrete deformation (Fig. 7-5 c) might have been caused by several governing factors such as: 1) progressive weakening of the lithologies in areas directly surrounding the fold limbs due to fluid infiltration (Cosgrove, 1993), 2) increasing strain rates in the basal décollement causing strain to localize in the hanging wall block, and 3) insufficient temperature to fold the lithologies, with the result that folds locked up and thrusts initiated. Furthermore, folding alone as the dominating deformation process in a fold-and-thrust belt is generally considered rare and is only reported from e.g. parts of the Zagros belt in Iran where the décollement is a thick layer of salt (Fakhari, 1994; In: Simpson, 2009). In order to obtain folding as the dominant deformation mechanism, a significant number of mechanical conditions are required, such as a very weak (salt) and thick décollement (Erickson, 1996; Simpson, 2009).

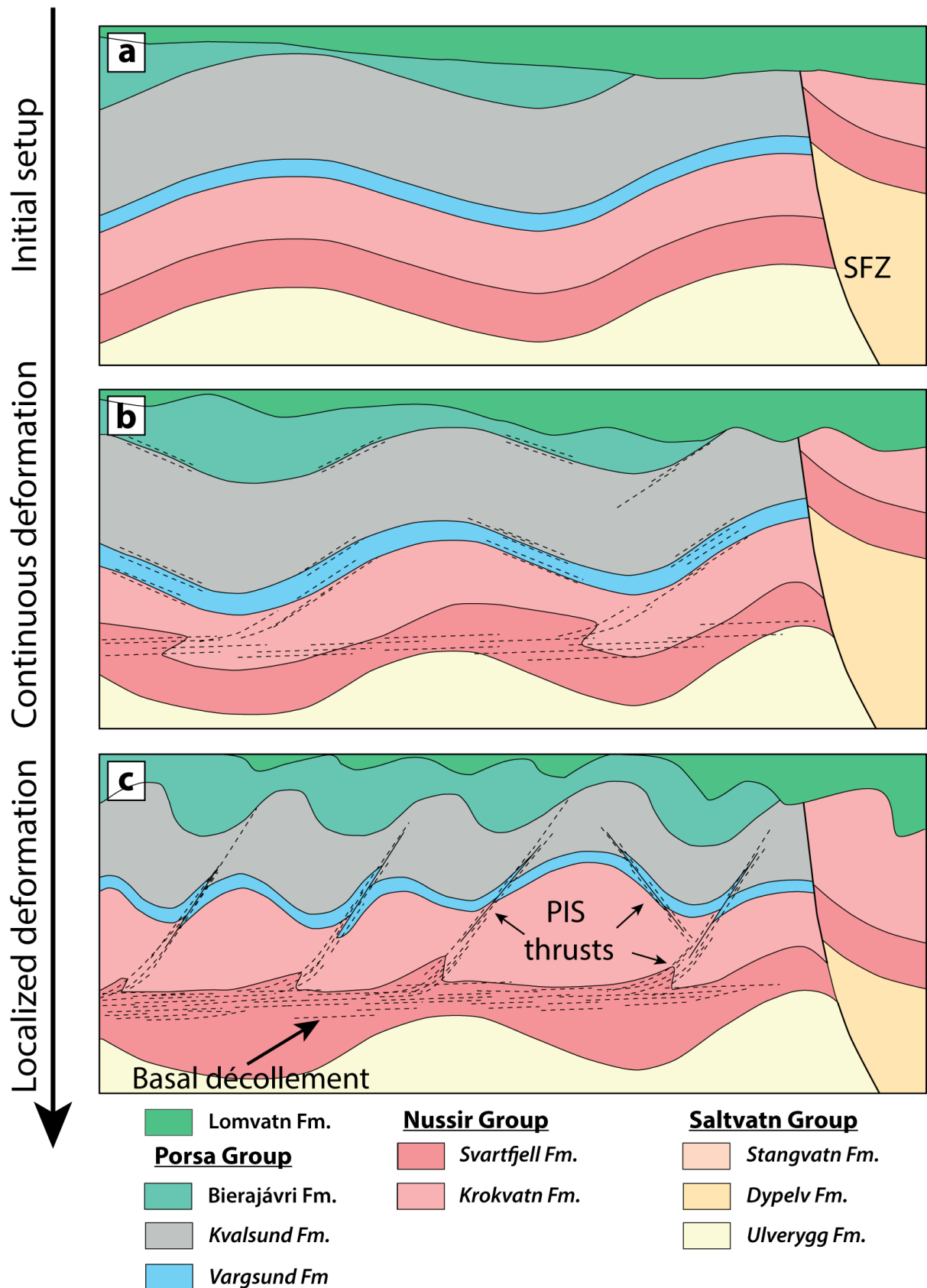
The model above is in agreement with the current theory on fault propagation, constrained in many fold-and-thrust belts from the presence of fault propagation folds, which generally constrain an upward propagation of faults (e.g. Eisenstadt and De Paor, 1987; McClay and Buchanan, 1992). Therefore, it is proposed that the thrusts within the PIS do indeed fan up from a relatively weak basal layer, at the contact to a relatively more competent lithology creating a necessary competence contrast to accommodate large amounts of strain. However, whether there was a complete decoupling or not remains uncertain. Furthermore, it is proposed that the shape of the thrusts are generally listric, which is in accordance with Coulomb theory when dealing with strong detachments, although, this is not systematically examined (Buiter, 2012).

### 7.1.3.3 Dolostone deformation

Evidences for a prolonged deformation history of dolostones are observable within the PIS (Fig. 7-6). The layer of Vargsund dolostones draping the Skinnfjellet anticline display parasitic folds generated through  $D_1$  and  $D_2$  episodes. Locally they are brecciated in the limbs of larger fold structures (Fig. 7-6 a). This is interpreted to be stage one of the dolostone deformation, when the other lithologies underwent flexural slip the dolostone was deforming by brittle deformation mechanisms, which is also constrained by Torgersen and Viola (2014). The brecciation likely opened the lithology for fluids and thereby facilitating chemical breakdown of the rock (see section 7.2.2.1). This led to grain size reduction, growth of weak phyllosilicates and progressive localization of strain until the rock could deform as a calc-mylonite (Fig. 7-6 b), mainly because of the greatly reduced friction of the phyllosilicates, such as talc (e.g. Torgersen and Viola, 2014; Viti and Colletini, 2009). Locally, these calc-mylonites are asymmetrically folded (Fig. 7-6 c), with axial planes suggesting top-to-the SE thrusting, thus suggesting that the folding of the fault zones is a progressive step in the evolution of the PIS thrusts, possibly a response to increasing temperatures and decreased strain rates as the nappe emplacement progressed.

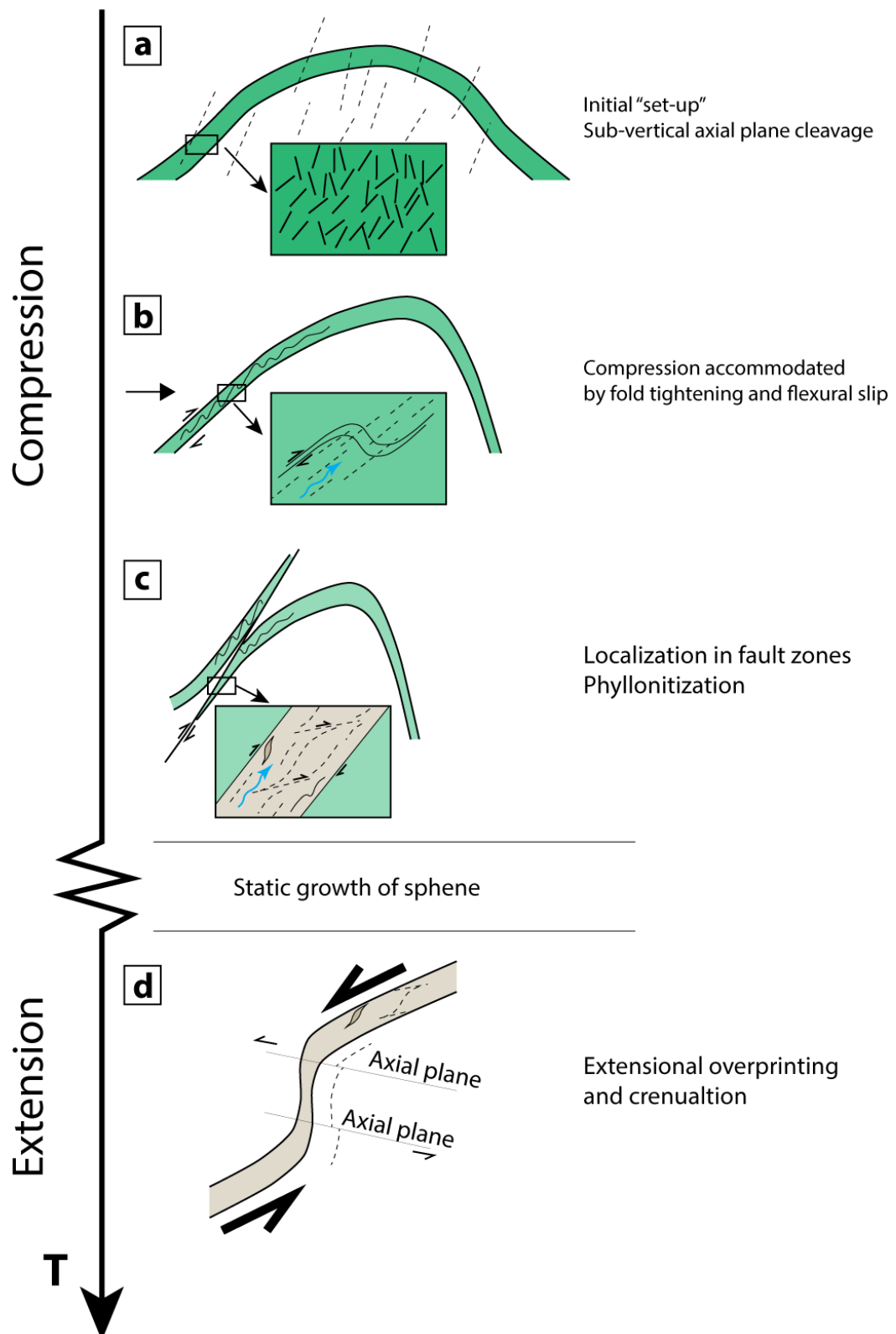
### 7.1.3.4 Major deformation structures within the PIS

Butler (1982) define three main localized deformation structures within fold-and-thrust belts: 1) Imbricate stacks, 2) Flat-ramp-flat structures, and 3) Duplexes. The formation and parameters governing the formation of these structures in systems with multiple décollements were investigated by Feng et al. (2015), which found that there were a strong dependence on décollement overlap where imbricate stacks formed when there were a  $> 15$  km gap between the décollements. In the PIS, the décollement candidates (Krokvatn, Kvalsund and Bierajávri formations) overlap significantly. With this in mind, and the fact that the present day orientations of the PIS faults are generally very steep, it is suggested that the PIS, at least at one stage, formed a duplex with the Krokvatn Formation as the floor thrust and a roof thrust at some level and possibly as high as the KNC basal detachment (see section 7.1.6).

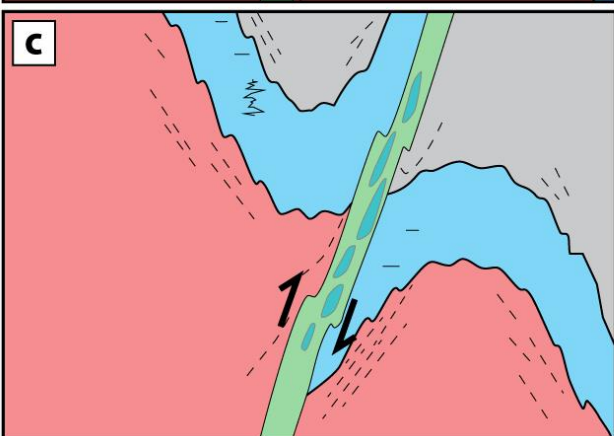
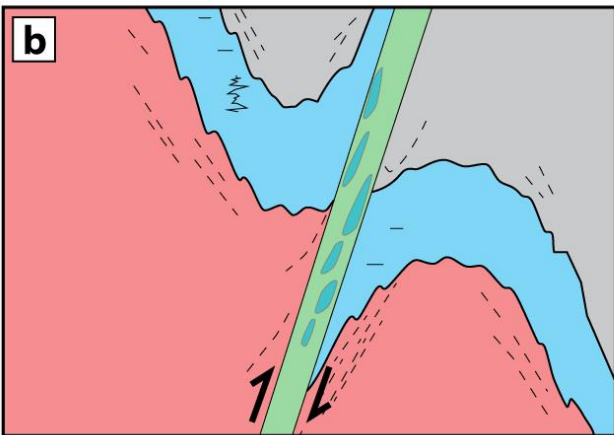
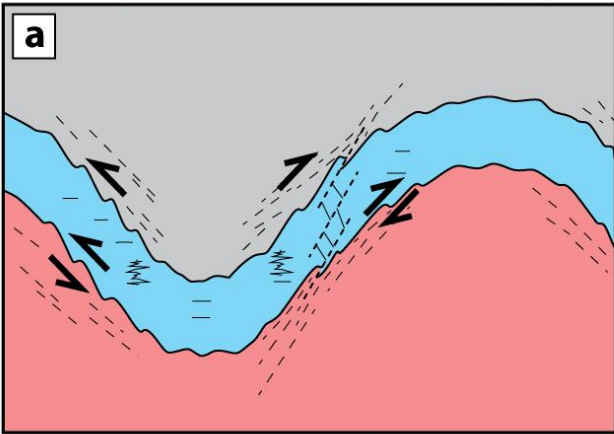
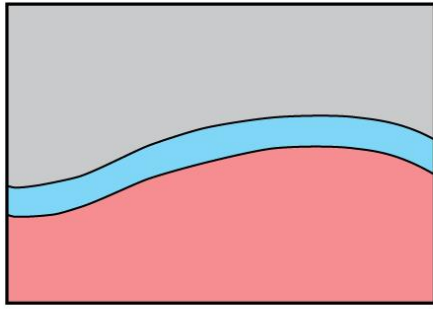


**Figure 7-4:** Simplified model of thrust development within the PIS. (a) Initial set up: Layers are openly folded and sediments are uplifted by the SFZ. (b) Decoupling along the Krokvatn Formation cause buckling and further tightening of the inherited folds. Saltvatn metasediments southeast of the SFZ function as a buttress. (c) Thrusts nucleate within the Krokvatn Formation and branch up, exploiting the sheared fold limbs.





**Figure 7-5:** (a) A pervasive axial planar cleavage developed during  $D_1$ . (b) Fold tightening led to flexural slip along the fold limbs, channelizing fluids along the foliation planes, causing reaction weakening. (c) Strain localization occurred when the rocks were weak enough to generate interconnected networks of phyllosilicates. (d) Some of the faults were reactivated normally. Locally the fault zones were folded and axial planar cleavages overprinting statically grown sphenes crystals (see fig 6-22 d).



**Figure 7-6:** Top: Initial, pre-Caledonian set up. (a) The dolostone layer acted as a relatively rigid layer during initial deformation and was brecciated while the other lithologies most likely were deforming by folding. This increased the permeability of the rock and promoted weakening reactions. (b) Weakening mechanisms caused strain to be accommodated and calc-mylonites to be progressively developed. (c) Increasing temperature and/or strain rate may have caused folding of the calc-mylonites during progressive nappe emplacement.

### 7.1.4 Timing of deformation along the SFZ

The SFZ is a major structure in the RTW, separating the PIS and the central parts of the RTW (Fig. 4-3). Unfortunately, the degree of exposure is very little and together with rough terrain, the observations and analysis could not provide entirely conclusive evidence for the below discussion, which should be taken as a preliminary working hypothesis.

The thickening of the Dypelv, Stangvatn and Gorahatjohka formations, in addition to their absence on the SE flank of the Ulverygg anticline, indicate syn-deformational deposition of the sediments in a fault bound basin (Fig. 4-4) between c. 2.13 and 2.05 Ga (Torgersen, 2015). The normal fault responsible for the basin formation is interpreted to be the precursor of the SFZ, which remained a weak link in the stratigraphy of the RTW and were reactivated during subsequent deformation episodes.

A subsidiary strand of the SFZ was dated by Torgersen (2015) by K-Ar on authigenic illite to  $584 \pm 12$  Ma ( $< 2 \mu\text{m}$  fraction), indicating an early Caledonian age for the reactivation of the fault zone.

In the present day orientation, the SFZ is mechanically highly misoriented as it displays dip-slip striations on a sub vertical fault plane with kinematic indicators suggesting top-to-the NW thrusting. However, if the fault developed as a listric normal fault during the pre-Svecofennian, a steep geometry of the upper parts of the SFZ is feasible. Subsequent  $F_1$  and  $F_2$  folding may have contributed to a further steepening of the fault plane. The lower levels of the fault, on the other hand, initially oriented at a much shallower dip, would not necessarily be brought into a mechanically unfavorable orientation and could thus accommodate strain during later Caledonian compression. In addition, detailed mapped sections across the fault revealed mesostructural, as well as microstructural, evidences for fluid accompanied faulting. This is interpreted to have caused a significant weakening of the fault and the formation of a thick, plastic fault gouge that could facilitate strain accommodation.

When following the fault along strike, the hanging wall expose the complete stratigraphy of the Saltvatn Group, which could indicate either a rotation of the hanging wall during faulting, i.e. a wrench fault or a cut effect of the Nussir syncline (Fig. 3-1; 6 and Fig. 4-4). Although, the structures observed today at one of the localities indicate dip-slip kinematics, these reflect the final movements of the fault and do not necessarily constrain the full evolution of the fault through time.



### 7.1.5 Reactivation history

If stresses are imposed on a theoretically homogenous crust, a “seed” or inhomogeneity is needed to localize deformation. In the natural crust, such “seeds” are not in deficit, rather there are plenty of zones of weakness that can, if suitably oriented, accommodate slip. When deformation is localized on these pre-existing weakness planes, mechanical reactivation takes place and in terrains such as the RTW, which have undergone several deformation events, reactivation of older structures is believed to be the norm (e.g. Mattila and Viola, 2014; Viola et al., 2009; Viola et al., 2012).

A decade ago, temporal constraints on fault activity were generally obtained indirectly based on the age of the affected lithologies and structures. In the last few years however, the understanding of intra fault zone processes, such as fault gouge development in brittle faults, and the instrumental capabilities have increased and enabled isotopic dating of deformation. One prerequisite is the presence of K to form the phyllosilicate minerals like illite or muscovite, which may grow synkinematically. Every time a fault slips the already existing illite grows, but also new illite crystals nucleate and starts to grow (Zwingmann and Mancktelow, 2004). This enables a grain size-sensitive age determination of the illite, where the smallest grain fraction will be the youngest and the larger fractions will be older (e.g. Zwingmann et al., 2010).

Torgersen et al. (2014) used K-Ar dating on authigenic, synkinematic illite formed during multiple deformation episodes in one of the outermost exposed faults of the PIS, the Kvenklubben Fault (KF). Their dating pointed to a complex history of several faulting events and, thanks to the combination of geochronology with the detailed analysis of the microstructures of the fault core, it was possible to date the existing fabrics and correlate them to specific age-constrained events. The K-Ar dating revealed that deformation along the KF occurred mainly during two episodes at c. 445 Ma and 121 Ma, thus two events separated in time by c. 320 million years. The earliest event at c. 445 Ma corresponds to the SE-NW compression and formation of the PIS during Caledonian deformation. The gouge yielding 121 Ma for the finest fraction, on the other hand, corresponds in a geologic perspective to a time dominated by extensional tectonics in the SW Barents Sea.

As for the KF, there are several other fault zones within the PIS that indicate extensional reactivation of earlier thrusts, such as for example, the SoFZ (section 6.2.7) and the GFZ (Section 6.2.8). Although fault rocks from these faults have not been dated, the similarities to the KF indicate a comparable structural evolution from thrust imbrication with related phyllonitization, and significantly reduced internal strength of the fault rocks (see section 7.2), to extensional reactivation of the weak ancient fault surface. The latter led to e.g. crenulation of the fault core and folding of the weak, phyllosilicate-rich layers (Fig. 6-21 and 7-5 d). The two deformation periods are separated by a significant time period of low tectonic activity. This is demonstrated for instance by the static overgrowth of sphene

crystals on the foliation (Fig. 6-22 d). An enrichment of these crystals are also found within crenulation and solution surfaces, indicating that a significant amount of dissolution occurred along these seams. Interestingly, the cleavage wraps around the sphene crystals indicating that the solution cleavage formed after the growth of the sphene crystals. Furthermore, the current orientation of the axial plane/solution cleavage surfaces of the folds indicates a sub-vertical  $\sigma_1$ , which is the expected orientation for extension to occur.

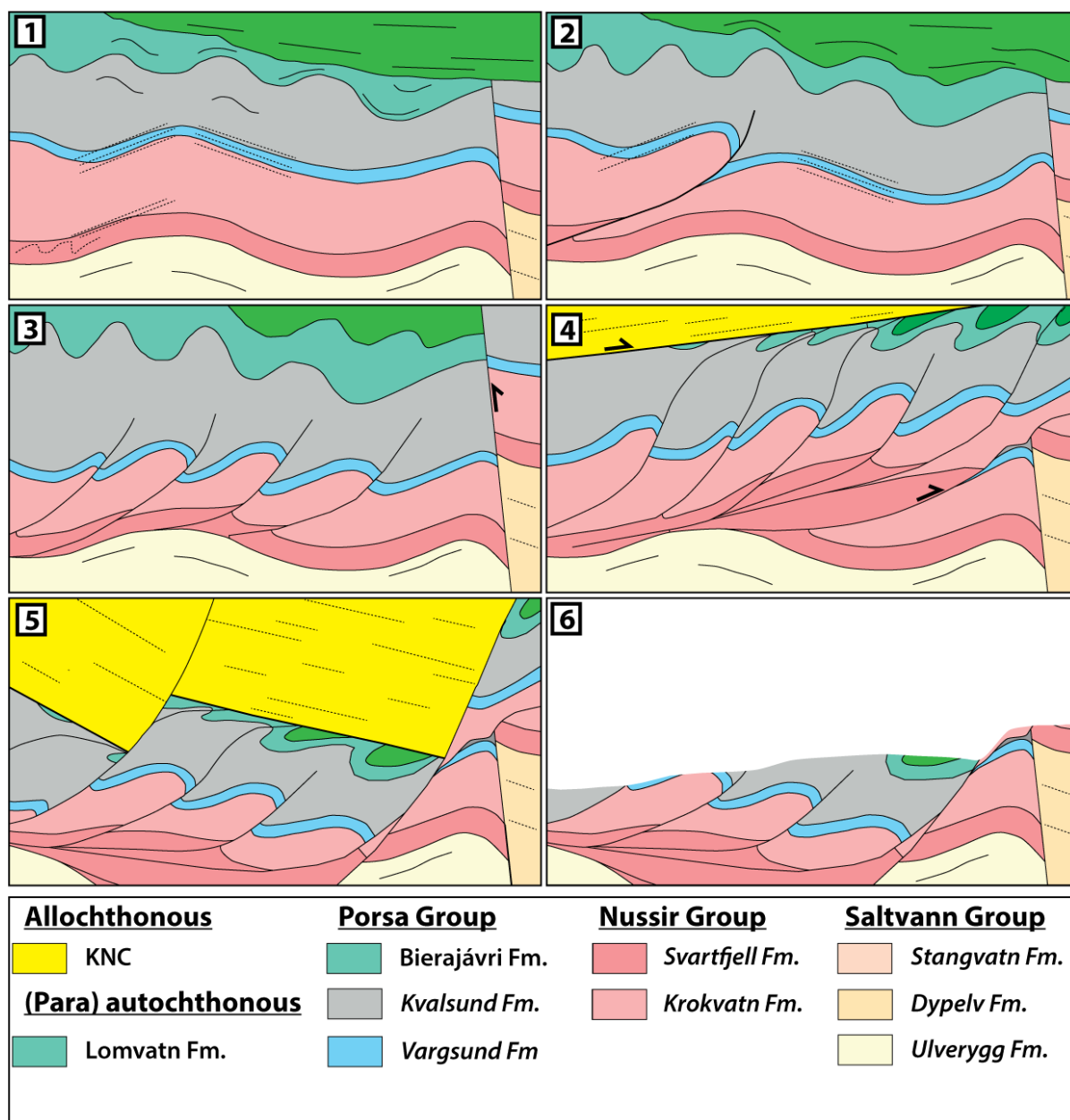
In general, normal reactivation of thrusts within the PIS is observed in the outermost regions, while in the more interior parts of the PIS, no structures indicating extensional reactivation have been observed. Nonetheless, the present day lithological relationship created by the WSFZ requires a significant amount of normal movement along the fault in order to juxtapose the Kvalsund Formation in the hanging wall to the stratigraphically lower Nussir group in the footwall (Fig. 4-5). In the northern parts of the WSFZ we know that the Nussir Group were thrust over the Vargsund and locally parts of the Kvalsund formations along the NFZ. At present day position, however, the Nussir Group is structurally sitting above the Kvalsund and Bierajávri formations in the hanging wall, which requires a significant amount of normal movement along the WSFZ (Fig. 7-7 4 and 5).

The c. 121 Ma extensional phase of the PIS dated by Torgersen et al. (2014) fits well with the opening of NE-SW-trending basins in the Barents Sea, which occurred at two different stages: 1) Devonian – Carboniferous, and 2) Triassic – Cretaceous (Faleide et al., 2010; Hansen et al., 2012). Roberts and Lippard (2005) propose that the Vargsund-Langfjorden fault, which bounds RTW to the NW, represent a Mesozoic structure. This fault runs sub-parallel to the PIS thrusts and has thus possibly reactivated preexisting structures. In addition, Torgersen et al. (2014) also dated a fault to the NE of the field area, yielding Carboniferous ages, which suggest that this early extensional phase may also have influenced the RTW.

#### **7.1.6 Conceptual model for the structural evolution of PIS**

As noted in the geological setting, the RTW was shortened and folded during the Svecofennian orogeny. Svecofennian folds accommodated overall NW-SE shortening and are still pristine in the central part of the RTW (Fig. 5-3 c, d and Fig. 6-2 a). Inside the PIS, however, they underwent structural reworking during the Caledonian orogeny, whereby they were refolded coaxially during the SE-ward emplacement and translation of the KNC. As the folds tightened (Fig. 7-7; 1), strain was preferentially accommodated in their limbs as these attained a favorable orientation with respect to the broad NW-SE Caledonian shortening stress field, hence their coaxiality with the earlier  $F_1$  Svecofennian folds. Due to the low peak metamorphic temperature during Caledonian deformation

(e.g. Dallmeyer et al., 1988; Torgersen and Viola, 2014), it is suggested that diffuse deformation by folding was not the optimal deformation mechanism to accommodate the imposed amount of shortening, such that when deformation started to localize, fluids were channelized and a progressive chemical and mechanical breakdown of the strained rocks initiated (see section 7.2 and sub chapters therein). Deformation progressed from being diffuse and continuous to more localized and partitioned, thus thrusts developed (Fig. 7-7; 2). The weakest lithologies, such as the Kvalsund, Bierajávri and the Lomvatn formations, continued to deform by fault-related folding as progressively more thrusts developed (Fig. 7-7; 3).



**Figure 7-7:** Conceptual sketch of the tectonic evolution of the PIS. Note that the Lomvatn Formation (not described in this text) overlies the Bierajávri Formation discordantly due to Neoproterozoic erosion and deposition. See text for further details.

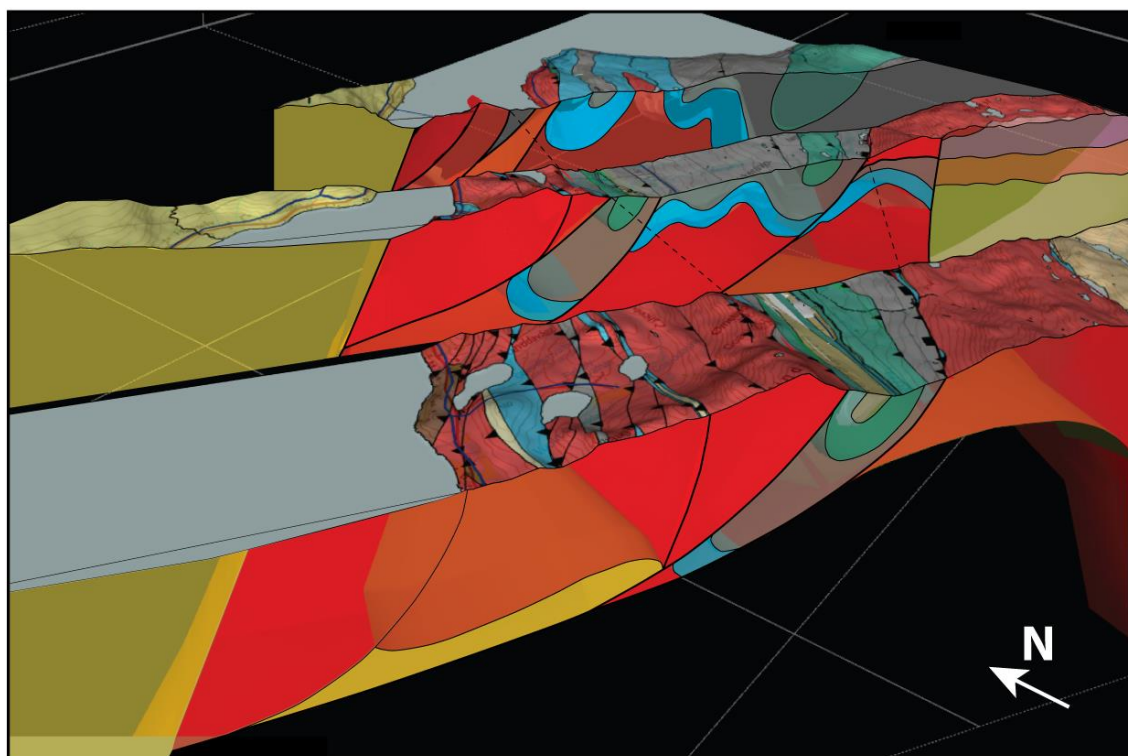


Whether the faults flattened out as a response to the change in rheology from the more competent Nussir Group is unknown as very little conclusive evidence of localized deformation is seen within the Kvalsund Formation, although, it is always challenging to identify and quantify strain in little competent, pervasively foliated lithologies.

Preliminary results on radiometric K-Ar on authigenic illites from the SFZ suggest that the fault were active during Caledonian times and in the present day orientation thus acted as a back thrust (Torgersen, 2015).

At stage four (Fig. 7-7; 4), rocks are increasingly compressed and shortened, leading to progressively larger displacement along the thrusts. During this stage, it is envisaged that the KNC were approaching the RTW and caused increased deformation and out of sequence faulting, forming the NFZ. As the KNC were emplaced, the individual faults within the PIS may have propagated through the overlying stratigraphy to form a duplex with the KNC basal décollement as the roof thrust. Furthermore as previously discussed (section 7.1.4), the Krokvatn Formation may have acted as a basal detachment for the entire PIS.

During the Mesozoic (Fig. 7-7; 5), extensional forces caused normal faulting, which selectively reactivated preexisting reverse faults inherited from the Caledonian compression. One of these faults was the WSFZ. Stage six shows the present day configuration of the PIS after the glacial erosion (Fig. 7-7; 6 and Fig. 7-8).



**Figure 7-8:** 3D cross sections constructed using Move (Midland Valley) and Adobe Illustrator. Cross sections are transparent to show lateral continuity of the layers and structures.

## 7.2 Fault weakening and deformation mechanisms

Boyer and Elliott (1982) wrote in the conclusion of their seminal paper on thrust systems that: “(...) by *untangling the large scale plate tectonics from descriptions of the smaller scale thrust systems both points of view will gain clarity and precision*”. In addition, by further untangling thrust systems from the perspective of the internal processes that are active within the deforming system, an even stronger fundamental understanding of the formation of thrust belts may be obtained.

This section deals with the fundamental weakening processes that made strain localization in the lithologically and mechanically heterogeneous stratigraphy in the PIS possible.

### 7.2.1 The role of fluid infiltration and overpressure

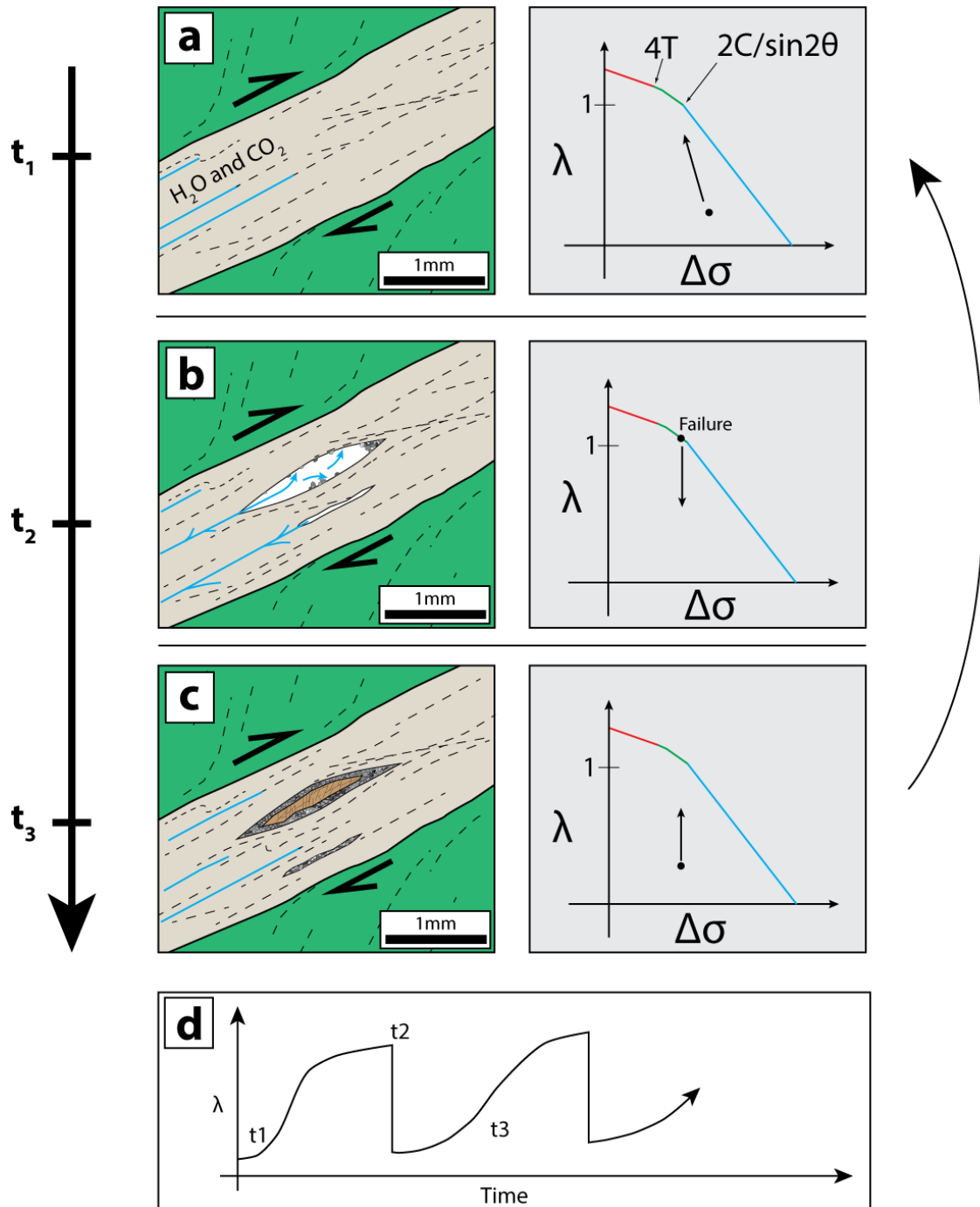
Hubbert and Rubey (1959) were the first authors to understand the fundamental role of fluids in thrust systems. Their legendary paper gave a mechanical explanation to the little understood “paradox” of overthrusting by considering the effective stresses, i.e.:

$$\sigma_{\text{eff}} = \sigma - P_f \quad (1)$$

where:  $\sigma_{\text{eff}}$  is the effective stress,  $\sigma$  is the lithostatic stress and  $P_f$  is the fluid pressure. If  $P_f$  approaches values close or equal to the lithostatic stress, the Coulomb theory predicts that the rock will fail (Coulomb, 1773). Cox (2010) proposed a new type of failure diagram where differential stress and pore fluid factor,  $\lambda$ , ( $\lambda = P_f / \sigma_1$ , with  $P_f$  for fluid pressure and  $\sigma_1$  the greatest compressive stress.) are plotted. This shows that failure may be attained by either increasing fluid pressure (hydraulic fracture) or increasing differential stresses (Fig. 2-11 or Fig. 7-9).

Clear evidence for fluid circulation is observed throughout the PIS and RTW. The studied rocks have undergone greenschist metamorphism, which is known to produce large amounts of H<sub>2</sub>O-CO<sub>2</sub> bearing fluids (Graham et al., 1983). Evidence for this is e.g. a locally pervasive calcite filled fracture cleavage observed throughout the internal RTW and locally within the PIS. Furthermore, within most of the PIS fault zones, quartz and calcite-filled veinlets are found. These are generally zoned with fine-grained quartz nucleating on the fracture walls and relatively coarse-grained, often fibrous calcite nucleating in the center of the veinlets. Locally they indicate several generations of opening, suggesting a behavior of cyclic fluid overpressurizing (Fig. 2-4 e). Such oscillations of fluid pressure are often related to fault-valve behavior, where the relative impermeable nature of, for example, a dolostone (Viola et al., 2006) will lead to a progressive increase in pressure if there is a steady supply of fluids into the system (Faulkner and Rutter, 2001; Fig. 7-9 a). When  $\lambda$  increases sufficiently, the rock fails and the fractures are subsequently sealed and healed by secondary mineral precipitation

(e.g. Cox, 1995; Sibson, 1992; Viola et al., 2006; Fig. 7-8 b, c). This process is associated with strain hardening of the system, as the veins and veinlets cause anisotropies in the strongly foliated phyllonite, which need to be broken down before steady state deformation may commence (Torgersen and Viola, 2014).



**Figure 7-9:** (a) When fluids are channelized along a low permeability zone, such as a phyllonitic fault zone, fluid pressure increase and  $\lambda$  approach unit value. (b) When the  $\Delta\sigma$  and  $\lambda$  is such that they touch the failure envelope the rock yields and becomes permeable which causes the  $\lambda$  value to decrease. (c) As the open spaces seal by precipitation from the fluid,  $\lambda$  may again increase, repeating the cycle. (d) schematic graph showing the evolution of  $\lambda$  through time.



In addition to promoting hydraulic fracturing with subsequent strain hardening, fluids also play a very important role in the softening of a fault zone through processes that promote reaction weakening such as e.g.: 1) decarbonation reactions, 2) carbonation reactions, 3) hydrolytic weakening, and 4) dissolution-precipitation, i.e. grain size reduction, promoting grain size sensitive creep, such as grain boundary sliding (e.g. Bestmann and Prior, 2003; Wightman et al., 2006). In addition, the replacement of e.g. feldspar with chlorite, which is seen throughout the PIS, leads to a volume loss, which may enhance porosity and thus self-reinforce the fluid flow (Wintsch et al., 1995). These processes will be described in the following sections.

### 7.2.2 Phyllonitization

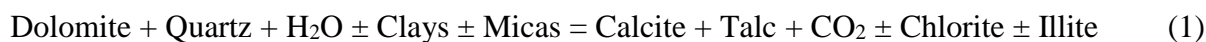
The Nussir metabasalts are generally spilitic and hydrated reflecting greenschist facies metamorphism (Pharaoh, 1985b; Reitan, 1963) with a paragenesis primarily comprising chlorite + actinolite + albite ± epidote ± sphene ± opaques (Reitan, 1963). The primary assemblage, however, appears to have been pyroxene/amphibole and plagioclase (possibly calcic; Fig. 5-9). In the relatively pristine greenstones of the PIS, there is seldom a pervasive foliation and thus there is generally not any form of alignment of anisotropic minerals. Within the fault zones, on the other hand, no primary textures are preserved as the rocks have undergone several types of reactions leading to a phyllonitization of the rock, wherein the primary mineral assemblage have undergone fluid-induced reactions to transform the metabasalt into a more phyllosilicate-rich rock, containing minerals such as chlorite, sericite and possibly talc. These reactions resulted in substantial weakening, fault nucleation and development, and allowed for significant strain to be accommodated. Three main reactions were of great significance during the phyllonitization of the PIS faults: 1) Dolomite decarbonation, 2) Metabasalt carbonation, and 3) Breakdown of feldspar. These reactions and their reactants and products are summarized in Table 4, below.

**Table 4:** Overview of reactions reactants and products.

<b>Reaction</b>	<b>Main reactants</b>	<b>Products</b>
Dolomite decarbonation	Dm + Qz	Cc + Ilt + Tlc + CO <sub>2</sub>
Metabasalt carbonation	Amp + Ep + H <sub>2</sub> O + CO <sub>2</sub>	Chl + Cc + Qz
Feldspar breakdown	Fld	White mica + alkalis

### 7.2.2.1 Dolomite decarbonation

At the pressure and temperature (< 250°) conditions reached in the northwestern parts of the RTW, dolomite deforms completely by brittle processes (e.g. Delle Piane et al., 2008; Wells et al., 2011). Delle Piane et al. (2007) show in a dolomite torsion experiment that strain may localize as chemical reactions break down dolomite to form secondary minerals together with a significant reduction in grain size, thus promoting grain size sensitive creep and strain localization. Within the Vargsund Formation, the same principles are observed, wherein strain is locally accommodated by deformation along discrete slip planes. The starting material was a relatively homogenous dolostone to dolomitic marble. As strain rate increased, large dolomite grains underwent pervasive twinning. Twinning, however, cannot accommodate large amounts of strain and, therefore, a more effective mechanism is necessary to sustain significant degrees of strain. Intracrystalline fractures, as observed in the NFZ (Fig. 6-6 a), indicate that the dolomite crystals underwent brittle failure. These were probably partially caused by the increasing fluid pressure produced by the equilibrium reaction leading to a progressive breakdown of dolomite into reaction products such as CO<sub>2</sub>, calcite and talc (Torgersen and Viola, 2014; reaction 1). Another possibility is that fracturing was caused by a progressive increase in strain rate as viscous intracrystalline deformation mechanisms are ineffective at the environmental conditions experienced within the PIS (Kjøll et al., 2015; In Press).



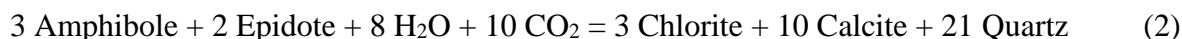
Fracturing increases the permeability of the system and leads to the escape of CO<sub>2</sub>, which promotes the breakdown of dolomite as the equilibrium reaction is pushed to the right. The production of calcite by decarbonation lowers the viscosity of the rocks because under the given environmental conditions calcite deforms efficiently by dislocation creep and grain boundary sliding and may, thus, localize strain more effectively than dolomite (Bestmann and Prior, 2003; Delle Piane et al., 2007).

Torgersen and Viola (2014) proposed a model wherein frictional processes and pressure solution caused the initiation of dolostones breakdown by allowing for the introduction of fluids and the subsequent chemical decomposition and formation of fine-grained weak minerals, such as calcite, talc, chlorite and illite (See reaction 1). Reaction 1 has been documented from both metamorphic contact aureoles and low angle normal faults (Holness, 1992; Viti and Collettini, 2009, respectively).

Several other types of decarbonation reactions may have been active throughout the PIS as e.g. phlogopite is observed at one locality, possibly indicating slightly higher temperature and a more impure dolostone composition (Masch and Heuss-Aßbichler, 1991; Wintsch et al., 1995).

### 7.2.2.2 Metabasalt carbonation

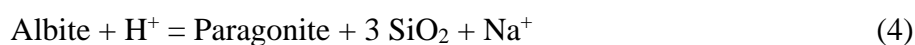
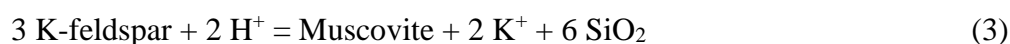
(Torgersen and Viola, 2014) reported a carbonation reaction of the metabasalt from the KF hanging wall. They proposed that this reaction was a softening mechanism that was genetically linked to the phyllonitization of the fault zone because it produces large amounts of chlorite. The following phyllonitization reaction is proposed by e.g. Graham et al. (1983), Skelton et al. (1997) and Skelton et al. (1995):



This reaction exploits the Fe and Mg in the amphibole and epidote present in the primary mineral assemblage to create chlorite. Wet chlorite has an average friction of 0,32 (e.g. Collettini et al., 2011; Ikari et al., 2009; Moore and Lockner, 2008) and can thus accommodate strain relatively easy. Chlorite is velocity strengthening, meaning that its friction increases with increasing sliding velocity, which promotes stable, aseismic creep (Collettini, 2011). The fault zones within the PIS contain large amounts of chlorite.

### 7.2.2.3 Feldspar breakdown

One of the primary minerals in a greenschist facies metabasalt is albite, which also may break down by fluid-assisted chemical reactions to produce phyllosilicate-rich assemblages. Generally, under the environmental/deformational conditions envisaged for the development of the PIS, albite and other feldspars will deform frictionally. This brittle deformation of feldspar results in a significant grain size reduction with a corresponding increase in surface area, enhancing the reactivity of metamorphic reactions. Some of the reactions that have been described in literature are:



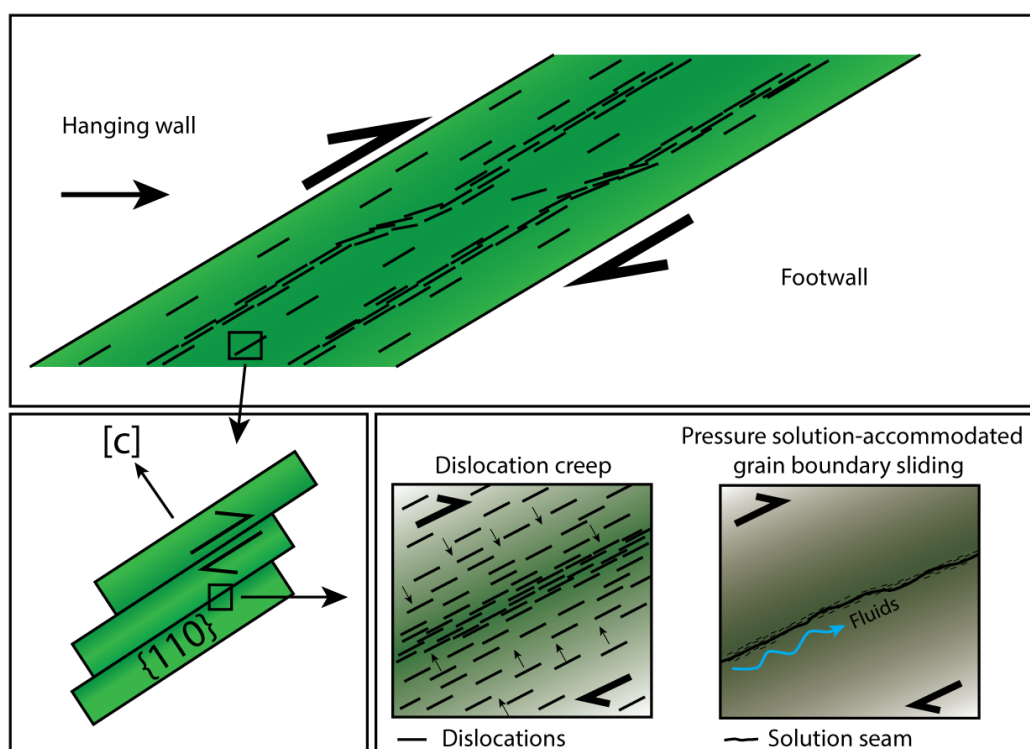
from O'Hara (1988) and Pirajno (2000), respectively. These reactions transform K- and Na-feldspar into phyllosilicates and quartz. For anorthite, a sausalitization process is more common due to the Ca component. During greenschist facies metamorphism in the RTW, however, anorthite was mostly transformed to albite and epidote (Reitan, 1963). Within the NFZ no anorthite is observed, only relatively pure albite, which is in agreement with the observations of Pharaoh et al. (1983).



### 7.2.3 Mechanical evolution of imbricate systems

All of the reactions discussed above contribute to the creation of phyllosilicate-rich mineral assemblages that greatly reduce the friction of fault zones (e.g. Jefferies et al., 2006; Niemeijer and Spiers, 2005; Tesei et al., 2012; Wibberley, 2005). These reactions are generally synkinematic and often promoted by the formation of secondary permeability in the fault rocks as overpressurized fluids induce hydraulic fracturing (Jefferies et al., 2006). Generally, phyllosilicates grow according to the imposed stress field and form a pervasive foliation in the affected rock. As these phyllosilicates are mostly velocity strengthening (Colletini et al., 2011) and possess a lower friction angle than the minerals they originate from, the fault rocks become weaker. These reactions are therefore strain softening (Wintsch et al., 1995).

Within the fault zones, the weak phyllonites deform primarily by two different mechanisms: 1) Dislocation creep (Mares and Kronenberg, 1993), and 2) Pressure solution-accommodated grain boundary sliding (Bos and Spiers, 2002). Dislocation creep is effective as the phyllosilicates within the fault zones generally are oriented with their basal plane, [001] *c*, parallel to the foliation, i.e. close to optimal for slip along the basal plane (Fig. 7-10), which is indeed the weakest plane in the phyllosilicates (Mares and Kronenberg, 1993). Pressure solution-accommodated grain boundary sliding, is similar to diffusion-accommodated grain boundary sliding and predicts frictional slip along the basal plane in contrast to diffusion (Fig. 7-10).



**Figure 7-10:** The anisotropic shape of phyllosilicates cause them to align within the fault zone, generally parallel to fault zone boundary. This leads to well oriented basal planes that either can slip viscously, by dislocation creep or frictionally by e.g. pressure solution-accommodated grain boundary sliding.

In order for strain to be accommodated there must be sufficient phyllosilicates to form an interconnected network such that they become the mechanically controlling phase. Tokle et al. (2013) found this threshold to be between 10% and 25% muscovite in their experimental study on quartzites. The fault rocks in the PIS generally contain far more than 25% phyllosilicates, which form interconnected, anastomosing networks around clasts of feldspar, dolomite and quartz. These networks contain very fine-grained chlorite, white mica and sometimes talc.

SEM analysis of the NFZ phyllonite reveal local enrichments of secondary phases such as sphene, alanite, zircon and apatite. These minerals are formed by relative immobile elements such as Zr, P and Ti, in comparison to alkalis and silica and therefore indicates a significant volume loss during the phyllonitization process (O'Hara, 1988). In every fault zone throughout the PIS, chlorite is abundant whereas talc has been observed at specific localities and often in relation to mafic intrusives and extrusives or decarbonated dolostone. Thick sequences of phyllonites, however, are generally found where metabasalts or mafic intrusives are involved in the deformation. This is in agreement with Wintsch et al. (1995), which propose that syndeformational phyllonitization is very common in mafic, Mg-rich rocks, where the Mg can be used to form mechanically weak minerals such as chlorite and talc (Viti and Collettini, 2009).

#### **7.2.4 Stick-slip vs. creep**

Chlorite is the main constituent of the phyllonites in the PIS, although other phyllosilicates such as muscovite, talc and clays are also present. All of these are velocity strengthening (Collettini, 2011), thus promoting aseismic creep. As briefly described above, an important parameter in order to induce aseismic creep is the degree of phyllonitization and, hence, the amount of phyllosilicates. Without interconnected layers of phyllosilicates, the strength of the fault rock is similar to that of the protolith (Tokle et al., 2013) and thus seismic stick-slip behavior is possible if the deformational/environmental conditions are appropriate.

Section 6.2.4 presents an extremely fine-grained discordant layer with injection veins within the LFZ (Fig. 6-12 e and Fig. 6-13 c and d) which may be interpreted as either an ultracataclasite or a pseudotachylyte (e.g. Bestmann et al., 2012; Magloughlin, 1992). Although detailed microstructural investigations would be required to verify the interpretation, this horizon could represent the first observation within the PIS of syndeformational frictional melt and thus strong evidence for coseismic deformation during the PIS development. This is in stark contrast to what one would conclude based on the analysis of the current structural characteristics of the PIS thrusts, that is, localization zones characterized by highly foliated and phyllosilicate-rich fault rocks.

Torgersen and Viola (2014) proposed that the KF and thus the PIS may have indeed nucleated and further deformed by seismic stick-slip behavior, as the thrusts deformed dolostones at temperatures below 250° (Fig. 7-6 a). Kjøl et al. (2015; In Press; see section 2) investigate deformed vein quartz at the brittle-ductile transition and link their results to those of Trepmann et al. (2007), which compare their experimentally deformed quartz to structures found in natural quartz deformed coseismically (See section 2 for further discussion). This indicates that the thrusts within the PIS may have deformed by seismic slip at the early stages of their development and then progressively weakened by strain softening reactions and formation of mechanically weak phyllosilicates.





## 8. Conclusions

This thesis presents the results from extensive field mapping, petrography and microstructural analysis of the Porsa Imbricate Stack (PIS), a Caledonian basement imbricate structure within the Repparfjord Tectonic Window in Northern Norway, that deformed under lower greenschist facies conditions by a combination of folding and fluid assisted faulting.

The key conclusions are summarized below and in section 2.7.

Detailed mapping had led to a refined folding history of the area, which can be divided in four phases:

- 1) Svecofennian – Open, upright
- 2) Svecofennian and/or Caledonian dextral transpression – Tight, vertical to reclined
- 3) Caledonian – Close to tight, inclined
- 4) Paleozoic and Mesozoic – Close, recumbent

Inherited Svecofennian folds were coaxially deformed and refolded during the early stages of the Caledonian orogeny, which led to shearing of the limbs by flexural slip. Contemporaneously, shortening was accommodated within the weak Krokvatn Formation, which acted as a relatively strong décollement where branching foreland verging faults nucleated and localized along the sheared fold limbs.

The switch from diffuse to localized deformation was facilitated by the channelizing of fluids along the limbs during flexural slip deformation. Alteration associated with the ingress of fluids caused reaction weakening of the limbs and enabled strain to localize and slip to be accommodated.

The processes causing the change from folding to faulting were the following:

- Ingress of fluids caused increasing pore fluid pressure, which led to hydraulic fracturing, increased permeability and veining. When the veins opened, fluid pressure dropped and precipitation of new minerals within the open spaces occurred. When the veins were sealed, fluid pressure could rebuild. This led to cyclic oscillations of the fluid pressure in a fault-valve behavior.
- The ingress of fluids led to a pervasive alteration of the host metabasalts into weak phyllonites. Three main reactions caused the extensive alteration of the fault rocks:
  - dolomite decarbonation
  - metabasalt carbonation
  - breakdown of Na-feldspar.

All these reactions caused growth of syntectonic, authigenic phyllosilicates such as chlorite, talc and white mica, which formed interconnected phyllosilicate-rich networks that greatly reduced the strength of the rocks and enabled slip to be easily accommodated by stable aseismic creep. The production of calcite caused further weakening of the system, as fine-grained calcite deformed by grain size sensitive creep at the environmental conditions constrained for the PIS.

- Due to the weak nature of phyllosilicates and the fine grain size of authigenic clays and micas, the active deformation mechanisms are interpreted to have been:
  - Dissolution-precipitation, as seen from the very fine grain size of quartz, albite and phyllosilicates within the phyllonites.
  - Diffusion-accommodated grain boundary sliding
  - Dislocation glide- and creep-accommodated viscous deformation of phyllosilicates and quartz

At a later stage, the dominating deformation mechanism switched from localized thrusting to diffuse folding, as apparent asymmetrically folding of the fault zones. This switch is interpreted to have occurred as Caledonian deformation intensified (e.g. increasing temperature) during the translation of the nappe complexes on top of the PIS.

Geometric relationships between lithologies separated by the Western Skinnfjellet Fault Zone (WSFZ) indicate that the fault possibly developed as an out of sequence thrust before it was reactivated normally, possibly during Mesozoic extensional deformation, and now juxtaposes Bierajávri metavolcanic tuffites against Nussir metabasalts. In addition, structural asymmetries found in fault zones such as SoFZ and GFZ indicate a more pervasive normal reactivation of the faults located in the outermost parts of the PIS.



## 9. Perspectives

Since Jensen's 1963 paper, the RTW has been studied in detail at least once every 10 years. Yet, in the last mapping campaign, the stratigraphy has been turned upside down (Smeplass, 2013; Torgersen, 2015) and yet more aspects of the complex geology of the RTW have been revealed. In particular, it would be interesting to investigate further the enigmatic Skinnfjellet Fault Zone, as it possibly represent a long-lived fault complex reactivated a number of times since early Proterozoic times. In its present-day orientation the SFZ is a highly misoriented fault and detailed microstructural work could possibly unravel some of the mechanisms causing strain to be accommodated. In addition, further work on the SFZ could shed light on its role as a buttress during incipient stages of PIS development.

In order to completely understand the transpressive event(s) more specific fieldwork will be necessary. By direct radiometric dating or indirect dating of e.g. overprinted fabrics, a better model may be constrained.

Further microstructural work by TEM on samples displaying bands of newly formed grains is important in order to test the model proposed in section 2 of this thesis and published in the journal *Solid Earth*, and to further constrain the active mechanisms at the brittle-ductile transition in quartz.



## References

- Adams, B. L., Wright, S. I., and Kunze, K., 1993, Orientation imaging: the emergence of a new microscopy: *Metallurgical Transactions A*, v. 24, no. 4, p. 819-831.
- Allen, P. A., and Allen, J. R., 2013, *Basin analysis: Principles and application to petroleum play assessment*, John Wiley & Sons.
- Atkinson, B. K., 1982, Subcritical crack propagation in rocks: theory, experimental results and applications: *Journal of Structural Geology*, v. 4, no. 1, p. 41-56.
- , 1984, Subcritical crack growth in geological materials: *Journal of Geophysical Research: Solid Earth (1978–2012)*, v. 89, no. B6, p. 4077-4114.
- Bachmann, F., Hielscher, R., and Schaeben, H., 2010, Texture analysis with MTEX—free and open source software toolbox: *Solid State Phenomena*, v. 160, p. 63-68.
- Batiza, R., and White, J. D., 2000, Submarine lavas and hyaloclastite: *Encyclopedia of volcanoes*, p. 361-381.
- Becker, A., 2000, The Jura Mountains—an active foreland fold-and-thrust belt?: *Tectonophysics*, v. 321, no. 4, p. 381-406.
- Bell, T., 1985, Deformation partitioning and porphyroblast rotation in meta-morphic rocks: a radical reinterpretation: *Journal of Metamorphic Geology*, v. 3, no. 2, p. 109-118.
- Bestmann, M., Pennacchioni, G., Nielsen, S., Göken, M., and De Wall, H., 2012, Deformation and ultrafine dynamic recrystallization of quartz in pseudotachylyte-bearing brittle faults: A matter of a few seconds: *Journal of Structural Geology*, v. 38, p. 21-38.
- Bestmann, M., and Prior, D. J., 2003, Intragranular dynamic recrystallization in naturally deformed calcite marble: diffusion accommodated grain boundary sliding as a result of subgrain rotation recrystallization: *Journal of Structural Geology*, v. 25, no. 10, p. 1597-1613.
- Bonini, M., 2007, Deformation patterns and structural vergence in brittle–ductile thrust wedges: an additional analogue modelling perspective: *Journal of Structural Geology*, v. 29, no. 1, p. 141-158.
- Bos, B., and Spiers, C. J., 2002, Frictional-viscous flow of phyllosilicate-bearing fault rock: Microphysical model and implications for crustal strength profiles: *Journal of Geophysical Research: Solid Earth*, v. 107, no. B2, p. ECV 1-1-ECV 1-13.
- Boyer, S. E., and Elliott, D., 1982, Thrust systems: *AAPG Bulletin*, v. 66, no. 9, p. 1196-1230.
- Buiter, S. J., 2012, A review of brittle compressional wedge models: *Tectonophysics*, v. 530, p. 1-17.
- Butler, R. W., 1982, The terminology of structures in thrust belts: *Journal of structural geology*, v. 4, no. 3, p. 239-245.
- , 1992, Thrust zone kinematics in a basement-cover imbricate stack: Eastern Pelvoux massif, French Alps: *Journal of structural geology*, v. 14, no. 1, p. 29-40.
- Chapple, W. M., 1978, Mechanics of thin-skinned fold-and-thrust belts: *Geological Society of America Bulletin*, v. 89, no. 8, p. 1189-1198.
- Chen, Y., Hjelen, J., Gireesh, S., and Roven, H., 2012, Optimization of EBSD parameters for ultra-fast characterization: *Journal of microscopy*, v. 245, no. 2, p. 111-118.
- Collettini, C., 2011, The mechanical paradox of low-angle normal faults: Current understanding and open questions: *Tectonophysics*, v. 510, no. 3-4, p. 253-268.
- Collettini, C., Niemeijer, A., Viti, C., Smith, S. A. F., and Marone, C., 2011, Fault structure, frictional properties and mixed-mode fault slip behavior: *Earth and Planetary Science Letters*, v. 311, no. 3–4, p. 316-327.
- Corfu, F., Roberts, R. J., Torsvik, T. H., Ashwal, L. D., and Ramsay, D. M., 2007, Peri-Gondwanan elements in the Caledonian Nappes of Finnmark, Northern Norway: Implications for the paleogeographic framework of the Scandinavian Caledonides: *American Journal of Science*, v. 307, no. 2, p. 434-458.



- Cosgrove, J., 1993, The interplay between fluids, folds and thrusts during the deformation of a sedimentary succession: *Journal of Structural Geology*, v. 15, no. 3, p. 491-500.
- Coulomb, C. A., 1773, Sur une application des règles de maximis et minimis à quelques problèmes de statique relatifs à l'architecture: *Mémoires de mathématiques et de Physique, Académie Royale des Sciences*, v. 7, p. 343-382.
- Cox, S. F., 1995, Faulting processes at high fluid pressures: an example of fault valve behavior from the Wattle Gully Fault, Victoria, Australia: *Journal of Geophysical Research: Solid Earth* (1978–2012), v. 100, no. B7, p. 12841-12859.
- Cox, S. F., 2010, The application of failure mode diagrams for exploring the roles of fluid pressure and stress states in controlling styles of fracture-controlled permeability enhancement in faults and shear zones: *Geofluids*, v. 10, no. 1-2, p. 217-233.
- Dahlen, F., 1984, Noncohesive critical Coulomb wedges: An exact solution: *Journal of Geophysical Research: Solid Earth* (1978–2012), v. 89, no. B12, p. 10125-10133.
- Dahlen, F., and Suppe, J., 1988, Mechanics, growth, and erosion of mountain belts: *Geological Society of America Special Papers*, v. 218, p. 161-178.
- Dahlen, F., Suppe, J., and Davis, D., 1984, Mechanics of fold-and-thrust belts and accretionary wedges: Cohesive Coulomb theory: *Journal of Geophysical Research: Solid Earth* (1978–2012), v. 89, no. B12, p. 10087-10101.
- Dallmeyer, R. D., Mitchell, J. G., Pharaoh, T. C., Reuter, A., and Andresen, A., 1988, K-Ar and Ar-40/Ar-39 Whole-Rock Ages of Slate Phyllite from Allochthonous Basement and Cover in the Tectonic Windows of Finnmark, Norway - Evaluating the Extent and Timing of Caledonian Tectonothermal Activity: *Geological Society of America Bulletin*, v. 100, no. 9, p. 1493-1501.
- Dallmeyer, R. D., Reuter, A., Clauer, N., and Liewig, N., 1989, Chronology of Caledonian tectonothermal activity within the Gaissa and Laksefjord Nappe Complexes (Lower Allochthon), Finnmark, Norway: evidence from K-Ar and Ar-Ar ages, *in* Gayar, R. A., ed., *The Caledonide Geology of Scandinavia*: London, Graham & Trotman, p. pp. 9-26.
- Daly, J. S., Aitchison, S. J., Cliff, R. A., Gayer, R. A., and Rice, A. H. N., 1991, Geochronological evidence from discordant plutons for a late Proterozoic orogen in the Caledonides of Finnmark, northern Norway: *Journal of the Geological Society*, v. 148, no. 1, p. 29-40.
- Dauids, C., Wemmer, K., Zwingmann, H., Kohlmann, F., Jacobs, J., and Bergh, S. G., 2013, K-Ar illite and apatite fission track constraints on brittle faulting and the evolution of the northern Norwegian passive margin: *Tectonophysics*, v. 608, no. 0, p. 196-211.
- Davis, D., Suppe, J., and Dahlen, F., 1983, Mechanics of fold-and-thrust belts and accretionary wedges: *Journal of Geophysical Research: Solid Earth* (1978–2012), v. 88, no. B2, p. 1153-1172.
- Davis, D. M., and Engelder, T., 1985, The role of salt in fold-and-thrust belts: *Tectonophysics*, v. 119, no. 1, p. 67-88.
- Dell'Angelo, L. N., and Tullis, J., 1996, Textural and mechanical evolution with progressive strain in experimentally deformed aplite: *Tectonophysics*, v. 256, no. 1, p. 57-82.
- Delle Piane, C., Burlini, L., and Grobety, B., 2007, Reaction-induced strain localization: Torsion experiments on dolomite: *Earth and Planetary Science Letters*, v. 256, no. 1–2, p. 36-46.
- Delle Piane, C., Burlini, L., Kunze, K., Brack, P., and Burg, J. P., 2008, Rheology of dolomite: large strain torsion experiments and natural examples: *Journal of Structural Geology*, v. 30, no. 6, p. 767-776.
- den Brok, S., and Spiers, C., 1991, Experimental evidence for water weakening of quartzite by microcracking plus solution-precipitation creep: *J. Geol. Soc. London*, v. 148, p. 541-548.
- den Brok, S. W. J., 1992, An experimental investigation into the effect of water on the flow of quartzite, Utrecht University.
- Derez, T., Pennock, G., Drury, M., and Sintubin, M., 2014, Low-temperature intracrystalline deformation microstructures in quartz: *Journal of Structural Geology*.
- Drury, M. R., and Urai, J. L., 1990, Deformation-related recrystallization processes: *Tectonophysics*, v. 172, no. 3, p. 235-253.

- Eisenstadt, G., and De Paor, D. G., 1987, Alternative model of thrust-fault propagation: *Geology*, v. 15, no. 7, p. 630-633.
- Elliott, D., 1980, Mechanics of thin-skinned fold-and-thrust belts: Discussion: *Geological Society of America Bulletin*, v. 91, no. 3, p. 185-187.
- Erickson, S. G., 1996, Influence of mechanical stratigraphy on folding vs faulting: *Journal of Structural Geology*, v. 18, no. 4, p. 443-450.
- Fairbairn, H., 1939, Correlation of quartz deformation with its crystal structure: *Am. Mineralogist*, v. 24, no. 6, p. 351.
- Fakhari, M., 1994, Khormoj 1: 250000 Geological Quadrangle Map: Geological Division of Exploration Management, NIOC.
- Faleide, J. I., Bjørlykke, K., and Gabrielsen, R. H., 2010, Geology of the Norwegian Continental Shelf, in Bjørlykke, K., ed., *Petroleum Geoscience: From Sedimentary Environments to Rock Physics*: Berlin Heidelberg, Springer-Verlag, p. 467-499.
- Faleide, J. I., Gudlaugsson, S. T., and Jacquart, G., 1984, Evolution of the western Barents Sea: *Marine and Petroleum Geology*, v. 1, no. 2, p. 123-150.
- Faulkner, D. R., and Rutter, E. H., 2001, Can the maintenance of overpressured fluids in large strike-slip fault zones explain their apparent weakness?: *Geology*, v. 29, no. 6, p. 503-506.
- Feng, L., Bartholomew, M. J., and Choi, E., 2015, Spatial arrangement of décollements as a control on the development of thrust faults: *Journal of Structural Geology*.
- Fitz Gerald, J., and Stünitz, H., 1993, Deformation of granitoids at low metamorphic grade. I: reactions and grain size reduction: *Tectonophysics*, v. 221, no. 3, p. 269-297.
- Flörke, O. W., Mielke, H. G., Weichert, J., and Kulke, H., 1981, Quartz with rhombohedral cleavage from Madagascar: *American Mineralogist*, v. 66, no. 5-6, p. 596-600.
- Fossen, H., 2010, *Structural geology*, Cambridge University Press.
- Fronzel, C., Dana, J. D., and Dana, E. S., 1962, *The System of Mineralogy: Silica Minerals*, Wiley.
- Fyfe, W., and Kerrich, R., 1985, Fluids and thrusting: *Chemical Geology*, v. 49, no. 1, p. 353-362.
- Gabellone, T., Gasparrini, M., Iannace, A., Invernizzi, C., Mazzoli, S., and D'antonio, M., 2013, Fluid channeling along thrust zones: the Lagonegro case history, southern Apennines, Italy: *Geofluids*, v. 13, no. 2, p. 140-158.
- Gayer, R. A., Rice, A. H. N., Roberts, D., Townsend, C., and Welbon, A., 1987, Restoration of the Caledonian Baltoscandian margin from balanced cross-sections: the problem of excess continental crust: *Transactions of the Royal Society of Edinburgh: Earth Sciences*, v. 78, p. 197-217.
- Gee, D. G., Fossen, H., Henriksen, N., and Higgins, A. K., 2008, From the early Paleozoic platforms of Baltica and Laurentia to the Caledonide Orogen of Scandinavia and Greenland: *Episodes*, v. 31, p. 44-51.
- Goodwin, L. B., and Tikoff, B., 2002, Competency contrast, kinematics, and the development of foliations and lineations in the crust: *Journal of Structural Geology*, v. 24, no. 6, p. 1065-1085.
- Graham, C., Greig, K., Sheppard, S., and Turi, B., 1983, Genesis and mobility of the H<sub>2</sub>O-CO<sub>2</sub> fluid phase during regional greenschist and epidote amphibolite facies metamorphism: a petrological and stable isotope study in the Scottish Dalradian: *Journal of the Geological Society*, v. 140, no. 4, p. 577-599.
- Hansen, J.-A., Bergh, S. G., and Henningsen, T., 2012, Mesozoic rifting and basin evolution on the Lofoten and Vesterålen Margin, North-Norway; time constraints and regional implications: *Norwegian Journal of Geology*, v. 91, p. 203-228.
- Hanski, E., and Melezhik, V., 2013, 3.2 Litho-and Chronostratigraphy of the Palaeoproterozoic Karelian Formations, Reading the Archive of Earth's Oxygenation, Springer, p. 39-110.
- Heilbronner, R., and Pauli, C., 1993, Integrated spatial and orientation analysis of quartz *c*-axes by computer-aided microscopy: *Journal of Structural Geology*, v. 15, no. 3-5, p. 369-382.
- Henderson, I. H. C., and Viola, G., 2011, Implementering av digital berggrunnskartlegging ved Norges Geologiske Undersøkelse - NGU: *Mineralproduksjon*, v. 1, no. 1, p. 83-101.

- Hilley, G., and Strecker, M., 2004, Steady state erosion of critical Coulomb wedges with applications to Taiwan and the Himalaya: *Journal of Geophysical Research: Solid Earth* (1978–2012), v. 109, no. B1.
- Hippertt, J., and Egydio-Silva, M., 1996, New polygonal grains formed by dissolution-redeposition in quartz mylonite: *Journal of Structural Geology*, v. 18, no. 11, p. 1345-1352.
- Hirth, G., and Beeler, N., 2015, The role of fluid pressure on frictional behavior at the base of the seismogenic zone: *Geology*, v. 43, no. 3, p. 223-226.
- Hirth, G., and Tullis, J., 1992, Dislocation creep regimes in quartz aggregates: *Journal of Structural Geology*, v. 14, no. 2, p. 145-159.
- Holness, M. B., 1992, Metamorphism and Fluid Infiltration of the Calc-silicate Aureole of the Beinn an Dubhaich Granite, Skye: *Journal of Petrology*, v. 33, no. 6, p. 1261-1293.
- Holtedahl, O., 1918, Bidrag til Finnmarkens Geologi: Norges geologiske undersøkelse, v. 84, p. 314 p.
- , 1932, Additional observations on the rock formations of Finnmark: *Norsk geologisk tidsskrift*, v. 11, p. 241-279.
- Holyoke, C. W., and Tullis, J., 2006, Mechanisms of weak phase interconnection and the effects of phase strength contrast on fabric development: *Journal of Structural Geology*, v. 28, no. 4, p. 621-640.
- Hubbert, M. K., and Rubey, W. W., 1959, Role of fluid pressure in mechanics of overthrust faulting I. Mechanics of fluid-filled porous solids and its application to overthrust faulting: *Geological Society of America Bulletin*, v. 70, no. 2, p. 115-166.
- Ikari, M. J., Saffer, D. M., and Marone, C., 2009, Frictional and hydrologic properties of clay-rich fault gouge: *Journal of Geophysical Research: Solid Earth* (1978–2012), v. 114, no. B5.
- Jansen, O. J., 1976, Strukturell og metamorf utvikling i den vestlige del av Komagfjord viduet og overliggende dekker [Unpublished Cand. Real. Thesis: University of Bergen].
- Jefferies, S. P., Holdsworth, R. E., Wibberley, C. A. J., Shimamoto, T., Spiers, C. J., Niemeijer, A. R., and Lloyd, G. E., 2006, The nature and importance of phyllonite development in crustal-scale fault cores: an example from the Median Tectonic Line, Japan: *Journal of Structural Geology*, v. 28, no. 2, p. 220-235.
- Kirkland, C. L., Daly, J. S., Chew, D. M., and M., P. L., 2008, The Finnmarkian Orogeny revisited: An isotopic investigation in eastern Finnmark, Arctic Norway: *Tectonophysics*, v. 460, p. 158-171.
- Kirkland, C. L., Daly, J. S., Eide, E. A., and Whitehouse, M. J., 2007, Tectonic evolution of the Arctic Norwegian Caledonides from a texturally- and structurally-constrained multi-isotopic (Ar-Ar, Rb-Sr, Sm-Nd, U-Pb) study: *American Journal of Science*, v. 307, no. 2, p. 459-526.
- Kirkland, C. L., Daly, J. S., and Whitehouse, M. J., 2006, Granitic magmatism of Grenvillian and late Neoproterozoic age in Finnmark, Arctic Norway - Constraining pre-Scandian deformation in the Kalak Nappe Complex: *Precambrian Research*, v. 145, p. 24-52.
- Kjøll, H. J., Viola, G., Menegon, L., and Sørensen, B. E., 2015, Brittle–viscous deformation of vein quartz under fluid-rich low greenschist facies conditions: *Solid Earth Discussions*, v. 7, no. 1, p. 213-257.
- Kronenberg, A. K., Segall, P., and Wolf, G. H., 1990, Hydrolytic weakening and penetrative deformation within a natural shear zone: The brittle–ductile transition in rocks, p. 21-36.
- Kronenberg, A. K., and Tullis, J., 1984, Flow strengths of quartz aggregates: Grain size and pressure effects due to hydrolytic weakening: *Journal of Geophysical Research: Solid Earth* (1978–2012), v. 89, no. B6, p. 4281-4297.
- Lahtinen, R., Garde, A. A., and Melezhik, V. A., 2008, Paleoproterozoic evolution of Fennoscandia and Greenland: *Episodes*, v. 31, no. 1, p. 20-28.
- Lahtinen, R., Korja, A., Nironen, M., and Heikkinen, P., 2009, Palaeoproterozoic accretionary processes in Fennoscandia: *Geological Society, London, Special Publications*, v. 318, no. 1, p. 237-256.



- Lippard, S. J., and Prestvik, T., 1997, Carboniferous dolerite dykes on Magerøy: new age determination and tectonic significance: *Norsk Geologisk Tidsskrift*, v. 77, p. 159-163.
- Lloyd, G. E., 2000, Grain boundary contact effects during faulting of quartzite: an SEM/EBSD analysis: *Journal of Structural Geology*, v. 22, no. 11, p. 1675-1693.
- Magloughlin, J. F., 1992, Microstructural and chemical changes associated with cataclasis and frictional melting at shallow crustal levels: the cataclasite-pseudotachylyte connection: *Tectonophysics*, v. 204, no. 3, p. 243-260.
- Mainprice, D., Hielscher, R., and Schaeben, H., 2011, Calculating anisotropic physical properties from texture data using the MTEX open-source package: Geological Society, London, Special Publications, v. 360, no. 1, p. 175-192.
- Mancktelow, N. S., Grujic, D., and Johnson, E. L., 1998, An SEM study of porosity and grain boundary microstructure in quartz mylonites, Simplon Fault Zone, Central Alps: *Contributions to Mineralogy and Petrology*, v. 131, no. 1, p. 71-85.
- Mancktelow, N. S., and Pennacchioni, G., 2004, The influence of grain boundary fluids on the microstructure of quartz-feldspar mylonites: *Journal of Structural Geology*, v. 26, no. 1, p. 47-69.
- Mares, V. M., and Kronenberg, A., 1993, Experimental deformation of muscovite: *Journal of Structural Geology*, v. 15, no. 9, p. 1061-1075.
- Masch, L., and Heuss-Aßbichler, S., 1991, Decarbonation Reactions in Siliceous Dolomites and Impure Limestones, in Voll, G., Töpel, J., Pattison, D. M., and Seifert, F., eds., *Equilibrium and Kinetics in Contact Metamorphism*, Springer Berlin Heidelberg, p. 211-227.
- Mattila, J., and Viola, G., 2014, New constraints on 1.7 Gyr of brittle tectonic evolution in southwestern Finland derived from a structural study at the site of a potential nuclear waste repository (Olkiluoto Island): *Journal of Structural Geology*, v. 67, p. 50-74.
- McClay, K., and Buchanan, P., 1992, Thrust faults in inverted extensional basins, *Thrust tectonics*, Springer, p. 93-104.
- McQuarrie, N., 2004, Crustal scale geometry of the Zagros fold-thrust belt, Iran: *Journal of Structural Geology*, v. 26, no. 3, p. 519-535.
- McSkimin, H., Andreatch Jr, P., and Thurston, R., 1965, Elastic moduli of quartz versus hydrostatic pressure at 25 and– 195.8 C: *Journal of Applied Physics*, v. 36, no. 5, p. 1624-1632.
- Melezhik, V., and Hanski, E., 2013, 3.1 The Early Palaeoproterozoic of Fennoscandia: *Geological and Tectonic Settings, Reading the Archive of Earth's Oxygenation*, Springer, p. 33-38.
- Melezhik, V. A., Prave, A. R., Hanski, E. J., Fallick, A. E., Lepland, A., Kump, L. R., and Strauss, H., 2012, *Reading the Archive of Earth's Oxygenation: Volume 1: The Palaeoproterozoic of Fennoscandia as Context for the Fennoscandian Arctic Russia - Drilling Early Earth Project*, Springer Science & Business Media.
- Menegon, L., Nasipuri, P., Stünitz, H., Behrens, H., and Ravna, E., 2011a, Dry and strong quartz during deformation of the lower crust in the presence of melt: *Journal of geophysical Research*, v. 116, p. B10410.
- Menegon, L., Pennacchioni, G., Heilbronner, R., and Pittarello, L., 2008, Evolution of quartz microstructure and c-axis crystallographic preferred orientation within ductilely deformed granitoids (Arolla unit, Western Alps): *Journal of Structural Geology*, v. 30, no. 11, p. 1332-1347.
- Menegon, L., Piazzolo, S., and Pennacchioni, G., 2011b, The effect of Dauphiné twinning on plastic strain in quartz: *Contributions to Mineralogy and Petrology*, v. 161, no. 4, p. 635-652.
- Moen, K., Hjelen, J., and Malvik, T., Preparation of Quartz samples for EBSD analysis [Poster], in *Proceedings Applied Mineralogy' 03*, Helsinki, 2003.
- Moore, D. E., and Lockner, D. A., 2008, Talc friction in the temperature range 25–400 C: Relevance for fault-zone weakening: *Tectonophysics*, v. 449, no. 1, p. 120-132.
- Niemeijer, A. R., and Spiers, C. J., 2005, Influence of phyllosilicates on fault strength in the brittle-ductile transition: insights from rock analogue experiments: Geological Society, London, Special Publications, v. 245, no. 1, p. 303-327.

- Nilsen, K. S., and Nilsson, L. P., 1996, Berggrunnskart; Vargsund: Norges Geologiske Undersøkelse, scale 1:50 000.
- Nussir, 2014a, Nussir ASA har økt ressursen på Nussir med 50% fra 44 til 66 mill tonn malm: [www.nussir.no](http://www.nussir.no).
- , 2014b, Årsberetning og årsregnskap for 2013, in KPMG, ed.: [www.nussir.no](http://www.nussir.no).
- O'Hara, K., 1988, Fluid flow and volume loss during mylonitization: an origin for phyllonite in an overthrust setting, North Carolina USA: *Tectonophysics*, v. 156, no. 1, p. 21-36.
- Ofstad, F., Baranwal, V., Koziel, J., Lynum, R., and Rodionov, A., 2013, Helicopter-borne magnetic, electromagnetic and radiometric geophysical survey in Repparfjord area, Alta and Kvalsund, Finnmark: NGU, 2013-027.
- Oftedahl, C., 1980, Geology of Norway: Norges geologiske undersøkelse. Contributions to the 26th International Geological Congress, v. 356, p. 3-114.
- Pharaoh, T., 1985a, The stratigraphy and sedimentology of autochthonous metasediments in the Repparfjord-Komagfjord Tectonic Window, west Finnmark, in Gee, D. G., and Sturt, B. A., eds., *The Caledonide Orogen - Scandinavia and Related Areas*, John Wiley & Sons Ltd, p. 347-372.
- , 1985b, Volcanic and geochemical stratigraphy of the Nussir Group of Arctic Norway—an early Proterozoic greenstone suite: *Journal of the Geological Society*, v. 142, no. 2, p. 259-278.
- Pharaoh, T., Macintyre, R., and Ramsay, D., 1982, K–Ar age determinations on the Raipas suite in the Komagfjord Window, Northern Norway: *Norsk Geologisk Tidsskrift*, v. 62, no. 1, p. 51-57.
- Pharaoh, T. C., and Pearce, J. A., 1984, Geochemical evidence for the geotectonic setting of early Proterozoic metavolcanic sequences in Lapland: *Precambrian Research*, v. 25, no. 1, p. 283-308.
- Pharaoh, T. C., Ramsay, D. M., and Jansen, Ø., 1983, Stratigraphy and structure of the northern part of the Repparfjord-Komagfjord Window, Finnmark, Northern Norway: *Norges Geologiske Undersøkelse Bulletin* v. 337, p. 1-45.
- Pirajno, F., 2000, *Ore deposits and mantle plumes*, Kluwer Academic Dordrecht.
- Platt, J., and Vissers, R., 1980, Extensional structures in anisotropic rocks: *Journal of Structural Geology*, v. 2, no. 4, p. 397-410.
- Prior, D. J., Boyle, A. P., Brenker, F., Cheadle, M. C., Day, A., Lopez, G., Peruzzo, L., Potts, G. J., Reddy, S., and Spiess, R., 1999, The application of electron backscatter diffraction and orientation contrast imaging in the SEM to textural problems in rocks: *American Mineralogist*, v. 84, p. 1741-1759.
- Prior, D. J., Mariani, E., and Wheeler, J., 2009, EBSD in the earth sciences: applications, common practice, and challenges, *Electron backscatter diffraction in materials science*, Springer, p. 345-360.
- Ramsay, D., and Sturt, B., 1977, A sub-Caledonian unconformity within the Finnmarkian nappe sequence and its regional significance: *Nor. geol. unders.*, v. 334, p. 107-116.
- Reitan, P. H., 1963, The geology of the Komagfjord tectonic window of the Raipas suite, Finnmark, Norway: *Norges Geologiske Undersøkelse Bulletin*, v. 221, p. 1-71.
- Reusch, H., 1891, Det Nordlige Norges geologi. Med bidrag af Dahll T., Corneliussen OA, med profiler og Dahll's Geologisk Kart over det nordlige Norge'(1: 1,000,000): *Nor. Geol. Unders.*, v. 3.
- Reusch, H. H., Dahll, T., and Corneliussen, O. A., 1891, *Det nordlige Norges geologi*, Aschehoug.
- Rhodes, S., 1976, The geology of the Kallak Nappe and its relationship to the N.E. margin of the Komagfjord Tectonic Window, Finnmark, Norway [Unpublished Ph.D. Thesis: University College of Wales].
- Rice, A., 1984, The significance of a thrust fault lineation in the Kalak Nappe Complex of Finnmark: *Norsk geologisk tidsskrift*, v. 64, p. 173-180.

- Rice, A. H. N., 1998, Stretching lineations and structural evolution of the Kalak Nappe Complex (Middle Allochthon) in the Repparfjord-Faegfjord area, Finnmark, northern Norway: *Norsk Geologisk Tidsskrift*, v. 78, no. 4, p. 277-289.
- , 2013, Restoration of the External Caledonides, Finnmark, North Norway, in Corfu, F., Gasser, D., and Chew, D. M., eds., *New Perspectives on the Caledonides of Scandinavia and Related Areas*, Volume Special Publications: London, Geological Society, p. 271-299.
- Rice, A. H. N., and Frank, W., 2003, The early Caledonian (Finnmarkian) event reassessed in Finnmark:  $^{40}\text{Ar}/^{39}\text{Ar}$  cleavage data from Varangerhaløya, N. Norway: *Tectonophysics*, v. 374, p. 219-236.
- Roberts, D., 2003, The Scandinavian Caledonides: event chronology, paleogeographic settings and likely modern analogues: *Tectonophysics*, v. 365, p. 283-299.
- Roberts, D., and Lippard, S. J., 2005, Inferred Mesozoic faulting in Finnmark: current status and offshore links: *Norges Geologiske Undersøkelse Bulletin*, v. 443, p. 55-60.
- Roberts, D., and Siedlecka, A., 2002, Timanian orogenic deformation along the northeastern margin of Baltica, Northwest Russia and Northeast Norway, and Avalonian-Cadomian connections: *Tectonophysics*, v. 352, no. 1-2, p. 169-184.
- Roberts, R. J., Corfu, F., Torsvik, T., Ashwal, L. D., and Ramsay, D. M., 2006, Short-lived mafic magmatism at 560-680 Ma in the northern Norwegian Caledonides: U-Pb zircon age from the Seiland Igneous Province: *Geological Magazine*, v. 143, p. 887-903.
- Sander, B., 1911, X. Über Zusammenhänge zwischen Teilbewegung und Gefüge in Gesteinen: *Zeitschrift für Kristallographie, Mineralogie und Petrographie*, v. 30, no. 3, p. 281-314.
- Sandstad, J. S., 2008, Geochemistry of drill cores from the Nussir copper deposit, Kvalsund, Finnmark, Northern Norway: *Geological Survey of Norway*, 2008:055.
- , 2010, Microscope and SEM (scanning electron microscope) investigations of thin sections from the Nussir copper deposits: *Geological Survey of Norway*, 2010:025.
- Schmid, S., and Casey, M., 1986, Complete fabric analysis of some commonly observed quartz c-axis patterns: *Mineral and Rock Deformation: Laboratory Studies: The Paterson Volume*, p. 263-286.
- Schneider, C. A., Rasband, W. S., Eliceiri, K. W., Schindelin, J., Arganda-Carreras, I., Frise, E., Kaynig, V., Longair, M., Pietzsch, T., and Preibisch, S., 2012, 671 nih image to imageJ: 25 years of image analysis: *Nature methods*, v. 9, no. 7.
- Schwartz, A. J., Kumar, M., Adams, B. L., and Field, D. P., 2009, *Electron backscatter diffraction in materials science*, Springer.
- Segall, P., and Simpson, C., 1986, Nucleation of ductile shear zones on dilatant fractures: *Geology*, v. 14, no. 1, p. 56-59.
- Sibson, R. H., 1992, Implications of fault-valve behaviour for rupture nucleation and recurrence: *Tectonophysics*, v. 211, p. 283-293.
- Siedlecka, A., 1975, Late Precambrian stratigraphy and structure of the north-eastern margin of the Fennoscandian Shield (East Finnmark-Timan Region): *Nor. geol. unders.*, v. 316, p. 313-348.
- Siedlecka, A., and Roberts, D., 1996, *Berggrunnskart; Finnmark fylke: Norges Geologiske Undersøkelse*, scale 1: 500 000.
- Simpson, G. D., 2006, Modelling interactions between fold-thrust belt deformation, foreland flexure and surface mass transport: *Basin Research*, v. 18, no. 2, p. 125-143.
- , 2009, Mechanical modelling of folding versus faulting in brittle-ductile wedges: *Journal of Structural Geology*, v. 31, no. 4, p. 369-381.
- Skelton, A. D. L., Bickle, M. J., and Graham, C. M., 1997, Fluid-flux and reaction rate from advective-diffusive carbonation of mafic sill margins in the Dalradian, southwest Scottish Highlands: *Earth and Planetary Science Letters*, v. 146, no. 3-4, p. 527-539.
- Skelton, A. D. L., Graham, C. M., and Bickle, M. J., 1995, Lithological and Structural Controls on Regional 3-D Fluid Flow Patterns during Greenschist Facies Metamorphism of the Dalradian of the SW Scottish Highlands: *Journal of Petrology*, v. 36, no. 2, p. 563-586.



- Slagstad, T., Melezhik, V. A., Kirkland, C. L., Zwaan, K. B., Roberts, D., Gorokhov, I. M., and Fallick, A. E., 2006, Carbonate isotope chemostratigraphy suggests revisions to the geological history of the West Finnmark Caledonides, North Norway: *Journal of Geological Society of London*, v. 163, no. 2, p. 277-289.
- Smeplass, H. F., 2013, Geological Investigations of the southeastern Part of the Repparfjord Tectonic Window.
- Stipp, M., and Kunze, K., 2008, Dynamic recrystallization near the brittle-plastic transition in naturally and experimentally deformed quartz aggregates: *Tectonophysics*, v. 448, no. 1, p. 77-97.
- Stipp, M., Stunitz, H., Heilbronner, R., and Schmid, S. M., 2002a, The eastern Tonale fault zone: a 'natural laboratory' for crystal plastic deformation of quartz over a temperature range from 250 to 700 degrees C: *Journal of Structural Geology*, v. 24, no. 12, p. 1861-1884.
- Stipp, M., Stunitz, H., Heilbronner, R., and Schmid, S. M., 2002b, Dynamic recrystallization of quartz: correlation between natural and experimental conditions: *Geological Society, London, Special Publications*, v. 200, no. 1, p. 171-190.
- Storti, F., Balanyá, J.-C., Crespo-Blanc, A., and Rossetti, F., 2003, Role of décollement material with different rheological properties in the structure of the Aljibe thrust imbricate (Flysch Trough, Gibraltar Arc): an analogue modelling approach: *Journal of Structural Geology*, v. 25, no. 6, p. 867-881.
- Strayer, L. M., Hudleston, P. J., and Lorig, L. J., 2001, A numerical model of deformation and fluid-flow in an evolving thrust wedge: *Tectonophysics*, v. 335, no. 1, p. 121-145.
- Sturt, B., Pringle, I., and Ramsay, D., 1978, The Finnmarkian phase of the Caledonian orogeny: *Journal of the Geological Society*, v. 135, no. 6, p. 597-610.
- Sturt, B. A., Pringle, I. R., and Roberts, D., 1975, Caledonian Nappe Sequence of Finnmark, Northern Norway, and the Timing of Orogenic Deformation and Metamorphism: *Geological Society of America Bulletin*, v. 86, p. 710-718.
- Stunitz, H., and Fitz Gerald, J., 1993, Deformation of granitoids at low metamorphic grade. II: Granular flow in albite-rich mylonites: *Tectonophysics*, v. 221, no. 3, p. 299-324.
- Stunitz, H., Fitz Gerald, J., and Tullis, J., 2003, Dislocation generation, slip systems, and dynamic recrystallization in experimentally deformed plagioclase single crystals: *Tectonophysics*, v. 372, no. 3, p. 215-233.
- Sundvoll, B., and Roberts, D., 2003, A likely Early Ordovician age for the regional, penetrative cleavage in the Gaissa Nappe Complex, northern Norway: *Norges Geologiske Undersøkelse Bulletin*, v. 441, p. 51-59.
- Tesei, T., Collettini, C., Carpenter, B. M., Viti, C., and Marone, C., 2012, Frictional strength and healing behavior of phyllosilicate-rich faults: *Journal of Geophysical Research: Solid Earth*, v. 117, no. B9, p. B09402.
- Tokle, L., Stunitz, H., and Hirth, G., The effect of muscovite on the fabric evolution of quartz under general shear, *in Proceedings AGU Fall Meeting Abstracts 2013*, Volume 1, p. 2559.
- Torgersen, E., 2015, Geological investigations of the Repparfjord Tectonic Window, northern Norway: Backtracking two billion years of geological history by structural analysis, K-Ar and Re-Os geochronology and carbonate chemostratigraphy [P.hD: Norwegian University of Science and Technology, 228 p.
- Torgersen, E., and Viola, G., 2014, Structural and temporal evolution of a reactivated brittle-ductile fault – Part I: Fault architecture, strain localization mechanisms and deformation history: *Earth and Planetary Science Letters*, no. 0, p. 205-220.
- Torgersen, E., Viola, G., Zwingmann, H., and Harris, C., 2014, Structural and temporal evolution of a reactivated brittle-ductile fault–Part II: Timing of fault initiation and reactivation by K–Ar dating of synkinematic illite/muscovite: *Earth and Planetary Science Letters*, p. 221-233.
- Treppmann, C. A., and Stöckhert, B., 2009, Microfabric of folded quartz veins in metagreywackes: dislocation creep and subgrain rotation at high stress: *Journal of Metamorphic Geology*, v. 27, no. 8, p. 555-570.

- Trepmann, C. A., Stöckhert, B., Dorner, D., Moghadam, R. H., Küster, M., and Röller, K., 2007, Simulating coseismic deformation of quartz in the middle crust and fabric evolution during postseismic stress relaxation—an experimental study: *Tectonophysics*, v. 442, no. 1, p. 83-104.
- Tullis, J., and Wenk, H.-R., 1994, Effect of muscovite on the strength and lattice preferred orientations of experimentally deformed quartz aggregates: *Materials Science and Engineering: A*, v. 175, no. 1, p. 209-220.
- van Daalen, M., Heilbronner, R., and Kunze, K., 1999, Orientation analysis of localized shear deformation in quartz fibres at the brittle-ductile transition: *Tectonophysics*, v. 303, no. 1-4, p. 83-107.
- Vernooij, M. G., den Brok, B., and Kunze, K., 2006a, Development of crystallographic preferred orientations by nucleation and growth of new grains in experimentally deformed quartz single crystals: *Tectonophysics*, v. 427, no. 1, p. 35-53.
- Vernooij, M. G., Kunze, K., and den Brok, B., 2006b, 'Brittle' shear zones in experimentally deformed quartz single crystals: *Journal of Structural Geology*, v. 28, no. 7, p. 1292-1306.
- Viola, G., Ganerod, G. V., and Wahlgren, C. H., 2009, Unraveling 1.5 Ga of brittle deformation history in the Laxemar-Simpevarp area, southeast Sweden: A contribution to the Swedish site investigation study for the disposal of highly radioactive nuclear waste (vol 28, art no TC5007, 2009): *Tectonics*, v. 28.
- Viola, G., Kounov, A., Andreoli, M., and Mattila, J., 2012, Brittle tectonic evolution along the western margin of South Africa: More than 500Myr of continued reactivation: *Tectonophysics*, v. 514, p. 93-114.
- Viola, G., Mancktelow, N. S., and Miller, J. A., 2006, Cyclic frictional-viscous slip oscillations along the base of an advancing nappe complex: Insights into brittle-ductile nappe emplacement mechanisms from the Naukluft Nappe Complex, central Namibia: *Tectonics*, v. 25, no. 3, p. TC3016.
- Viola, G., Sandstad, J. S., Nilsson, J. P., and Heincke, B., 2008, Structural and ore geological studies in the northwestern part of the Repparfjord Window, Kvalsund, Finnmark, Norway, p. 93.
- Viti, C., and Collettini, C., 2009, Growth and deformation mechanisms of talc along a natural fault: a micro/nanostructural investigation: *Contributions to Mineralogy and Petrology*, v. 158, no. 4, p. 529-542.
- Vollbrecht, A., Stipp, M., and Olesen, N. Ø., 1999, Crystallographic orientation of microcracks in quartz and inferred deformation processes: a study on gneisses from the German Continental Deep Drilling Project (KTB): *Tectonophysics*, v. 303, no. 1, p. 279-297.
- Wang, K., and Hu, Y., 2006, Accretionary prisms in subduction earthquake cycles: The theory of dynamic Coulomb wedge: *Journal of Geophysical Research: Solid Earth (1978–2012)*, v. 111, no. B6.
- Wells, R., Holyoke, C., Wojtal, S., and Newman, J., Low temperature rheology of calcite and dolomite: experiment and nature, *in Proceedings AGU Fall Meeting Abstracts 2011, Volume 1*, p. 2174.
- Wibberley, C. A. J., 2005, Initiation of basement thrust detachments by fault-zone reaction weakening: *Geological Society, London, Special Publications*, v. 245, no. 1, p. 347-372.
- Wightman, R. H., Prior, D. J., and Little, T. A., 2006, Quartz veins deformed by diffusion creep-accommodated grain boundary sliding during a transient, high strain-rate event in the Southern Alps, New Zealand: *Journal of structural geology*, v. 28, no. 5, p. 902-918.
- Wintsch, R. P., Christoffersen, R., and Kronenberg, A. K., 1995, Fluid-rock reaction weakening of fault zones: *J. Geophys. Res.*, v. 100, p. 13021-13032.
- Zwingmann, H., and Mancktelow, N., 2004, Timing of Alpine fault gouges: *Earth and Planetary Science Letters*, v. 223, no. 3-4, p. 415-425.
- Zwingmann, H., Mancktelow, N., Antognini, M., and Lucchini, R., 2010, Dating of shallow faults: New constraints from the AlpTransit tunnel site (Switzerland): *Geology*, v. 38, no. 6, p. 487-490.





## Appendix A

## – EBSD settings: Acquisition and post processing

**Table A1:** Acquisition settings used during EBSD analysis.

Sample area	Size ( $\mu\text{m}$ )	Accelerating voltage (kV)	Tilt (degrees)	Magnification	Working distance (mm)	Step size ( $\mu\text{m}$ )	Exposure time ( $\mu\text{s}$ )
HJK_001_01	825 x 825	20	70	150x	25,3	2	9950
HJK_001_02	824 x 824	20	70	150x	25,3	2	9950
HJK_001_03	824 x 824	20	70	150x	25,3	2	9950
HJK_001_04	824 x 824	20	70	150x	25,1	2	9950
HJK_001_05	824 x 824	20	70	150x	25,1	2	9950
HJK_001_06	824 x 824	20	70	150x	25,4	2	9950
HJK_001_07	824 x 824	20	70	150x	25,4	2	9950
HJK_001_08	300 x 824	20	70	150 x	25,4	2	9950
HJK_001_09	824 x 824	20	70	150x	25,4	2	9950
HJK_001_10	824 x 824	20	70	150x	26,0	2	9950
HJK_001_11	824 x 824	20	70	150x	25,7	2	9950
HJK_001_12	824 x 824	20	70	150x	25,7	2	9950
HJK_001_13	824 x 824	20	70	150x	25,5	2	9950
HJK_001_14	324 x 756	20	70	150x	25,7	2	9950

**Table A2:** Results from EBSD indexation

<b>Sample area</b>	<b># points</b>	<b># good points</b>	<b># disregarded points</b>	<b>Indexation %</b>	<b>Average Confidence index</b>
HJK_001_01	169744	167033	2711	98,40	0,3
HJK_001_02	169744	165960	3784	97,77	0,24
HJK_001_03	169744	166743	3001	98,23	0,3
HJK_001_04	169744	167041	2703	98,41	0,28
HJK_001_05	169744	158999	10745	93,67	0,66
HJK_001_06	169744	156331	13413	92,10	0,35
HJK_001_07	169744	165267	4477	97,36	0,37
HJK_001_08	61800	60754	1046	98,31	0,19
HJK_001_09	169744	164362	5382	96,83	0,48
HJK_001_10	169744	165275	4469	97,37	1,26
HJK_001_11	169744	166948	2796	98,35	0,66
HJK_001_12	169744	168889	855	99,50	0,69
HJK_001_13	61236	61198	38	99,94	0,67

Table A3: EBSD partition specifications.

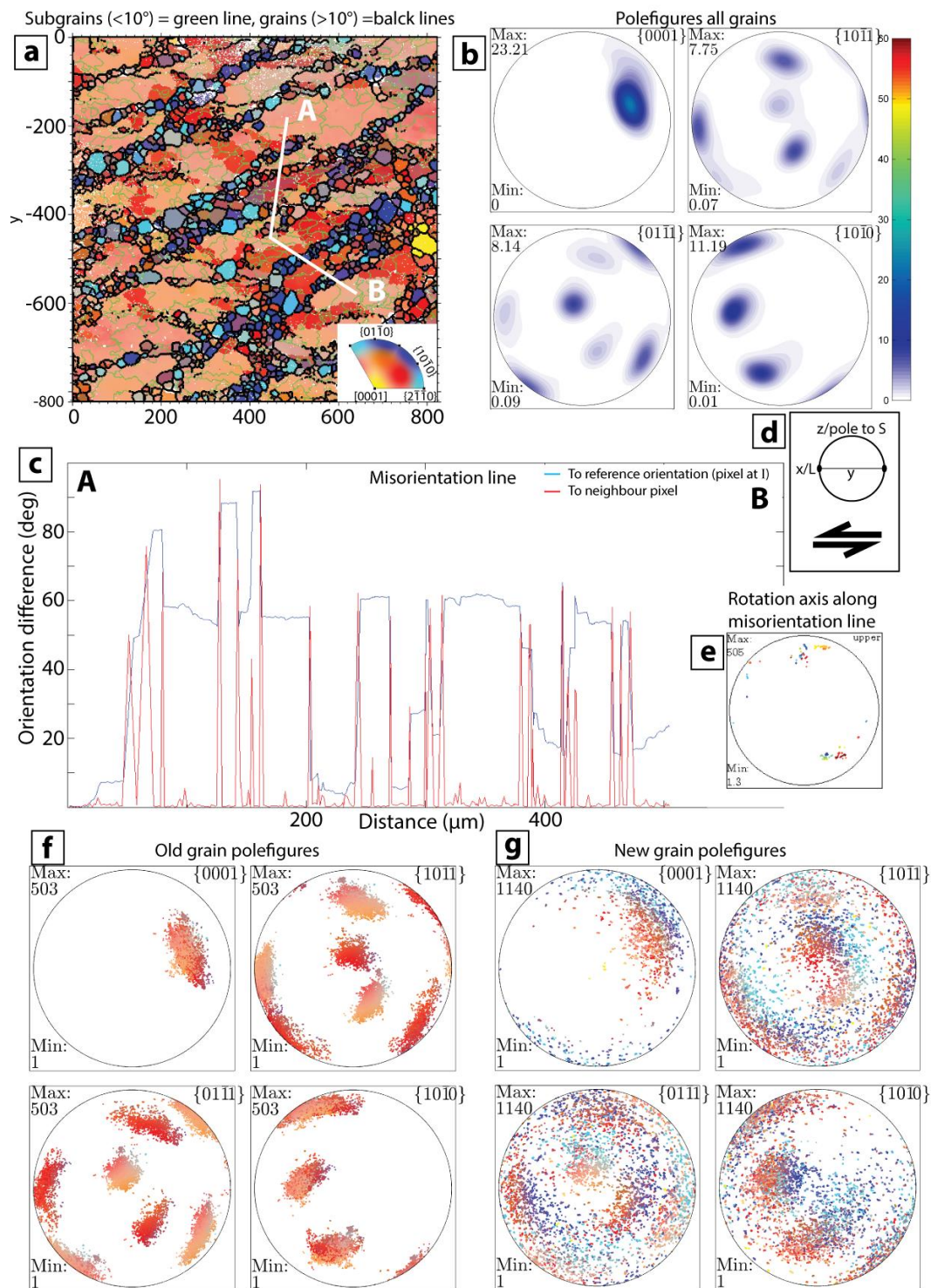
Sample area	Old Grain: Grain size (px)	Old Grains: Aspect ratio	Separating command:   = or, & = and	New Grains: Grain size (px)	New grains: Aspect ratio	Separating command:   = or, & = and
HJK_001_01	>= 1000	>= 1.3	&	<= 400	<= 2.0	&
HJK_001_02	>= 1000	>= 1.4	&	<= 400	<= 2.0	&
HJK_001_03	>= 1000	>= 2.0		<= 550	<= 1.5	&
HJK_001_04	>= 3500	>= 1.9		<= 400	<= 2.0	&
HJK_001_05	>= 800	>= 1.8	&	<= 400	<= 1.6	&
HJK_001_06	>= 1000	>= 1.2	&	<= 500	<= 1.6	&
HJK_001_07	>= 20000	>= 5.0		<= 500	<= 1.5	&
HJK_001_08	>= 1000	>= 4.0		<= 500	<= 1.6	&
HJK_001_09	>= 10000	>= 4.0		<= 600	<= 3.0	&
HJK_001_10	>= 800	>= 5.0		<= 700	<= 1.8	&
HJK_001_11	>= 1000	>= 1.8	&	<= 700	<= 1.8	&
HJK_001_12	>= 400	>= 1.2	&	<= 500	<= 2.0	&
HJK_001_13	>= 1000	>= 2.2		<= 800	<= 2.0	&



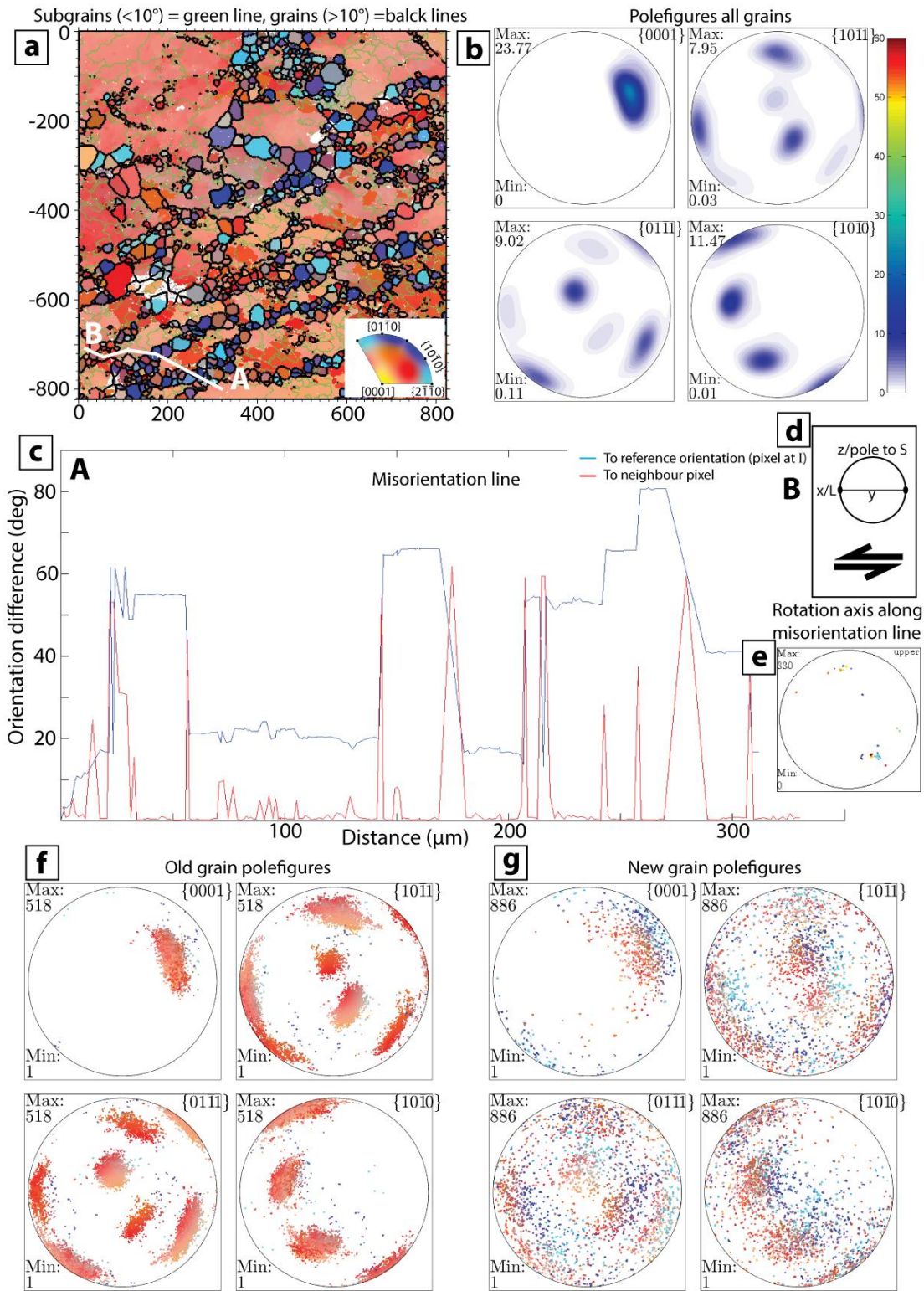


## Appendix B

- EBSD data not Published

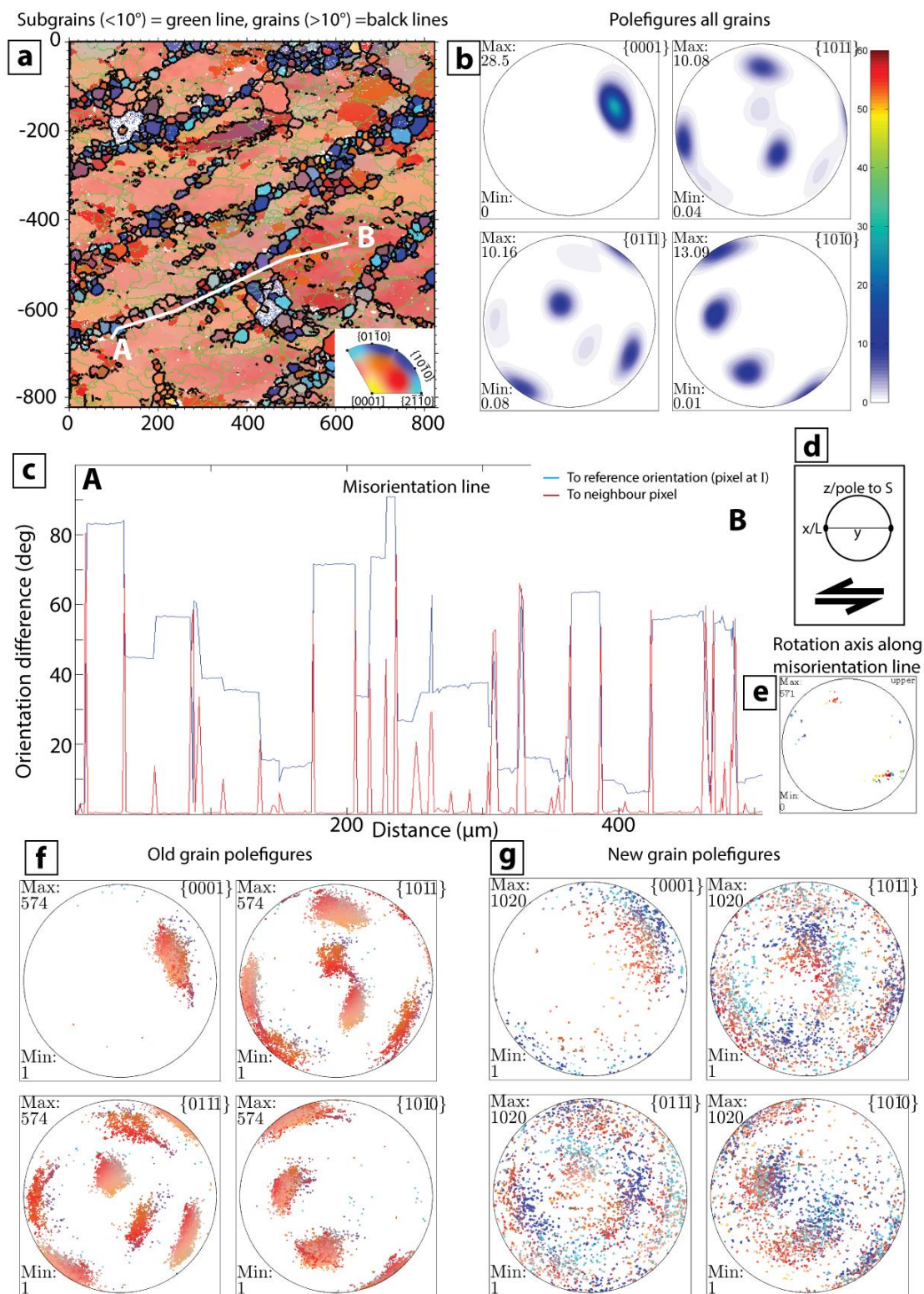


**Figure B1:** (a) EBSD map color-coded after insert. White line shows trace of misorientation plot in (c). (b) Contoured polefigures of  $\{c\}$ ,  $\{r\}$ ,  $\{z\}$  and  $\{m\}$ . (c) Misorientation plot from white line in (a). (d) Sample and map orientation. (e) Rotation axes from misorientation plot in (c). (f) Polefigures for old grains. Same crystallographic axes as in (a). Color-coded as EBSD map. (g) Polefigures for new grains. Same crystallographic axes as in (a). Color-coded as EBSD map.



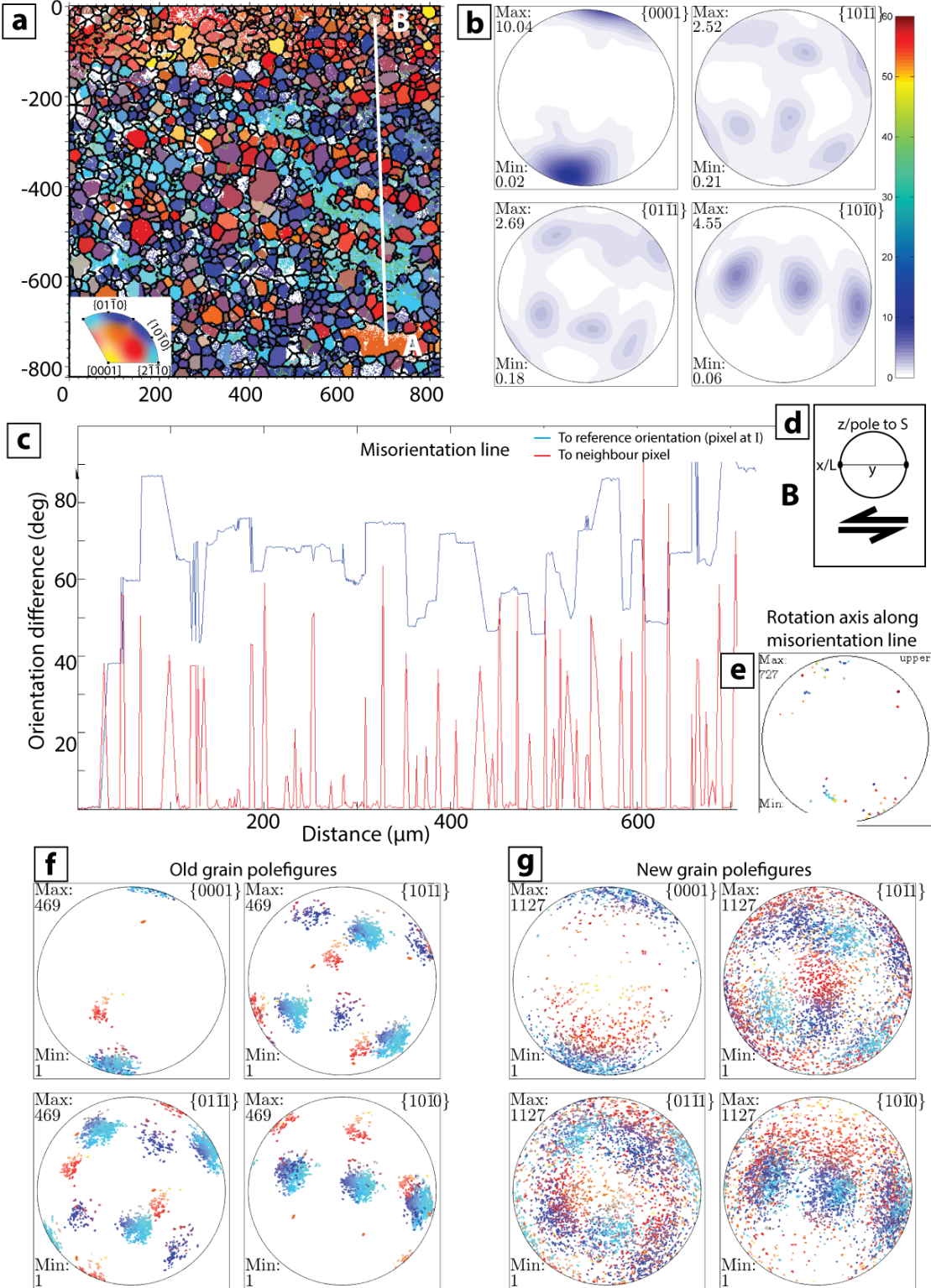
**Figure B2:** (a) EBSD map color-coded after insert. White line show trace of misorientation plot in (c). (b) Contoured polefigures of  $\{c\}$ ,  $\{r\}$ ,  $\{z\}$  and  $\{m\}$ . (c) Misorientation plot from white line in (a). (d) Sample and map orientation. (e) Rotation axes from misorientation plot in (c). (f) Polefigures for old grains. Same crystallographic axes as in (a). Color-coded as EBSD map. (g) Polefigures for new grains. Same crystallographic axes as in (a). Color-coded as EBSD map.





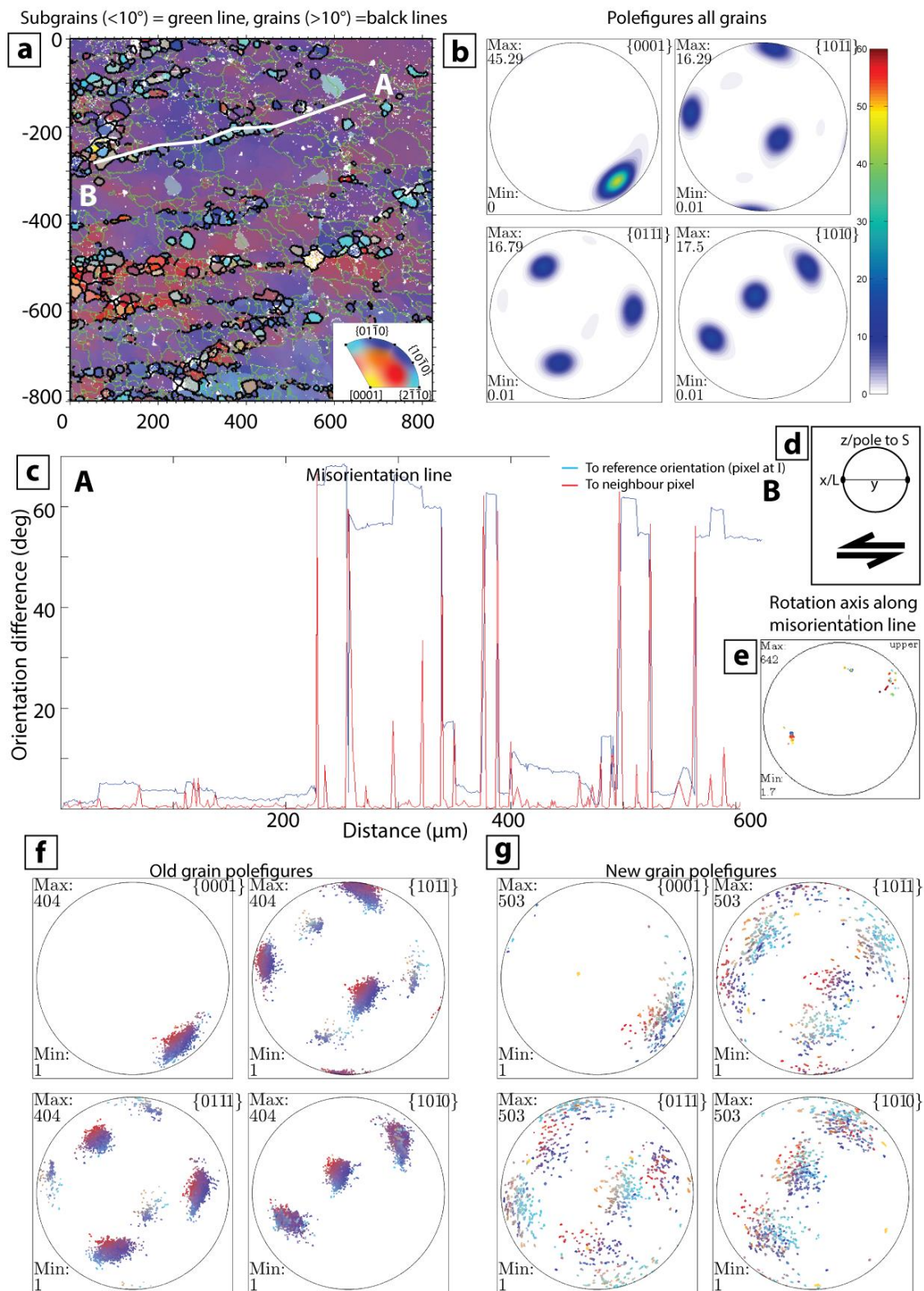
**Figure B3:** (a) EBSD map color-coded after insert. White line show trace of misorientation plot in (c). (b) Contoured polefigures of  $\{c\}$ ,  $\{r\}$ ,  $\{z\}$  and  $\{m\}$ . (c) Misorientation plot from white line in (a). (d) Sample and map orientation. (e) Rotation axes from misorientation plot in (c). (f) Polefigures for old grains. Same crystallographic axes as in (a). Color-coded as EBSD map. (g) Polefigures for new grains. Same crystallographic axes as in (a). Color-coded as EBSD map.

Subgrains ( $<10^\circ$ ) = green line, grains ( $>10^\circ$ ) = black lines



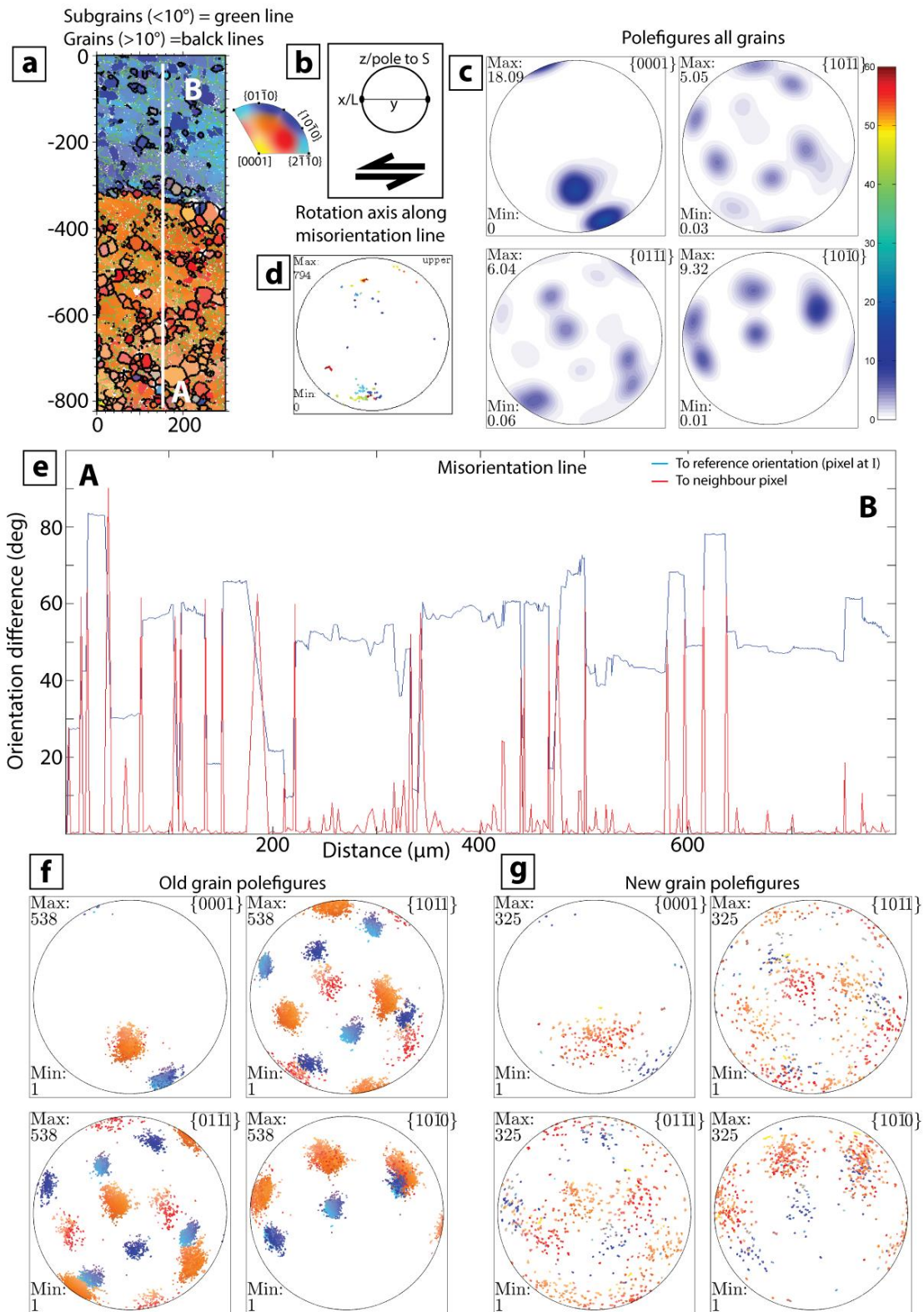
**Figure B4:** (a) EBSD map color-coded after insert. White line show trace of misorientation plot in (c). (b) Contoured polefigures of  $[c]$ ,  $\{r\}$ ,  $\{z\}$  and  $\{m\}$ . (c) Misorientation plot from white line in (a). (d) Sample and map orientation. (e) Rotation axes from misorientation plot in (c). (f) Polefigures for old grains. Same crystallographic axes as in (a). Color-coded as EBSD map. (g) Polefigures for new grains. Same crystallographic axes as in (a). Color-coded as EBSD map.



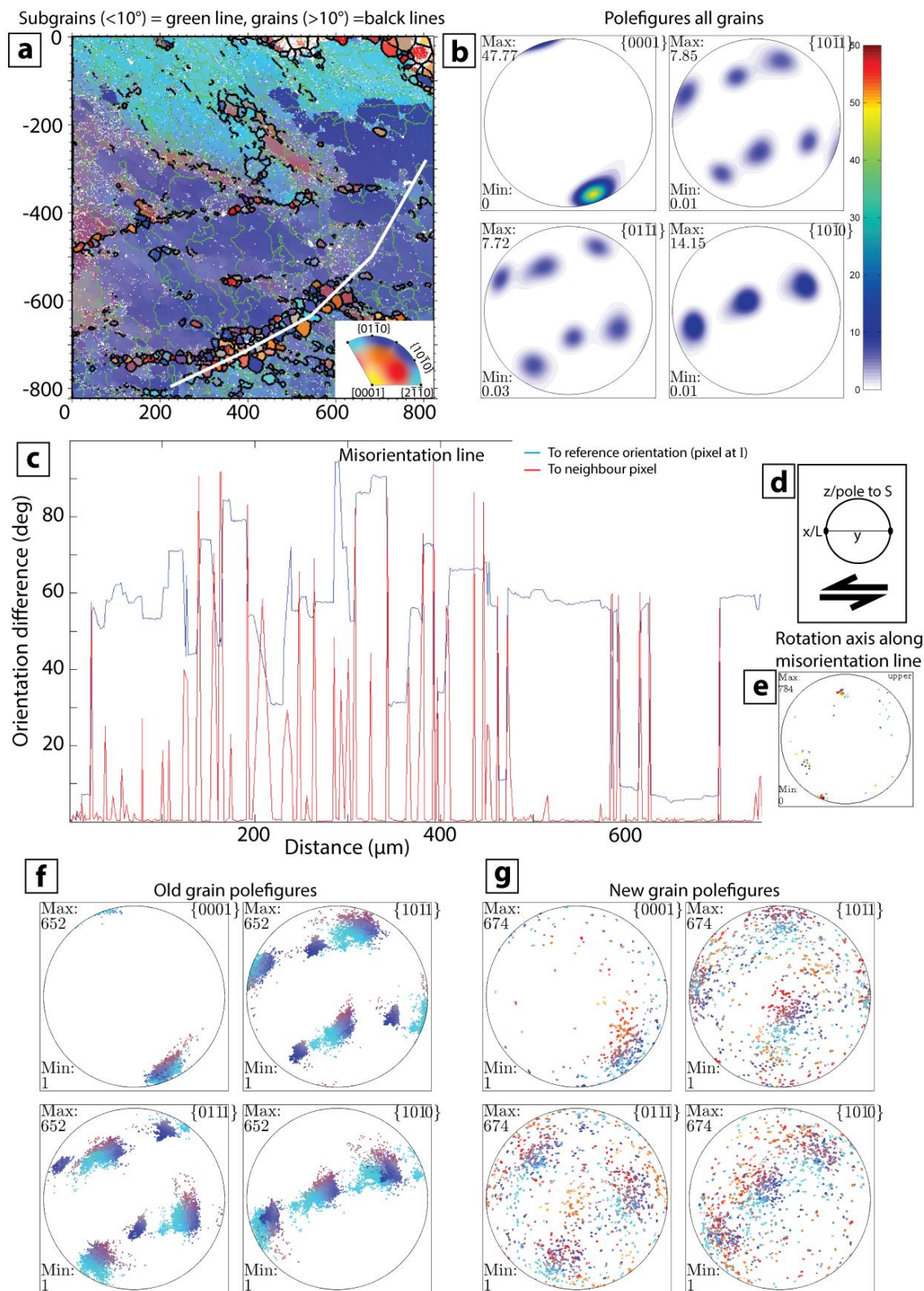


**Figure B5:** (a) EBSD map color-coded after insert. White line show trace of misorientation plot in (c). (b) Contoured polefigures of  $\{c\}$ ,  $\{r\}$ ,  $\{z\}$  and  $\{m\}$ . (c) Misorientation plot from white line in (a). (d) Sample and map orientation. (e) Rotation axes from misorientation plot in (c). (f) Polefigures for old grains. Same crystallographic axes as in (a). Color-coded as EBSD map. (g) Polefigures for new grains. Same crystallographic axes as in (a). Color-coded as EBSD map.





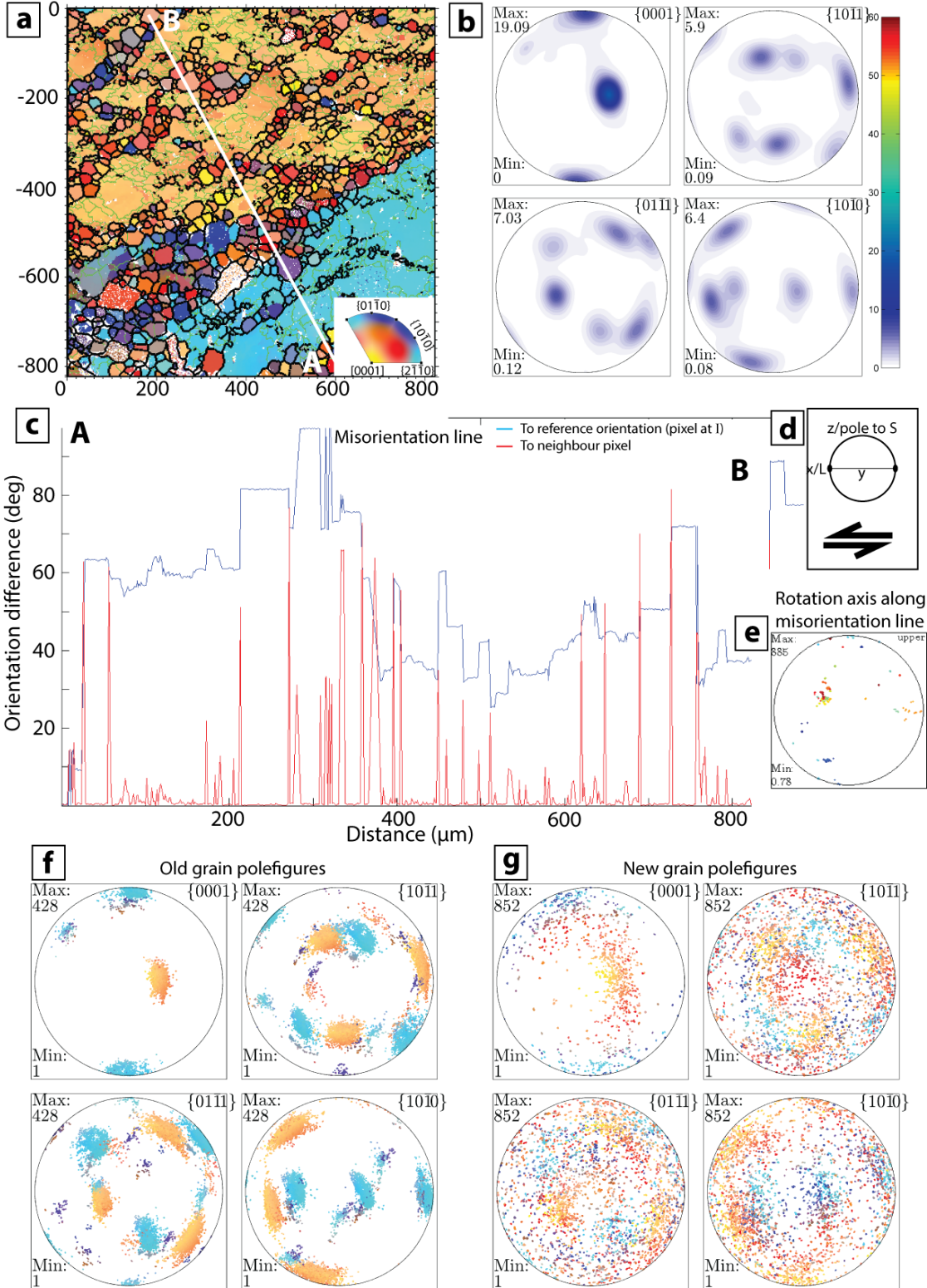
**Figure B6:** (a) EBSD map color-coded after insert. White line show trace of misorientation plot in (e). (b) Sample and map orientation. (c) Contoured polefigures of  $\{c\}$ ,  $\{r\}$ ,  $\{z\}$  and  $\{m\}$ . (d) Rotation axes from misorientation plot in (e). (e) Misorientation plot from white line in (a). (f) Polefigures for old grains. Same crystallographic axes as in (a). Color-coded as EBSD map. (g) Polefigures for new grains. Same crystallographic axes as in (a). Color-coded as EBSD map.



**Figure B7:** (a) EBSD map color-coded after insert. White line show trace of misorientation plot in (c). (b) Contoured polefigures of  $\{c\}$ ,  $\{r\}$ ,  $\{z\}$  and  $\{m\}$ . (c) Misorientation plot from white line in (a). (d) Sample and map orientation. (e) Rotation axes from misorientation plot in (c). (f) Polefigures for old grains. Same crystallographic axes as in (a). Color-coded as EBSD map. (g) Polefigures for new grains. Same crystallographic axes as in (a). Color-coded as EBSD map.

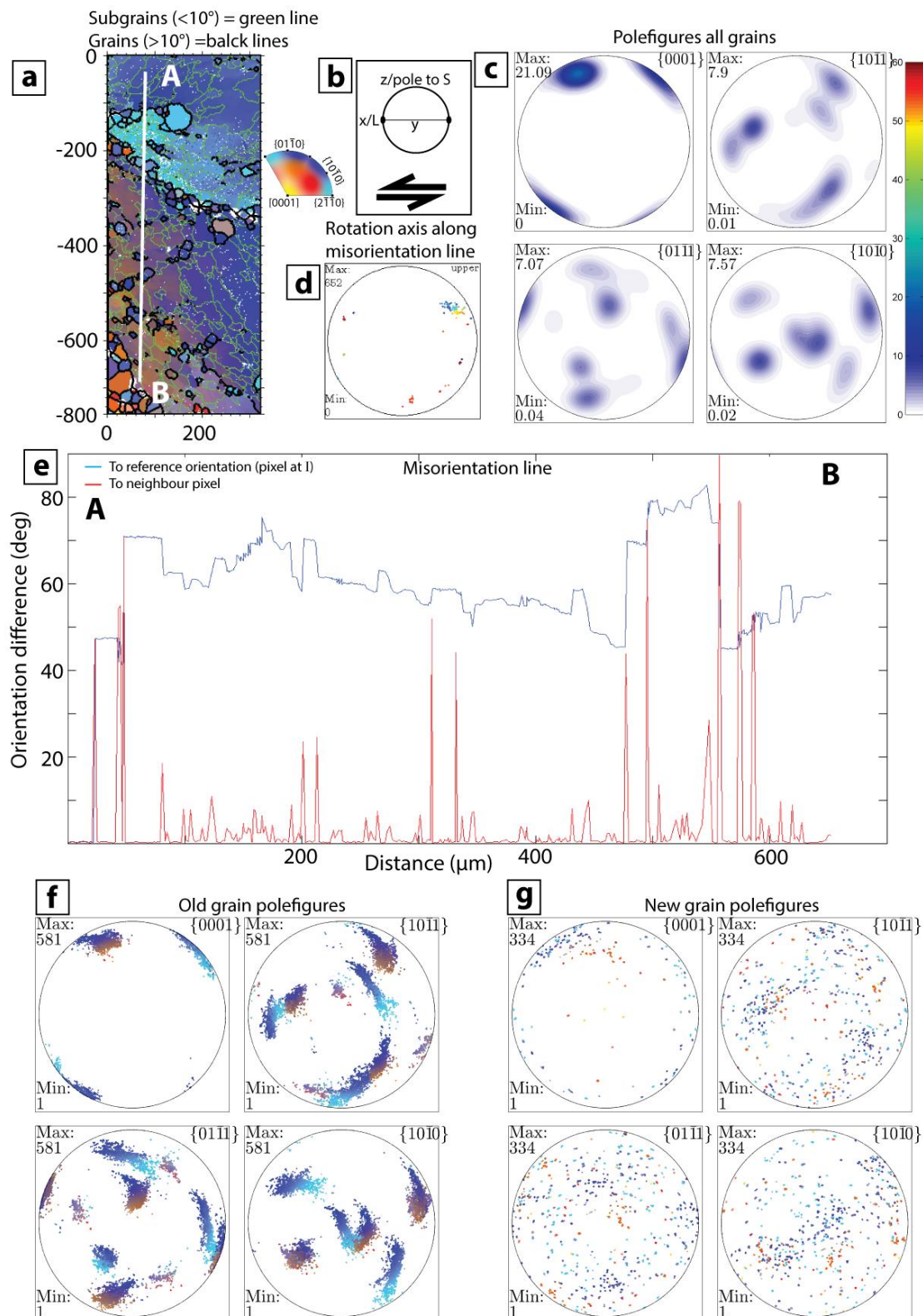


Subgrains ( $<10^\circ$ ) = green line, grains ( $>10^\circ$ ) = black lines



**Figure B8:** (a) EBSD map color-coded after insert. White line show trace of misorientation plot in (c). (b) Contoured polefigures of  $\{c\}$ ,  $\{r\}$ ,  $\{z\}$  and  $\{m\}$ . (c) Misorientation plot from white line in (a). (d) Sample and map orientation. (e) Rotation axes from misorientation plot in (c). (f) Polefigures for old grains. Same crystallographic axes as in (a). Color-coded as EBSD map. (g) Polefigures for new grains. Same crystallographic axes as in (a). Color-coded as EBSD map.





**Figure B6:** (a) EBSD map color-coded after insert. White line show trace of misorientation plot in (e). (b) Sample and map orientation. (c) Contoured polefigures of  $\{c\}$ ,  $\{r\}$ ,  $\{z\}$  and  $\{m\}$ . (d) Rotation axes from misorientation plot in (e). (e) Misorientation plot from white line in (a). (f) Polefigures for old grains. Same crystallographic axes as in (a). Color-coded as EBSD map. (g) Polefigures for new grains. Same crystallographic axes as in (a). Color-coded as EBSD map.



## Appendix C

### – Coordinates for figures

**Table C1:** Coordinates given in WGS 84, UTM zone 34N.

Figure	Sub-figure	North	East
5-3	a-d	621112,90	7817068,29
	e	621563,84	7819742,16
5-4	a, c, d, e and f	621143,64	7819990,82
	b	610155,41	7816849,48
5-5	a	611006,36	7816622,72
	b	610616,94	7816631,63
	c	619506,16	7820118,98
	d	619507,41	7820182,89
	e	612740,25	7819202,85
5-6	a	613709,65	7819652,56
	b, c and d	613179,14	7819806,92
5-7		613782,25	7819602,42
5-8	a and d	606145,77	7819822,43
	c	612291,96	7819507,45
	e	612530,43	7820025,92
	f	620560,27	7820836,62
5-9	a and e	607155,38	7823719,82
	b	607873,52	7824095,56
	c	605298,16	7822106,04
	d	607188,41	7823661,59
	f	604099,51	7820520,31
5-10	a, b and d	c. 612266,21	c. 7820262,11
	c	612510,78	7823588,80
	e	604882,69	7821045,19
	f	607392,99	7822417,90
5-11	a	613046,90	613046,90
	b and c	613435,55	7825683,58
	d and f	610858,96	7823108,42
5-12	a	608274,02	7819101,48
	b	607992,63	7819307,18
	c	612375,13	7825360,60
	d	609175,87	7821067,96
	e	605301,29	7820591,91
	f	614694,85	7822495,23
6-2	a	621112,90	7817068,29
	b	606308,25	7822087,43
	c	612670,91	7820002,19
	d	607157,65	7821967,30
	e	605939,75	7820105,94
	f	605360,40	7820451,51
6-4	b	612322,18	7820529,48
	c and d	612539,48	7820376,93
6-5		612539,48	7820376,93
6-6		612322,18	7820529,48
6-7		610275,07	7817062,98
6-10		612740,25	7819202,85
6-11		609866,12	7819835,87
6-12		608236,08	7822092,28
6-14	a and d	608342,05	7824182,67
	b	607479,88	7822651,54
	c	607390,78	7822574,67
6-15		606035,14	7820067,66
6-17		603829,82	7819306,85
6-19		605360,40	7820451,51
6-20	a	605258,78	7820452,99
	b and c	605301,29	7820591,91
	d and e	605189,16	7820533,63
6-21		605500,29	7821932,64





**Appendix D**

**– Geological map of the PIS**